Technical University of Munich
TUM Campus Straubing for Biotechnology and Sustainability

On the Application of Plate Heat Exchangers in Adsorption Processes

Makram Shokry Ebid Mikhaeil

Complete reprint of the dissertation approved by the TUM Campus Straubing for Biotechnology and Sustainability of the Technical University of Munich for the award of the Doktor der Ingenieurwissenschaften (Dr.-Ing).

Chair: Prof. Dr.-Ing. Jakob Burger

Examiners:

1. Prof. Dr.-Ing. Matthias Gaderer
2. Prof. Dr.-Ing. Belal Dawoud
3. Prof. Dr.-Ing. Majid Bahrami

The dissertation was submitted to the Technical University of Munich on 27 June 2023 and accepted by the TUM Campus Straubing for Biotechnology and Sustainability on 27 September 2023.

I dedicate this thesis to my parents, who have been the pillars of my life and the driving force behind my pursuit of knowledge. In particular, I dedicate this work to my beloved father, who passed away a few months ago. His unwavering love, support, and encouragement have been a constant source of inspiration throughout my academic journey. Although he is no longer with us, his memory will continue to guide and motivate me in all my future endeavors.

Rest in peace, Dad. This is for you.

Declaration

I hereby declare that except where specific reference is made to the work of others, the contents of this dissertation are original and have not been submitted in whole or in part for consideration for any other degree or qualification in this, or any other university. This dissertation is my own work and contains nothing which is the outcome of work done in collaboration with others, except as specified in the text and Acknowledgements. This dissertation contains fewer than 65,000 words including appendices, bibliography, footnotes, tables and equations and has fewer than 120 figures.

Makram Mikhaeil
December 2023

Acknowledgements

I would like to express my deepest gratitude to my supervisor, Prof. Belal Dawoud, for giving me the opportunity to work in his laboratory and for sharing his vast knowledge and experience with me. His guidance, support, and encouragement have been invaluable throughout my research journey.

I am also grateful to my supervisor, Prof. Matthias Gaderer, for his insightful comments, constructive feedback, and unwavering support. His expertise and guidance have been instrumental in shaping my research project.

I would like to extend my sincere appreciation to the laboratory technician, Mr. Martin Kerscher, for his invaluable technical support and assistance throughout my stay in the laboratory. Mr. Kerscher's expertise and dedication in the preparation and installation of experimental equipment and setups have been crucial to the success of my research project. His passion for his work and his unwavering commitment to the Laboratory of Sorption Processes are truly inspiring.

I would like to thank my colleague in the laboratory, Mr. Jeremy Weindler, for his constant support, helpful discussions, and willingness to listen.

Furthermore, I would like to express my heartfelt gratitude to the Catholic Academic Exchange Service (in German: Katholische Akademische Ausländer-Dienst, KAAD) for their generous scholarship and financial support throughout my PhD study. The opportunity provided by KAAD has enabled me to pursue my academic aspirations and has been instrumental in the successful completion of this research.

I am sincerely grateful to the BayWISS Joint Academic Partnership "Energy" for their invaluable support that has significantly contributed to the success of my PhD study.

Finally, I would like to express my deepest gratitude to my parents and my family for their unwavering love and support throughout my academic journey. Their encouragement and support have been my constant source of inspiration and motivation.

Thank you all for your support and guidance. This work would not have been possible without your help.

Abstract

The application of the thermally driven adsorption (TDAd) systems seems to be highly promising to enable sustainable cooling and heating, as the driving energy is low-grade heat, which is abundantly available from solar and waste heat sources. In addition, the TDAd systems enable the use of water as refrigerant, which has neither a global warming potential (GWP) nor an ozone depletion potential (ODP). However, the TDAd systems are still, by far, less efficient, and more expensive than traditional vapour compression systems.

The heat exchangers applied in the TDAd systems, so far, are taken from other applications and has always shown either a poor performance or a severe corrosion under the relevant operating conditions. On the other hand, the manufacturing technology of the nickel brazed stainless steel Plate Heat Exchanger (PHE) becomes quite affordable and offers significantly high thermal efficiency with high level of design flexibility, compactness and reliability. However, no PHEs designed dedicatedly for the application in the TDAd systems are available in the market. Accordingly, innovative PHEs must be dedicatedly designed for the application in the TDAd systems, in order to realize high and reliable performance as well as low manufacturing costs.

In this thesis, design flow chart relying on experimental and numerical approaches was developed and followed to come up with the best design of the Adsorber Plate Heat Exchanger (APHE). The design flow chart includes small-scale and full-scale experimental investigations of different commercially available PHEs adapted in the lab to act as adsorbers. Experimental investigation has been performed on small-scale adsorbent samples of different heat and mass transfer characteristic length (HTCL and MTCL) to understand their effect on the adsorption and desorption kinetics. Based on the obtained results, it can be concluded that the adsorption kinetics inside the adsorbent domain of an APHE are mainly dominated by the MTCL, whereas the desorption kinetics are dominated by the HTCL. In order to optimize the design of the APHE, a 3-D mathematical model simulating the performance of a real APHE was developed in COMSOL Multiphysics and validated against our obtained experimental results. Finally, innovative configuration of the APHE was developed and the 3-D simulation model was utilized in the systematic assessment of both HTCL and MTCL of

the new design. Moreover, the 3-D model was applied to predicted the performance of the newly designed APHE.

This thesis aimed also to investigate the application of the plate-type heat exchanger as evaportor in the adsorption appliances. To this aim, an experimental and analytical study on the evaporation mechanism in a closed-structured PHE employed as a stagnant water evaporator was conducted. Two endoscopes were mounted inside the investigated evaporator to visualize the evaporation mechanism when performing adsorption-evaporation processes under different boundary conditions. It turned out that the evaporation mechanism was a partially covered, thin film evaporation. A heat transfer analysis was performed to evaluate the heat transfer coefficient of the thin film evaporation inside the investigated evaporator. Besides, an analytical model has been developed to correlate the overall evaporator heat transfer coefficient with the adsorption potential and the time rate of change of the water uptake in the adsorber.

The results obtained in this thesis imply the appropriateness of the PHE application in the adsorption systems, which could bring several advantages in terms of the system compactness and, accordingly, the specific power density of the system. Besides, the construction cost of the adsorption appliance may be considerably reduced if the closed-structure PHEs are adopted for use, as there is no longer a need to place neither the adsorber/desorber nor the evaporator/condenser inside a larger vacuum chamber, which is quite bulky and costly. The extremely durable operation because of the no corrosion potential is a special added advantage.

Kurzfassug

Die Anwendung von thermisch betriebenen Adsorptions- (TDAd) Systemen erscheint äußerst vielversprechend für nachhaltige Kühl- und Heizlösungen, da die Antriebsenergie Niedertemperaturwärme ist, welche reichlich aus Abwärme und solaren Energiequellen verfügbar ist. Darüber hinaus ermöglichen die TDAd-Systeme den Einsatz von Wasser als Kältemittel, das weder ein Treibhauspotenzial noch ein Ozonabbaupotenzial besitzt. Allerdings sind die TDAd-Systeme bisher bei weitem weniger effizient und teurer als herkömmliche Dampfkompressionssysteme.

Die in den TDAd-Systemen bisher verwendeten Wärmeübertrager stammen aus anderen Anwendungen und haben entweder eine schlechte Leistung oder leiden unter schwerer Korrosion bei den relevanten Betriebsbedingungen. Auf der anderen Seite ist die Fertigungstechnologie für plattenverschweißte Edelstahl-Plattenwärmeübertrager (PHE) erschwinglich geworden und bietet eine deutlich höhere Wärmeübertragungseffizienz, sowie ein hohes Maß an Designflexibilität, Kompaktheit und Zuverlässigkeit. Allerdings sind derzeit keine PHEs speziell für den Einsatz in TDAd-Systemen auf dem Markt erhältlich. Daher müssen innovative PHEs speziell für die Anwendung in TDAd-Systemen entwickelt werden, um eine hohe und zuverlässige Leistung, sowie geringere Herstellungskosten zu erreichen.

In dieser Dissertation wurde ein Design-Flussdiagramm entwickelt, das sich auf experimentelle und numerische Ansätze stützt zur Entwicklung eines optimalen Designs für den Adsorber-Plattenwärmeübertrager (APHE). Das Design-Flussdiagramm umfasst experimentelle Untersuchungen im kleinen Maßstab, sowie im vollen Maßstab verschiedener kommerziell erhältlicher PHEs, die im Labor als Adsorber eingesetzt wurden. Experimentelle Untersuchungen wurden an kleinen Proben von Adsorbenten mit unterschiedlicher, sogenannter charakterischer Wärme- und Stoffübertragungslänge (HTCL und MTCL) durchgeführt, um deren Auswirkungen auf die Adsorptions- und Desorptionskinetik zu verstehen. Basierend auf den erhaltenen Ergebnissen kann abgeleitet werden, dass die Adsorptionskinetik innerhalb des Adsorbensbereichs eines APHEs hauptsächlich durch die MTCL bestimmt wird, während die HTCL für die Desorptionskinetik hauptauschlaggebend ist. Um das Design des APHE zu optimieren, wurde ein 3D-mathematisches Modell entwickelt, das

die Leistung eines realen APHEs in COMSOL Multiphysics simuliert und mit den erhaltenen experimentellen Ergebnissen validiert wurde. Schließlich wurde eine innovative Konfiguration des APHE entwickelt, und das 3D-Simulationsmodell ist zur systematischen Bewertung von HTCL und MTCL des neuen Designs zum Einsatz gekommen. Darüber hinaus wurde das 3D-Modell zur Vorhersage der Leistung des neu entwickelten APHE verwendet.

Diese Dissertation zielt auch darauf ab, die Anwendung des Plattenwärmeübertragers als Verdampfer in Adsorptionsgeräten zu untersuchen. Zu diesem Zweck wurde eine experimentelle und analytische Studie zum Verdampfungsmechanismus in einem geschlossenen PHE als ruhendem Wasserverdampfer durchgeführt. Zwei Endoskope wurden im untersuchten Verdampfer installiert, um den Verdampfungsmechanismus bei der Durchführung von Adsorptions-Verdampfungsprozessen unter verschiedenen Randbedingungen zu visualisieren. Es stellte sich heraus, dass der Verdampfungsmechanismus eine teilweise bedeckte Dünnschichtverdampfung war. Eine Wärmeübertragungsanalyse wurde durchgeführt, um den Wärmeübertragungskoeffizienten der Dünnschichtverdampfung im untersuchten Verdampfer zu bewerten. Darüber hinaus wurde ein analytisches Modell entwickelt, um den Gesamt-Wärmeübertragungskoeffizienten des Verdampfers mit dem Adsorptionspotenzial und der zeitlichen Änderungsrate der Wasseradsorption im Adsorber in Beziehung zu setzen.

Die in dieser Dissertation erhaltenen Ergebnisse deuten auf die Eignung der PHE-Anwendung in Adsorptionssystemen hin, was mehrere Vorteile in Bezug auf die Kompaktheit des Systems und damit auf dessen spezifische Leistungsdichte mit sich bringen könnte. Darüber hinaus könnten die Baukosten der Adsorptionsgeräte erheblich reduziert werden, durch Verwendung von geschlossenen PHEs. Dadurch besteht kein Bedarf mehr, weder den Adsorber/Desorber noch den Verdampfer/Kondensator in einer größeren, meist sperrigen und kostenspieligen Vakuumkammer, zu platzieren. Der äußerst wiederstandsfähige Betrieb aufgrund des fehlenden Korrosionspotenzials ist ein besonderer Vorteil.

Table of contents

List of figures

List of tables

Nomenclature

A	Area, m^2
C	Specific heat capacity, $J.kg^{-1}.K^{-1}$
D_{eff}	effective diffusion coefficient, $m^2.s^{-1}$
d_p	Adsorbent particle diameter, m
E_a	Activation energy of surface diffusion, $J.mol^{-1}$
F	Dubinin-Polanyi potential or the adsorption potential, $kJ.kg^{-1}$
m	mass, kg
h_{fg}	Latent heat of the water evaporation, $J.kg^{-1}$
K_{app}	Apparent permeability of adsorbent bed, m^2
k	Thermal conductivity, $W.m^{-1}.K^{-1}$
P	Water Vapour pressure, $W.m^{-1}.K^{-1}$
q_{in}	Specific heat added to the adsorber heat exchanger, $J.{kg_{ad}}^{-1}$
$q_{s,ADHEx}$	Sensible heat added to adsorber heat exchanger components, $J.{kg_{ad}}^{-1}$
R	Gas constant $J.kg^{-1}.K^{-1}$
R^2	Coefficient of determination,-
r	Ratio of characteristic time constant,-
r_p	Adsorbent particle radius, m
T	Temperature, °C, K
t	Time, s
u	Velocity vector, $m.s^{-1}$
w	Water uptake, $g.(100g)^{-1}$
w^*	Water uptake at equilibrium state, $g.(100g)^{-1}$

Greek letters

Δh_{ads}	Isosteric heat of adsorption, $kJ.mol^{-1}$
Δw	Differential water uptake, $g.(100g)^{-1}$
ε	Porosity,-
μ	Dynamic viscosity, $Pa.s$
ρ	Density, $kg.m^{-3}$
$\sigma_{\Delta w_f}$	Measurement uncertainty of the final differential water uptake, $g.(100g)^{-1}$
τ	characteristic time constant, s

Scripts

0	initial
ads	adsorbent
b	bed
$cond$	cond
des	desorption
eq	equivalent
ev	evaporator
f	final, film
h	heat source
m	metal
max	maximum
min	minimum
p	particle
$precool.$	precooling
$preheat.$	preheating
sat	saturation
t	total
v	water vapour

Abbreviations

APHE	Adsorber Plate Heat Exchanger
ARD	Average Relative Deviation
COP	Coefficient Of Performance
HTCL	Heat Transfer Characteristic Length, *mm*
HTF	Heat Transfer Fluid
LPJ	Large Pressure Jump
LTJ	Large Temperature Jump
MTCL	Mass Transfer Characteristic Length, *mm*
RMSD	Root Mean Square Deviation
SCP	Specific Cooling Power, $W.kg_{ad}{}^{-1}$
SP	Specific Power output, $W.kg_{ad}{}^{-1}$
S/m	Ratio of the heat transfer surface area to the adsorbent dry mass, $m^2.kg^{-1}$
$TDAd$	Thermally driven adsorption
TF	Test Frame

Chapter 1

Introduction

Nearly half of the energy demand in buildings was consumed in 2021 for space and water heating, resulting in 2450 million tons of direct CO2 emissions [1]. According to the International Energy Agency, the global demand for air conditioning (space cooling and heating) is expected to grow very rapidly over the next 30 years, contributing to 49.4% of global electricity demand growth [2]. Regarding the direct consumption of fossil fuels for space heating, according to the latest figures [1], more than 60% of heating energy demand of buildings is still met by direct consumption of fossil fuels. Efficient and low-carbon heating and cooling technologies are, therefore, gaining more importance worldwide, especially those focusing on the exploitation of low-grade heat sources.

Through this PhD study, a unique contribution to the R&D sector of one of the most promising technologies targeting the exploitation of low-grade heat sources (T<100 °C) [3–5] for meeting the space heating and cooling demands of buildings and, accordingly, mitigating the global warming potential will be introduced. The technology of thermally driven adsorption (TDAd) systems, like chillers, heat pumps [6, 7] and thermal storage [8, 9], is a promising sustainable solution for covering cooling and heating demands of buildings and vehicles [10–12]. However, such technology is not yet mature [13, 14] and further R&D activities are still required on the level of the adsorption materials, system components and system management. This PhD shall contribute to the R&D on the system components level, with an open eye not only on the performance, but also on the sustainability and compactness of the system.

A TDAd system is mainly composed of a number of heat exchangers (HEs) connected together but functioning differently. Apart from the HEs integrated into the TDAd systems for the heat and mass recovery, a typical TDAd system consists mainly of three HEs, namely the adsorber/desorber, the evaporator and the condenser. Indeed, there are many research communications dealing with the investigation and development of the adsorber/desorber,

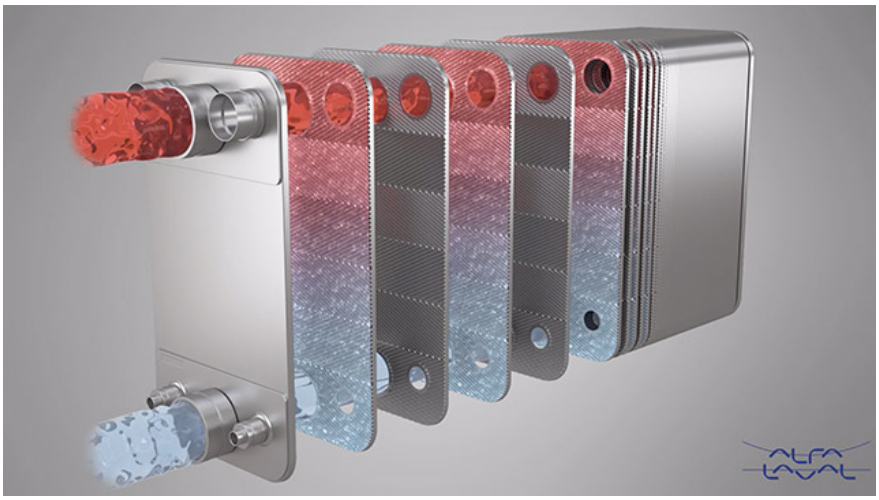

Fig. 1.1 Configuration of a nickel-brazed stainless steel plate heat exchanger (PHE) available commercially from AlfaLaval[1], Sweden.

but with little attention to sustainability, long-term durability and system compactness. In addition, there is a noticeable lack of research addressing the investigation and development of HEs for use as evaporator and condenser in the TDAd systems.

1.1 Application of PHE in TDAd systems

The HEs applied in the TDAd systems, so far, are taken from other applications and has always shown either a poor performance or a severe corrosion under the relevant operating conditions. On the other hand, the manufacturing technology of nickel-brazed stainless steel plate heat exchangers (PHEs) is quite affordable and offers a great design flexibility. A PHE is a type of compact heat exchanger that makes use of a set of thin metal plates to transfer heat from one fluid to another. Figure 1.1[1] shows the configuration of a nickel-brazed stainless steel PHE. One of the peculiarities of the PHEs that plays a significant role in the heat transfer between the fluids and metal plates is the existence of corrugations on the plate surfaces [15], i.e. chevrons or dimples of different forms, dimensions or angles (see Figure 1.2[2]). In fact, these heat exchangers are characterized by a significantly higher thermal efficiency combined with high compactness and reliability.

However, no PHEs designed dedicatedly for the application in the TDAd systems are available in the market. Accordingly, innovative PHEs must be dedicatedly designed for the

[1] www.alfalaval.com
[2] www.technoserviceco.com

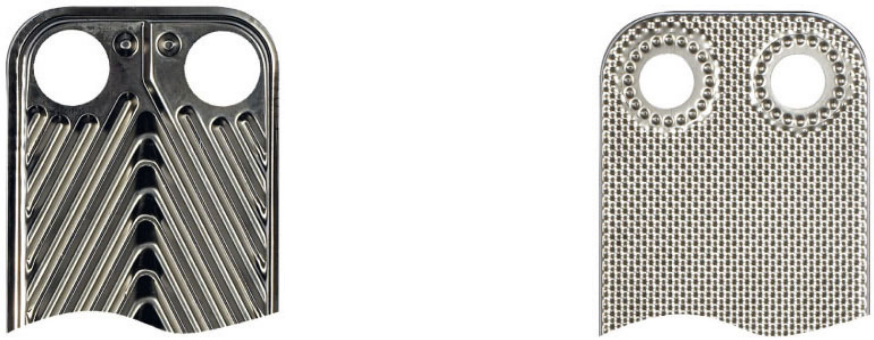

(a) (b)

Fig. 1.2 Individual plate of a PHE[2], (a) chevron form (b) dimple form

application in the TDAd systems, in order to realize high and reliable performance as well as low manufacturing costs.

1.2 Objective of the thesis

The main objective of this thesis is, therefore, to develop and design a highly efficient, compact and sustainable plate-type adsorber heat exchanger for the application in the TDAd systems.

To this aim, the development and design flow chart depicted in Figure 1.3, which relies on experimental and numerical approaches, will be followed to come up with an optimized design of the Adsorber Plate Heat Exchanger (APHE). The development and design flow chart includes experimental investigation of different commercially available PHEs adapted to act as adsorbers. In the meanwhile, small-scale adsorbent samples of the same Heat and Mass Transfer Characteristic Lengths (HTCL and MTCL) of the adsorbent domain inside the investigated APHEs shall be carefully designed and experimentally investigated using a Volumetric Large Temperature Jump (V-LTJ) kinetic setup. The kinetic results of each investigated APHE and its representative adsorbent sample shall be compared. Obtaining a good matching between the kinetics of both small-scale samples and full-scale APHEs is the way to step into the next stage of the proposed development and design flow chart, which aims to experimentally investigate small-scale adsorbent samples of different HTCL and MTCL to fully understand their effect on the adsorption and desorption kinetics. In order to optimize the design of the APHE, a 3-D mathematical model simulating the performance of a real APHE shall be developed in COMSOL Multiphysics and validated against the obtained experimental results. In the last stage of the development and design flow chart, innovative configurations of the APHE shall be developed and the 3-D simulation model

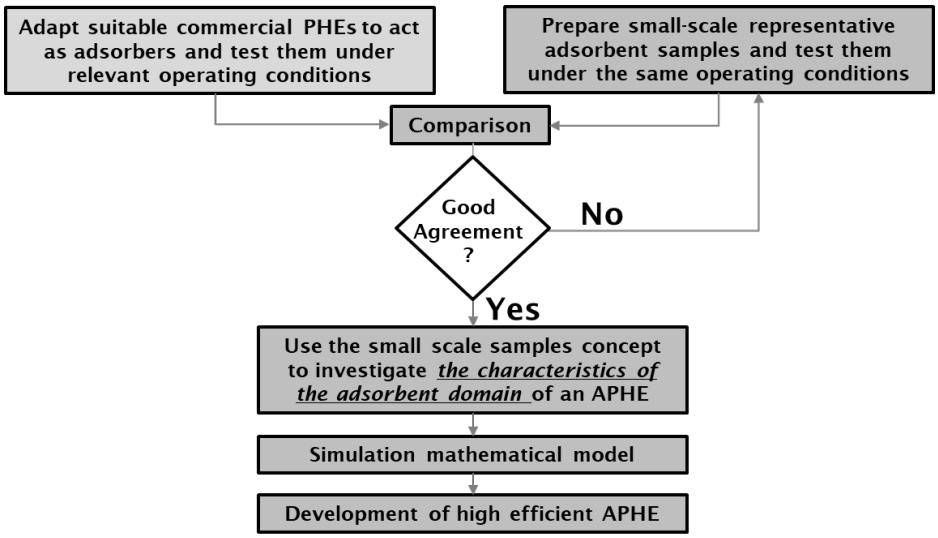

Fig. 1.3 APHE's development and design flow chart

shall be utilized in the assessment of both HTCL and MTCL of the new design. Finally, the 3-D model will be utilized in predicting the performance of the newly designed APHE.

Beside the design optimization of the APHE, this thesis aims to investigate the application of the plate-type heat exchanger as evaportor in the adsorption appliances. To this aim, an experimental and analytical study on the evaporation mechanism in a closed-structured PHE employed as a stagnant water evaporator is conducted. Endoscopes are mounted inside the investigated evaporator to visualize the evaporation mechanism when performing adsorption-evaporation processes under different boundary conditions. A heat transfer analysis is performed to evaluate the heat transfer coefficient of the evaporation inside the investigated evaporator. Besides, an analytical model is developed to correlate the evaporator performance with the adsorber performance.

1.3 Structure of the thesis

The thesis is composed of the following chapters:

- **Chapter 2** discusses the state of the art of the heat exchangers applied in the TDAd systems. The techniques of measuring the adsorption and desorption kinetics of small-scale adsorbent samples will be discussed. Moreover, the published results in literature on the matching between small-scale kinetic measurements and full-scale ones will be presented and discussed.

- **Chapter 3** presents the adaptation work done on two different commercially available plate heat exchangers to realize lab-scale Adsorber Plate Heat Exchangers (APHEs). In addition, the chapter presents the experimental investigation results of the adsorption and desorption kinetics of the two APHEs. A new methodology developed to prepare small-scale adsorbent samples representative in terms of the heat and mass transfer characteristic lengths (HTCL and MTCL) to the adsorbent domain inside the investigated APHEs is presented. The experimental kinetic results of the small-scale adsorbent samples are presented and compared to the results of the APHEs.

- **Chapter 4** presents the development of a 3-D mathematical model implemented in COMSOL Multiphysics software. The model calibration and validation against the APHEs' kinetic results are presented.

- **Chapter 5** presents the performance predicted of an innovative open structured APHE designed recently by the research team of the Laboratory of Sorption Process (LSP) at OTH Regensburg. The methodology introduced in Chapter 2, to prepare small-scale adsorbent sample representative to the adsorbent domain of a real APHE, beside the 3-D simulation model presented in Chapter 4 are applied to predict the performance of the newly introduced APHE of the LSP's research team.

- **Chapter 6** presents experimental and analytical investigation of the effect of the HTCL and the MTCL on the adsorption and desorption kinetics of small-scale adsorbent samples prepared dedicatedly to be representative to the adsorbent domain inside two different open structured APHEs (presented in Chapter 3 and 5).

- **Chapter 7** introduces an innovative design concept of a closed structured APHE. In addition, the 3-D simulation model is utilized to assess the HTCL and MTCL of the new design and applied to predicted the performance.

- **Chapter 8** presents the application of the plate-type heat exchanger as an evaportor in an adsorption appliance. An experimental and analytical study on the evaporation mechanism in a closed-structured PHE employed as a stagnant water evaporator is presented. Besides, the chapter introduces an analytical model, which correlates the overall evaporator heat transfer coefficient with the adsorption potential and the time rate of change of the water uptake in the adsorber.

- **Chapter 9** summarizes the results of the thesis and addresses some future research topics.

Chapter 2

State of the art of the heat exchangers applied in the adsorption systems

In this chapter, the basic definitions and fundamentals of TDAd systems are first presented. Then, a very specific literature review on the aspects most related to the objectives of this dissertation is presented and discussed. In addition, the sustainability of the adsorber heat exchanger, the fundamentals of proper selection of the adsorbent-adsorbate working pair, the configuration of the adsorber heat exchanger, the kinetic setups, and the matching between full-scale and small-scale adsorption kinetic measurements are covered.

The last section of this chapter (Section 2.11) presents the state of the art of evaporator heat exchangers applied so far in adsorption appliances with particular emphasis on the use of plate heat exchangers with water as a refrigerant.

2.1 Adsorption phenomenon

Adsorption is a process in which the molecules of a fluid come into contact with the surface of a solid substance and adhere to it. When the adsorption phenomenon is caused mainly by van der Waals forces and electrostatic forces between the adsorbate molecules and the molecules forming the surface of the adsorbent, without any chemical bonding, the process is called physical adsorption. When the adsorbate and adsorbent interact chemically, the process is called chemical adsorption or chemisorption. Unlike physical adsorption, chemical adsorption assumes that molecules cannot move freely on or within the surface. The release of fluid molecules from the solid surface is called desorption, which is the opposite process of adsorption.

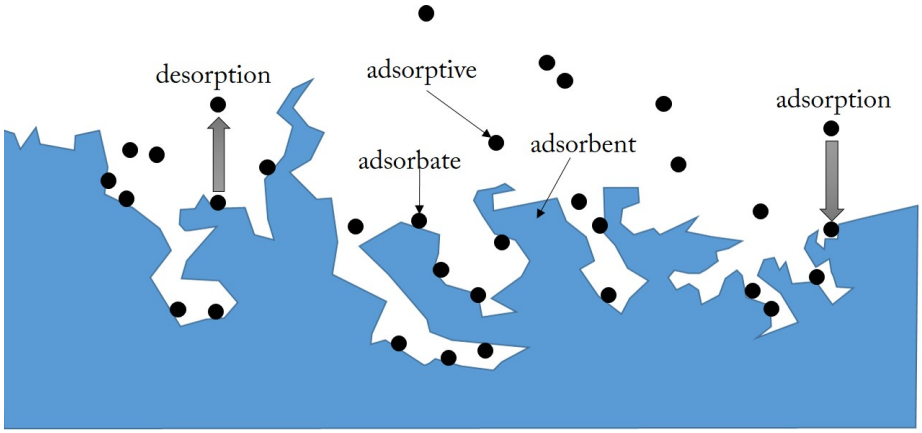

Fig. 2.1 Physical adsorption phenomenon

It is important to know the properties of the materials involved in the adsorption process. The porous solid that adsorbs and desorbs the fluid is called the adsorbent. Adsorbents are characterized by extremely large internal surface area and high polarity. The fluid molecules that do not adhere to the surface are called adsorptive, and the molecules that do adhere are called adsorbates. This is clearly shown in Figure 2.1.

The capacity of adsorption is denoted by w, which is defined as the ratio between the mass of the adsorbate $m_{adsorbate}$ and the mass of the dry adsorbent $m_{adsorbent}$.

$$w = \frac{m_{adsorbate}}{m_{adsorbent,dry}} \tag{2.1}$$

The maximum adsorption capacity, which depends mainly on the internal surface area and void fraction of the adsorbent, cannot be fully utilized because of mass transfer limitation involved in adsorbate-adsorbent interacting processes. In order to estimate the dynamics of the adsorption process, it is necessary to have information on adsorption equilibrium. When the adsorbent is in contact with the surrounding fluid (adsorbate), adsorption takes place and after a sufficiently long time, the adsorbent and the surrounding adsorbate reach equilibrium. At the equilibrium state, the rates of attaching and detaching or adsorbing and desorbing molecules become equal. The development of an equilibrium model of an adsorbent-adsorbate pair is described in several works, such as [16]. It includes usually experimental measurements of adsorption isotherms, using e.g. a thermo-gravimetric analyser (TGA), and fitting the obtained experimental data to a proper equilibrium model, such as Langmuir, Dubinin-Astakhov or Freundlich model. The following equation refers to the Dubinin-Astakhov model, which is the most commonly used.

$$w[g.g^{-1}] = w_o exp(-(\frac{F}{E})^n) \tag{2.2}$$

Where w_o $[g.g^{-1}]$, n and E $[kJkg^{-1}]$ are fitting parameters. F is the adsorption potential or the Dubinin-Polanyi potential,

$$F = -R.T.ln(\frac{P}{P_{sat}}) \tag{2.3}$$

Where P is the adsorbate vapour pressure and P_s is the saturated adsorbate pressure at temperature T.

2.2 Basic TDAd system

Knowledge of the fundamentals of the adsorption phenomenon is of great importance for the development of new systems and the improvement of the existing technology. Adsorption refrigeration/heat pump cycles are based on the adsorption of a refrigerant onto an adsorbent at low pressure. For cyclic operation, the adsorption process must be followed by a desorption process that consumes low-grade heat (T<100 °C). The basic configuration of an adsorption chiller/heat pump consists of three connected heat exchangers. Figure 2.3 shows the so-called three-heat exchangers configuration. The first heat exchanger is filled in with an adsorbent material and is called the adsorber/desorber. The second heat exchanger contains refrigerant and acts as an evaporator, meanwhile the first heat exchanger acts as adsorber. The third heat exchanger acts as a condenser, meanwhile the first heat exchanger acts as desorber. Initially, the adsorber/desorber is separated from both evaporator and condeser by Valve 1 (V1) and Valve 2 (V2), respectively. During the preheating process, heat is applied to the adsorber HEx resulting in increasing the temperature of the adsorbent. A small amount of the refrigerant is, then, released into the closed vapour phase, which induces a pressure increase until the pressure reaches the condenser pressure. At this point, the desorption process starts, by keeping V1 closed and opening V2 to connect the adsorber/desorber with the condenser (Figure 2.2b). Heating the adsorbent in its heat exchanger (desorber) drives out the refrigerant from the adsorbent. The desorbed refrigerant gas condenses in the condenser, releasing the latent heat of condensation until the end of the desorption phse (Figure 2.2b). Then the adsorber/desorber has to be separated again form both evaporator and condenser (V1 and V2 are closed). A cooled heat transfer fluid (HTF) (mostly at ambient temperature) shall pass through the adsorber/desorber to cool down the adsorbent inside. This causes the refrigerant surrounding the adsorbent in the adsorber to be adsorbed and, consequently, the pressure in the adsorber decreases until it reaches the level of the evaporator pressure. Such process is called the precooling process (Figure 2.2c). Figure 2.2d shows the adsorption process, in which V1 is open and V2 is closed. As the adsorbent is cooled and has low content of the

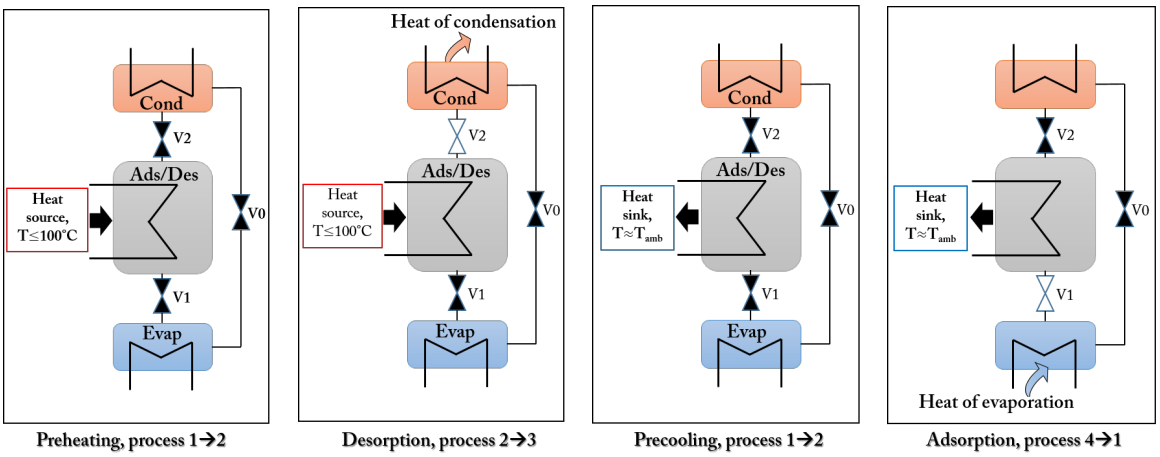

Fig. 2.2 Operation cycle of a three-heat exchangers adsorption chiller, (a) preheating, (b) desorption, (c) precooling, and (d) adsorption

adsorbed refrigerant, it sucks the refrigerant from the evaporator causing the refrigerant to evaporate and resulting in the production of the cooling effect. To keep a cyclic operation, the adsorber/desorber should return to its initial state. This means the two valves shall be closed and a HTF at high temperature shall be allowed to pass through the adsorber/desorber to raise its temperature and, accordingly, the pressure of the refrigerant inside. During the preheating process of the next cycle (Figure 2.2a).

From the previous brief description of the cycle, it can be concluded that it is an intermittent cycle since the useful cooling occurs only during the adsorption phase (Figure 2.2d).

2.3 Ideal adsorptive cycle

It belongs to the ideal processes that the desorption-condensation takes place at constant pressure (Figure 2.2b), which is determined by the condenser temperature, while the evaporator temperature determines the pressure of the adsorption-evaporation (Figure 2.2d) process.

Figure 2.3 presents the ideal working cycle of the adsorption chiller, described above, on Clapeyron diagram, where the vertical axis represents the adsorbate (refrigerant) pressure (P), the horizontal axis represents the adsorbent temperature (T). Thus, the horizontal lines on the diagram represent constant values of P, the so-called isobars, and the vertical lines represent constant values of T, so-called isotherms. Each inclined line represents a constant value of w (see Equation 2.1), which is termed as an isoster. The equilibrium model of an adsorbent-adsorbate pair refers to the correlation(s) describing the relationship between P,

T and w. To give the reader sense of the T and P values on a real adsorption chiller/heat pump, the values depicted on the cycle, in Figure 2.3 are for the silica gel-water pair upon applying an evaporator temperature of 5°C, a condenser temperature of 35°C and a driving heat (desorption) temperature of 90°C. For the silica gel-water pair, four different equilibrium models have been found in the literature [17–19]. The values of T and P of point (2) (T_2 and P_2) and point (4) (T_4 and P_4) depicted on the figure are in accordance with the equilibrium model introduced in [17].

The cycle processes could be reprsented on the Clapeyron diagram as follows:

- The desorption and adsorption isobars are determined from the intersection points of vertical isotherms representing the condensation and the evaporation temperatures (T_{cond}, T_{evap}) respectively with the refrigerant vapour pressure line (the left-most last black dashed line).
- The value of w at the end of the desorption process represented by the inclined line that passes through the intersection point of the desorption temperature (T_h) isotherm and the isobar that gives the desorption-condensation pressure (P_{cond}), point (3).
- The precooling process begins after the completion of the desorption process (point (3)) and ends as the system pressure becomes equal to the adsorption-evaporation pressure (P_{evap}), where the adsorption process begins, point (4).
- Adsorption process starts at point (4) and comes to end at point (1), which is determined by the intersection point of the vertical isotherm representing the adsorption-end or the condenser temperature and the isobar representing the adsorption-evaporation pressure.
- The preheating process starts from point (1) and ends at point (2), which is determined by the intersection point of the isoster passing through point (1) and the isobar representing the desorption-condensation pressure.
- Isobaric desorption process starts at point (2) and comes to end at point (3).

The two most common performance indicators of the adsorption chillers and heat pumps are the efficiency and the power density. Efficiency is measured by the coefficient of performance (COP), which is defined as the ratio of the useful (cooling/heating) energy output to the total energy input for isosteric heating (Q_h) and desorption (Q_{des}) .

$$COP = \frac{Q_{useful}}{Q_{add}} \tag{2.4}$$

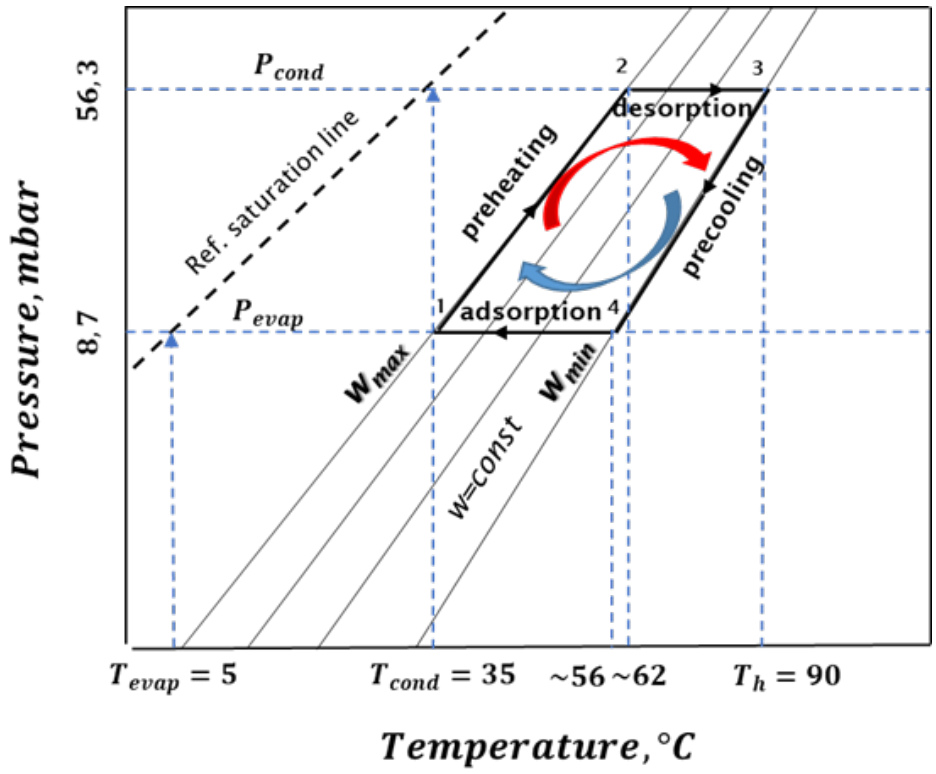

Fig. 2.3 Ideal periodic adsorption chiller cycle on Clapeyron diagram

Where,

$$Q_{add} = Q_h + Q_{des} \tag{2.5}$$

In case of chiller:

$$Q_{useful} = Q_{evap} \tag{2.6}$$

In case of heat pump:

$$Q_{useful} = Q_{cond} + Q_{ads} \tag{2.7}$$

where Q_{cond} and Q_{ads} are the heat release from the condenser (during the desorption-condensation phase) and the adsorber (during the adsorption-evaporation phase), respectively.

Power density, on the other hand, represents the average useful (cooling/heating) power per unit mass (denoted by SP) or volume (denoted by VSP).

$$SP = \frac{Q_{useful}}{t_{cycle}.m} \tag{2.8}$$

where, t_{cycle} the cycle time and m refers to the mass of the used adsorbent material [20–23], the adsorber heat exchanger or the whole chiller/heat pump system.

$$VSP = \frac{Q_{useful}}{t_{cycle}.V} \tag{2.9}$$

where, V refers to the volume of the used adsorbent material [24], the adsorber heat exchanger [25, 20] or the whole chiller/heat pump system [26, 27].

2.4 Research categorization

Research an development activities in the field of the of TDAd systems can be categorized into three main areas:

- The first is the area of developing novel adsorbents, such as the new family of composite adsorbents called selective water sorbents (SWS) [28, 29], the biomass derived adsorbents [30, 31] and the metal organic frameworks (MOFs) [32–35]. Rocky et al [36] presented a comprehensive review on the composite adsorbents. Different adsorbent families suitable for the application in the adsorption heat pumps, chillers and thermal storage systems are listed and compared in [37–40].

- The second research area is the design improvement of the system components, such as developing heat exchangers to act as adsorber/desorber [41, 42, 26] or as evaporator/condenser [43] for the application in the adsorption heat transformation systems.

- The last research area concerns the system management and integration, such as: (i) the adsorption cycle time and the time allocation of the adsorption and desorption phases [25], (ii) the heat and mass recovery [44], which aims at enhancing the system coefficient of performance (*COP*), (iii) the improvement of the adsorption and the desorption dynamics by initiating the processes with different techniques, i.e. pressure initiated and temperature initiated [45], (iv) the development of new concepts for specific applications, such as integrating a vapour compression system to an adsorption system [46] and integrating heat pipes into a finned tube adsorber heat exchanger [47].

Instead of a general discussion of the three aforementioned research areas of the TDAd systems, the next sections present and discuss a very specific literature review on the aspects most related to the objective of this thesis.

2.5 Adsorber sustainability

The adsorber/desorber heat exchanger (Ad-HEx) is the core component of an adsorption system. Realizing highly efficient and durable Ad-HExs is crucial for improving the performance and sustainability of adsorption appliances. Concerning the durability, special care has to be taken regarding the adsorbent material as well as the Ad-HEx construction material(s). The cycling stability of the adsorbent material deems to be a crucial requirement for building a sustainable adsorption system. Many adsorbents, which seem highly promising in terms of the adsorption capacity, thermal properties and diffusion characteristics do suffer from poor hydrothermal cycling [48]. Aside from the mechanical robustness of the adsorbent, some non-desired inert gases could be released upon conducting successive adsorption and desorption processes. It is related to adding some organic binding materials in the coating process of the adsorbents [20]. Therefore, the release of non-condensable gases from binder degradation is expected in coated adsorber heat exchangers, leading to a significant reduction of their start of life performance [49]. In-situ crystallization technology has been utilized to produce coating adsorbents without a binder content [50–52], however this technology is quite costly and a very limited thickness can only be realized (20 -150 microns) [53].

The utilization of loose pellets of adsorbents inside the adsorber heat exchanger is a cheaper alternative to coating or in-situ crystallization. Figure 2.4 shows the three different forms of the adsorbent material [53]. Loose pellets offer a high cycling stability than coatings [53] as well as a high mass transfer area per unit mass. Indeed, the heat transfer characteristics of in-situ crystalized coatings are quite high compared to the loose pellets, leading to high specific power outputs (per $kg_{adsorbent}$). The limited coating thickness restricts, however, the Coefficient of Performance (*COP*) and the volumetric storage density [53], if applied as a

storage system. On the other hand, making use of loose pellets results in relatively high *COP* and volumetric storage density with a comparable specific power output (per $kg_{adsorbent}$) with the binder-coating form, if the pellets' size and the adsorbent bed thickness are carefully optimized. In [54–56], it was demonstrated that a layer of loose pellets can provide the same specific power of a coated adsorbent layer. Table 2.1 compares between the three forms of the adsorbent material.

The construction material of the Ad-HEx has to be highly resistive against corrosion, otherwise inert gases will release out of corrosion reactions resulting in a continuous performance reduction and, on the long term, in destroying the heat exchangers and, consequently, the whole machine [20, 57]. For small-scale systems dedicated for single and double family houses, where the installation of a vacuum pump for maintenance is not allowed, aluminium has to be avoided as a construction material of the Ad-HEx, as it is subjected to high corrosion rates under pure water vapour, ethanol and methanol atmospheres [58, 57, 59].

Moreover, the type of the adsorber heat exchanger plays a significant role in the system sustainability. For instance, the application of finned-circular and finned-flat tube heat exchangers attracted the research highest interest so far. Comparisons between several Ad-HEXs with different designs have been reported in [60, 61]. The authors concluded that the finned-circular and finned-flat tube Ad-HEX provide the best performance in comparison with other adsorber designs. Indeed, at the first thought, the application of finned-circular and -flat tube HEXs seems to be the best choice, thanks to their wide availability and large heat transfer surface area. Concerning the system's specific power output (*SP*), adsorber heat exchangers that provide large area for the heat transfer are quite favourable. However, when the sustainability is taken into consideration, they could suffer in the long term from high heat transfer resistance at the interface between the root of the extended surfaces (fins) and the main tube surface [62]. See Figure 2.5a. As the fins are normally made of aluminium or copper and the tubes of copper or stainless steel, corrosion does take place with all known refrigerants for TDAd systems; namely water, ammonia, methanol or ethanol [63, 64, 57]. In case of applying a composite sorbent including salt like CaCl2, LiBr or LiCl, the leakage of the salt does not only lead to performance degradation, it could also completely damage the adsorber heat exchanger as the corrosion becomes more pronounced [65] and probably the fins completely lose contact with the main tube surface. Also, if the finned circular-tube or flat-tube heat exchangers are made of a highly resistive material such as stainless steel, the poor thermal contact at the interface between the fins' root and the main tube surface can only be avoided if the fins are perfectly brazed to the tubes, which implies an additional corrosion potential.

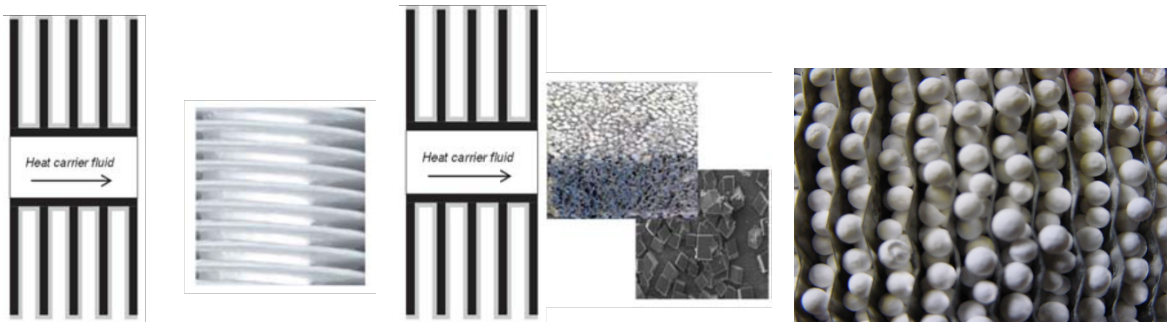

(a) (b) (c)

Fig. 2.4 Forms of the adsorbent material, (a) binder-based coating, (b) in-situ crystallization and (c) loose pellets (grains)

Table 2.1 Comparison between the different forms of the adsorbent material

Binder-based coating	**In-situ crystallisation coating**	**Loose grains**
Good heat transfer properties	High heat transfer properties	Good heat transfer properties if the grain size is selected carefully
Limited amount of adsorbent per unit of HEx volume	Limited amount of adsorbent per unit of HEx volume	high amount of adsorbent per unit of HEx volume
Low thermal stability	Good thermal stability	High thermal stability
High production cost	Very High production cost	Low production cost

To sum up, besides the adsorbent and its binder system have to be stable, the construction material and the type of the adsorber heat exchanger should also be carefully selected.

2.6 Adsorbent-adsorbate appropriateness

The adsorbent-adsorbate equilibrium properties, their thermal properties and the mass diffusion characteristics do very much influence the performance of an adsorption appliance. For instance, some MOFs, such as MIL-100 and MIL-101 families, have recently attracted high attention due to their high capacity of water adsorption [66]. Figure 2.6 depicts the variation of the water uptake (w) against the adsorption potential (F) of water in different adsorbents, namely Siogel [17, 18], Zeolites 13X [67], AQSOA-Z02 [68], AQSOA-Z01 [68], and Metal-Organic Frameworks (MOFs), MIL-101(Cr) and MIL-NH2-125 [19]. Assuming that $T_{ev}/T_{cond}/T_h$=10/30/80°C are the operating conditions of an investigated adsorption chiller for which a suitable working pair has to be selected. As depicted in Figure 2.6, the

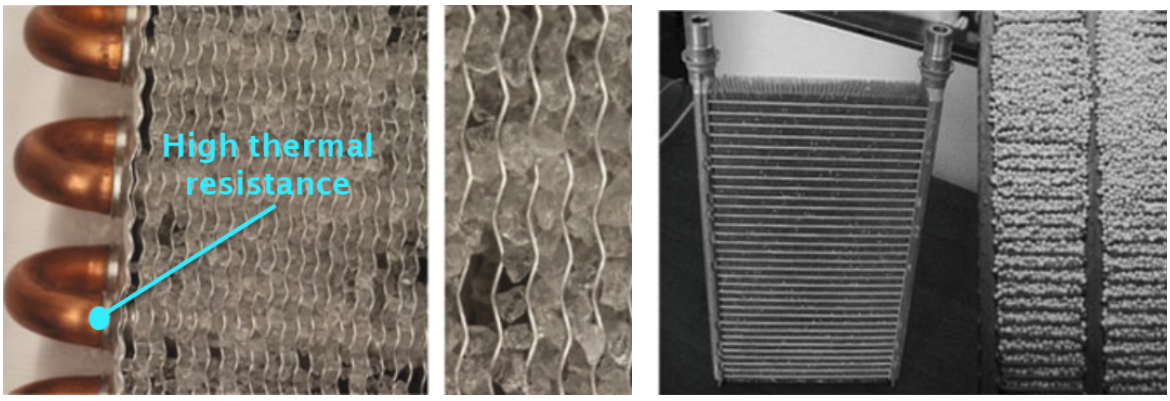

(a) (b)

Fig. 2.5 Most commonly applied HExs in the adsorption field,(a) finned-circular-tube (rectangular or annular fins) and (b) finned flat tube

maximum differential water uptake of an adsorption chiller (Δw_{max}) obtainable at 10/30/80°C can be determined from the intersection between the vertical black lines referring to the minimum and the maximum adsorption potentials (F_{min} and F_{max}) and the $w-F$ curve of the working pair [69, 70]. The F_{min} and F_{max} are the minimum and maximum adsorption potential taking place in an adsorptive cycle of an adsorption chiller, i.e. F at points (3) and (1) depicted on Figure 2.3. F_{min} and F_{max} can be evaluated using the following equations;

$$F_{min} = R.T.ln(\frac{P_{sat}(T_{cond})}{P_{sat}(T_{ev})}) \tag{2.10}$$

$$F_{max} = R.T.ln(\frac{P_{sat}(T_h)}{P_{sat}(T_{cond})}) \tag{2.11}$$

The maximum differential water uptake (Δw_{max}) obtained from the two $w-F$ curves of the MOF adsorbents, i.e. MIL-NH2-125 and MIL-101(Cr), are the highest values. They amount to 0.254 and 0.176 $g.g^{-1}$, respectively. At first thought, the application of NH2-MIL-125 represents the best choice, then MIL-101(Cr) comes second. However, in the study presented by Graf et al. [19], other aspects are presented that must be considered in the selection of the right adsorbent.

Graf et al. [19] have carried out experimental investigations on the dynamics of water adsorption on the two aforementioned MOFs; i.e, MIL-101(Cr) and MIL-NH2-125, and compared them with Siogel, which is characterized by a relatively lower capacity for water adsorption. The study showed that, for the common temperature set 10/30/80 °C, MIL-101(Cr) has demonstrated the highest adsorption capacity, but with significantly lower COP (-19%) and volumetric cooling power (-66%) than Siogel. MIL-NH2-125 demonstrated

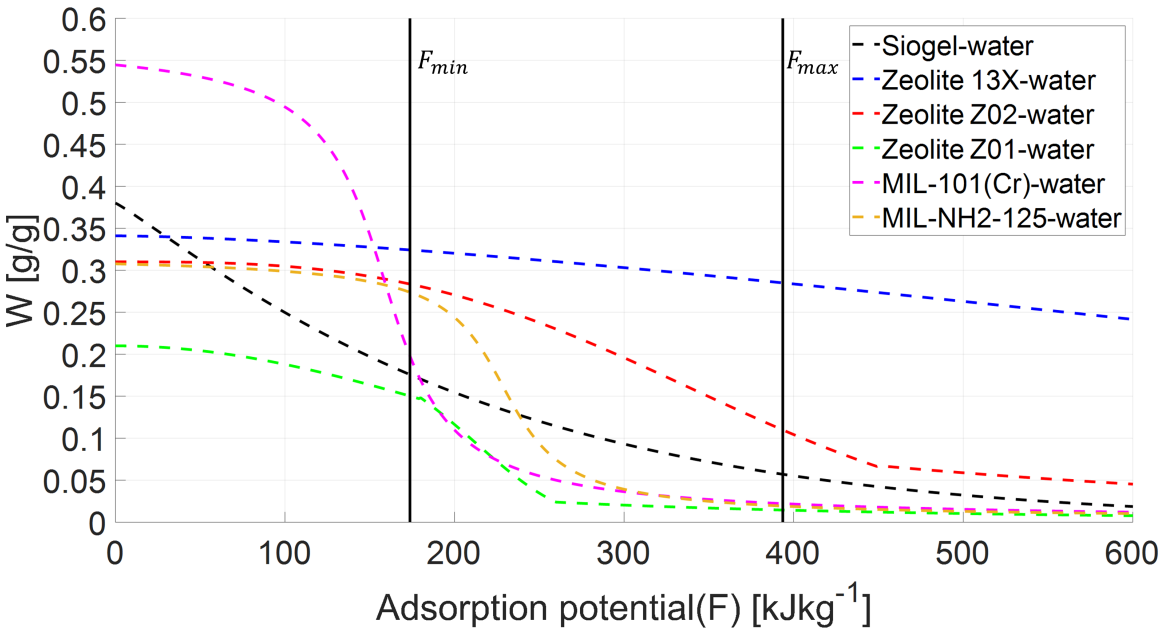

Fig. 2.6 Variation of the water uptake, w, against adsorption potential, F, for different working pairs

improvement in the COP by 18% compared with Siogel, but with a reduction in the power density by 28%. From the results, they concluded that, the low performance of the two investigated MOFs compared with Siogel are due to the non-matched shape of their isotherms to the specific operating temperatures. Finally, they returned the low efficiency of the MOFs to their lower density and lower heat and mass transfer characteristics compared with Siogel.

2.7 Adsorber HEx configuration

This section discusses the design of the finned tube adsorber heat exchanger, which is most commonly applied in the field. In addition, some specially designed adsorber heat exchangers that have unique performance are separately addressed. Finally, the application of the brazed plate heat exchanger as an adsorber/desorber is discussed.

2.7.1 Finned tube adsorber heat exchanger

As mentioned previously, the finned-circular and finned-flat tube heat exchangers are the most commonly applied in the adsorption machines. Their investigation dominate the research activities in the field. Several communications addressed the optimization of the distance between the fins and fin geometry, thickness, and height [71–73]. The fin pitch and fin

height are indicators for both the heat and mass transfer paths in the adsorbent domain of the adsorber, respectively. However, few studies addressed the optimization of such parameters experimentally. Kubota et al. [74] presented the improvement in *SCP* and *COP* values of a finned tube adsorber heat exchanger, introduced in [75], after utilizing a numerical simulation model for optimizing the HEX design [72]. They reported in [74] that the optimized HEX (having a fin-bitch of 2.32 mm) can achieve more than twice higher cooling output per unit adsorber volume than the un-optimized one (having a fin-bitch of 5 mm) [75].

In [41, 42] an analysis of variance (ANOVA) has been conducted for evaluating the weightiness of each design and operating parameter, upon applying finned circular-tube heat exchanger to act as an adsorber in sorption cooling system (SCS). It was illustrated that, the contribution of the fin thickness to the *COP* of the SCS amounts to 48.67% in case of constructing the Ad-HEx from copper and applying silica gel-water as a working pair [41], which is reduced to 29% as reported in [42], upon constructing the Ad-HEX from aluminium and applying the composite adsorbent ($CaCl_2$ in silica gel). In addition, the contribution of the fin thickness to the *COP* of the SCS, upon applying aluminium finned-plate Ad-HEX, has been reported in [42] to be 33%. Abd Elhady and Hamed [76] investigated numerically the effect of the fin design parameters on the performance of a two-bed SCS and reported a reduction in the *COP* by 9.4% upon increasing the fin thickness of a finned-circular tube Ad-HEx from 0.2 mm to 0.4 mm.

Finally, before closing this section, it is important to mention that the effect of the thermal resistance at the fin-root-surface interface on the overall heat transfer coefficient is usually ignored in the analytical and numerical studies, which should not be the case. Few studies demonstrated, however, that this interfacial heat transfer resistance governs the heat transfer in the Ad-HEx and, hence, its performance [77–79, 62].

2.7.2 Specifically designed adsorber heat exchangers

Some specially designed adsorber heat exchangers with unique configurations are presented in the literature. The most interesting are the ones presented in [42, 80]. Bahrehmand and Bahrami [42] proposed an optimized adsorber HEX prototype, which has been fabricated by completely machining a finned plate adsorber HEX with a fin thickness of 1 mm out of an aluminium block. Figure 2.7 shows the two halves of the machined finned plate adsorber HEx introduced in [42]. They applied coating composite adsorbent, CaCl2 impregnated in silica gel. For enhancing the heat transfer in the adsorbent, graphite flakes have been added. They reported that their adsorber can achieve SCP of 1005 $W.kg^{-1}$ and a COP of 0.60. More recently, Darvish et al. [80] introduced pin fin adsorber heat exchanger made of copper. They applied the same adsorbent applied in [42]. The best performance reported

Fig. 2.7 Two halves of the machined finned plate adsorber HEx introduced in [33]

for this adsorber is 1160 $W.kg^{-1}$ for the SCP and 0.68 for the COP. Such values reported in [42, 80] are very promising, but the stability of the coating still needs to be intensively investigated. Moreover, as their production methodology is too expensive for a market product, more developments are needed to approach the performance of the optimized HEX by an affordable and sustainable design.

2.7.3 Brazed plate adsorber heat exchanger

The application of an embossed plate heat exchanger made of copper to act as an adsorber heat exchanger has been suggested for the first time by Hong et al. [81]. A numerical parametric study with the application of the SWS-1L[1] and water as an adsorbent-adsorbate pair has been conducted. The optimal values of the COP and the specific cooling power (SCP) reported in [81] at operating conditions of 15 °C evaporator temperature, 30°C condenser temperature and 80°C desorption temperature amount to 0.512 and 662.8 $W.kg^{-1}$, respectively. However, the authors in [81] did not discuss the manufacturability of their suggested embossed plate heat exchanger and did not report on any corrosion potential, which their PHE would face if it is made of copper, as reported, and some salt may leak out of the SWS-1L [65]. Dawoud [82] introduced a nickel-brazed plate heat exchanger composed of stainless-steel thin sheets (0.3 mm in thickness), to be highly resistive against any potential corrosion, and designed

[1] a composite adsorbent obtained by impregnating mesoporous silica gel with CaCl2

dedicatedly to act as an adsorber heat exchanger. The key design advantages of the APHE introduced by Dawoud [82] is the extremely reduced volume of the heat transfer fluid (HTF) domain compared to the adsorbent domain, while keeping the uniformity of the temperature distribution over the heat exchanger's plates.

As the *SP* and the *COP* are the most important performance indicators of an adsorption appliance, the proper design of the Ad-HEx is a trade-off between the design parameters governing the heat and mass transfer in the adsorbent domain and the thermal capacity of the Ads-HEx[83, 41].

2.8 Overview on SP and COP in the literature

Rogala et al [61]. did a survey that covered 10 research papers (published from 2005 to 2016) to compare different adsorber heat exchangers in terms of the obtained SCP and COP. The comparison involved adsorber heat exchangers of two different working pairs, namely silica gel-water and zeolite-water. The configurations of the compared adsorbers were also different, including plate-fin-and-tube, finned-tube with annular fins, flate-tube and plate-fin adsorber heat exchangers. The operating temperatures, T_{ev}=11-20°C, T_{cond}=28-35°C and T_h=80-90°C. Grain size ranges 0.1 to 1.5 mm. The authors concluded that a single bed, lab scale, adsorption chiller integrating a plate-fin-and-tube adsorber heat exchanger demonstrated the best performance. Strictly speaking, Specific Cooling Power (SCP) up to 394 $W.kg^{-1}$, VCP of 223 $W.m^{-3}$ and COP higher than 0.6 upon applying zeolite-water working pair, 15/35/90°C as operating conditions, cycle time of 7 min., adsorption to desorption time ratio=2.5.

Bau [70] conducted a survey that included 64 adsorption chillers. The COP values ranged from 0.01 to 0.84, and the SCP ranged from 5.7 to 820 $W.kg^{-1}$. Bau attributed the wide range of COP and SCP values not only to the adsorption chiller design, but also to the different input conditions, such as the type of adsorber heat exchanger, working pair, operating temperatures, thermal management, system configuration, cycle time, and others. Bau reported that the values obtained in his study are very difficult to compare for evaluating and improving the intrinsic performance of an adsorber design. For useful comparison, it is necessary to know and eliminate the design-independent influences on the *COP* and *SCP*.

Sharafian et al. [60] did a survey included 57 research papers, in which different adsorber plate heat exchangers are introduced. The authors made the comparison between the adsorber heat exchangers in terms of the *SCP* and the *COP*. The evaluation of the *SCP* and the *COP* in each research paper has been done upon applying certain adsorber configuration, number of beds, working pair, operating temperatures, cycle time and heat and mass recovery approach.

Aristov [84] and Bahrehmand [85] compared between different commercial adsorption chillers, of different trade marks, models and sizes. It is very clear that such comparisons are not useful in evaluating the different designs of the adsorber heat exchangers. In fact, useful comparison can be performed if the influences of the operation conditions, working pair, cycle time, number of beds, heat and mass recoveries are eliminated.

2.9 Kinetics' investigation of adsorption and desorption processes

The fundamental principle of the adsorption heat transformation processes is to perform a change in the equilibrium state of an adsorbent-adsorbate pair between one state of high concentration and another state of low concentration of the adsorbate in the adsorbent. The transformation between these two states can be isobaric or isothermal. The isobaric processes are initiated by a temperature change of the adsorbent-adsorbate pair at constant pressure of the adsorbate, while the isothermal processes are initiated by a pressure change of the adsorbate at constant temperature. Therefore, an isobaric or even quasi-isobaric adsorption or desorption process initiated by a temperature change is referred to in the literature as a large temperature jump (LTJ) adsorption or desorption process. The adsorption and desorption processes that occur in conventional adsorption chillers and heat pumps are of the LTJ type, triggered by a temperature change between the heat sink temperature (290-310 K) and a low-grade heat source (330-400 K) [84, 86, 87].

The isothermal, pressure initiated, adsorption and desorption processes are mainly used for the heat amplification processes [84, 88, 89] . In the literature, such processes are called large pressure jump (LPJ) adsorption and desorption processes. Figure 2.8 shows LTJ and LPJ adsoprtion processes ploted on a Clapeyron diagram.

Combined LTJ and LPJ adsorption and desorption processes are very common in the adsorption heat storage systems [90].

2.9.1 Kinetics' investigation of full-scale adsorber/desorber

The performance indicators (SP and COP) of a real adsorption chiller/heat pump can not inform clearly about the dynamic performance of the adsorber/desorber heat exchanger.

To study the adsorption and desorption kinetics of a real adsorber/desorber heat exchanger, Tokarev and Aristov [91] introduced the so-called Thermal Response Large Temperature Jump (T-LTJ) method to estimate the instantaneous adsorbate loading from the measured adsorber and desorber powers obtained during the adsorption and desorption processes,

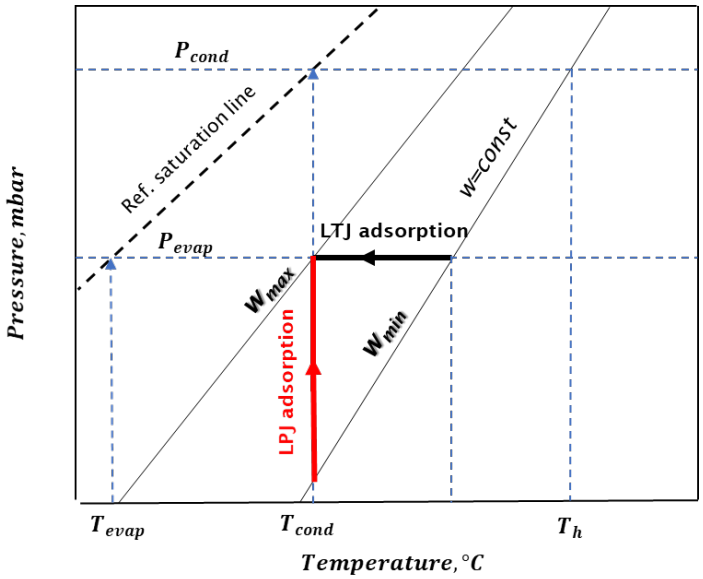

Fig. 2.8 LTJ and LPJ adsorption processes depicted on Clapeyron diagram

respectively. They performed a blind process (disconnecting the evaporator/condenser from the adsorber/desorber) and an active adsorption/desorption process. Figure 2.9 shows the adsorber powers over time obtained during an active process and the corresponding blind process. By subtracting the results of the blind experiment from those of the active adsorption experiment, the temporal adsorption heat can be obtained. The time cumulative integration of the heat of adsorption (indicated by the green area in Figure 2.9) can be given by the following equation,

$$Q_{adsorption}(t) = \int_0^t (\dot{Q}_{active} - \dot{Q}_{blind}).dt \tag{2.12}$$

The temporal adsorbate uptake (w) can be estimated from the time cumulative integration of the heat of adsorption ($Q_{adsorption}$) as following,

$$w(t) = w_o + \frac{Q_{adsorption}(t)}{m_{dryads.}.\Delta h_{ads}(w)} \tag{2.13}$$

where, w_o is the initial adsorbate uptake and $\Delta h_{ads}(w))$ is the isosteric heat of adsorption.

In this thesis (Chapter 3), a slight modification to the T-LTJ method [91] is introduced. Strictly speaking, Instead of performing blind and active adsorption/desorption processes and estimating the temporal adsorbate uptake from the temporal cumulative integrations of the heat of adsorption/desorption, the temporal cumulative integrations of the heat of evaporation/condensation are utilized.

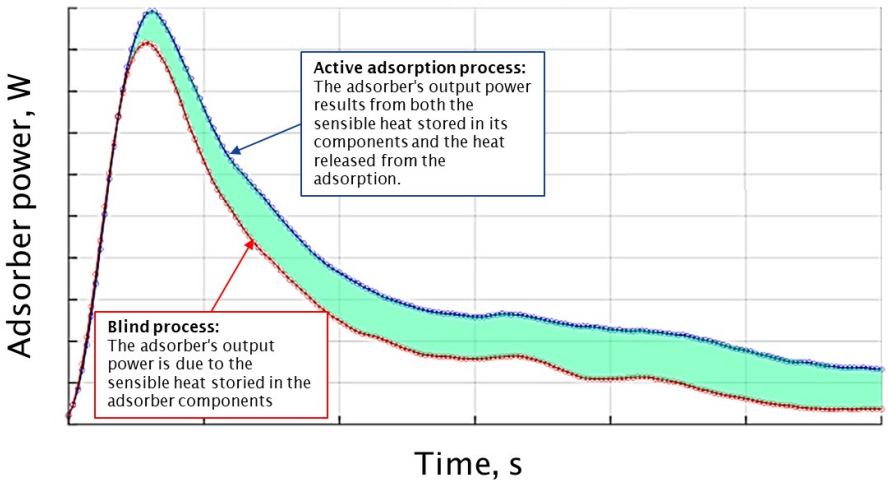

Fig. 2.9 Thermal response large temperature jump (T-LTJ) methodology

2.9.2 Kinetic's investigation of small-scale adsorbent sample

An experimental setup to study the adsorption and desorption kinetics of small scale adsorbent samples according to the LPJ technique was developed by Dawoud in [92].

Concerning the kinetic setup that allows LTJ adsorption and desorption processes to be performed on small adsorbent samples or small pieces of real adsorber heat exchangers, there are four LTJ versions in the literature: Volumetric (V) version [93–95], Gravimetric (G) version [96], Calorimetric (C) version [97] and Thermal (T) version [91]. The kinetic setup installed in the Laboratory of Sorption Processes (LSP) at OTH Regensburg is a V-LTJ one. Since the most commonly used versions of LTJ kinetic setups are the volumetric and gravimetric versions, the V-LTJ and G-LTJ kinetic setups are briefly described in the next sections.

V-LTJ kinetic setup

A V-LTJ kinetic setup essentially consists of three compartments. The first compartment of the setup is a constant volume vapour vessel. The temperature of this vessel is controllable by a water circuit coupled to a circulating thermal bath (Thermostat) (see Figure 2.10, Thermostat 1). The second compartment is the measuring cell where the adsorbent sample is placed for testing. The surface temperature of the sample holder in the measuring cell is controlled by an oil circuit connected to two circulating thermal baths (Thermostat 3 and 4). A three-way valve (3WV) is installed in the oil circuit of the sample holder of the measuring cell, which allows either the oil supplied by Thermostat 3 or the oil supplied by Thermostat 4 to pass through the oil circuit of the sample holder. Thermostat 3 is set to the

initial temperature of the desorption or the adsorption process, while Thermostat 4 is set to the desired final temperature for the desorption or adsorption processes being performed. By turning the 3WV to the position where the heated/cooled oil flows into the measuring cell, either a desorption or an adsorption process can be started. The third compartment is the steam generator, to which a heating/cooling bath (Thermostat 2) is connected in order to adjust the temperature of the liquid refrigerant water filled in it and, consequently, the water vapour pressure in the steam generator in order to reach the equilibrium state at the beginning of the adsorption or desorption process being carried out.

It is relevant to note that Thermostat 1 also serves to control the temperature of the outer surface of the interconnecting tubes of the setup (not shown in Figure 2.10) to prevent any undesirable local vapor condensation.

The execution of a typical LTJ (i.e., isobaric) adsorption process using V-LTJ kinetic setup involves the following sequences:

- Heating and evacuating the vapour vessel and the measuring cell (100°C), in which the investigated adsorbent sample is placed, for one hour. The valves V1,V2 and V4 are open, while V3 is closed during this process.

- Valve V1 is closed and the vacuum pump is switched off. The sample holder of the measuring cell is cooled down to the set adsorption start temperature (T_4 in Figure 2.3 which is set on Thermostat 3). Meanwhile, the steam generator is set to the saturation temperature corresponding to the desired pressure of the adsorption process (Thermostat 2). As a preparation for the LTJ adsorption process, Thermostat 4, which still separated from oil circuit of the sample holder, is set to the end temperature of the planned adsorption process (T_1 in Figure 2.3). Then, valve V3 is opened to fill both the vapour vessel and the measuring cell with the vapour supplied by the steam generator. This process takes 2 hours to reach the equilibrium state.

- The temperature of the vapour vessel, connections and valves is maintained at 35 °C for adsorption processes and 60 °C for desorption processes to avoid the condensation of water on the inner surface of the system components.

- For initiating an adsorption process, the 3WV is turned to allow the cold oil of Thermostat 4 to pass through the sample holder and, accordingly, cool down the adsorbent sample to the end temperature of the planned adsorption process.

- The adsorbent sample will adsorb the refrigerant vapour surrounding it and, accordingly, the amount of vapour filling the vapour vessel and the measuring cell will decrease. Since the setup is a constant volume system, the temporal vapour pressures recorded

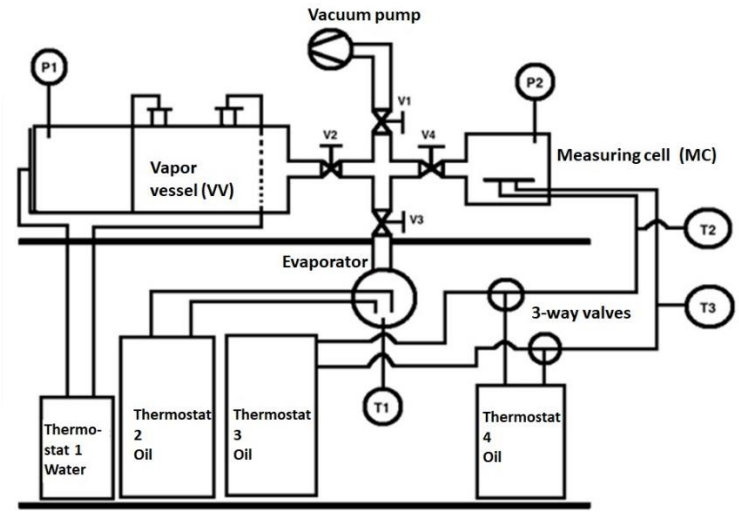

Fig. 2.10 Schematic diagram of a V-LTJ kinetic setup

for the vapour vessel and the measuring cell indicate the amount of water vapour adsorbed in the adsorbent sample under investigation. The following equation gives the instantaneous amount of water adsorbed in time duration Δt,

$$\Delta m(t) = \frac{V_{VV}}{R}[\frac{P(t+\Delta t)}{T(t+\Delta t)} - \frac{P(t)}{T(t)}]_{VV} + \frac{V_{MC}}{R}[\frac{P(t+\Delta t)}{T(t+\Delta t)} - \frac{P(t)}{T(t)}]_{MC} \tag{2.14}$$

where, V, P, T and R refer to volume, vapour pressure, temperature and gas constant, respectively. The subscripts VV and MC refer th the vapour vessel and the measuring cell, respectively.

Accordingly, the instantaneous water uptake $w(t)$ of the adsorbent sample can be given by;

$$w(t) = w_o + \sum_0^t \frac{\Delta m(t)}{m_{dryads.}} \tag{2.15}$$

where, w_o and $m_{dryads.}$ refer to the initial water uptake and the dry mass of the adsorbent sample, respectively.

The specifications of the V-LTJ kinetic setup installed in the Laboratory of Sorption Processes at OTH Regensburg are given in Appendix A. The uncertainty analysis of the water uptake measurements is also given there.

G-LTJ kinetic setup

Figure 2.11 shows a schematic diagram of a G-LTJ kinetic setup. The setup follows the LTJ procedure as an approach to study the adsorption and desorption dynamics of an adsorbent sample or a small fragment of a real adsorber heat exchanger (5-600 g dry adsorbent mass) under typical operating conditions of the adsorption appliances. The kinetic setup of the G-LTJ includes the direct evolution of the adsorbate concentration in the adsorbent by dynamic weight measurement. The main components of the setup are a gravimetric weighing unit on which the investigated fragment is placed. The other components are vacuum chambers 1 and 2. Vacuum chamber 1 contains the weighing unit, i.e. it houses the weighing unit and the investigated Ad-HEX. Vacuum chamber 2 serves as the evaporator/condenser during the isobaric adsorption/desorption phases. The two chambers are connected by the electropneumatic valve (V5, see Figure 2.11). As shown in the figure, the AD-HEX under investigation is connected to two circulating thermal paths (TCR1 and 2) that allow sudden cooling or heating to initiate an LTJ adsorption or desorption process, respectively. The temperature of the evaporator/condenser is controllable via TCR3.

The execution of a typical LTJ (i.e., isobaric) adsorption process using G-LTJ kinetic setup involves the following sequences:

- Heating and evacuating the vapour chamber 1, in which the investigated adsorbent sample or Ad-HEX is placed, for one hour. The valves V6 is open, while V5 and V7 is closed during this process.
- Valve V6 shall be closed and V5 open. The vacuum pump is switched off. The Ad-HEX in chamber 1 is cooled down to the set adsorption start temperature (T_4 in Figure 2.3 which is set on Thermostat TCR1). Meanwhile, the evaporator in chamber 2 is set to the saturation temperature corresponding to the desired pressure of the adsorption process (TCR3). As a preparation for the LTJ adsorption process, TCR 2, which still separated from oil circuit of the Ad-HEx under investigation, is set to the end temperature of the planned adsorption process (T_1 in Figure 2.3). This process takes 2 hours to reach the equilibrium state.
- The temperature of the walls of chamber 1, the connections and the valves is maintained at 35 °C for adsorption processes and 60 °C for desorption processes to avoid the condensation of water on the inner surface of the system components.
- For initiating an adsorption process, the cold oil of TCR2 will be allowed to pass through the Ad-HEX and, accordingly, cool down the adsorbent inside to the end temperature of the planned adsorption process.

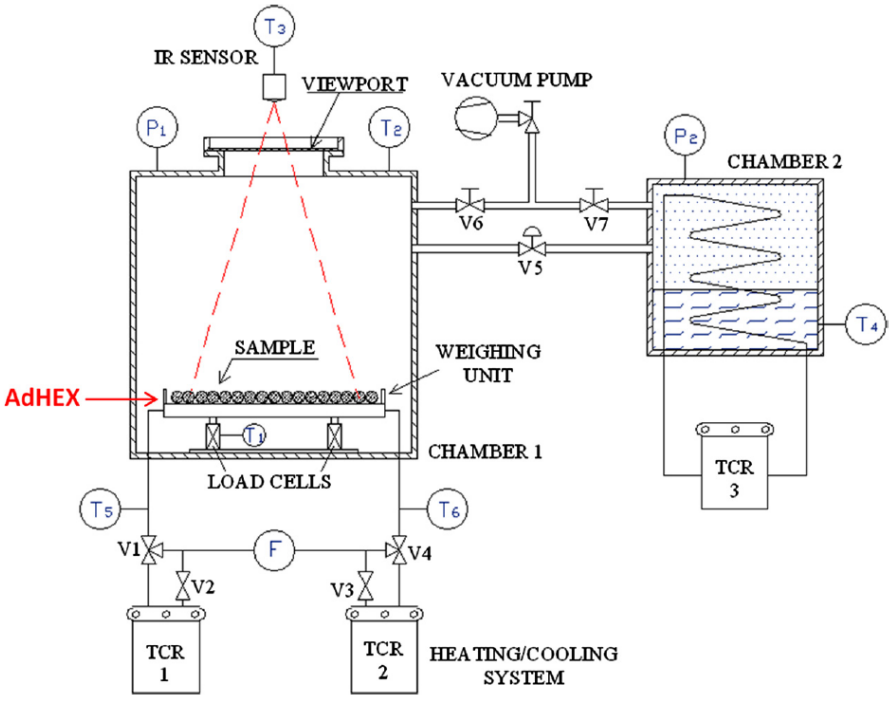

Fig. 2.11 Schematic diagram of a G-LTJ kinetic setup [90]

- The adsorbent inside the Ad-HEX adsorbs the refrigerant vapour surrounding it, causing a rapid pressure drop of the water vapour in the system, inducing an evaporation process in the evaporator located in chamber 2 of the system. Since the setup is equipped with a load cell (weighing unit), the temporal evolution of the water vapour adsorbed in the Ad-HEX can be measured directly.

2.10 Matching between full-scale and small-scale measurements

The adsorption dynamics obtained upon conducting adsorption processes on small adsorbent samples in form of monolayer or even multilayers (if ≤ 4) of adsorbent grains seem to be very promising. Chakraborty et al. [98] have estimated 5 $kW.kg^{-1}$ as a specific cooling power of an adsorption chiller having the adsorbent in form of a monolayer of loose silica gel pellets. In [99, 96], the effect of varying the thickness of adsorbent sample of AQSOA-Z02 grains in different size ranges on the adsorption dynamics has been investigated. The ratio of the heat transfer surface area to the adsorbent dry mass (S/m) is introduced as a design parameter. The influence of S/m ratio on the specific cooling power, *SCP*, for different

adsorbent grain sizes has been carefully studied. For one adsorbent, the S/m ratio is, indeed, inversely proportional to adsorbent thickness of the adsorbent bed (i.e. the length of the heat transfer path). It was concluded in [99] that, for the grain size range of 0.2-0.9 mm, the average *SCP* of the adsorption chiller is linearly proportional to the (S/m) ratio of the Ad-HEX.

So far, the publications dealing with the experimental investigation of small-scale adsorbent samples for predicting the performance of real adsorber heat exchangers showed differences in the adsorption and desorption dynamics of up to a factor of 10 in favour of the small-scale adsorbent samples. Aristov et al. [100] investigated the adsorption dynamics of small adsorbent samples configured in different layer numbers (n: 1-8) and with different grain sizes. They defined, for the first time, the ratio (S/m). The ratio (S/m) can be used as a configuration characteristic factor of the adsorbent sample instead of the number of the lose grain layers. From the ratio (S/m) and the average grain size of the sample, the average number of the grain layers composing the sample can be estimated. Although the specific output powers estimated from the experimental data of the investigated samples, if they could be applied in real adsorber heat exchangers, were very promising, the experimental data of the investigated adsorber heat exchangers, which have similar (S/m) and grain size, demonstrated specific output powers 2 to 10 times lower than those estimated from the small samples [100, 84]. This quite large difference is returned in [100, 84] to some imperfections in the system components and to some issues related to process organization, such as cycle time, isobaric phase durations, heat and mass recovery and residual air.

Dawoud [95] investigated the adsorption kinetics of water vapour on small-scale AQSOA-Z02 coated samples and compared them to the adsorption kinetics of two different full-scale coated adsorber heat exchangers with the same adsorbent material at similar operating conditions. The thickness of the tested consolidated adsorbent layers was in the range of 150 to 500 μm. The experimental results discussed in [95] indicated that in general, increasing the adsorbent layer thickness leads to lower adsorption kinetics, however the small-scale samples demonstrated at least twice higher adsorption kinetics than those of the full-scale coated adsorber heat exchangers. Dawoud [95] returned the difference in the kinetic results between the small-scale and full scale adsorbers to their difference in the heat capacities and heat transfer coefficients.

Beside the attributions reported in [100, 84, 95], those differences in the adsorption dynamics between the small-scale samples and the full-scale adsorbers should be, in addition, dedicatedly investigated from the perspective of the combined heat and mass transfer characteristics prevailing in both small-scale adsorbent sample and the adsorbent domain of the investigated adsorber heat exchanger. In other words, the equality of S/m ratio between the

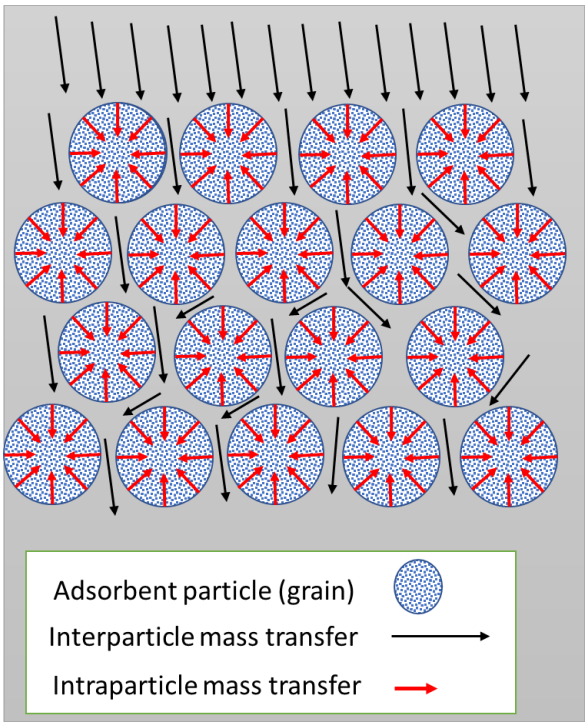

Fig. 2.12 Mass transfer in an adsorbent bed

small-scale adsorbent sample and the investigated adsorber heat exchanger reflects similarity in the heat transfer resistance, however it should be recalled that an adsorption process is a combined heat and mass transfer process, which takes place inside the adsorbent bed of the adsorber heat exchanger.

In fact, the mass transfer resistances facing the adsorbate (vapour) flow in the adsorbent are classified into interparticle and intraparticle resistances. Figure 2.12 distinguishes between them. The length of the vapour diffusion path in the adsorbent bed determines the interparticle mass transfer resistance, while the size of the adsorbent grains determines the intraparticle resistance.

The interparticle mass transfer resistance can be accounted for in a simulation model using Darcy's law [133], which gives a relationship between the vapour flow velocity through a granular adsorbent bed and the associated pressure drop. Darcy's law states that the vapour velocity and the pressure drop in the adsorbent are linearly proportional, as depicted in the following equation,

$$\vec{u_v} = -\frac{K_{app}}{\mu}.\nabla p \tag{2.16}$$

with $-\frac{K_{app}}{\mu}$ being the proportional factor. K_{app} is the flow permeability and μ is the vapour viscosity. This factor,$-\frac{K_{app}}{\mu}$, belongs to the interparticle mass transfer resistance. A low value of this factor refers to high interparticle mass transfer resistance in the adsorbent. The following relation gives K_{app} as a function in the bed porosity (ε_b) and the average diameter of the adsorbent grains (d_p).

$$K_{app} = \frac{\varepsilon_b^3 d_p^2}{150(1-\varepsilon_b)^2} \tag{2.17}$$

This means that the interparticle mass transfer resistance does not rely on the type of the adsorbent materiel. Contrary, the intraparticle mass transfer resistance relays mainly on the type of the adsorbent material, which defines the effective diffusion coefficient (D_{eff}) appearing in the Linear Driving Force (LDF) model [133].

$$\frac{\partial w}{\partial t} = \frac{15 D_{eff}}{r_p^2}(w^* - w) \tag{2.18}$$

The LDF model is the most applied model for considering the intraparticle mass transfer resistance (discussed later in Chapter 4, Section 4.4).

Accordingly, when preparing a small-scale adsorbent sample for use in predicting the dynamic performance of an adsorber heat exchanger, the following parameters should be made identical to those of the adsorbent bed (domain) of the adsorber heat exchanger [101].

- The adsorbent grain size,
- The S/m ratio or the length of the heat transfer path (termed afterwards in this thesis as the heat transfer characteristic length, HTCL),
- The length of the refrigerant vapour diffusion path inside the adsorbent bed (termed afterwards as the mass transfer characteristic length, MTCL).

Moreover, some other aspects should be considered. For example, the fin efficiency of the extended surfaces (fins) of the adsorber heat exchanger shall be accounted for upon estimating the effective heat transfer surface area. In addition, the vapour transfer area into the adsorbent domain of the investigated adsorber heat exchanger should be represented also in the small-scale adsorbent sample.

2.11 Evaporator heat exchangers in adsorption appliances

This section deals with the evaporator heat exchanger of the adsorption appliances. It should be recalled that one of the objectives of this thesis is to study the application of a closed structured plate heat exchanger as an evaporator for the adsorption appliances.

Applying plate heat exchangers (PHEx) instead of finned-and-tube or falling film ones could result in highly compact and efficient adsorption systems. The application of asymmetric plate heat exchangers (APHEx), which are characterized by heat transfer between two separated domains of unequal volumes, to act as evaporator/condenser in the adsorption systems could come with the advantage of realizing high heat transfer coefficients and low-pressure drops leading to a significant enhancement in the heat and mass transfer rates [102].

The majority of research studies that dealt with the application of PHEs for evaporation and condensation processes handled typical vapour compression refrigerants such as R22, R134a, R290, R245fa, and NH3 [103–107], which except NH3 are not suitable for the adsorption appliances. A complete set of heat transfer correlations for PHEs under a wide range of application conditions is given in [103, 104]. The correlations listed include single and two-phase applications, with different refrigerants, mainly R134a, R22, NH3 and NH3/water mixtures. The tested configurations are different, but the vast majority of correlations are given for chevron-types PHEs. More recently, in [108], a summary of correlations for low-GWP refrigerants, which have been developed recently for replacing the most severe refrigerants of the VCR systems, was introduced. The refrigerants handled in [108] are R-290, R-1270, R-600, R-1234ze(E), R-1234ze(Z) and R-152a. In the same work, correlations available for condensation are reported. It has been found that the evaporation heat transfer coefficient (HTC) increases with increasing the refrigerant vapour quality and mass flux [103–105] as well as with increasing the heat flux and the refrigerant saturation temperature [105]. In [109], the authors developed new correlations for estimating the condensation heat transfer coefficient for different refrigerants inside a brazed, herringbone-type plate heat exchanger.

The effect of the dimples on the heat transfer inside a PHE, between the plates' surface and a stream of air, water and water/air mixture, is reported in [110, 111], [112] and [113, 114], respectively. The heat transfer enhancement is measured by means of the Nusselt number ratio between dimpled surface and smooth surface (Nu/Nu_0). It was found that the existence of dimples can result in a remarkable enhancement in the heat transfer coefficient (up to factor, Nu/Nu_0=2). In fact, the topology (corrugations) of the plates composing the PHE do influence the flow patterns inside the PHE. In [115], a visualized investigation on the flow patterns of an air/water mixture in a chevron PHE was presented.

The previously described literature survey on heat transfer correlations for PHEs is subjected to limitations when it comes to the application in adsorption systems due to the following items:

- The results of various analysis on large datasets showed that it is not possible to extrapolate the correlations developed from their original conditions range [103, 108, 109]. In fact, the boundary conditions for sorption systems are extremely different from those of refrigerants used in vapor compression cycles;
- The majority of correlations refer to chevron or herringbones PHEXs, making it difficult to generalize the results for other plate topologies.
- Two-phase heat transfer is evaluated for refrigerants working at atmospheric or higher pressures, whereas water (even in atmospheric conditions) is not generally considered.
- The effect of the dimples as heat transfer enhancers in a PHE has been studied mainly for water/air streams, which makes it difficult to derive correlations for the operation in an adsorption appliance.

Few studies dealt with the evaporation of water as a refrigerant in a PHE under atmospheric pressure. In [116], the flow boiling heat transfer in a vertical-chevron-type PHE at low mass fluxes ($200 < Re < 600$) and under atmospheric conditions is investigated.

The evaporation of water under sub-atmospheric conditions has also been investigated in some studies. For instance, in [117, 118] water evaporation in a fin-and-tube heat exchanger, where pool boiling regime has been realized, has been investigated. In [119, 120], water evaporation on the surface of tubes with microscopic fin structures and microporous coating layers, which provide a capillary effect and, consequently, enable realizing wetted tube surface with a thin water film, has been investigated. It has been reported that the heat transfer coefficient increases with the evaporation temperature. Besides, it has been recommended to make the filling level of the evaporator heat exchanger as low as possible, but the tube's surface should be kept always wet.

Giraud et al.[121] investigated the water evaporation on vertical smooth plate under sub-atmospheric conditions (under the typical operating conditions of the LiBr/H2O sorption chillers). It has been reported in [121] that during the water evaporation in the vertical channel three successive flow regimes were observed with zero measured cooling capacity during the first flow regime, which was characterized by appearance and quick collapse of bubbles at the channel inlet. During the two latter flow regimes, three different areas, upper, middle and lower were identified in the channel. The authors attributed the achieved cooling

capacity mainly to the evaporation of the liquid film formed on the upper area of the channel. The authors concluded that the higher the mass flux and thus the thinner the liquid film, the higher also the achieved cooling capacity [121]. Song et al. [122] introduced another study addressed the heat transfer characteristics in an evaporator PHE of a LiBr/H2O sorption chiller. The plates' surface of the evaporator PHE studied in [122] was corrugated, chevron type with high angle. In [123] the same evaporator introduced in [121] has been investigated against an adsorption module with silica gel. The effect of the filling level on the cooling capacity of the adsorption cycle has been estimated. It has been concluded that the heat transfer coefficient and the cooling capacity increase with the filling level of the evaporator heat exchanger. It was found a critical value for the filling level, further increase in the filling level resulted in a rapid decrement in both HTC and the cooling capacity.

In [124], the authors investigated the thin film evaporation mode of water in a partially flooded finned-circular-tube HEx at sub-atmospheric conditions. The major factor of influence on the thin film evaporation has been found to be the mass flow rate of the heat transfer fluid (HTF). Increasing the HTF's mass flow rate increases the flow turbulence and, accordingly, increases the overall heat transfer coefficient of the evaporator heat exchanger.

Chapter 3

Performance prediction of APHEs using small-scale adsorbent samples

This chapter presents the results of an experimental study on the adsorption and desorption kinetics of two differently structured, commercially available, plate heat exchangers (PHEs) produced by Alfa Laval, Sweden. The PHEs are basically developed to be applied as gas cooler heat exchangers. Therefore, The PHEs have been adapted first to work as adsorber plate heat exchangers (APHEs) and are then experimentally investigated in the Laboratory of Sorption Processes (LSP) at OTH Regensburg, Germany.

A new procedure is introduced to prepare test frames allowing the realization of representative small-scale adsorbent samples to the investigated APHEs. In addition, evaluating the matching between the obtained experimental adsorption and desorption kinetic results of the full-scale adsorbers and small-scale representative samples is introduced. The adsorption and desorption kinetics of the small-scale adsorbent samples are measured in the existing V-LTJ kinetic setup [93, 125, 95] (see Section 2.9.2) at similar operating conditions of the investigated APHEs. For the full-scale measurements, a slight modification to the thermal response LTJ methodology [91] (see Section 2.9.1), is introduced; namely, to estimate the instantaneous water loading from the measured evaporator or condenser power during adsorption or desorption processes, respectively, rather than carrying out a blind (disconnecting the evaporator/condenser from the adsorber/desorber) and an active adsorption process and estimate the temporal water uptake from the measured temporal heat of adsorption. The

---

Contents of this chapter have been reprinted from:
M. Mikhaeil, M. Gaderer and B. Dawoud." Experimental investigation of the adsorption and desorption kinetics on an open-structured asymmetric plate heat exchanger, matching between small-scale and full-scale results". Frontiers in Energy Research 10 (2022), with permission from Frontiers.
Contributions of the author: Conceptualization, Methodology, Investigation, Formal analysis, Writing original draft.

last should be obtained by subtracting the results of the blind experiment from those of the active adsorption experiment [91]. The results obtained from both small-scale and full-scale investigations at four typical operating conditions of adsorption appliances have been compared and discussed in detail. Based on the obtained kinetic results of the small-scale sample, a completely new evaluation methodology has been introduced to estimate the expected evaporator and condenser powers of one of the full scale adsorbers. Such theoretical results have been compared with those obtained upon investigating the corresponding full-size APHE.

3.1 Open-structured PHE as adsorber/desorber and its test setup

The first selected PHE in this study is the "GLX30" PHE (AlfaLaval, GLX30), which is the only, nickel-brazed, stainless steel, open-structured PHE available in the market. Formerly, this heat exchanger was obtainable form AIREC©, Sweden, under the trade name “Cross-30” PHE. The GLX30 PHE, depicted in Figure 3.1a, comprises a stack of multi, nickel-brazed plate-pairs made of stainless steel 316L. For the sake of mechanical stability of the GLX30 PHE, two flat and thick end plates are integrated to the stack by brazing. The plates composing the heat exchanger channels are embossed (dimpled) in two different forms and arranged together to form a stack of parallel plate-pairs. The plates have up-and-down dimples with different profiles and heights. Such configuration results in two asymmetric and separated domains, one domain for the gas flow and the second is for the liquid flow, and each domain comprises several identical subdomains. The volume ratio between the two asymmetric domains of the GLX30 PHE, namely the gas domain to the liquid domain, amounts to 1.91. Each HTF subdomain (HTF channel), existing inside a single plate-pair, has an inlet and an outlet port. Those HTF subdomains compose together the HTF domain of the whole GLX30 PHE.

The “GLX30” is a crossflow, gas-liquid plate heat exchanger, thus the other domain inside the GLX30 is specified for the gas flow. This means that the GLX30 is not primarily designed to act as an adsorber heat exchanger. However, the open gas domain can be filled in with loose grains of the adsorbent. Using a suitable stainless-steel sieve on each side for preventing the adsorbent grains from falling out, the GLX30 PHE can act as an adsorber heat exchanger. Figure 3.1b shows the adapted GLX30 PHE to work as an adsorber plate heat exchanger (APHE). The spaces (gaps) existing between the successive plate-pairs are utilized as an adsorbent domain and filled with 842 grams of the loose microporous Siogel

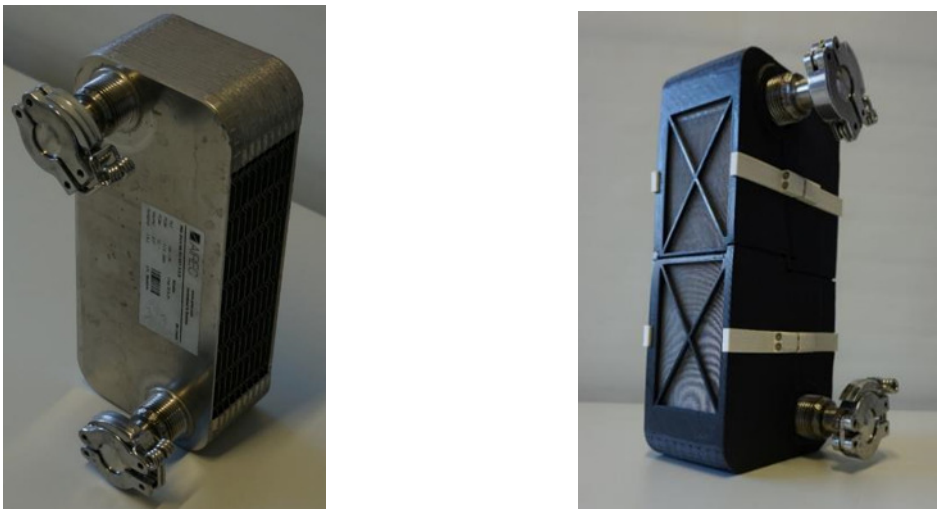

(a) (b)

Fig. 3.1 The GLX30 adapted as an adsorber heat exchanger (The open sides for vapour flow into/out of the adsorbent domain are covered by a stainless-steel sieve to prevent the loose pellets from falling). (a) Before being filled in with the adsorbent, (b) adapted and filled in with Siogel grains.

(Oker Chemie, Germany) in the grain size range of 0.71 to 1.0 mm. Table 3.1 illustrates more specifications of the GLX30 PHE.

A special test setup has been established to investigate the adsorption and desorption kinetics of the full-scale GLX30 APHE. The setup, depicted schematically in Figure 3.2, consists mainly of two compartments, the evaporator/condenser unit and adsorber/desorber unit. The evaporator/condenser unit is a double helical tube heat exchanger fixed inside a vacuum tight chamber made of stainless steel and equipped with inlet and outlet ports for the internal double helical tube HEx. Two temperature sensors are mounted on the inlet and outlet ports of the evaporator/condenser unit for measuring the temperature of HTF passing through the internal helical tube heat exchanger. In addition, a flow rate sensor is adapted to measure the volume flow rate of the HTF inside the evaporator/condenser ($\dot{V}_1$).

For an effective evaporation operation, a falling film evaporator concept has been developed and realized inside the evaporator/condenser chamber. The adsorber/desorber unit is another vacuum tight chamber made of stainless steel, in which the adapted APHE (3.1b) is mounted. The chamber is equipped with side connection ports for feeding the internally mounted APHE with the HTF. Two temperature sensors are mounted on the connection ports to measure the temperature of the HTF at the inlet and outlet of the APHE. The volume flow rate of the HTF inside the adsorber/desorber loop ($\dot{V}_2$) is measured by the flow rate sensor.

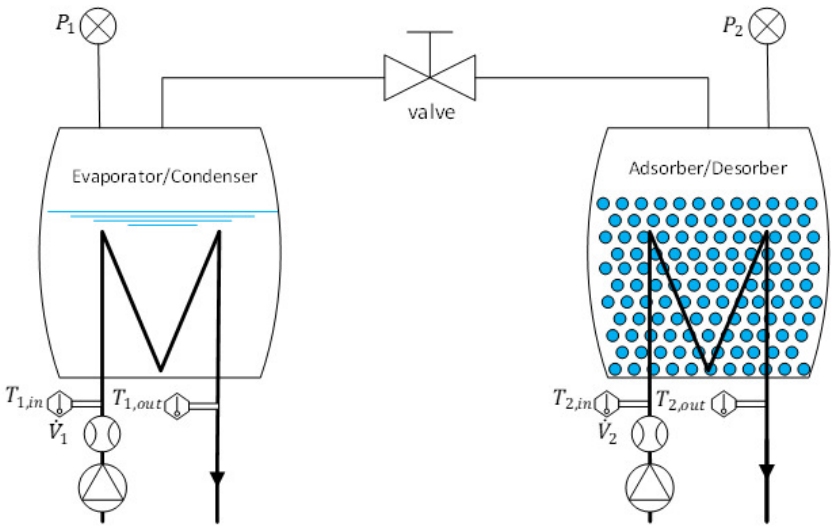

Fig. 3.2 Schematic drawing of the test setup.

Both chambers are equipped, at the top part, with vacuum-tight ports, for connecting vacuum pressure transducers ($P1$ & $P2$), and 50 mm diameter ports, to which, central vacuum flanges are welded, to enable connecting the two chambers together through a vacuum tight tube having a vacuum gate valve of DN50. Figure 3.3 illustrates the realized test setup for the GLX30 APHE in the Laboratory of Sorption Processes (LSP) of OTH-Regensburg, Germany.

3.1.1 Closed-structured PHE as adsorber/desorber and its test setup

To realize a test setup for investigating the performance of a closed structured PHE acting as an adsorber/desorber for the application in the adsorption processes, a pair of identical closed-structure asymmetric plate heat exchangers produced by Alfa Laval©, Sweden, with trade name of GL50 was used. Thus, a GL50 PHE of 20 plates was employed to act as an evaporator/condenser and connected with another identical GL50 PHE acting as adsorber/desorber. Investigating the evaporation and condensation mechanisms of the adsorbate in the GL50 evaporator/condenser PHE is out the focus of this chapter. The GL50 PHE is a stack of multi-nickel-brazed parallel plates made of stainless-steel. The brazing of the plates together forms two separated and non-identical domains inside the PHE. The GL50 PHE is designed to exchange heat between two fluids (gas and liquid). Therefore, each domain shall be occupied by a flowing fluid, which enters the HEx from an inlet port and leaves from an outlet port. Moreover, the design of the GL50 PHE allows the draining of the condensed droplets in case of using it for cooling a condensable gas. Table 3.1 illustrates more specifications of the GL50 PHE.

Fig. 3.3 Realized test setup for investigating the APHE at the LSP of OTH-Regensburg, Germany.

Table 3.1 Technical specifications of the investigated PHEs

Heat exchanger specification	GLX30 PHE	GL50 PHE
Basic dimensions (LxWxH) (mm)	278X123X69	278X123X83
Number of Plates	19	20
HTF's Inlet and outlet ports diameter (mm)	22.3	18
Diameter the adsorbent domain's ports (mm)	-	56.3
Volume for adsorbent domain (L)	1.14	1.06
Volume of the HTF domain (L)	0.57	0.9
Mass (kg)	3.9	3.4

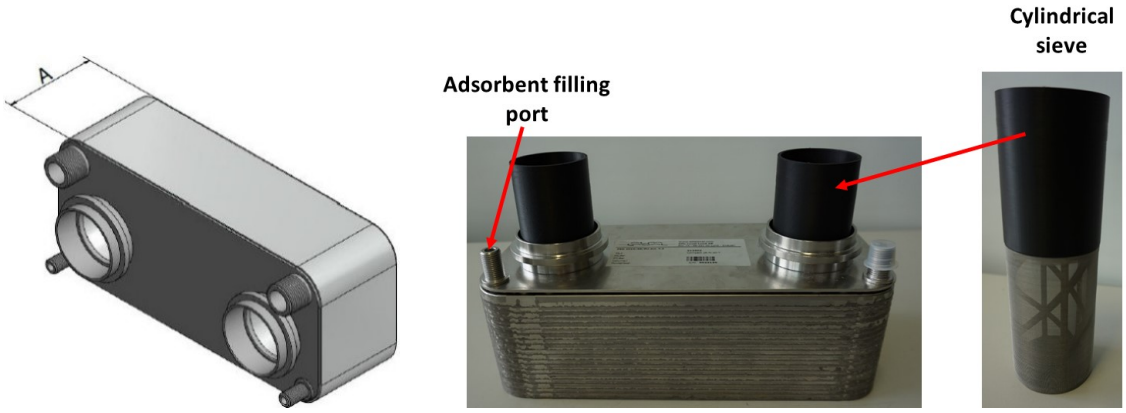

(a) (b)

Fig. 3.4 The GL50 PHE of 20 plates (A=83.0 mm). (a) 3D drawing of the GL50 PHE, (b) Placing the cylindrical sieves in the vapour manifolds of the GL50 PHE

From the above description, it is clear that the GL50 PHE is not designed to act as an adsorber/desorber. Therefore, adaptation work is required before being suitable to act as an adsorber/desorber. The GL50 PHE should enable the heat exchange between a HTF passing through the fluid domain and an adsorbent material occupying the gas domain. The volume ratio between the GL50 PHE's domains is 1.66 and the bigger domain has the two big ports (see Figure 3.4). From the Coefficient Of Performance (COP) point of view, it is favorable to select the smaller domain for the HTF and the larger one for the adsorbent material, thus low heat capacity ratio of the Adsorber (K_{AdsHX}) [20] and, accordingly, high COP can be realized. Another advantage of using the larger domain for the adsorbent is the larger ports (see Figure 3.4), which can be utilized to connect the adsorber/desorber to the evaporator/condenser with a lower mass transfer resistance.

In order to use adsorbent in form of loose grains and preventing the grains from falling out of the GL50 APHE in the manifolds of the refrigerant (adsorbate) vapour, a special construction allowing the vapour to pass through while preventing the adsorbent grains from falling out has been designed. It is a 3D printed cylindrical frame with a piece of fine stainless-steel sieve mounted annularly (see Figure 3.4b). Two pieces of the special construction have been realized by machining and mounted in the vapour manifolds of the GL50 APHE. To fill the APHE with the adsorbent grains, one of the two small ports for the condensate draining has been utilized. To realize the highest possible filling density of the adsorbent in the GL50 APHE, it has been mounted on a vibratory shaker during the filling process with the adsorbent grains. The GL50 APHE has been filled with 790 gram of dry Siogel grains produced by Oker Chemie©, Germany, in the size range of 0.71-1.0 mm.

Figure 3.5 depicts a scheme and a 3D drawing of the test setup configuration. The setup consists, as prementioned, mainly of two compartments. The first is a GL50 PHE adapted to work as adsorber/desorber and the second is another identical GL50 PHE (without any adaptation) to work as evaporator/condenser. The two PHEs are connected together through two separated pipelines. The connection pipes allow the refrigerant vapour to transfer between the two PHEs. Two vacuum gate valves ($V2.1$ and $V2.2$) are mounted on the pipelines to allow separating the two PHEs from each other. Two pressure transducers ($P1$ & $P2$) are mounted on the pipelines connecting the two PHEs together (see Figure 3.5) to measure the pressure of the refrigerant vapour in the two PHEs separately, i.e., the vapour pressure inside the adsorber/desorber and the evaporator/condenser. Finally, two vacuum valves ($V1.1$ and $V1.2$) are mounted on the pipelines to allow evacuating the two PHEs separately. In addition, the valve used to evacuate the evaporator/condenser could be used also to fill it with the refrigerant.

The pipelines and valves are all made of stainless steel. To prevent the undesired local vapour condensation on the inner surface of the connection piping and valves, especially during the condensation-desorption processes, a controlled heating cable is wrapped around them to keep their wall temperature 5 K higher than the condensation temperature. A leak test has been successfully carried out. The setup has been well insulated to minimize the heat lost/gained to/from the surrounding. Figure 3.6 shows the realized test setup at the LSP of OTH-Regensburg, Germany.

After 6-hour evacuation of the entire test setup, the two gate valves (V2.1 and V2.2) have been closed to separate the evaporator/condenser from the adsorber/desorber. An external tank filled with degassed water, which shall be used as refrigerant (adsorbate), has been placed on a high-sensitive balance and connected to the evaporator/condenser through valve V1.1 mounted for evacuation and filling the evaporator /condenser with the refrigerant. A cold HTF (5°C) has been allowed to pass through the evaporator/condenser to cool it down and enables condensation of the water vapour coming out from the external tank. After accumulating 225 gram of the degassed water in the evaporator/condenser valve $V1.1$ has been closed. The amount of water (refrigerant) used has been determined based on the amount of the dry adsorbent in the adsorber/desorber and the planned testing conditions. The amount of water should be a little higher than the maximum amount of water, which could be adsorbed during any of the adsorption-evaporation processes. A much higher amount of the refrigerant results in higher film thickness in the evaporator/condenser during the adsorption-evaporation and desorption-condensation processes limiting the kinetics of the processes.

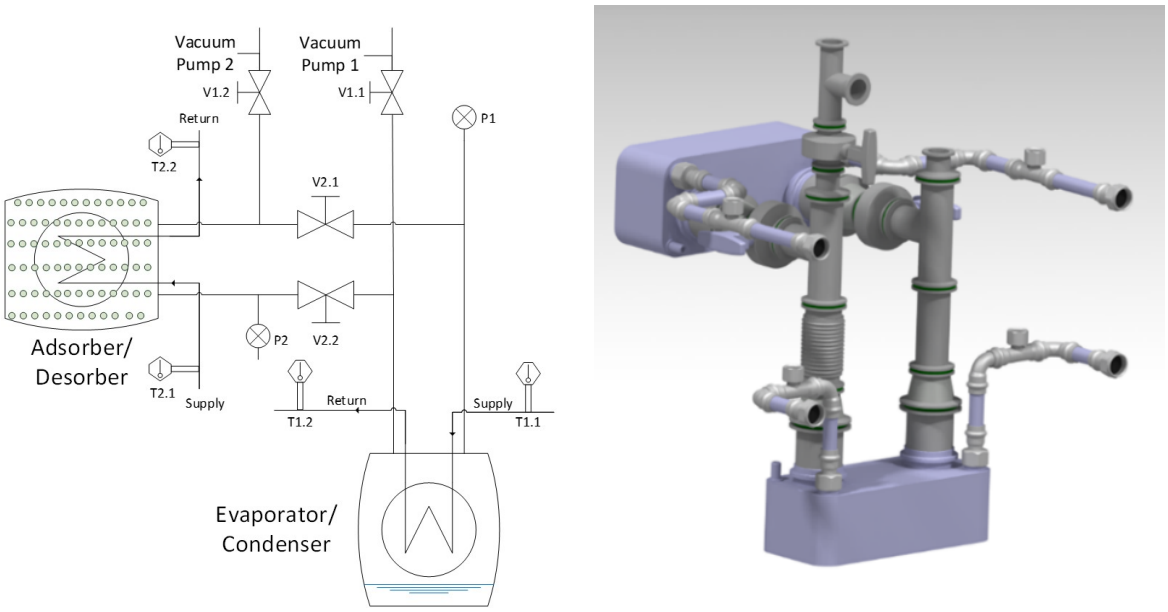

(a) (b)

Fig. 3.5 Layout of the GL50 APHE test unit. (a) Schematic layout including the most important sensors and actuators, (b) 3D-drawing of the assembled components

Fig. 3.6 Realized test unit for investigating the GL50 APHE at the LSP of OTH-Regensburg, Germany.

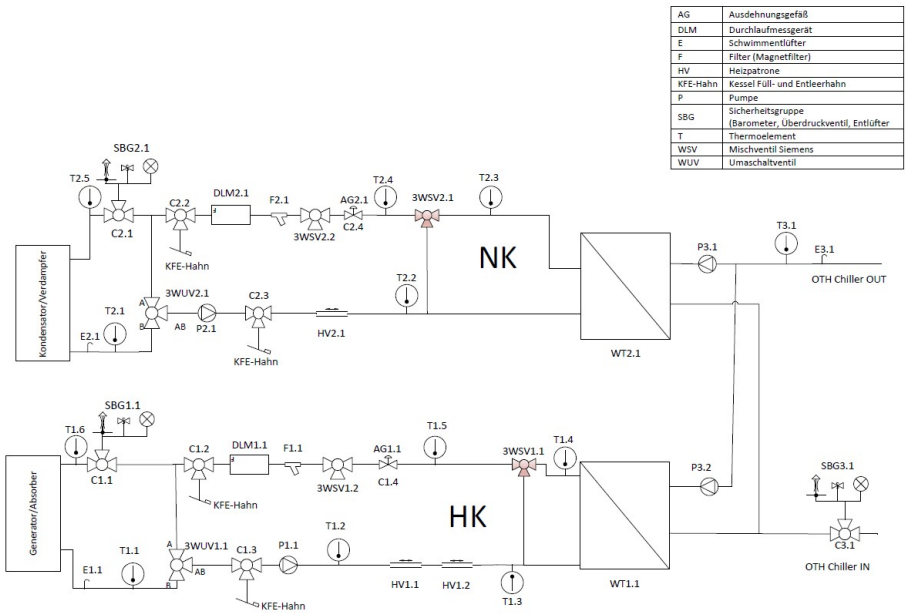

Fig. 3.7 Schematic layout of the hydraulic setup installed at OTH Regensburg

3.2 Hydraulic setup

In order for the experimental investigations of adsorption / evaporation and desorption / condensation operation phases of different adsorption heat transformation processes to be carried out at controlled operating conditions, a dedicated hydraulic setup has been developed and mounted in the LSP of OTH Regensburg. The hydraulic setup, which is depicted schematically in Figure 3.7, comprises two separated hydraulic circuits, a primary and a secondary circuit. The primary circuit (lower loop designated as HK) feeds the adsorber/desorber heat exchanger, whereas the secondary one (upper loop designated as NK) feeds the evaporator/condenser heat exchanger. A high precision measuring and control system has been established, which is monitored and interfaced via a specially developed LabVIEW code. Via the LabVIEW code, the desired temperature and flow rate of the HTF on each hydraulic circuit can be realized

In addition, the control system allows sudden falling and rising of the HTFs temperature on the primary circuit, enabling carrying out large-temperature-jump (LTJ) adsorption and desorption processes similar to the processes taking place in real adsorption heat pumps and chillers [93, 125, 95]. The type and accuracy of the individual sensors applied for measuring the pressure of the refrigerant vapour in both vessels and the inlet and outlet temperatures and flow rate of the HTFs passing through the units are listed in Table A.1 of Appendix A. The measurements have been carried out at the following values for evaporator (T_{ev}), condenser

Fig. 3.8 Realized hydraulic setup at OTH Regensburg

or adsorption-end (T_{cond}) and desorption-end (T_h) temperatures; T_{ev} = 10 & 15°C, T_{cond} = 30 & 35°C, and T_h = 90°C.

Furthermore, thanks to the gate valves connecting the adsorber/desorber to the evaporator/condenser in both constructed test setups, adsorption and desorption processes similar to the processes taking place in adsorption storage systems can be experimentally investigated. Moreover, it allows the experimental investigation of adsorption units according to the large pressure jump (LPJ) method developed in [92], which replicates the processes taking place in adsorption heat storage and heat transformation systems. Figure 3.8 shows the realized hydraulic setup installed in the LSP of OTH Regensburg.

3.3 Evaluation of the instantaneous water uptake

In this section, a slight modification to the T-LTJ method [91] (see Section 2.9.1) is introduced. Rather than conducting blind and active adsorption/desorption processes and estimating the temporal water uptake from the temporal cumulative integrations of the heat of adsorption/desorption, the temporal cumulative integrations of the heat of evaporation/condensation are utilized. In other words, the time integration of the instantaneous power of the evaporator or condenser have been applied to estimate the temporal amount of refrigerant evaporated

from the evaporator and adsorbed in the adsorber or the amount water vapour desorbed from the desorber and condensed in the condenser during each adsorption or desorption process, respectively. First, the measurements of the volume flow rate of HTF passing through the evaporator/condenser ($\dot{V}_1$) and the temperature difference between the HTF's inlet and outlet of the evaporator/condenser heat exchanger ($T_{1,in} - T_{1,out}$) have been utilized to evaluate the instantaneous evaporator/condenser power ($\dot{Q}$) according to Equation 3.1.

$$\dot{Q} = \dot{V}_1.\rho.C_p.(T_{1,in} - T_{1,out}) \tag{3.1}$$

The instantaneous specific (per kg of adsorbent) evaporator/condenser power ($\dot{q}$) is given by Equation 3.2.

$$\dot{q} = \frac{\dot{Q}}{m_{ads}} \tag{3.2}$$

where m_{ads} is the mass of the dry adsorbent filled in the investigated APHE.

The time integration of the instantaneous evaporator/condenser power ($\dot{q}$) results in the total evaporation/condensation energy up to each time point ($q(t)$). The integration can be done by implementing the simplest numerical integration method, i.e., the rectangular (midpoint) rule, as following

$$q(t) = \int_0^t \dot{q}.dt = \sum_{i=0}^{n} (\dot{q}_i \times \Delta t_i) = \Delta t_i \sum_{i=0}^{n} \dot{q}_i \tag{3.3}$$

Where, $i = 0$ to N is a counter for the measured points and Δt is the measuring time step (1 s). The water uptake obtained in an adsorption process (w_{ads}) is defined in Equation 3.4 and in a desorption process (w_{des}) in Equation 3.5.

$$w_{ads}(t) = w_o + \frac{q(t)}{h_{fg}(T_{ev})} \tag{3.4}$$

$$w_{des}(t) = w_o + \frac{q(t)}{h_{fg}(T_{cond}) + c_{p,v}(T_v - T_{cond})} \tag{3.5}$$

Where, w_o is the initial water uptake, which is evaluated from the equilibrium model of the water/Siogel working pair presented in [18], $h_{fg}(T)$ is the latent heat of evaporation/condensation at given evaporator/condenser temperature. T_v is the temperature of the water vapour leaving the desorber. The following equation (Equation 3.6) is used for calculating the $h_{fg}(T)$ [126] at given evaporator/condenser temperature (T).

$$h_{fg}(T) = 1.91846 \times 10^6.[T/(T - 33.91)]^2 (J.kg^{-1}) \tag{3.6}$$

The specific moving average evaporation/condensation power obtained in an adsorption/desorption process ($\bar{q}$) is calculated as,

$$\bar{\dot{q}} = \frac{1}{t}.q(t) \tag{3.7}$$

The uncertainty analysis of the water uptake estimation, the instantaneous and moving average evaporator and condenser power measurements are presented in Appendix A.

3.4 Small-scale adsorbent samples preparation

3.4.1 GLX30 APHE's representative adsorbent sample

In the GLX30 APHE, the thickness of the adsorbent filling the gap between every two successive plate-pairs (the adsorbent layer's thickness) as well as the mass diffusion path length of the adsorbate (water vapour) in the adsorbent layers are limiting the combined heat and mass transfer in the adsorbent domain. Due to the surface topology of the plate-pairs, the adsorbent layers have variant thickness. Figure 3.9a illustrates a 2-D sketch of one of the plate-pairs composing the investigated APHE. The figure does not depict the complex surface topology of the plate-pair, since the adsorbent half-layer contacting the front side of the plate-pair appears in the figure and covers the topologies. Figure 3.9b depicts two different cross sections of the sketch depicted in Figure 3.9a, namely cross sections A-A and B-B (see section locations in Figure 3.9a). The metal and the HTF subdomain of the plate-pair and the two adsorbent half-layers contacting the two sides of the plat-pair appear in the cross sections (Figure 3.9b).

As the HTF passes quasi-equally through the spaces inside the plate-pairs (HTF channels), assuming, from the heat transfer perspective, a thermal symmetry plane for each adsorbent layer, which shall divide it at the middle and pass parallel to the plates of the APHE, is quite reasonable. This implies that at the upper and lower sides of the cross sections shown in Figure 3.9b, thermal symmetry boundary conditions could be considered. Therefore, half of the thickness of an adsorbent layer existing between two successive plate-pairs refers to the heat transfer characteristic length (HTCL) of the investigated APHE. Indeed, the thickness of the adsorbent layers is variant; however, 6 mm is the most prevailing thickness of the adsorbent layers. As the investigated APHE is of open-structure, where the adsorbent layers in the spaces between the successive plat-pairs are receiving/delivering the refrigerant vapour equally from/to both open sides, a mass transfer symmetric plane dividing each adsorbent layer at the middle and parallel to the open sides of the APHE could be considered. The mass transfer symmetric plane is represented in Figure 3.9a and Figure 3.9b by the C-C line.

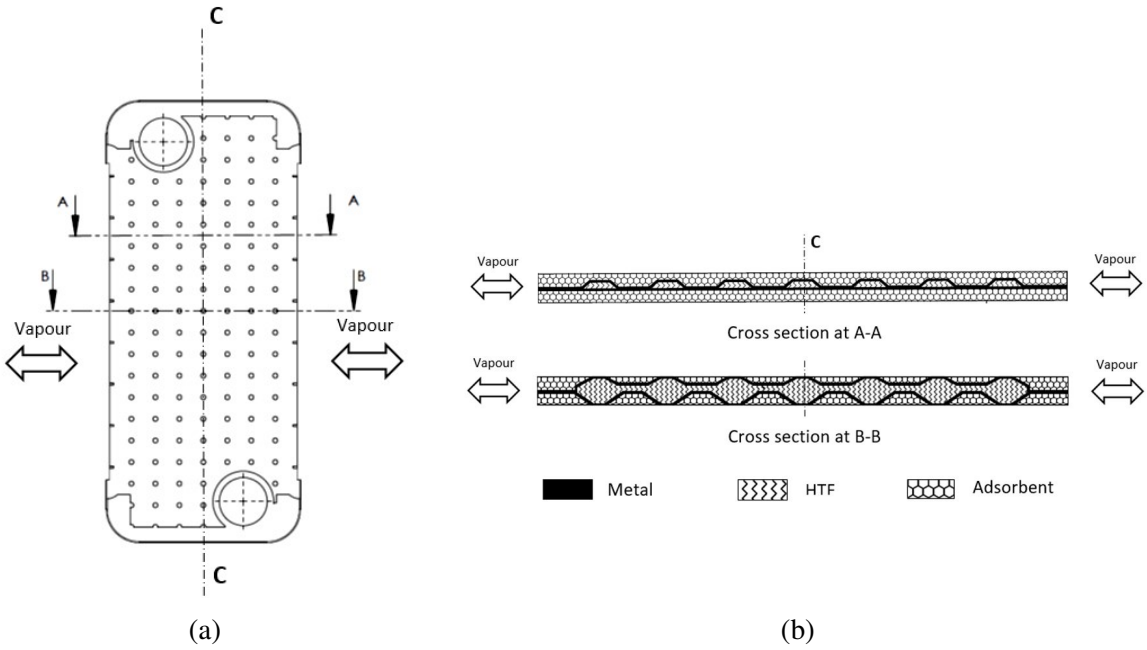

(a) (b)

Fig. 3.9 Cross sections in two successive plate pairs of the GLX30 APHE. (a) 2-D sketch of one of the plate-pairs, (b) Cross sections at A-A and at B-B

Accordingly, half the width of the APHE could be defined as the mass transfer characteristic length (MTCL) of the adsorbent domain of the investigated APHE.

For predicting the adsorption and desorption kinetics of the GLX30 APHE, using a small-scale adsorbent sample, dedicated small structure (test frame) fabricated from polyether ether ketone (PEEK), which is an insulation material and with low out-gassing characteristics under vacuum, is used to realize a small adsorbent sample out of the Siogel applied in the investigated GLX30 APHE and with thickness and the length corresponding to the heat and mass transfers' characteristic lengths (HTCL & MTCL) of the GLX30 APHE, respectively. Strictly speaking, a frame was prepared to realize an adsorbent sample with thickness of 3 mm, which is corresponding to the HTCL of the GLX30 APHE and a length of 58.5 mm, which is corresponding to the APHE's MTCL.

The structure (test frame) shall enable the refrigerant vapour (adsorbate) to enter to/leave from the adsorbent sample placed inside it only from a small slot, at which a piece of a fine sieve shall be installed to prevent the grains from falling out of the structure. The slot shall be existing on one side allowing the refrigerant vapour to diffuse in longitudinal direction through the adsorbent sample. At the down side of the PEEK construction a stainless steel (SS) substrate of 0.3 mm thickness shall be mounted to allow the heat transfer between the sample and the sample holder inside the measuring cell, on which the sample shall be placed during the experimental investigations. The PEEK construction and the SS substrate shall be

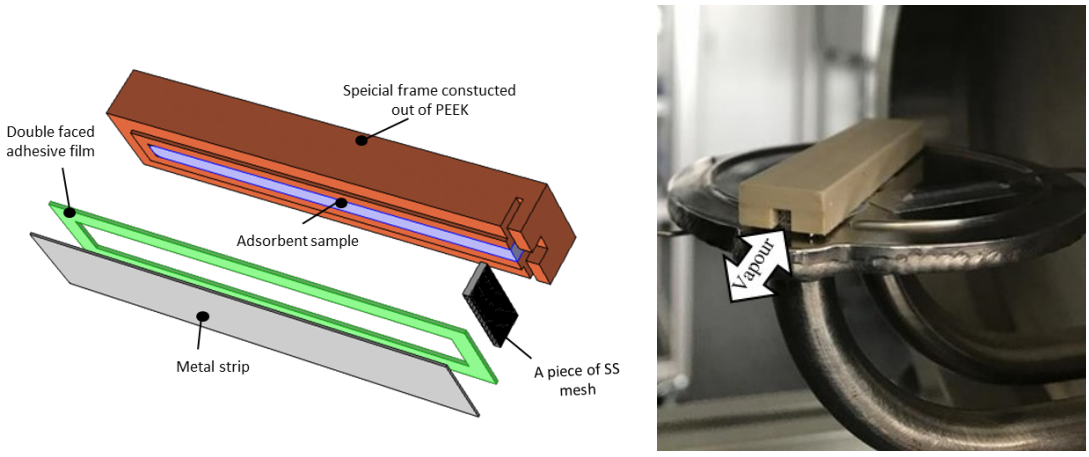

(a) (b)

Fig. 3.10 Test frame prepared to realize small-scale representative adsorbent sample for the GLX30 APHE; (a) test frame configuration, (b) final fabricated test frame filled with Siogel and placed on the sample holder of the kinetics' setup measuring cell

sealed together by a special double-sided adhesive film after filling the construction with the adsorbent grains.

As the maximum expected measured differential water uptake of the Siogel under the desired operating conditions does not excess 25 g/100g, the mass of the samples that will be tested in the sorption kinetics' setup is limited to 320 mg, in order to allow the adsorption or desorption measurements under quasi isobaric ($\Delta p < 2$ mbar) conditions. Based on this limitation of the sample mass, the width of the sample has been determined to 3 mm. Figure 3.10b shows the configuration of the test frame and Figure 3.10b shows the final fabricated test frame filled with Siogel and placed on the sample holder inside the measuring cell of the kinetic setup.

3.4.2 GL50 APHE's representative adsorbent sample

Since the successive plates in the GL50 APHE are not flat but dimpled, the equivalent thickness of one adsorbent sub-domain could be calculated by dividing the volume of the adsorbent sub-domain by its projected area (the red shaded area in Figure 3.11a). This results in an equivalent thickness of 4.5 mm. From the heat transfer point of view, since every adsorbent sub-domain exists between two successive plate-pairs is subjected to equivalent cooling/heating effects from the upper and lower sides during the adsorption/desorption processes, a set of successive parallel symmetric planes dividing the successive adsorbent sub-domains could be considered. However, the test frame, which shall be placed on top of the sample holder of the VLTJ kinetic setup is subjected to cooling/heating from one side

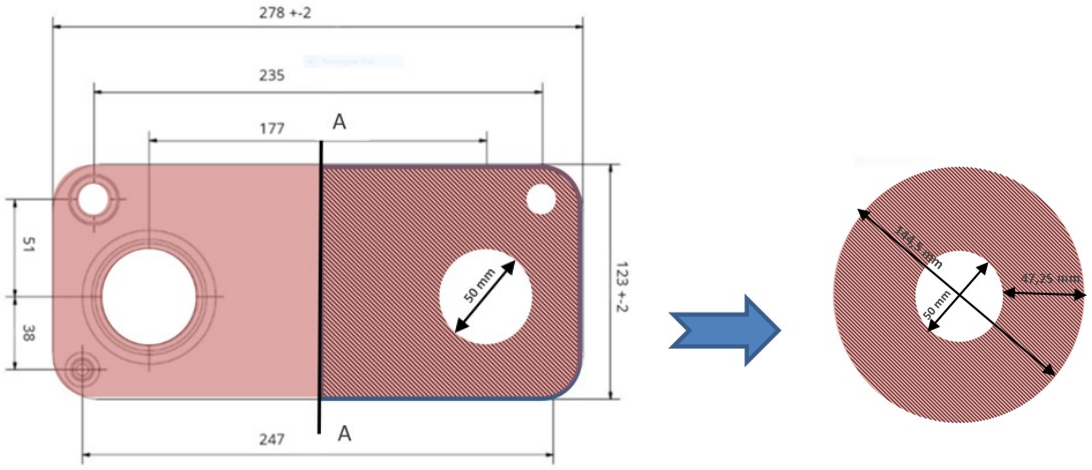

(a) (b)

Fig. 3.11 Evaluation of the equivalent vapour diffusion path length in the GL50 APHE. (a) projected area of the adsorbent domain of the GL50 APHE, (b) equivalent regular shaped

(the bottom side). The height of the adsorbent sample inside the test frame shall equal to half of the equivalent thickness between two successive heating/cooling plates inside the APHE (2.25 mm). The upper side should be the heat transfer symmetry plane, which shall be thermally isolated.

The GL50 APHE receives/delivers the water vapour (adsorbate) equally from/to the two identical vapour ports, depicted in Figure 3.4. Therefore, from the mass transfer point of view, this APHE is symmetric around the A-A plane and the vapour flows in the adsorbent domain in each part around the A-A plane are identical. The dashed area presented in Figure 3.11a is one of the two identical areas and should be sufficient to calculate the equivalent length of the vapor diffusion path in the APHE.

Since the vapour coming in/out from each vapour port flows almost radially through the adsorbent in both identical parts of the APHE, around A-A plane, the equivalent length of the diffusion path could be evaluated from the equivalent regular shaped area of one of the two identical heat exchangers parts around A-A. The equivalent regular shaped area has been assumed equal to an area between to concentric circles, where the diameter of the inner circle equals to the diameter of one vapour port (50 mm). Figure 3.11b illustrates this equivalent regular shaped area. The diameter of the outer circle that makes the area of the equivalent regular shape in Figure 3.11b equal to the area of the dashed part in Figure 3.11a is 144.5 mm. Thus, it can be considered that the radial distance between the inner circle and the outer circle of the shape shown in Figure 3.11b is the equivalent length of the vapor diffusion path

Table 3.2 HTCL and MTCL of the adsorbent samples representative to the investigated APHEs

Representative adsorbent sample specification	GLX30 APHE	GL50 APHE
HTCL, i.e. adsorbent thickness (mm)	3.0	2.25
MTCL, i.e. Vapour diffusion path length (mm)	58.50	47.25

in the adsorbent domain of the GL50 APHE. This distance amounts to 47.25 mm and should be the length of the adsorbent domain inside the test frame.

The frame of the GL50 APHE has been also fabricated from PEEK, which is filled with Siogel grains in the same previously mentioned size. The Frame has been sealed with SS substrate in the same manner followed for the GLX30's test frame. Table 3.2 compares between the two adsorbent samples representative to the investigated APHEs in terms of the HTCL and the MTCL.

3.5 Results

As mentioned previously, the adsorbent representative samples are specifically designed to predict the adsorption and desorption kinetics of the APHEs introduced in this chapter. Therefore, in this section comparisons between the instantaneously measured water uptake of the APHEs and their representative samples at different operating conditions, namely adsorption and desorption processes according to the Large Temperature Jump (LTJ) technique at evaporator temperatures of 10 and 15°C, condenser (adsorption-end) temperatures of 30 and 35°C and driving source (desorption end) temperature of 90°C, are presented and discussed. In addition, the instantaneous as well as the moving average evaporator and condenser powers estimated from the adsorption and desorption kinetic results of the small-scale adsorbent sample representative to the GLX30 APHE are compared to the powers obtained from the evaporator/condenser unit, against which the GLX30 APHE has been experimentally tested at the previously mentioned operating conditions.

3.5.1 Adsorption kinetics

Figure 3.12 illustrates the adsorption kinetics measurements obtained upon performing adsorption processes on the GLX30 APHE and its representative adsorbent sample under different sets of operating conditions. Figure 3.13 illustrates the results of the GL50 APHE and its representative adsorbent sample under the same sets of operating conditions of the GLX30 APHE. As depicted in Figures 3.12a-3.12d and Figures 3.13a-3.13d, there are small

differences in the adsorption kinetics between the APHEs and their representative small-scale adsorbent samples at all applied operating conditions. In general, the adsorption kinetics of the small-scale samples are slightly slower than those obtained from the full-scale APHEs. To define a criterion for evaluating the difference in the adsorption kinetics between the APHEs and their representative adsorbent samples, the experimental adsorption kinetic data of each are fitted to the exponential form presented in Equation. 3.8.

$$w(t) = w_o + \Delta w_f(1 - exp(-t/\tau)) \tag{3.8}$$

where $w(t)$ is the instantaneous water uptake, w_o is the initial water uptake, Δw_f refers to the final or equilibrium differential water uptake $(w_f - w_o)$, and τ is the characteristic time constant. The exponential curve fittings are depicted also in Figure 3.12 and Figure 3.13. As shown in the figures, all adsorption kinetic curves of each APHE and its representative adsorbent sample follow the expressed exponential behaviour by Equation. 3.8. Comparison between the adsorption kinetics of each the APHE and its representative adsorbent sample at every set of operating conditions could be made throughout the values of the time constants (τ) of the fitting exponential forms. Table 3.3 illustrates the values of τ and the coefficient of determination (R^2). The relative deviation in the τ value (*RD*) between each APHE and its representative adsorbent sample at every applied set of operating conditions is used to evaluate the adsorption kinetic deviation of the representative adsorbent sample from the adsorption kinetic of the APHE at every set of operating conditions. For the GLX30, the maximum *RD* value is obtained at operating conditions of 15/30/90°C and amounts to 23.7%, whereas the minimum RD value is 6.4% and obtained at operating conditions of 15/35/90°C. The matching between the full-scale and small-scale adsorption measurements of the GL50 APHE is much better (see Figure 3.13). Strictly speaking, for the GL50, the maximum *RD* value is obtained at operating conditions of 10/30/90°C and amounts to 2.28%, whereas the minimum RD value is 0.69% and obtained at operating conditions of 10/35/90°C. Table 3.3 shows the RD values obtained in all conducted adsorption processes for both investigated APHEs. Such results are very promising, as in the literature, according to [84], the typical factor of the difference in the adsorption dynamics between the full-scale and the small-scale measurements is 2 to 10.

The difference in the adsorption kinetics between the APHEs and their representative adsorbent samples can be attributed to the difference in the pressure courses of variation between the water vapour surrounding the APHEs in their experimental test setups and that surrounding the small adsorbent samples in the measuring cell of the V-LTJ kinetic setup, which have been recorded during the experimental processes and depicted also in Figure 3.12 (lower curves) and Figure 3.13 (lower curves). Since the mass of water vapour filling the

Table 3.3 Time constant of the exponential fitting (τ) and its (R^2) value of the **adsorption** kinetic data obtained at each set of operating conditions for the APHEs (Full-scale) and their representative adsorbent samples (Small-scale).

Operating Condition		GLX30 APHE			GL50 APHE		
		Full-Scale	Small-Scale	RD [%]	Full-Scale	Small-Scale	RD [%]
15/30/90	τ [s]	788.5	975.6	+23.72	807.7	810.6	+0.36
	R^2	0.9922	0.9890		0.9983	0.9915	
15/35/90	τ [s]	632.1	591.3	+6.45	600.3	591.0	-1.55
	R^2	0.9922	0.9894		0.9977	0.9893	
10/30/90	τ [s]	630.6	700.0	+11.00	654.3	669.2	+2.28
	R^2	0.9982	0.9923		0.9981	0.9889	
10/35/90	τ [s]	541.5	586.1	+8.20	490.6	487.2	+0.69
	R^2	0.9982	0.9913		0.9908	0.9956	

internal volume of the constant-volume kinetic setup (i.e., the internal volume of the vapour vessel, the measuring cell, and the connection pipes between them) continuously decreases during the adsorption process, the pressure of the water vapour surrounding the investigated sample in the measuring cell decreases with the time of adsorption. The maximum pressure drop is reached at the end of the adsorption process and it is limited here to 2 mbar, as explained in Section 3.4.

In the adsorption kinetic measurements of the APHEs, the time course of pressure variation of the water vapour surrounding each APHE in its experimental setup is quite similar to that takes place in adsorber of a real adsorption chiller or a heat pump. In other words, the pressure of the vapour surrounding the adsorber drops sharply during the first few seconds and then starts to be recovered and approaches its initial level at the end of the process upon reaching the corresponding equilibrium state. Such behavior has been faced in the lab-scale setups as well as in real adsorption heat pumps and chillers [127].

The differences in the adsorption kinetics between the adsorbers and the small-scale adsorbent samples are quite small at the condenser temperature of 35°C. This can be attributed to the lower differential water uptake obtained in case of conducting adsorption processes with higher condenser (adsorption-end) temperature, leading to lower drop in the pressure of the vapour surrounding the small-scale adsorbent sample in the measuring cell and accordingly, lower difference in the pressure course between the water vapour surrounding the APHE and that surrounding its small-scale adsorbent sample in measuring cell of the V-LTJ kinetic setup.

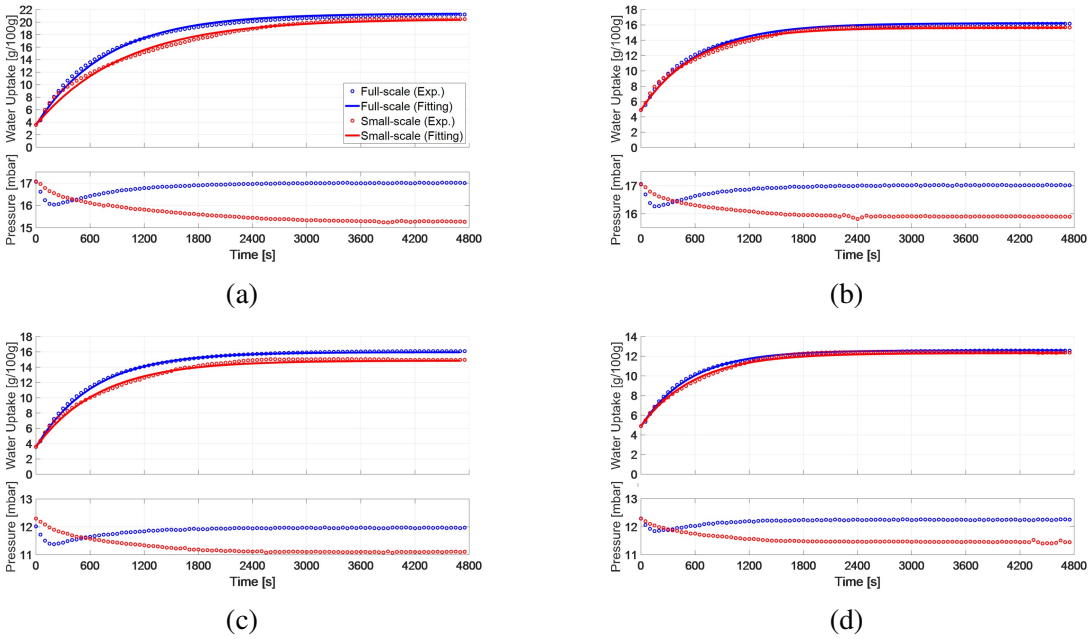

Fig. 3.12 Adsorption kinetic (upper) and vapour pressure (lower) curves of the GLX30 APHE (full-scale measurements) and its representative adsorbent sample (smallscale measurements) at evaporator, condenser/adsorption-end and desorption temperatures of (a) 15/30/90°C, (b) 15/35/90°C, (c) 10/30/90°C, (d) 10/35/90°C.

3.5.2 Desorption kinetics

Figure 3.14 and Figure 3.15 depict the desorption kinetic data obtained from the experimental investigation of the APHEs and their representative adsorbent samples upon performing LTJ desorption processes at different sets of operating conditions. Indeed, the desorption kinetics of the APHEs and the small-scale adsorbent samples are remarkably faster if compared with the adsorption kineties. As depicted in Table 3.4, the GLX30 APHE demonstrates a faster desorption kinetics by an average factor of 2.85 relative to the adsorption kinetic. For the GL50 APHE, this factor amounts to 3.73. In addition, it is obvious that, the desorption kinetics of the small-scale representative samples are higher than those obtained from the full-scale APHEs. The relative deviation in the desorption kinetic's characteristic times between full-scale and small-scale measurements is clearly higher than the RD of the adsorption characteristic times. Strictly speaking, for the GLX30, the *RD* amounts to -36.2% in favor of the small-scale sample at the boundary condition 10/35/90°C, which increases to -45.7% at 15/30/90°C. For the GL50, the *RD* values do not differ significantly from the values of the GLX30, -32.0% in favor of the small-scale sample at the boundary condition 15/35/90°C, which increases to -43.7% at 15/30/90°C.

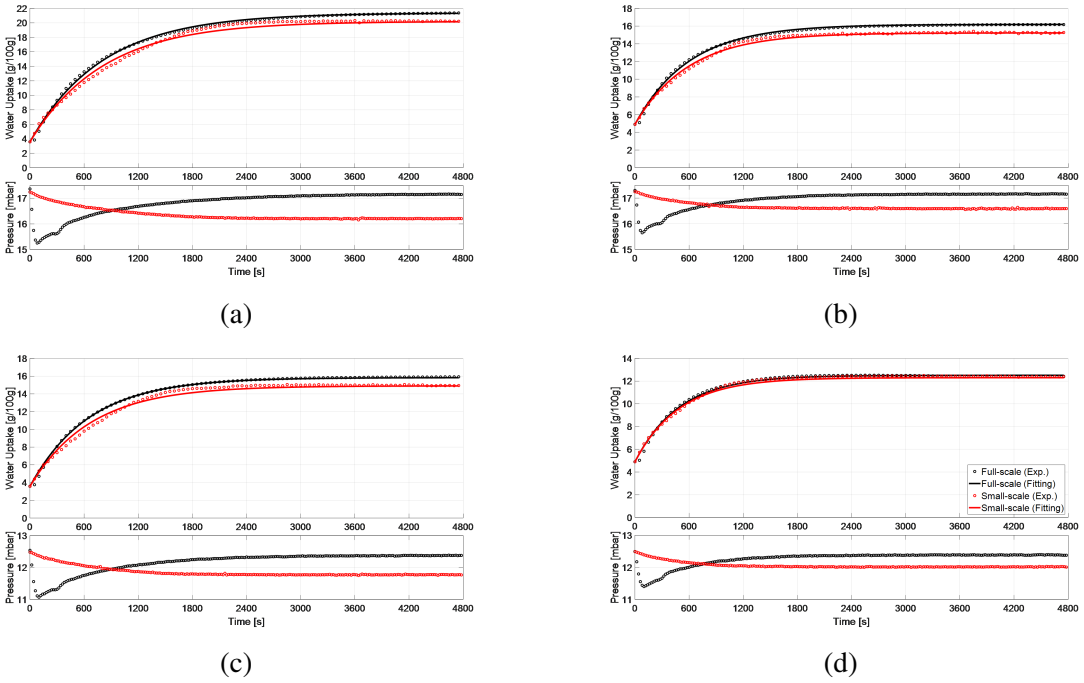

Fig. 3.13 Adsorption kinetic (upper) and vapour pressure (lower) curves of the GL50 APHE (full-scale measurements) and its representative adsorbent sample (smallscale measurements) at evaporator, condenser/adsorption-end and desorption temperatures of (a) 15/30/90°C, (b) 15/35/90°C, (c) 10/30/90°C, (d) 10/35/90°C.

Table 3.4 Time constant of the exponential fitting (τ) and its (R^2) value of **the desorption** kinetic data obtained at each set of operating conditions for the APHEs (Full-scale) and their representative adsorbent samples (Small-scale).

Operating Condition		**GLX30 APHE**			**GL50 APHE**		
		Full-Scale	**Small-Scale**	**RD [%]**	**Full-Scale**	**Small-Scale**	**RD [%]**
15/30/90	$\boldsymbol{\tau}$ [s]	244.7	132.9	-45.7	192.4	108.3	-43.7
	R^2	0.9979	0.9756		0.9982	0.9799	
15/35/90	$\boldsymbol{\tau}$ [s]	213.2	129.7	-39.2	168.3	114.5	-32.0
	R^2	0.9945	0.9787		0.9990	0.9644	
10/30/90	$\boldsymbol{\tau}$ [s]	221.3	122.9	-44.4	154.7	96.25	-37.8
	R^2	0.9967	0.9752		0.9985	0.9708	
10/35/90	τ [s]	228.0	145.5	-36.2	167.5	107.8	-35.6
	R^2	0.9888	0.9531		0.9976	0.9461	

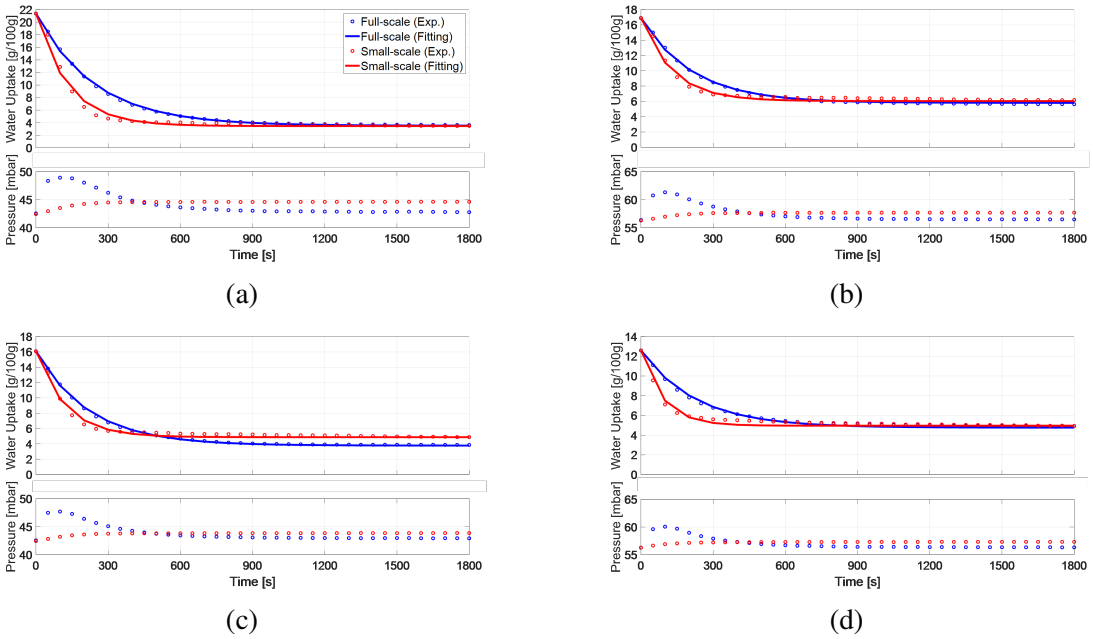

Fig. 3.14 Desorption kinetic (upper) and vapour pressure (lower) curves of the GLX30 APHE (full-scale measurements) and its representative adsorbent sample (small-scale measurements) at evaporator, condenser/adsorption-end and desorption temperatures of (a) 15/30/90°C, (b) 15/35/90°C, (c) 10/30/90°C, (d) 10/35/90°C.

The relatively large difference in the desorption kinetics between each APHE and its small-scale adsorbent sample can be attributed to the large difference in the pressure course of variation between the water vapour surrounding the APHE in its test setup and that surrounding its small adsorbent sample in the measuring cell of the V-LTJ kinetic setup, which are illustrated in the bottom diagrams of Figure 3.14 and Figure 3.15. For instance, at 15/30/90°C, the pressure of the water vapour surrounding the GLX30 APHE in its test setup reaches to maximum value of 48.5 mbar in the first 110 s from the beginning of the desorption process and then starts to fall. After around 450 s, the pressure becomes equal to the pressure inside the small-scale V-LTJ apparatus. Recalling the overall time needed for reaching equilibrium under this boundary condition, this means that the pressure of the full-scale apparatus was above that of the small-scale one over 50% of the process time, which explains why the desorption kinetics of the full-scale GLX30 APHE are slower than those of the small-scale measurements. This is also the case in the other three boundary conditions. The same explanation is also valid for the GL50 APHE. As shown in Figures 3.12 and 3.14 (lower diagrams) as well as Figures 3.13 and 3.15(lower diagrams), the maximum vapour pressure drop in all conducted adsorption processes on the APHE does not exceed 1 mbar in the GLX30 experimental setup and 2 mber in the GL50 setup, whereas the maximum

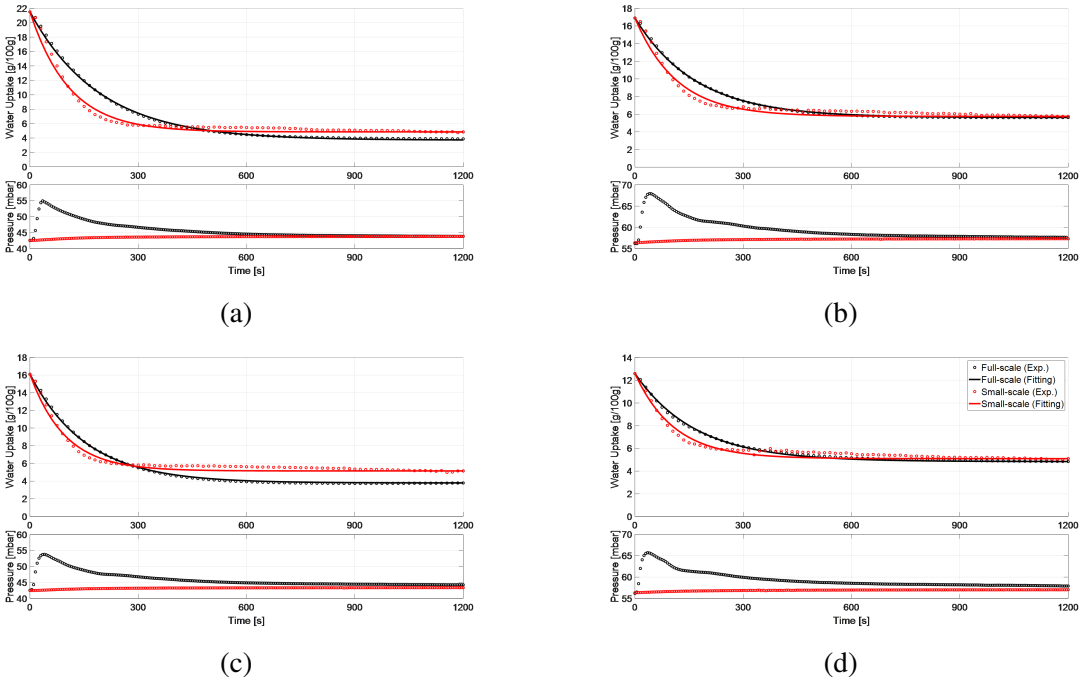

(a) (b)

(c) (d)

Fig. 3.15 Desrption kinetic (upper) and vapour pressure (lower) curves of the GL50 APHE (full-scale measurements) and its representative adsorbent sample (smallscale measurements) at evaporator, condenser/adsorption-end and desorption temperatures of (a) 15/30/90°C, (b) 15/35/90°C, (c) 10/30/90°C, (d) 10/35/90°C.

vapour pressure jump in the desorption processes exceeds 6 and 12 mbar in the GLX30 and GL50 experimental setup, respectively. This explains the deviation in the desorption kinetics.

The deviation between the desorption small-scale and full-scale results is quite acceptable, as the adsorption time is always longer than the desorption time (an average factor of 2.85 and 3.73 exist between the adsorption and desorption characteristic times for the GLX30 and the GL50, respectively), which means it plays the dominant role in estimating the cycle time of a real adsorption appliance. Considering the obtained very good matching between the adsorber kinetics of better than 24% for the GLX30 and 3% for the GL50 (in average 12.37% and 0.45%, for the GLX30 and the GL50, respectively), the introduced methodology to design small-scale samples is quite promising for reducing the time and cost of developing efficient adsorber plate heat exchangers.

3.5.3 Evaporator and Condenser powers

As the pressure difference between the water vapour surrounding each APHE in its experimental setup and that surrounding the representative adsorbent sample in the measuring cell is the cause of the difference in the adsorption and desorption kinetics as well as the final differential water uptake, comparing each APHE with its representative adsorbent sample only from the perspective of the temporal change of the water loading could be misleading. In other words, the success of predicting the performance of a real adsorber heat exchanger using small-scale representative adsorbent sample has to be judged from the perspective of the adsorption system output, such as the evaporator and condenser output powers. Accordingly, comparisons between the instantaneous and moving average specific powers obtained from the evaporator/condenser units of the full-scale setups and the evaporation and condensation powers estimated from the adsorption and desorption kinetic results of the small-scale adsorbent samples may be more suitable indicators for the ability of a representative small-scale adsorbent sample in predicting the performance of a real adsorber heat exchanger. In the next section, the instantaneous and moving average specific powers obtained from the evaporator/condenser unit, against which the GLX30 APHE was tested, and the evaporation and condensation powers estimated from the adsorption and desorption kinetic results of the GLX30's small-scale adsorbent sample will be compared and discussed.

Instantaneous Evaporator and Condenser Power

Figures 3.16 and 3.17 present comparisons between the instantaneous specific evaporation and condensation powers obtained from the evaporator/condenser unit of the GLX30 APHE's test setup and the instantaneous specific evaporation and condensation power estimated from

the kinetic results of the corresponding small-scale adsorbent sample tested in the V-LTJ kinetic setup, respectively. The estimated instantaneous specific evaporator and condenser power based on the measured kinetic data of the small adsorbent sample have been estimated according to Equations 3.9 and 3.10, respectively.

$$(\dot{q}_{ev})_{small-scale} = \frac{dw}{dt}.h_{fg}(T_{ev}) \tag{3.9}$$

$$(\dot{q}_{cond})_{small-scale} = \frac{dw}{dt}.(c_{p,v}(T_v - T_{cond}) + h_{fg}(T_{ev})) \tag{3.10}$$

Where, $(\dot{q}_{ev})_{small-scale}$ and $(\dot{q}_{cond})_{small-scale}$ are the estimated instantaneous specific evaporator and condenser power based on the measured performance of the small-scale adsorbent sample, respectively, $\frac{dw}{dt}$ is the rate of water vapour adsorption/desorption, $h_{fg}(T)$ refers to the latent heat of water evaporation/condnesation at the applied T, and T_v is the temperature of the water vapour leaving the desorbing sample in the V-LTJ kinetic setup. The specific heat of water vapour at constant pressure $c_{p,v}$ has been assumed constant and equal to 1920 $J.kg^{-1}.K^{-1}$.

As shown in Figure 3.16, at all applied operating conditions, there is a good agreement between the measured evaporation power from the evaporator/condenser unit of the experimental setup built to investigate the GLX30 APHE and the evaporation power estimated from the adsorption kinetics data of the corresponding small-scale adsorbent sample according to Equation 3.9.

On the other hand, the condensation power estimated from the desorption kinetic results of the small-scale adsorbent sample at all applied operating conditions do not match very well with the power obtained from the evaporator/condenser unit obtained during the desorption-condensation processes on the GLX30 APHE (see Figure 3.17). This can be explained by the large difference in the temporal pressure courses of the water vapour surrounding the GLX30 APHE and that surrounding its small adsorbent sample in their test setups during all conducted desorption processes. Nevertheless, it is obvious that the condensation energy is quite equal in both test methodologies.

Time-Averaged Evaporator and Condenser Powers

The time-averaged instantaneous specific evaporator and condenser power, which can be alternatively described as the moving average specific evaporator and condenser power is another useful indicator for evaluating the kinetic data of the small-scale measurements. Equation 3.11 describes the mathematical formula for estimating the evaporator specific power out of the measured data of the small-scale sample. In other words, such a moving

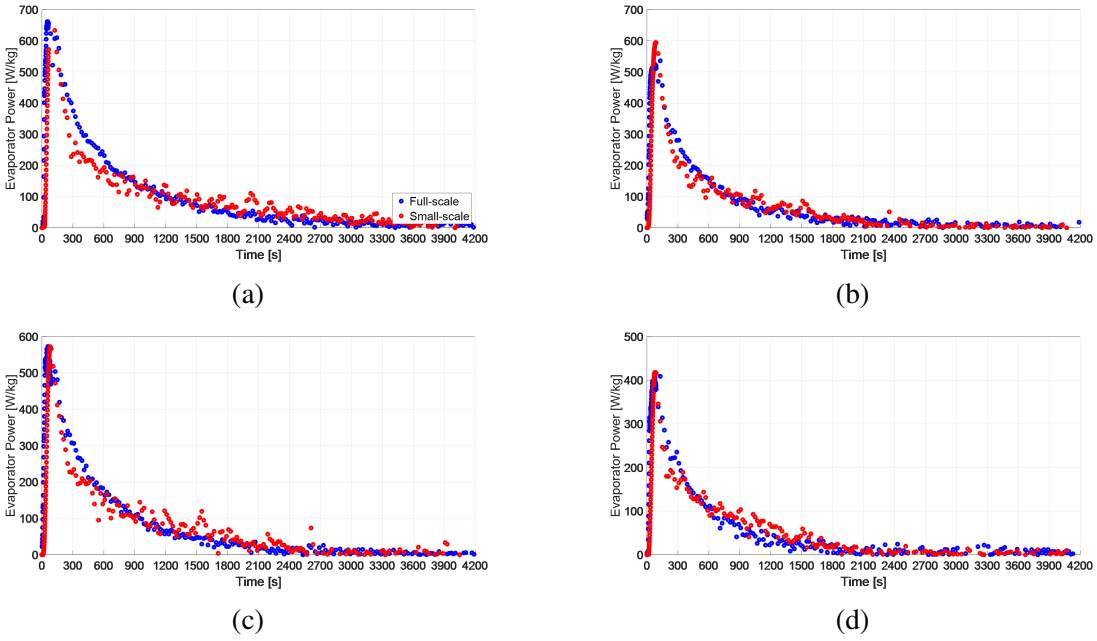

Fig. 3.16 Instantaneous specific **evaporation** power of evaporator/condenser unit of the GLX30 experimental setup (full-scale) and that estimated from the kinetic results of the adsorbent sample (small-scale), at (a) 15/30/90°C, (b) 15/35/90°C, (c) 10/30/90°C, (d) 10/35/90°C.

average specific evaporator power at a certain duration point (t) is the average evaporator power achievable, if the time assigned to the adsorption-evaporation process equals that duration (t). The obtained moving average evaporator powers for both full- and small-scale measurements are illustrated in Figure 3.18 under the four tested operating conditions.

$$(\overline{\dot{q}_{ev}})_{small-scale} = \frac{w(t) - w_o}{t}.h_{fg}(T_{ev}) \tag{3.11}$$

At the beginning of each tested processes, the driving force for adsorption is at its maximum value. Accordingly, the adsorption kinetics are the fastest and $\overline{\dot{q}_{ev}}$ increases sharply and reaches to maximum value in a short time. Afterwards it starts to drop with a slowing rate. For instance, at 15/30/90°C, $\overline{\dot{q}_{ev}}$ of the full-scale setup reaches 526.5 $W.kg_{dry}^{-1}$ adsorbent in the first 189 s, then it decreases and reaches 257.4 $W.kg_{dry}^{-1}$ adsorbent at the time required to reach 80% of the final or equilibrium differential water uptake (Δw_f) ($\tau_{80\%}$ = 1297 s). At the same operating condition, i.e., 15/30/90°C, $\overline{\dot{q}_{ev}}$ estimated from the small-scale sample adsorption kinetic measurements reaches 554.9 $W.kg_{dry}^{-1}$ adsorbent (5.4% higher than that of full-scale setup) in the first 139 s. $\overline{\dot{q}_{ev}}$ of the sample reaches 182.2 $W.kg_{dry}^{-1}$ adsorbent (29.2% less than that of full-scale setup) at the characteristic time $\tau_{80\%}$ of 1725 s. Such a new evaluation methodology of the measured kinetic data of the small-scale adsorbent sample

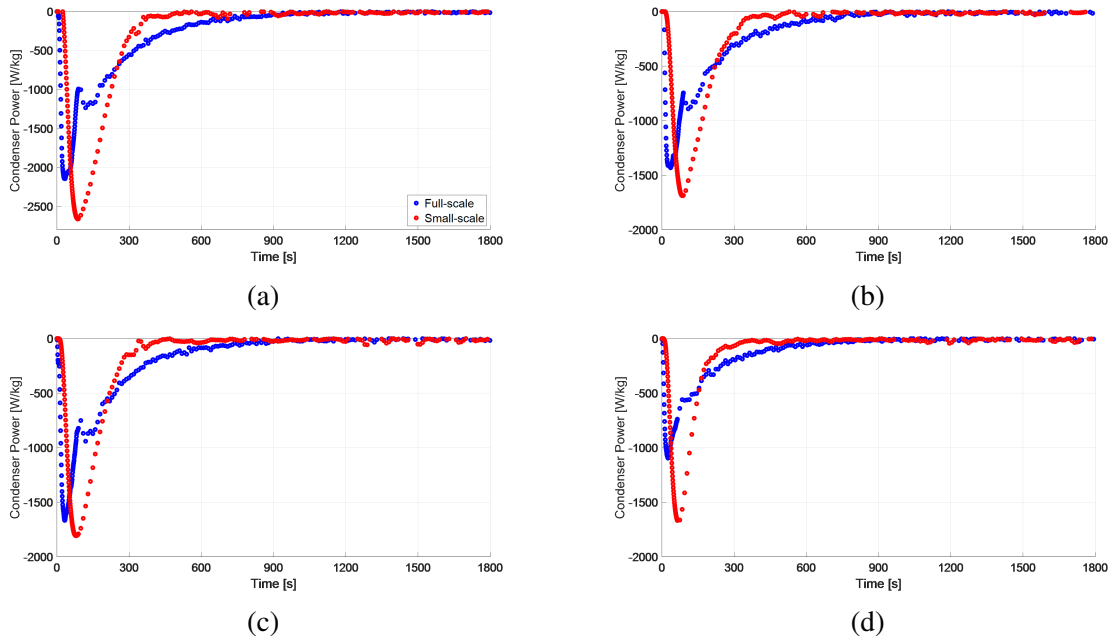

Fig. 3.17 Instantaneous specific **condensation** power of evaporator/condenser unit of the GLX30 experimental setup (full-scale) and that estimated from the kinetic results of the adsorbent sample (small-scale), at (a) 15/30/90°C, (b) 15/35/90°C, (c) 10/30/90°C, (d) 10/35/90°C.

is quite effective in determining the adsorption phase duration based on the target specific evaporator power to be realized.

Equation 3.12 describes the mathematical formulae for estimating the moving average specific condenser power out of the measured desorption kinetic data of the small-scale sample representative to the GLX30 APHE.

$$(\overline{\dot{q}_{cond}})_{small-scale} = \frac{w(t) - w_o}{t}.(h_{fg}(T_{cond}) + C_{p,v}(T_v - T_{cond})) \tag{3.12}$$

Figure 3.19 illustrates the obtained moving average specific condenser powers of both full- and small-scale measurements of the GLX30 under the four sets of operating conditions. As depicted in Figure 3.19, the condensation powers estimated from the small-scale measurements are higher than those obtained from the full-scale measurements. The average relative deviation (*ARD*) in the moving specific average power is estimated according to Equation 3.13. Table 3.5 presents the estimated *ARD* for both moving average evaporator and condenser powers based on Equation 3.13.

$$ARD = \frac{100}{n}\sum_{1}^{n}\frac{|\overline{\dot{q}}_{full-scale} - \overline{\dot{q}}_{small-scale}|}{\overline{\dot{q}}_{full-scale}} \tag{3.13}$$

Table 3.5 Average relative deviation (*ARD*) of the moving average specific evaporator and condenser powers between the full-scale and small-scale measurements of the GLX30 APHE under the four tested operating conditions.

Operating conditions	$ARD_{\overline{\dot{q}_{ev}}}$, %	$ARD_{\overline{\dot{q}_{cond}}}$, %
15/30/90	15.1	28.4
15/35/90	13.2	25.4
10/30/90	14.8	28.7
10/35/90	5.4	24.6

With a maximum ARD of 15.1% in the moving average evaporator power, it is evident again, that a good matching between full- and small-scale measurements is reached. Contrary to that, the *ARD* in the moving average specific condenser power between the full- and small-scale measurements ($ARD_{\overline{\dot{q}_{cond}}}$) ranges between 24.6 and 28.7%, at the operating conditions of 10/35/90°C and 10/30/90°C, respectively. The reason behind the higher difference in the moving average condensation powers is the large difference in the pressure course of variation between the full- and small-scale test setups, as explained before.

The obtained good agreements between the adsorption water uptake data (Figure 3.12), instantaneous specific evaporator power (Figure 3.16) and the moving average specific evaporator power (Figure 3.18) between the GLX30 APHE and its small-scale representative sample at all tested operating conditions implies the strength of the introduced methodology, which has been verified in this work, to utilize the V-LTJ kinetic setup to precisely predict the performance of real adsorber heat exchangers before building them. Of course, special attention must be paid for analyzing the heat and mass transfer characteristics of the adsorbent domain of the adsorber heat exchanger before deciding on the dimensions of its representative test frame as described and applied in this work. Accordingly, design optimizations can be easily carried out based on the small-scale measurements before stepping to the fabrication and validation development phases, which shall save enormous development time and cost.

3.6 Conclusion

This chapter addressed the degree of matching between the adsorption and desorption kinetic measurements between two commercial, one open and one closed structured asymmetric plate heat exchangers adapted to act as an adsorbers/desorbers and small-scale adsorbent samples prepared dedicatedly to be representative for the adsorbent domains inside the investigated adsorber/desorber plate heat exchangers (APHEs) from the perspective of both heat and mass transfer characteristic lengths. To this aim, special test setups have been

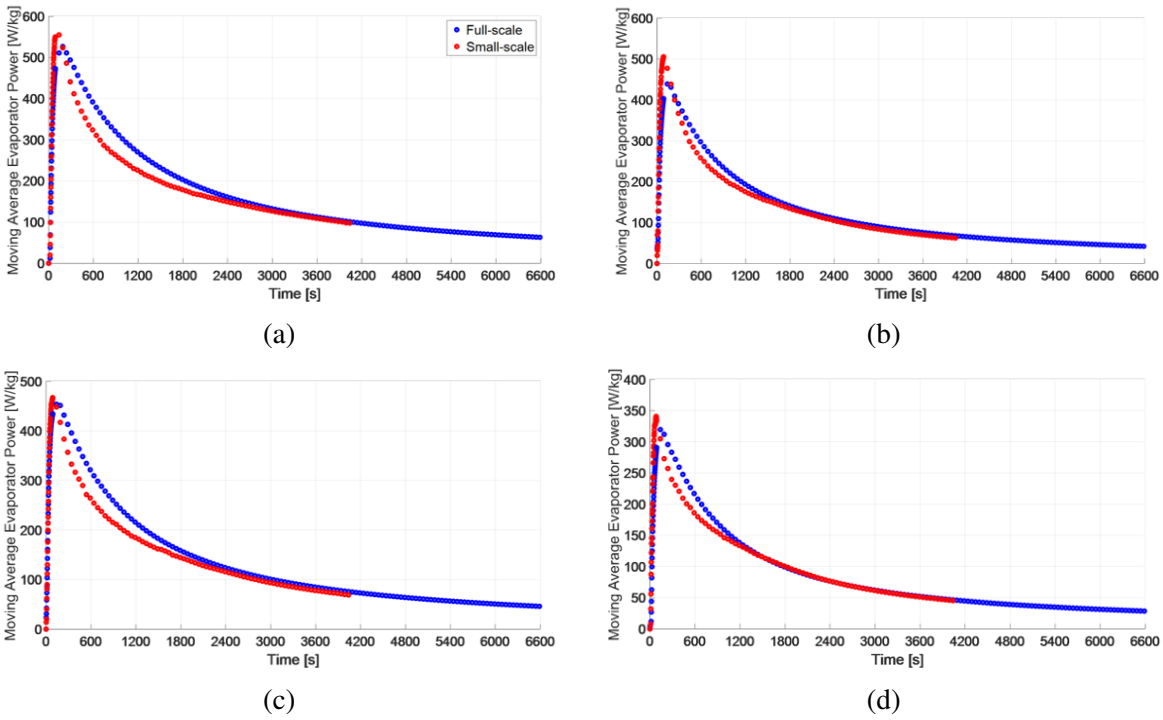

Fig. 3.18 Specific moving average **evaporation** power of the evaporator/condenser unit (full-scale) and that estimated from the kinetic results of the adsorbent sample (small-scale), at (a) 15/30/90°C, (b) 15/35/90°C, (c) 10/30/90°C, (d) 10/35/90°C.

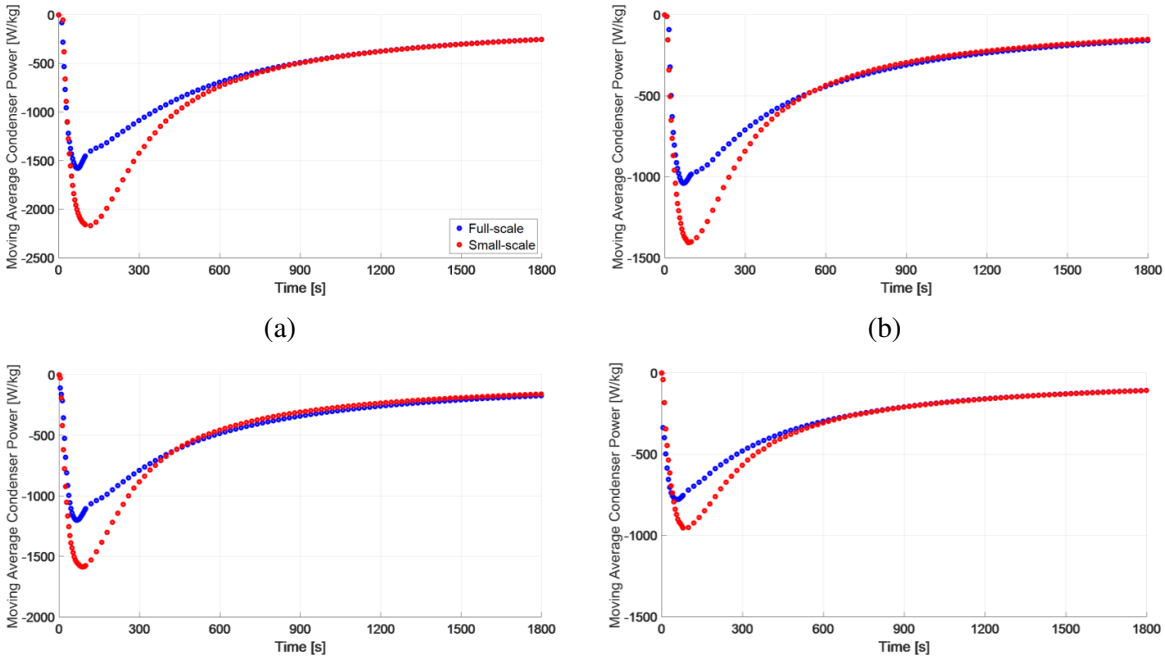

Fig. 3.19 Specific moving average **condensation** power of the evaporator/condenser unit (full-scale) and that estimated from the kinetic results of the adsorbent sample (small-scale), at (a) 15/30/90°C, (b) 15/35/90°C, (c) 10/30/90°C, (d) 10/35/90°C.

established to investigate the adsorption and desorption kinetics of the full-scale APHEs. A slight modification in the thermal response (LTJ) methodology [91] has been introduced. The adsorption and desorption kinetic investigation of the small-scale representative adsorbent samples has been conducted using a Volumetric Large Temperature Jump (V-LTJ) kinetic setup [93]. In addition, the kinetic data of the small-scale adsorbent sample representative to one of the two investigated APHEs, namely the GLX30 APHE, have been utilized for estimating the expected instantaneous and moving average powers of the evaporator/condenser heat exchanger, against which the GLX30 APHE has been tested. The obtained small-scale and full-scale results have been compared and the main outcomes are summarized as follows:

- All kinetic results of the small-scale adsorbent samples and the APHEs have been fitted to an exponential form with coefficient of determination (R^2) values better than 0.9461.
- A very good matching between the small-scale and full-scale adsorption kinetic measurements has been obtained, with average relative deviation (*RD*) in the characteristic time constant of the exponential form (τ) by 12.3% for the GLX30 and 1.22% for the GL50.
- The APHEs demonstrated faster desorption kinetics than its adsorption kinetics by an average factor of 2.85 for the GLX30 and 3.73 for the GL50. This is in phase with previous measurements and puts in evidence that the duration of the adsorption phase dominates the cycle time of the related adsorption appliance.
- The *RD* in the desorption kinetics' characteristic time (τ) between the full-scale and the small-scale measurements for both APHEs was clearly higher than the *RD* of the adsorption characteristic times.
- The relatively large difference in the desorption kinetics between the APHEs and the small-scale adsorbent samples was attributed to the large difference in the pressure course of variation between the water vapour surrounding the APHEs in their test setups and that surrounding the small adsorbent samples in the measuring cell of the V-LTJ kinetic setup, implying a weak condenser performance of the test setups leading to higher water vapour pressures and, correspondingly, slower desorption kinetics.
- The instantaneous and moving average specific evaporator power estimated from the adsorption kinetics data of the small-scale adsorbent sample representative to the GLX30 APHE matched very well with the ones obtained directly from the evaporator/condenser unit, against which the GLX30 APHE has been tested, with an average relative deviation (*ARD*) between 5.4 and 15.1% for the moving average power.

- The condenser moving average power estimated from small-scale measurements of the GLX30 were higher than those obtained from the full-scale measurements, with an *ARD* between 24.6 and 28.7%, which is attributed to the weak condenser performance of the full-scale test unit, leading to excessively higher pressure.

Despite the relatively higher deviations of the desorption kinetic data, very good agreements have been obtained for the adsorption kinetics regarding the temporal water uptake, instantaneous specific evaporator power and the moving average specific evaporator power between the APHEs and their small-scale representative samples at all tested operating conditions. This puts in evidence the strength of the introduced methodology to mimic the heat and mass transfer characteristics of the adsorbent domain of a plate-type adsorber heat exchanger by dedicatedly design a test frame for a small-scale adsorbent sample, to be investigated with e.g. the V-LTJ kinetic setup to precisely predict the performance of the real adsorber heat exchangers before building it. Accordingly, design optimizations also concerning the influence of the adsorbent type and grain-size can be easily investigated on the small-scale level before realizing the full-scale heat exchanger, which shall save development time and cost.

Chapter 4

Developed 3D simulation model; calibration and validation against experimental data

Thanks to the high computational power of the modern computers, the numerical simulation of the physical phenomena became, recently, quite effective for the development and the design optimization of the engineering components. The verification of the validity of the numerical model requires, however, relevant experimental data. In some cases, special experimental investigations are additionally required to estimate first some relevant parameters of the governing equations composing the numerical simulation model. Therefore, the conditions of the conducted experiments should be carefully considered.

The development of a highly efficient heat exchanger to act as adsorber/desorber for the adsorption systems is quite crucial for obtaining high system efficiency. The physics behind the work of the adsorber/desorber heat exchanger are entangled. It involves unsteady conductive heat transfer in solid (the heat exchanger metal), unsteady convective heat transfer in the flowing heat transfer fluid (HTF), unsteady mass diffusion of the adsorbate in the adsorbent and unsteady conductive heat transfer in the adsorbent. In addition, the exothermic/endothermic nature of the adsorption/desorption process (heat of adsorption) and temporal variation in the thermal properties of the applied adsorbent-adsorbate pair during the conducted adsorption and desorption processes should be taken into consideration. For instance, Rouhani et al. [128], presented the dependence of the AQSOA-Z02 zeolite thermal conductivity on the water uptake. Uddin et al. [129], showed the high dependence of the specific heat capacity of the different carbon based adsorbents on temperature.

Survey of the different numerical models coupling the different physics equations, which govern the work of the adsorber/desorber heat exchanger, has been introduced in [130].

The simulation models of the adsorbent domain inside the adsorber/desorber are classified into the following three main types, lumped parameters (LP), heat transfer (HT) and more sophisticated heat and mass transfer (HMT) models. The LP model assumes a uniform distribution of temperature, pressure and refrigerant content inside the whole adsorbent bed [131]. The HT model takes spatial distribution of the adsorbent temperature into account, but neglect the mass transfer resistance through the porous adsorbent medium [79]. The more complex HMT model accounts for combined heat and mass transfer during the adsorption/desorption of adsorbate into/from the adsorbent bed and are able to describe the variation of the adsorbent temperature, adsorbate pressure and uptake with time and space [132].

Indeed, the HMT model is the most advanced one, however it can predict preciously the performance of an adsorber/desorber heat exchanger, if it is fed with; (1) correct thermal properties of the HEX metal, HTF and adsorbent-adsorbate pair, (2) initial and boundary conditions, and (3) proper heat and mass transfer parameters. The HMT model can moreover be applied to estimate the coupled heat and mass transfer parameters of an adsorbent-adsorbate working pair of an adsorber/desorber, if it is fed with a set of relevant experimental data and integrated with an optimization model to estimate the heat and mass transfer parameters.

In this chapter, a HMT model shall be developed for simulating the performance of the experimentally investigated full-scale APHEs (see Chapter 3). The model shall be implemented in a commercial software, namely "COMSOL Multiphysics". The conjugate heat transfer module integrated in COMSOL shall be applied to account for the heat transfer between the model components, i.e. water vapour, adsorbent grains, metal surface and HTF. This means that defining the heat transfer coefficients between model components is not required. The developed simulation model will first be implemented on a 2D geometry (rectangular) representative to a small-scale adsorbent sample of 3 mm thickness placed in a top-open frame and tested in the V-LTJ kinetic setup. The small-scale adsorbent sample receives/delivers the refrigerant vapour from/to its top surface. Thus the interparticle mass trnasfer resistance in this adsorbent sample is quite low and can be neglected. The numerical model implementation on the adsorbent sample geometry aims to estimate the effective diffusion coefficient of water vapour in the Siogel grains (D_{eff}) by best fitting the obtained numerical results to the experimental data obtained from the investigation conducted on the above described small-scale adsorbent sample. The optimization module integrated in COMSOL shall be applied to perform the best fitting and estimating the values of D_{eff} at different applied boundary conditions. The obtained values of D_{eff} shall be applied in the

implementation of the developed numerical model on the 3D geometries of the investigated Full-scale APHEs

4.1 Estimation of D_{eff} of water vapour in Siogel grains

To simulate an adsorbent bed, predetermination for D_{eff} of the applied adsorbent-adsorbate pair is necessary. As discussed in the last chapter (Chapter 3), water was applied as adsorbate and the silica "Siogel" was applied as the adsorbent material in all conducted full-scale and small-scale experiments. Only one study [19] reported the value of D_{eff} of water vapour in Siogel grains has been found in the literature. As the reported values in [19] are for large temperature jump (LTJ) adsorption and desorption processes associated to only one set of operating conditions, namely $T_{ev} = 10$°C, $T_{cond} = 30$°C and $T_{des} = 80$°C, it is necessary to estimate D_{eff} values at all sets of operating conditions applied in the experimental investigations (full-scale and small-scale) discussed in Chapter 3.

Thus, estimation of D_{eff} values of the water adsorption in the Siogel adsorbent grains at different operating conditions, namely T_{ev}=5, 10 and 15 °C against T_{cond}=30 and 35°C and T_{des}=90 °C, has been conducted. The estimation of D_{eff} values is done by best fitting the numerical to the experimental data of a cuboidal adsorbent sample of thickness 3 mm (equivalent to the HTCL of the GLX30 APHE) placed in an open test frame and investigated experimentally using the V-LTJ kinetic setup. Figure 4.1a shows the design of the frame and Figure 4.1b shows the realized frame filled with 320 g (dry mass) of the Siogel grain (size range: 0.71 to 1.0 mm) and placed on the sample holder in the measuring cell of the V-LTJ kinetic setup installed in the laboratory of sorption processes (LSP) at OTH Regensburg. The width of the adsorbent sample placed inside the frame amounts to 3 mm. The height (thickness) of the adsorbent sample inside the frame amounts to 3 mm. The numerical simulation model has been implemented using COMSOL Multiphysics on a 2D geometry (rectangle shape) representative to the adsorbent sample.

Note that the transfer of the water vapour in the adsorbent sample tested in the open frame faced negligible interparticle mass transfer. This means using the experimental data of the adsorbent sample tested in the open frame in estimating the values of D_{eff} leads to less error and shorter computational time compared to the adsorbent samples tested in the frames explained in Chapter 3. See Appendix B for more information about the fabrication of the open test frame and the fitting of the simulation results to the experimental data.

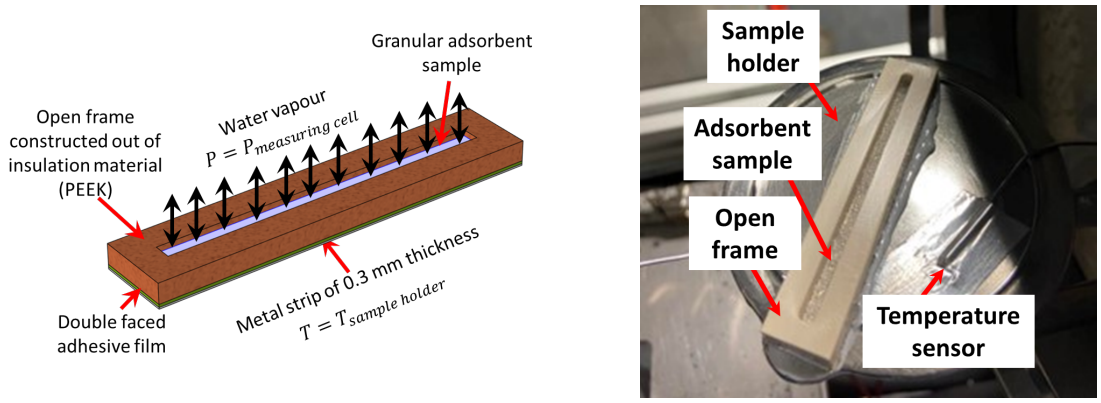

(a) (b)

Fig. 4.1 Test frame used for D_{eff}-estimation of the Siogel-water working pair, (a) 3D-drawing, (b) realized test frame filled with the Siogel grains and place on the sample holder of the V-LTJ kinetic setup

4.2 3-D modeling of a repeated section of the Ads-PHE

To develop mathematical models for predicting the sorption performance of the investigated Ads-PHEs and, at the same time, consume reasonable computational times, appropriate representative sections of both investigated Ads-PHEs for the numerical study should be carefully selected. Since the investigated Ads-PHEs consist of several identical plate-pairs, the adsorbent and the HTF domains between the successive plates are identical as well. Therefore, the numerical simulations of only a repeated section of each investigated Ads-PHE can predict their performance preciously. The selection of such repeated section differs from the "GLX30" Ads-PHE to the "GL50" Ads-PHE. The "GLX30" Ads-PHE consists of several sets of two differently stamped core plates in addition to the two end plates. Each plate type has a different stamping geometry on each side. Every plate type shall be surrounded by two of the other type upon building the stack of the whole PHEX. It follows that the two alternatively repeated domains for the adsorbent and the HTF are asymmetric. As a representative section, from which the whole Ads-PHE can be built up, one complete HTF domain surrounded by two halves of the adsorbent domain is chosen. Because of the two differently stamped plates, the two halves of the adsorbent domains are not identical. Figure 4.2 depicts the selected representative intermediate section of the "GLX30" Ads-PHE, which consists, as explained before, of three contacted parts representing the domain of the adsorbent (purple colored), the HTF domain (light blue colored) and the metal plates themselves (gray colored).

The arrows along the two sides of the two halves of the adsorbent domains illustrate the water vapour flow direction into it (during adsorption) and out of it (during desorption). The

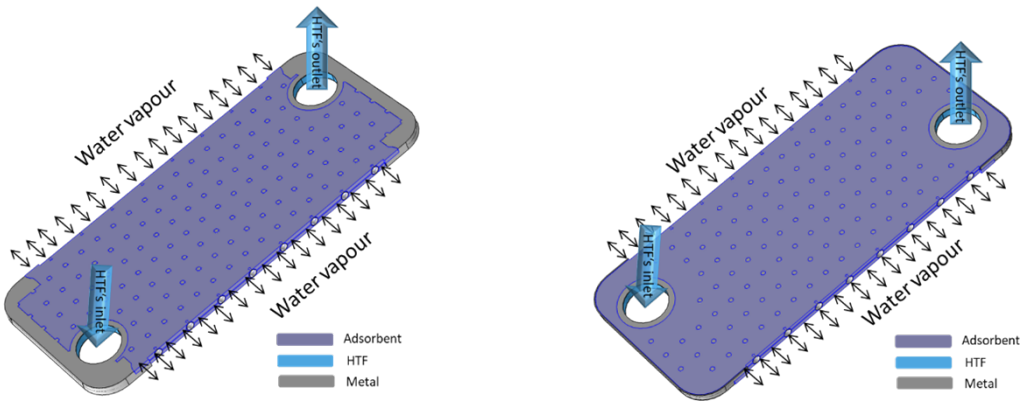

(a) (b)

Fig. 4.2 Intermediate representative domain of the GLX30 Ads-PHE selected for the numerical simulation, (a) Plate type I (top plate of the HTF domain) with half of the adsorbent domin on top of it, (b) 180° rotated plate type II (lower plate of the HTF domain) with half of the adsorbent domain adjacent to it

vertical wide arrows shows the HTF flow direction into the flow distribution port or out of the flow collecting port. Indeed the flow distribution port conveys the HTF equally into all HTF domains of the whole PHE. In the same time, the flow collection port receives the HTF from all HTF domains after having exchanged heat with the adsorbent domains.

The “GL50” Ads-PHE consists of a single stamped plate, however with two different stamping profiles on each side as can be seen in Figure 4.3. Figure 4.3a depicts the upper side of the plate with a half adsorbent domain on top of it, while Figure 4.3b illustrates the lower side of the plate with half HTF domain adjacent to it. The intermediate representative section of the “GL50“ Ads-PHE for the simulation model, depicted in Figure 4.3, comprises, therefore, one plate, one half adsorbent subdomain on top of it and one half HTF subdomain below it.

4.3 Model Assumptions

For both the 2-D (for the adsorbent sample) and the 3-D (for the representative section of each PHE) models, the following assumptions are adopted:

- The adsorbent grains are spherical with a uniform size and porosity.
- As each adsorbent subdomain in the investigated APHEs is subjected to cooling/heating effect equality from two plates, a heat transfer symmetrical plane dividing each adsorbent subdomain is considered of the representative sections of both Ads-PHE is

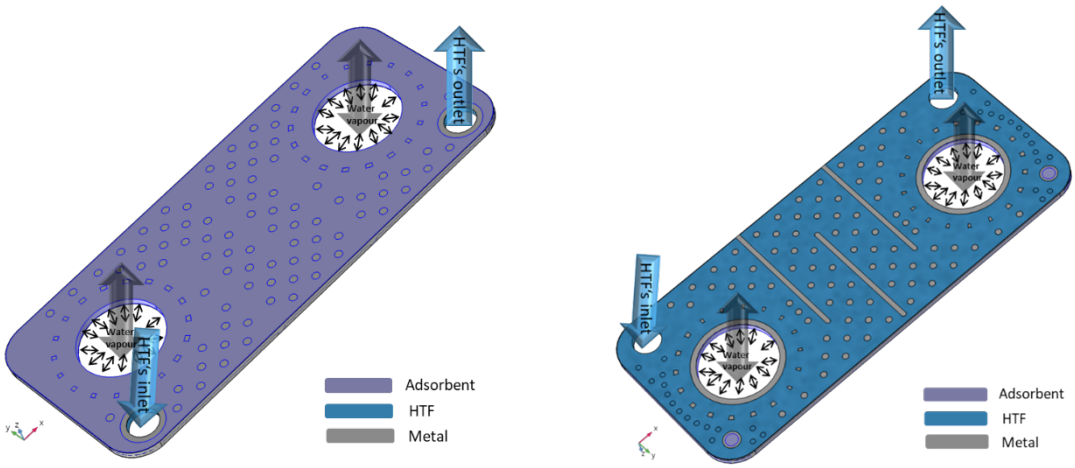

(a) (b)

Fig. 4.3 Intermediate representative domain of the GL50 Ads-PHE selected for the numerical simulation, (a) Side I, in contact with half of the adsorbent domain, (b) Side II, in contact with half of the HTF domain

perfectly insulated. That is due to the existence of a minimum/maximum of temperature, pressure and uptake during the successive adsorption and desorption phases, respectively.

- Local thermal equilibrium is assumed between the adsorbent, the adsorbed water and the water vapour.
- The thermo-physical properties of the dry adsorbent grains are assumed constant.
- Water vapour is treated as an ideal gas
- The pressure of water vapour entering into or leaving the Ads-PHEs during the adsorption/desorption process is variant and set equal to the recorded values in the experimental work.

In addition, the following two assumptions are adopted for the 2-D model of the small-scale adsorbent sample tested inside the V-LTJ kinetic setup.

- The temperature distribution over the sample holder of the measuring cell is considered uniform. The sample holder is small and effectively cooled down and heated up, thus assuming a uniform temperature distribution over its surface is quite reasonable.
- Perfect thermal insulation at the upper surface and the side surfaces of the adsorbent sample inside the open test frame (see Figure 4.1a).

Based on the above assumptions and description of the selected sections of the investigated Ads-PHEs, the governing equations described in the following section have been applied.

4.4 Governing Equation

As mentioned before, the 2-D mathematical model is specifically developed to account for the combined heat and the mass transfer within the adsorbent sample of the kinetic setup. The sample holder surface temperature is measured continuously during the adsorption and desorption experiments. The sensor used to measure sample holder surface temperature is fixed very close to the position, where the adsorbent sample is placed (see Figure 4.1b). Therefore, the experimentally measured sample holder surface temperature is applied as a thermal boundary condition at the bottom side of the adsorbent sample. Accordingly, the following conservation equations for the heat and mass transfer in the adsorbent sample are adopted.

Energy balance for the adsorbent

The energy balance for the adsorbent can be described by Equation 4.1 after neglecting the viscous dissipation and the work done by pressure [130].

$$\rho C_{p_{eq}} \frac{\partial T}{\partial t} + \nabla(-k_{eq} \nabla T) + \nabla(\rho_v C_{p_v} \vec{u}_v T) = (1-\varepsilon_t)\rho_{ad} \Delta h_{ad} \frac{\partial w}{\partial t} \tag{4.1}$$

Herein, $\rho C_{p_{eq}}$ represents the equivalent heat capacity of the adsorbent bed. The bed can be described as a porous medium of adsorbent grains. The grains contain water in their gas phase as well as in their adsorbate phase. Based on the heat capacity of the adsorbent grains, where the vapour and the adsorbate are co-existing and the heat capacity of the vapour surrounding the grains, the equivalent heat capacity $\rho C_{p_{eq}}$ is determined as follows [130]:

$$\rho C_{p_{eq}} = (1-\varepsilon_t)\rho_{ad}(1+w)C_{ad,wet} + \varepsilon_t \rho_v C_{p_v} \tag{4.2}$$

The bed total porosity is given by Equation 4.3 in [134].

$$\varepsilon_t = \varepsilon_b + (1-\varepsilon_b)\varepsilon_p \tag{4.3}$$

The water vapour is treated as an ideal gas and the vapour density can be calculated as:

$$\rho_v = \frac{P}{RT} \tag{4.4}$$

The equivalent thermal conductivity of the adsorbent porous medium (k_{eq}) is described by equation 4.5 [135].

$$k_{eq} = (1-\varepsilon_t)k_{ad,wet} + \varepsilon_b k_v \tag{4.5}$$

where $k_{ad,wet}$ is the average thermal conductivity of the wet adsorbent.

Mass balance for the adsorbate

Equation 4.6 describes the mass conservation of the adsorbate (water) within the whole system incorporating both adsorbed and the vapour phases [134]. Indeed, water vapour transfers from the vapour phase into the adsorbed phase during adsorption and vice versa during desorption.

$$\varepsilon_t \frac{\partial \rho_v}{\partial t} \nabla(\rho_v \vec{u_v}) = -(1-\varepsilon_t)\rho_{ad} \frac{\partial w}{\partial t} \tag{4.6}$$

In Equation 4.7, $\frac{\partial w}{\partial t}$ describes the time rate of change of the water uptake per unit mass of dry adsorbent. The intra-particle mass transfer resistance inside the adsorbent grains affects this rate. The well-known linear driving force model [133] is applied to account for such mass transfer resistance as described by Equation 4.7,

$$\frac{\partial w}{\partial t} = \frac{15 D_{eff}}{r_p^2}(w^* - w) \tag{4.7}$$

Where D_{eff} represents the effective diffusion coefficient, r_p the radius of the adsorbent grains, w^* the equilibrium uptake at the instantaneous pressure and temperature and w the temporal water uptake inside the adsorbent grain.

The equilibrium correlation between pressure, temperature and water uptake for Sio-gel/Water pair is described by the Dubinin-Astakov-Equation 4.8,

$$w^* = w_o \exp(-(\frac{F}{E})^n) \tag{4.8}$$

$$F = RT \ln(\frac{P_{sat}}{P}) \tag{4.9}$$

where the parameters w_o, E and n have been listed in [17, 18]. The adsorption potential F is defined by Equation 4.9.

If the vapour velocity and, correspondingly, the pressure losses throughout the adsorbent bed are relatively low, the Darcy's law can be applied instead of the momentum conservation equation [136]. The Darcy's law (Equation 4.10) describes the velocity of the vapour as a viscous flow through the porous medium.

$$\vec{u_v} = -\frac{K_{app}}{\mu}.\nabla p \tag{4.10}$$

Where K_{app} is the permeability of the bed, which can be estimated according to Equation 4.11, which has been introduced by Ruthven [135].

$$K_{app} = \frac{\varepsilon_b^3 d_p^2}{150(1-\varepsilon_b)^2} \tag{4.11}$$

Beside the previously described equations for the combined heat and mass transfer encountered in the adsorbent sample tested in the kinetic setup, the following energy and momentum conservation equations for the Ads-PHE's metal and HTF domains are adopted for the 3-D mathematical model developed to simulate the representative intermediate domains of the proposed Ads-PHE.

Energy balance for the APHE's metal

$$\rho_m C_m \frac{\partial T}{\partial t} + \nabla(-k_m \nabla T) = 0 \tag{4.12}$$

Where C_m and k_m are the heat capacity and the thermal conductivity of the metal, respectively.

Energy balance for the HTF

The energy balance for the heat transfer fluid (HTF) is described by Equation 4.13, from which the instantaneous temperature distribution along the Ads-PHE can be estimated.

$$\rho_f C_{p_v} \frac{\partial T}{\partial t} + \nabla(-k_f \nabla T) = -\nabla(\rho_f C_{p_v} \vec{u_f} T) \tag{4.13}$$

Herein, C_{p_v} and k_f are the specific heat capacity and the thermal conductivity of the HTF, respectively. The $\vec{u_f}$ is the HTF's velocity vector. The HTF is assumed to be water, which has a relatively low thermal conductivity ($k_f = 0.59 W^{-1}.m^{-1}.K^{-1}$). Therefore, heat transfer in the HTF is dominated by convection rather than conduction.

Momentum balance for the HTF

The following momentum conservation equation accounts for the HTF's velocity distribution along the Ads-PHE. The flow regime inside the narrow flow channels of the introduced Ads-

PHE is laminar. The following momentum (4.14) and mass conservation (4.15) equations are applied [137].

$$\rho_f \frac{\partial u_f}{\partial t} + \rho_f (u_f.\nabla) u_f = \nabla.[-pl + \mu(\nabla u_f + (\nabla u_f)^T) - \frac{2}{3}\mu(\nabla.u_f)l] + F \tag{4.14}$$

$$\frac{\partial \rho_f}{\partial t} + \nabla.(\rho_f u_f) = 0 \tag{4.15}$$

4.5 Initial conditions

The pressure, temperature, and adsorbate uptake distributions inside the experimentally tested adsorbent sample in the kinetic setup as well as the adsorbent domain of the investigated APHEs are considered uniform at the initial state. The initial pressure of water vapour inside the adsorbent equals the saturation pressure corresponding to applied evaporator temperature (T_{evap}) in the adsorption processes and condenser temperature (T_{cond}) in the desorption processes. The initial temperature of the adsorbent is the corresponding adsorption/desorption start temperature ($T_{ads-start}$/$T_{des-start}$), which has been determined at the different applied operating conditions from the available equilibrium model of the Siogel/water pair [17]. The values of the $T_{ads-start}$ and $T_{des-start}$ are recorded in Table 4.1. For the metal and HTF domains of the selected sections for simulating the APHEs, a uniform temperature distribution of $T_{ads-start}$ and $T_{des-start}$ is assumed at the initial state in the adsorption and desorption processes, respectively.

Table 4.1 Applied temperature initial and end conditions

T_{evap}, ° C	$T_{ads-start}$, ° C	T_{cond} = $T_{ads-end}$, ° C	$T_{des-start}$, ° C	T_h=$T_{des-end}$, ° C
5.0	58.5	30.0	57.1	90.0
	53.2	35.0	68.4	
10.0	66.1	30.0	50.5	
	58.7	35.0	58.8	
15.0	70.5	30.0	44.5	
	62.4	35.0	55.1	

4.6 Boundary conditions

For the numerical simulation of the experimentally tested adsorbent sample, the instantaneously recorded temperature of the sample holder and the pressure of the water vapour

inside the measuring cell are utilized as the related boundary conditions for the adsorbent domain. The sensor used to measure the sample holder surface temperature is fixed very close to the position, where the adsorbent sample is placed (see Figure 4.1b). Therefore, the experimentally measured sample holder surface temperature (changes from $T_{ads-start}$ to $T_{ads-end}$ in the adsorption and from $T_{des-start}$ to $T_{des-end}$ in the desorption) is applied as a thermal boundary condition at the bottom side of the adsorbent sample. For the other sides, insulation boundary conditions are applied ($\frac{\partial T}{\partial n} = 0$). Since the frame, where the sample is placed inside, allows the vapour to enter only from the upper side (see Figure 4.1a), the experimentally recorded pressure variation inside the measuring cell is applied as the boundary condition at the sample upper side, while zero normal pressure gradient ($\frac{\partial P}{\partial n} = 0$) is assumed on all other boundaries.

For the selected sections to simulate the APHEs, symmetric heat and mass transfer boundary conditions ($\frac{\partial T}{\partial n} = 0$ and $\frac{\partial P}{\partial n} = 0$) are applied at the symmetry planes described before. In addition, insulation boundary conditions ($\frac{\partial T}{\partial n} = 0$) are applied at all outer sides of the adsorbent and metal domains. At the water vapor entrance to/exit from the adsorbent domain of each investigated APHE, a pressure boundary condition is applied. The values of the pressure input to the model are the values recorded during the experimental investigations of the considered APHEs. At the HTF's inlet port, fully developed flow with flow rate and temperature as recorded in the experimental work are applied.

4.7 Implementation

The commercial COMSOL Multiphysics® code, which employs the transient finite element multi-dimensional modelling, is applied for all simulation tasks. First, a 2-D geometry representative for the experimentally investigated adsorbent sample is implemented. The adsorbent domain is treated as a porous media. The physical properties of Siogel/water pair required for the simulation work are taken from [17, 18]. The "heat transfer in porous medium" module integrated in COMSOL is applied to account for the energy conservation. The "Darcy's law" module is applied to account for the inter-particle mass transfer resistance. The "chemical reaction" module is employed to represent the linear driving force (LDF) model, which accounts for the intra-particle diffusion resistance. The integrated optimization module is applied to estimate the parameters of the diffusion coefficient of water vapour into the Siogel grains by best fitting the experimental results obtained by the kinetic setup.

Afterwards, the 3-D geometries for the selected sections of the APHEs are implemented in COMSOL Multiphysics®. The "conjugate heat transfer" module integrated in COMSOL Multiphysics® is applied instead of the "heat transfer in porous medium" module to account

for the heat transfer on the three contacted domains; namely the porous medium of the adsorbent, the metal and the HTF domains. The main advantage of applying this module is that there is no need to define convective heat transfer coefficients at the contact surfaces between the related domains [138]. The other modules applied in the simulation of adsorbent sample are applied also to account for the mass transfer in the tested adsorbent domain of the selected adsorbent domains of the APHEs. The estimated values of D_{eff} are fed to the "chemical reaction" module to account for the intraparticle mass diffusion resistance inside the adsorbent grains. In addition, the integrated "laminar flow" module is applied to account for the momentum conservation in the HTF.

The effect of the grid size and number of elements on the accuracy of the simulation results has been carefully investigated. To this aim, the number of grid elements has been changed and it turned out, that a grid of 2100392 elements for the "GL50" APHE and 2580902 for the "GLX30" APHE were adequate to obtain grid-independent results. The model has been solved in transient mode for 4000 s with a variant time step between 0.01 and 0.1 s. The relative tolerance has been set to 0.001.

4.8 Results

In this section, the values estimated for the D_{eff} by best fitting the obtained experimental data with numerical results using COMSOL's optimization module are discussed. Moreover, the results obtained from the 3D model developed to simulate the representative sections of the APHEs are presented and thoroughly discussed.

4.8.1 Estimated D_{eff} of the applied Siogel/water pair

Table 4.2 depicts the D_{eff} values obtained by best fitting the simulation model to the experimental data of the adsorbent sample at all applied operating conditions. The root mean square deviation (*RMSD*) [139] of the obtained D_{eff} values according to Equation 4.16 is also shown in Table 4.2.

$$RMSD = \sqrt{\frac{1}{t_{90\%}} \int_{o}^{t_{90\%}} (w_{rel,exp} - w_{rel,sim})^2 . dt} \tag{4.16}$$

Where $t_{90\%}$ is the time to reach 90% of the final differential water uptake. $w_{rel,exp}$ and $w_{rel,sim}$ are the relative water uptakes obtained from the experimental work and simulation, respectively. Comparisons between $w_{rel,exp}$ and $w_{rel,sim}$ of the adsorption and desorption

processes of the adsorbent sample used to evaluate D_{eff} are presented in Appendix B. The mean value of D_{eff} values shown in Table 4.2 is about 1.25E-10 $m^2.s^{-1}$.

Our values for D_{eff} are in order of magnitude of those reported by Aristov et al. [140] for the Fuji silica gel. Aristov et al. [140] reported values for D_{eff} between 2.1 E-11 and 1.5 E-10 $m^2.s^{-1}$ in temperature range from 28.8 to 64.0 °C.

Table 4.2 D_{eff} values obtained from best fitting of the simulation model to the experimental data of the adsorbent sample

Operating conditions	**Adsorption**		**Desorption**	
$T_{evap}/T_{cond}/T_h$ **, ° C**	D_{eff}, m^2/s	RMSD	D_{eff}, m^2/s	RMSD
15/30/90	1.2E-10	0.048	1.0E-10	0.100
15/35/90	1.3E-10	0.090	1.2E-10	0.082
10/30/90	1.3E-10	0.042	1.2E-10	0.060
10/35/90	1.3E-10	0.064	1.2E-10	0.062
5/30/90	1.3E-10	0.041	1.2E-10	0.048
5/35/90	1.3E-10	0.077	1.3E-10	0.045

4.8.2 Applying the obtained D_{eff} values in the 3D model

The obtained values of D_{eff} have been applied in the 3D simulation model built to simulate the performance of the two APHEs investigated experimentally in Chapter 3.

GLX30 APHE results

As depicted in Figure 4.4, the model built to simulate the performance of the experimentally investigated APHEs has been excellently succeeded to predicted the adsorption kinetics of the GLX30 APHE at the four applied sets of operating conditions. The *RMSD* values given in Table 4.3 refers to the degree of matching between the experimental and the numerical results of the GLX30 APHE.

Table 4.3 RMSD values of the GLX30 APHE

Operating Conditions $T_{evap}/T_{cond}/T_h$**, °C**	**Adsorption**	**Desorption**
15/30/90	0.081	0.165
15/35/90	0.131	0.156
10/30/90	0.129	0.169
10/35/90	0.056	0.086

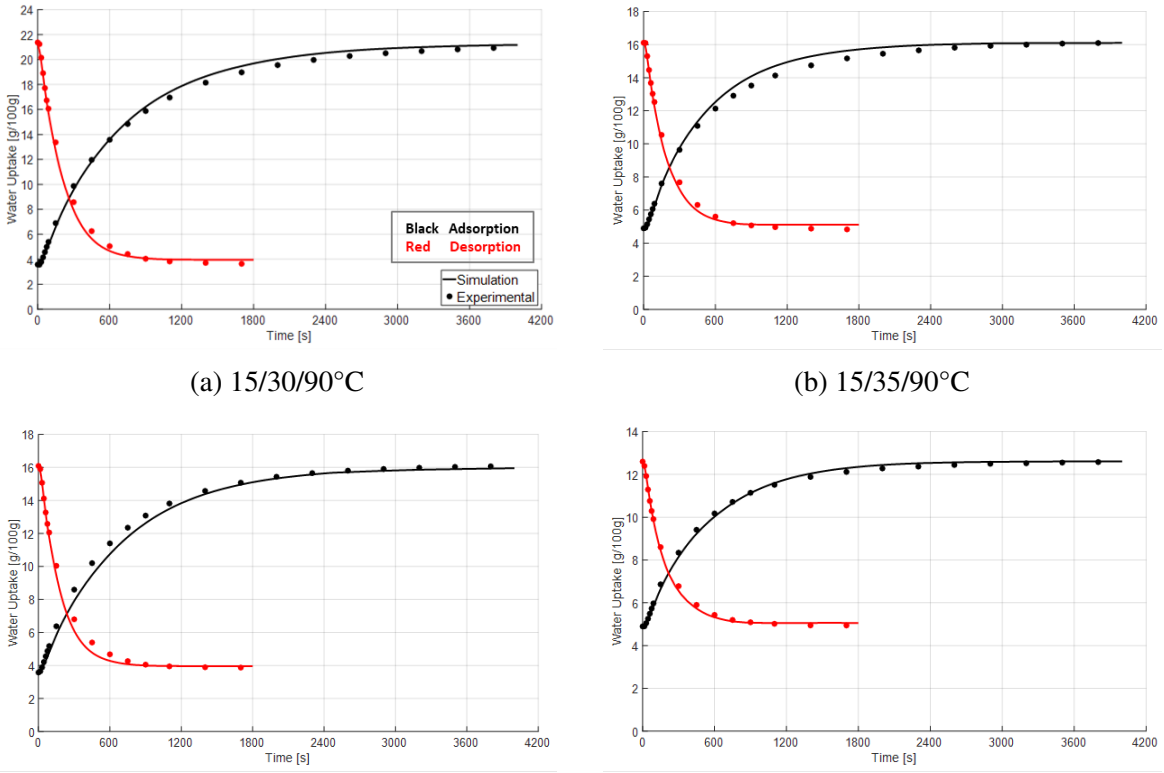

(a) 15/30/90°C

(b) 15/35/90°C

(c) 10/30/90°C

(d) 10/35/90°C

Fig. 4.4 Simulation results compared to the experimental data of the GLX30 APHE, obtained upon applying the obtained D_{eff} values

GL50 APHE results

Figure 4.5 shows another evidence of the excellent adsorption kinetics predictability of the 3D developed model. As depicted, the simulation model has been excellently succeeded to predicted the adsorption kinetics of the GL50 APHE at the four applied sets of operating conditions upon conducting the processes with the two vapour valves open as well as only one vapour valve open. Refer to Table 4.4 to check the degree of agreement between the experimental and numerical results of the GL50 APHE.

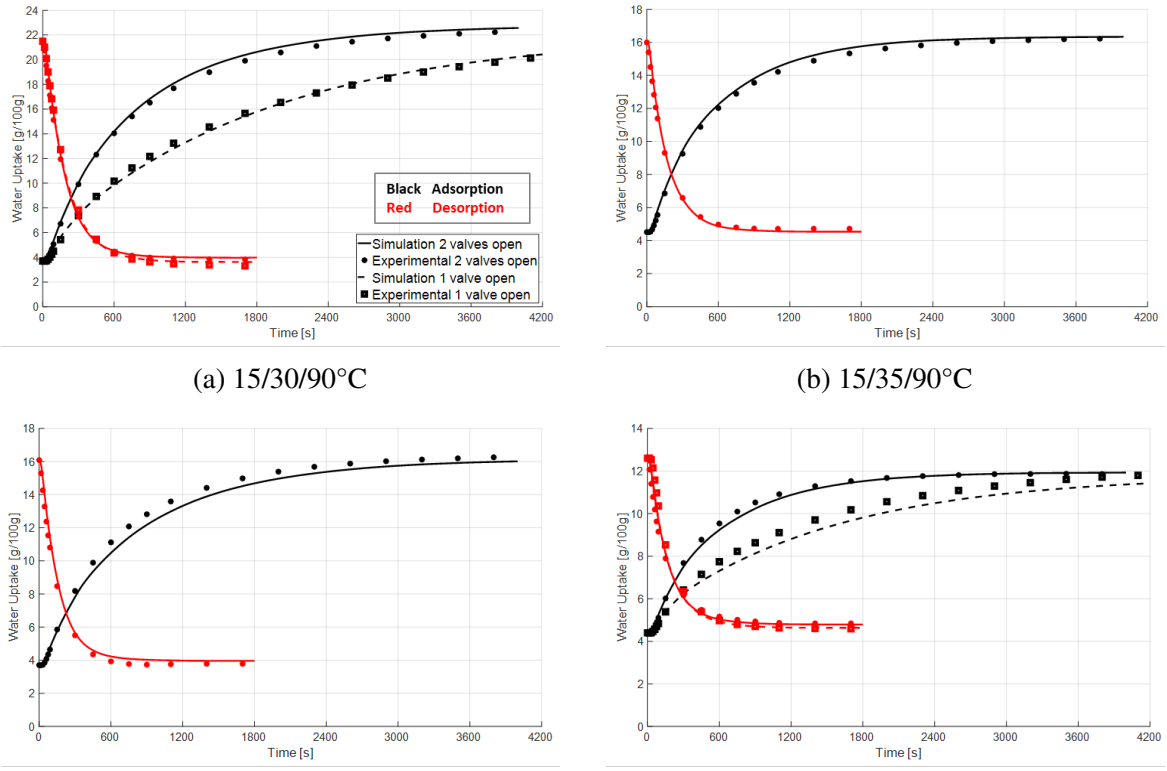

(a) 15/30/90°C

(b) 15/35/90°C

(c) 10/30/90°C

(d) 10/35/90°C

Fig. 4.5 Simulation results compared to the experimental data of the GL50 APHE, obtained upon applying the obtained D_{eff} values

4.9 Discussion

4.9.1 T, P and w distributions

GLX30 Vs GL50

As presented above, the developed 3D simulation model can predict the dynamic performance of an APHE very accurately. Accordingly, the model can be used to investigate the influence of various design parameters on the dynamic performance of the APHE. In addition, the model can be used to optimize the design of an APHE, as will be presented in Chapter 7. In the next paragraphs, the numerically obtained spatial and temporal distributions of the temperature, the pressure and the water uptake in the adsorbent domains of the two investigated APHEs shall be presented and discussed for better understanding of the influence of the various design parameters.

Figure 4.6 depicts the spatial temperature distribution over the adsorbent domain of the GLX30 and the GL50 APHEs after 600 s of an adsorption process corresponding to set of

Table 4.4 RMSD values of the GL50 APHE

Operating Conditions $T_{evap}/T_{cond}/T_h$, **°C**	**Adsorption**	**Desorption**
15/30/90	two valves open: 0.038, one valve open: 0.055	two valves open: 0.092, one valve open: 0.101
15/35/90	0.054	0.089
10/30/90	0.099	0.113
10/35/90	two valves open: 0.097, one valve open: 0.088	two valves open: 0.111, one valve open: 0.150

operating conditions 15/30/90 °C. As shown in the figure, the temperature distribution over the adsorbent domains of both APHEs is highly uniform. However, it seems that the GLX30 suffers from poor cooling near the two open sides of the adsorbent domain. Moreover, Figure 4.6a shows that the temperature distribution on the two sides, side I and II, of the adsorbent domain of GLX30 are not identical. This can be attributed to the different topology of the two plates forming the plate-pairs of the GLX30 APHE. In other words, the cooling from the two plates surrounding an adsorbent subdomain in the GLX30 is not symmetric around the plane passing through the interfacial surfaces, where the dimples on the two plate surrounding the adsorbent subdomain are brazed together.

Figures 4.7a and 4.7b show the vapor pressure distributions in the adsorbent domain of the two investigated APHEs, GLX30 and GL50, respectively, after 10 minutes (600 s) from starting an adsorption process corresponding to set of operating conditions 15/30/90°C.

As discussed in Section 4.8.2, the adsorption dynamics are very much influenced by the length of the vapour diffusion path in the adsorbent domain of the APHE. Due to the relatively high interparticle mass transfer resistance, in the adsorption processes, the vapour pressure gradually decreases as the vapour moves far away from the vapour inlet ports of the APHE. For the GLX30 APHE, the vapour pressure decreases in the direction normal to the symmetric mass transfer plane of the APHE, which is located at the middle distance between the two open sides of the adsorbent domain of the APHE. For the GL50 APHE with the two vapour valves open, the symmetric mass transfer plane is located in the middle distance between the two vapour ports of the APHE.

Despite the shorter distance between the vapour inlet and the mass transfer symmetry plane in the GL50 APHE compared to the GLX30 APHE, the vapour pressure in the region near the mass transfer symmetry plane in the GL50, i.e. at the middle distance between the two vapour ports, is lower than in the region near the mass transfer symmetry plane in the GLX30. It can be said that the radial diffusion results in a higher pressure drop than the linear diffusion. Therefore, the lower vapour pressure near the mass transfer symmetry

plane in the GL50 can be attributed to the semi-radial diffusion of the vapour from the two vapour ports towards the mass transfer symmetry plane in the GL50 APHE. However, the radial distances that the refrigerant vapor travels from its ports towards the three sides of the adsorbent region surrounding each vapour port are relatively short. Thus, semi-linear diffusion can be considered from each vapour port towards its three surrounding sides of the adsorbent domain, see the vapour pressure distribution in the adsorbent surrounding the vapour ports in Figure 4.7b. This explains why, despite the linear diffusion of the refrigerant vapor in the small-scale experimental adsorbent sample prepared to be representative of the adsorbent domain inside the GL50 APHE, it succeeded in predicting very accurately the adsorption dynamics of the GL50 at all applied operating conditions (see Chapter 3).

Figure 4.8 compares between the two APHEs in terms of the spatial water uptake distribution after 600s of starting an adsoprtion process at 15/30/90°C. Recall that the water uptake depends on the temperature of the adsorbent (T) and the pressure of the refrigerant vapour (P),

$$w = f(T,P) \tag{4.17}$$

Thus, the spatial water uptake distributions depicted in Figure 4.8 can be explained from the temperature distributions (Figure 4.6) and the pressure distributions (Figure 4.7) on the adsorbent domains of the two investigated APHEs. It can be seen that the water uptake in the region near the mass transfer symmetry plane in the GL50 is low compared to it in the region near the mass transfer symmetry plane in the GLX30. However, in the region near the vapor inlet ports, the water uptake in the GL50 is higher than the water uptake in the region near the open sides of the adsorbent domain in the GLX30. It can be concluded that the pattern of water uptake distribution matches very well the pattern of the pressure distribution in the adsorbent domain of each APHE. Thus, the relatively low adsorption dynamics of the two investigated APHEs (see Chapter 3) can be attributed to the poor interparticle mass transfer in their adsorbent domains, since the refrigerant vapour has to diffuse/flow over relatively long distances to reach all regions inside the adsorbent domains.

Influence of the interparticle mass transfer on the adsorption dynamic

To better understand the effect of interparticle mass transfer in the adsorbent domain on the adsorption dynamics, Figures 4.9, 4.10 and 4.11 show the T, P, and w distributions on the adsorbent domain of the GL50 in cases where only one vapour port is open and the two vapour ports are open. When only one vapour port is open, the vapour has to travel even longer distances in the adsorbent domain to reach the regions away from the opened vapour

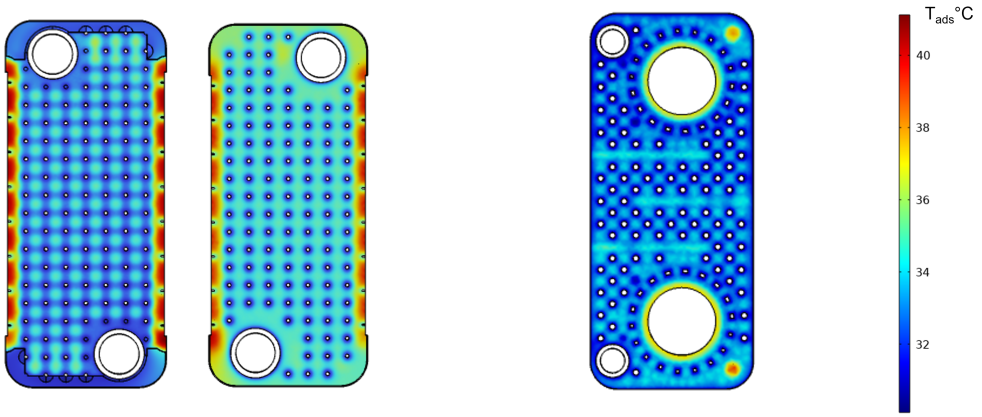

(a) (b)

Fig. 4.6 Spatial temperature distribution over the adsorbent domains of the investigated APHEs at time=600 s of an adsorption process, namely 15/30/90 °C (a) GLX30 (side I (left) and side II (right)),(b) GL50

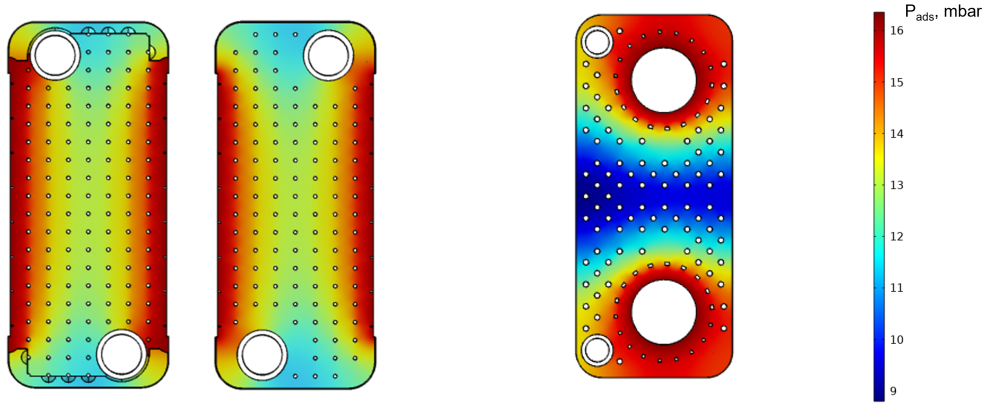

(a) (b)

Fig. 4.7 Spatial vapour pressure distribution over the adsorbent domains of the investigated APHEs at time=600 s of an adsorption process, namely 15/30/90 °C (a) GLX30 (side I (left) and side II (right)),(b) GL50

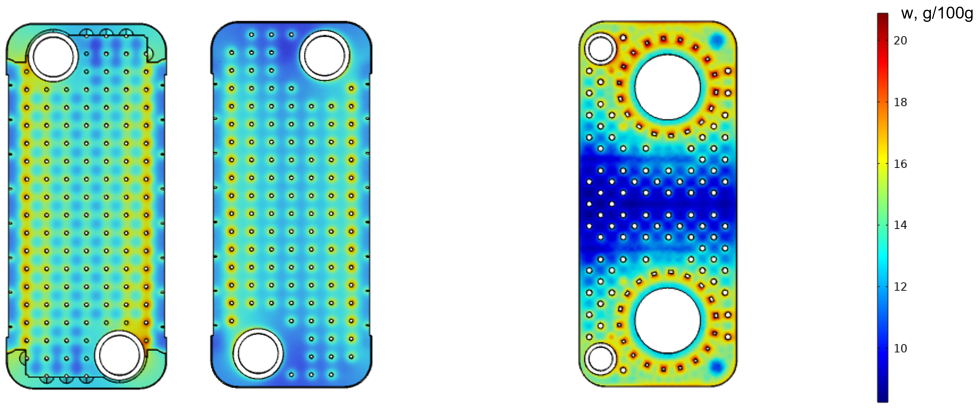

(a) (b)

Fig. 4.8 Spatial water uptake distribution over the adsorbent domains of the investigated APHEs at time=600 s of an adsorption process, namely 15/30/90 °C (a) GLX30 (side I (left) and side II (right)),(b) GL50

port. Figure 4.9 shows that the temperature of the adsorbent domain of the GL50 is lower when only one vapour port is open than when the two vapour ports are open. This can be attributed to the poor adsorption rates with only one vapour port open, particularly near the closed vapour port (i.e. top vapour port in Figures 4.9, 4.10 and 4.11), which implies a low release of adsorption heat and, accordingly, lower temperature of the adsorbent.

Figure 4.10a shows a rather widely distributed pressure in the adsorbent domain of the GL50 for the case where only one vapour port is open, with quite low vapour pressure in the top part of the adsorbent domain, which is relatively far from the active vapour port (the bottom vapour port) of the APHE. The pattern of the water uptake distribution depicted in Figure 4.11a matches very well with the pattern of the pressure distribution depicted in Figure 4.10a. This is a further evidence that the adsorption dynamics of APHEs are severely limited by the interparticle mass transfer of the refrigerant vapour (adsorbate) inside the adsorbent domains.

Influence of the interparticle mass transfer on the desorption dynamic

The effect of interparticle mass transfer on the desorption dynamics can be understood from Figures 4.12, 4.13 and 4.14, which show the T, P, and w distributions on the adsorbent domain after 180 s of starting a desorption process, at 15/30/90°C, of the GL50 in cases where only one vapour port is open and the two vapour ports are open. Figure 4.12 shows quite similar temperature distribution on the adsorbent domain in the two cases, i.e. only one port open Vs two ports open. Concerning the pressure, quite wide distribution has

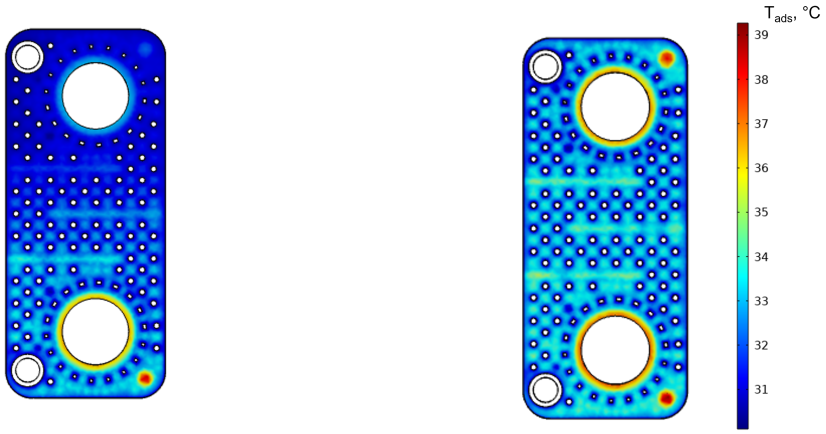

(a) (b)

Fig. 4.9 Spatial temperature distribution over the adsorbent domain of the GL50 APHE at time=600 s of an adsorption process, namely 15/30/90 °C, (a) 1 vapour valve is open, (b) 2 vapour valves are open

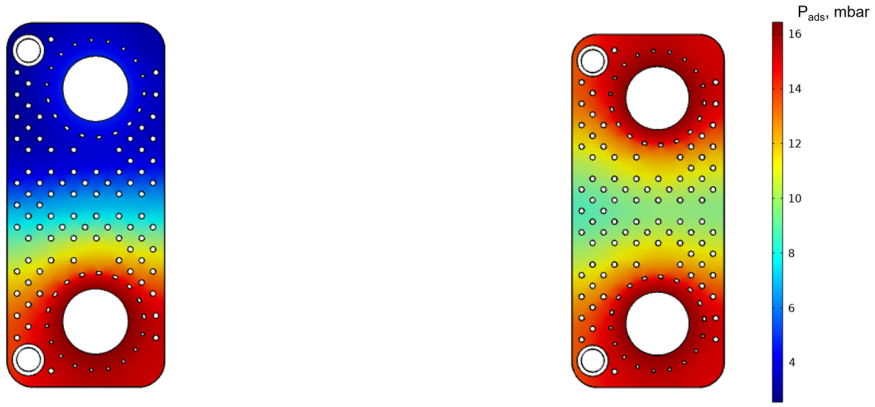

(a) (b)

Fig. 4.10 Spatial vapour pressure distribution over the adsorbent domain of the GL50 APHE at time=600 s of an adsorption process, namely 15/30/90 °C, (a) 1 vapour valve is open, (b) 2 vapour valves are open

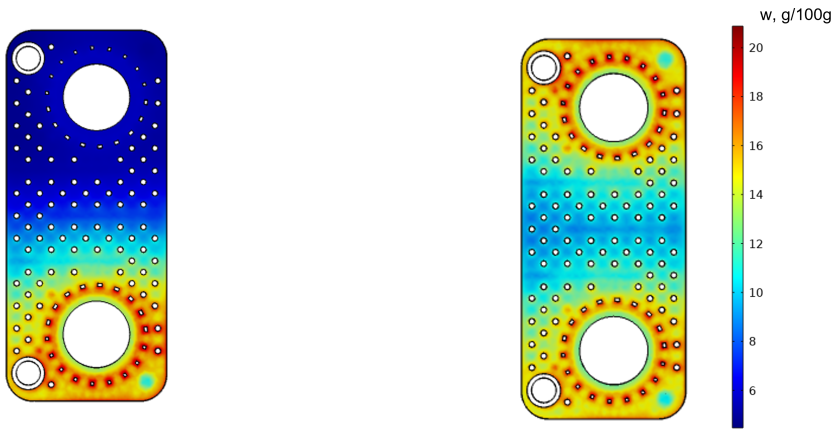

(a) (b)

Fig. 4.11 Spatial water uptake distribution over the adsorbent domain of the GL50 APHE at time=600 s of an adsorption process, namely 15/30/90 °C, (a) 1 vapour valve is open, (b) 2 vapour valves are open

been obtained in case of only one vapour port open compared to the case of the two ports open, see Figures 4.13a and 4.13b. However, the quite different pressure distributions on the adsorbent domain in the two cases, i.e., 1 open port vs. 2 open ports, are not greatly reflected in the water uptake distributions shown in Figure 4.14. Figures 4.14a and 4.14b show quasi-similar water uptake distributions. This is also in accordance with the time variations of the average water uptake (desorption kinetics curves) of the GL50 obtained experimentally and numerically at 15/30/90 °C in case of 1 open vapour port versus 2 open vapour ports. See Figure 4.5a. It can be concluded that, in contrast to the adsorption, the desorption dynamics of APHEs are only slightly limited by the interparticle mass transfer of the refrigerant vapour (adsorbate) in the adsorbent domains.

4.9.2 MTCL assessment

As shown in chapter 3, the experimental adsorption kinetic data of a small-scale adsorbent sample in cuboidal shape with height corresponding to the HTCL and length corresponding to the MTCL of GLX30 APHE agreed excellently with the adsorption kinetic data of the full-scale GLX30 APHE.

As indicated in Section 4.9.1, the MTCL is the most important design parameter of an APHE. In this section, the simulation model presented in Section 4.1 of this chapter will be applied to a 2D geometry representative of the cuboidal adsorbent sample tested in a closed test frame, like the test frame of the GLX30 APHE described in Chapter 3, Section 3.4.

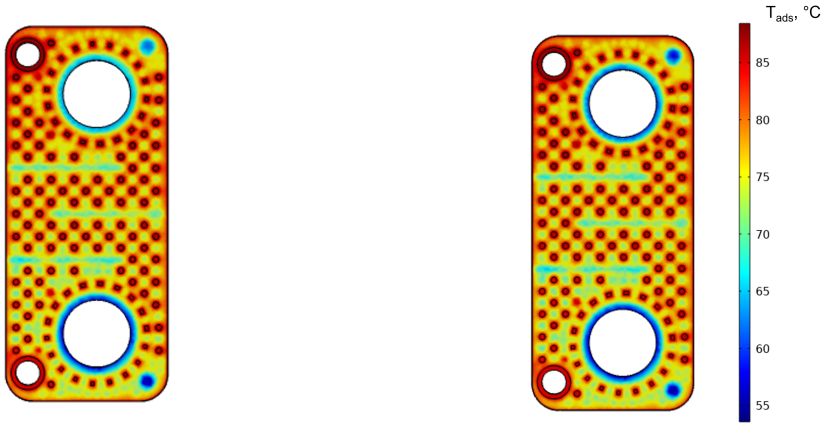

(a) (b)

Fig. 4.12 Spatial temperature distribution over the adsorbent domain of the GL50 APHE at time=180 s of a desorption process, namely 15/30/90 °C, (a) 1 vapour valve is open, (b) 2 vapour valves are open

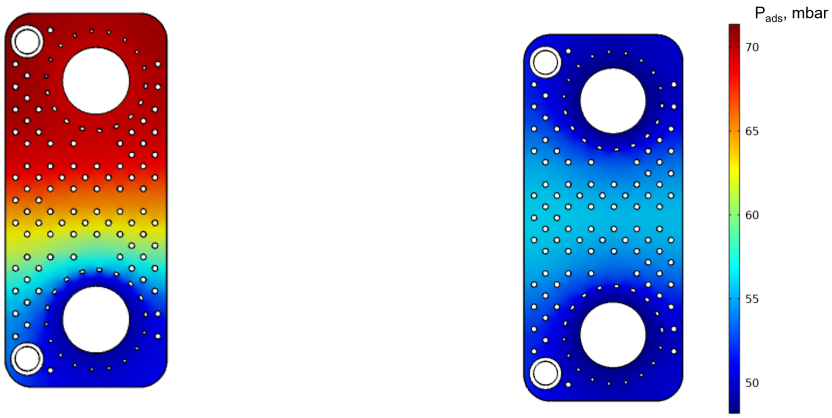

(a) (b)

Fig. 4.13 Spatial vapour pressure distribution over the adsorbent domain of the GL50 APHE at time=180 s of a desorption process, namely 15/30/90 °C, (a) 1 vapour valve is open, (b) 2 vapour valves are open

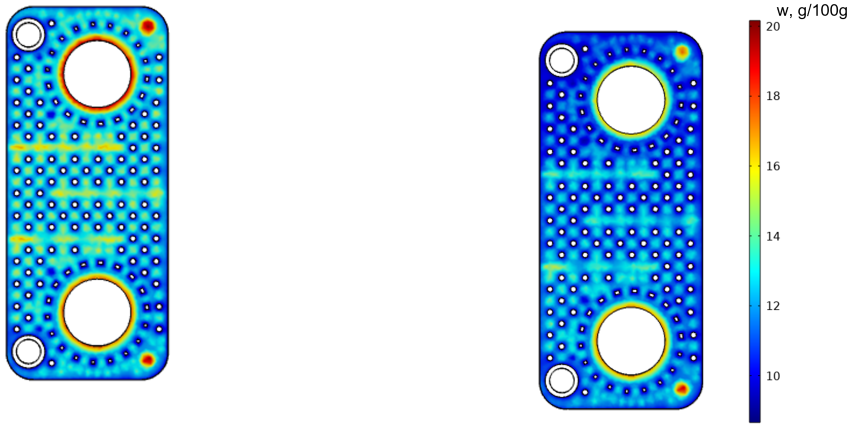

(a) (b)

Fig. 4.14 Spatial water uptake distribution over the adsorbent domain of the GL50 APHE at time=180 s of a desorption process, namely 15/30/90 °C, (a) 1 vapour valve is open, (b) 2 vapour valves are open

The objective is to investigate the effect of the MTCL on the adsorption kinetics of an open-structured APHE in which the refrigerant vapor diffuses almost linearly from the open sides of the adsorbent domain towards its mass transfer symmetry plane.

It is obvious that the lower the MTCL, the higher the adsorption dynamics of the APHE and, accordingly, the higher the specific power output (*SP*) of the adsorption system. In fact, optimizing the MTCL only with respect to SP leads to zero value. However, extremely low MTCL result in a quite small width of the APHE, which means difficulties in the fabrication of the APHE, high pressure losses in the HTF domain inside the APHE, low mass ratio of the adsorbent to the heat exchanger (metal+HTF) and low mass ratio of the APHE to its vacuum chamber.

Figure 4.15 depicts a rectangle, i.e. 2D geometry, representative to the cuboidal adsorbent sample. The geometry has been implemented in COMSOL Multiphysics. the height of the rectangle is 3 mm, which is the HTCL of the GLX30 APHE. The length of the rectangle corresponds to the MTCL of the represented APHE. While the HTCL remains fixed at 3 mm, the MTCL is varied from 18.5 to the 58.5 mm (the MTCL of the GLX30 APHE). The red edge of the rectangle represents the inlet slot of refrigerant vapour to the adsorbent sample. The blue edge refers to the contact surface of adsorbent sample to the metal in the represented APHE. As depicted in the figure at the inlet slot, i.e. the red edge, pressure boundary condition is applied. Here, the pressure recorded experimentally for the evaporator, against which the GLX30 APHE has been tested experimentally (see Chapter 3) is applied. The

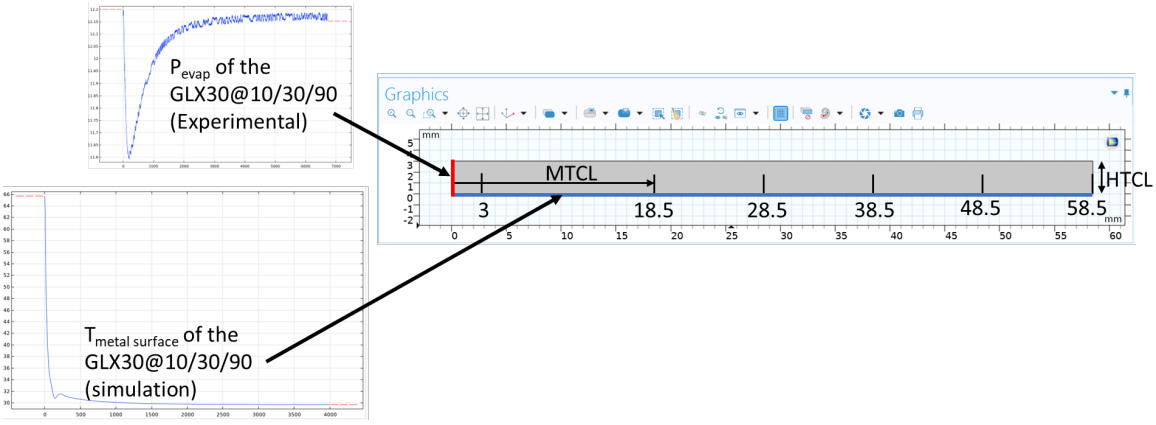

Fig. 4.15 Applied boundary conditions on the adsorbent sample representative to the GLX30 APHE at 10/30/90°C

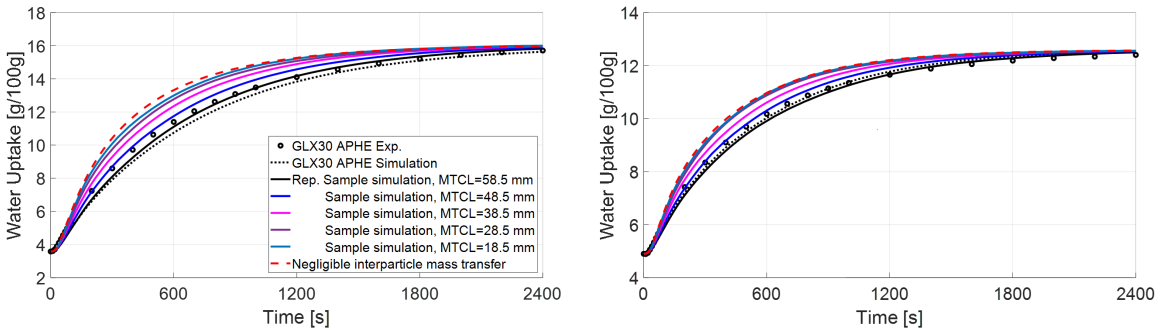

(a) (b)

Fig. 4.16 Effect of the MTCL on the adsoprtion kinetic, simulation with applying the boundary conditions of the GLX30 APHE at; (a) 10/30/90 and (b) 10/35/90°C

plates' average surface temperature obtained numerically for the GLX30 APHE is applied as a thermal boundary condition of the simulated adsorbent sample, i.e. at the blue edge of the rectangle dipicted in Figure 4.15. For the two other edges of the rectangle thermal insulation and no flow boundary conditions are applied, i.e. $\frac{\partial T}{\partial n} = 0$.

Figures 4.16a and 4.16b depict the effect of the MTCL on the adsorption kinetics at 10/30/90°C and 10/35/90°C, respectively. The dashed red curve in each figure presents the adsorption kinetic in case of negligible mass transfer resistance between particles, i.e., with quite low MTCL. This has been considered in the simulation by setting the interparticle mass transfer resistance to zero. The figures dipict also the adsorption kinetics data obtained experimentally and numerically for the GLX30 APHE. As can be seen from the figures, the adsorption kinetics obtained at a MTCL of 28.5 mm or less are very close to the highest kinetics obtained at negligible mass transfer resistance between particles, i.e. MTCL=zero.

Figure 4.17 shows the relation between the characteristic time constant (τ) of the exponential fitting of the kinetic results depicted in Figure 4.16 and the MTCL. Table 4.5 gives the values of τ depicted in Figure 4.16 and their R^2-values. In addition, Table 4.5 gives the τ-values of exponential fittings of the adsorption kinetic data obtained experimentally and numerically for the GLX30 APHE. As can be seen in Figures 4.16 and 4.17, the adsorption kinetics obtained at a MTCL of 28.5 mm or less are very close to the highest kinetics obtained at negligible interparticle mass transfer resistance. As shown in Figure 4.17 τ value at MTCL of 28.5 mm is higher than the τ at negligible interparticle mass transfer resistance by about 13.5% for 10/30/90 °C and 5.7% for 10/35/90°C.

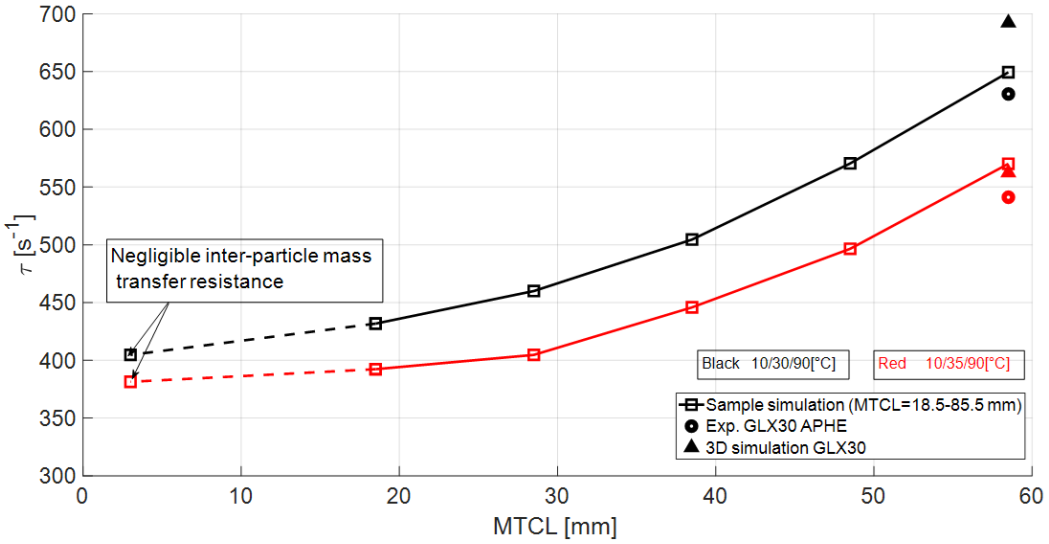

Fig. 4.17 MTCL vs τ, simulation with applying the boundary conditions of the GLX30 APHE at 10/30/90 and 10/35/90°C

4.10 Conclusion

A dynamic heat and mass transfer (HMT) simulation model was developed to simulate the adsorption and desorption kinetics of an adsorber plate heat exchanger (APHE). For estimating the D_{eff} values of the water vapour adsorption into the applied adsorbent material (granular Siogel, 0.71-1.0 mm), the model was applied to a 2D geometry representative to a granular Siogel adsorbent sample with negligible interparticle mass transfer resistance, previously investigated using the kinetic V-LTJ setup, see Appendix B. The obtained D_{eff} values were fed into the implementation of the mathematical model on the 3D geometries representative to the APHEs experimentally investigated in Chapter 3, i.e., the GLX30 and the GL50 APHEs. Excellent agreement has been obtained between the numerical results

Table 4.5 Time constant of the exponential form (τ) and its (R^2) value of the adsorption kinetic data obtained at two sets of operating conditions, namely 10/30/90 and 10/35/90°C, for the GLX30 APHE (experimental and simulation) and its representative adsorbent sample (simulation with applying the boundary conditions of the GLX30 APHE).

Operating Conditions (°C)	Exponential fitting parameters	GLX30 Experimental	GLX30 Simulation	Sample Simulation					
				MTCL (mm)					
				58.5	48.5	38.5	28.5	18.5	Negligible
10/30/90	τ (s^{-1})	626.2	692.2	649.4	570.5	504.5	460.0	431.8	404.8
	R^2	0.9991	0.9984	0.9990	0.9992	0.9988	0.9983	0.9981	0.9966
10/35/90	τ(s^{-1})	538.5	562.4	570.1	496.5	445.8	404.7	392.3	381.4
	R^2	0.9980	0.9978	0.9990	0.9988	0.9987	0.9982	0.9984	0.9981

and the experimental data of the two investigated APHEs. The distributions of temperature, vapour pressure, and water uptake on the adsorbent domains of the two investigated APHEs were discussed. Finally, the simulation model was used to investigate the effect of the MTCL on the adsorption kinetics of an open-structured APHE. It was found that a MTCL of 28.5 mm or less results in adsorption kinetics very close to the adsorption kinetics obtained in case of negligible interparticle mass transfer resistance (MTCL $\approx$ zero) in the adsorbent domain of an open structured APHE. Strictly speaking, it was found a relative deviation between the time constant (τ) values of the exponential fittings of the adsorption kinetic results obtained at MTCL=28.5 mm and MTCL $\approx$ zero amounts to less than 13.6%.

Chapter 5

Investigation of an innovative open structured APHE

The Performance of an innovative adsorber plate heat exchanger (APHE) [82], which was developed recently by the team of the Laboratory of Sorption Processes (LSP) at OTH Regensburg for application in adsorption heat pumps, chillers and thermal energy storage systems, will be investigated experimentally and numerically in this chapter. This APHE is referred here to the OTH APHE. The OTH APHE has been developed as a successor adsorber heat exchanger for a gas-fired adsorption heat pump [141], in which a finned-tube heat exchanger has been coated with the zeolite AQSOA-FAM-Z02. Therefore, the investigations carried out in this chapter involve the application of AQSOA-FAM-Z02 as adsorbent and water as adsorbate. Indeed Siogel is less expensive than zeolite AQSOA FAM Z02, however the latter has a higher water adsorption capacity compared to the former, as stated in Section 2.6. Although the adsorption capacity is not the only factor affecting the performance indicators (COP and SCP) of adsorption chillers, as discussed in Section 2.6, it is believed that the application of AQSOA FAM-Z02 would result in better performance, since the heat and mass transfer characteristics of the AQSOA FAM-Z02-water pair are not far from those of the Siogel-water pair [142] .

A test frame has been constructed as a representative segment of the introduced APHE for applying loose grains of AQSOA FAM Z02. Adsorption kinetic measurements have been carried out in a volumetric large-temperature-jump (V-LTJ) setup [93, 125] under typical operating conditions of adsorption processes. The transient 2-D mathematical model

---

Contents of this chapter have been reprinted from:
M. Mikhaeil, M. Gaderer and B. Dawoud." On the development of an innovative adsorber plate heat exchanger for adsorption heat transformation processes; an experimental and numerical study". Energy 207 (2020), with permission from Elsevier.
Contributions of the author: Conceptualization, Model, Investigation, Validation, Writing original draft.

developed in Chapter 4 has been applied for the simulation of tested sample inside the V-LTJ setup. The measured temporal uptake variations with time have been fed to the model, through which a micro-pore diffusion coefficient at infinite temperature of 2E-4 $m^2.s^{-1}$ and an activation energy of 42.1 $kJ.mol^{-1}$ have been estimated. The 3-D model developed in Chapter 4 was used to simulate the combined heat and mass transfer inside the OTH APHE. The 3-D model was implemented in COMSOL software as done in Chapter 4.

5.1 The OTH APHE

To completely avoid corrosion, the developed APHE [82] has been designed as an open-structured stack of multi-nickel-brazed parallel plate-pairs made of stainless steel 316L, wherein each plate-pair comprises an inlet and an outlet port of 16 mm diameter for the HTF. The dimensions of one plate is 400 mm in length and 54 mm in width. It should be recalled that the MTCL of an open-structured APHE is equal to half of its width. Thus, the MTCL of the presented APHE is 27 mm, which is within the recommended range based on the discussion in Section 4.9.2 of Chapter 4. The plate thickness amounts to 0.3 mm. Figure 5.1a depicts the upper part of the APHE showing the exit port for the HTF, which is connected to the inlet port by seven parallel flow channels, each has an internal diameter of 2 mm. The clearance between each two successive plate-pairs in the stack amounts to 3 mm, which shall be filled in with loose adsorbent grains. The stacked plate pairs shall be Nickel-brazed together on the annular rings of the inlet and outlet ports of the HTF to form the APHE. A suitable cage made of two segments of a perforated stainless steel sheet has been developed for the APHE to be mounted inside, in order to prevent the adsorbent grains from falling out of the heat exchanger [82]. Figure 5.1b shows the APHE mounted inside the adsorber/desorber chamber, which shall be connected to the evaporator/condenser chamber via the vapour duct [82]. Figure 5.1c presents the cross section A-A of Figure 5.1a to illustrate the gap between two successive plate pairs, which is open from both sides and shall be filled in with the adsorbent grains. Water vapour can penetrate, therefore, into the adsorbent grains from both sides of the stacked APHE.

The number of the plate-pairs composing the APHE is determined according to the required space volume for the adsorbent material. To provide a space volume of 1 L, the APHE shall consist of 24 plate-pairs.

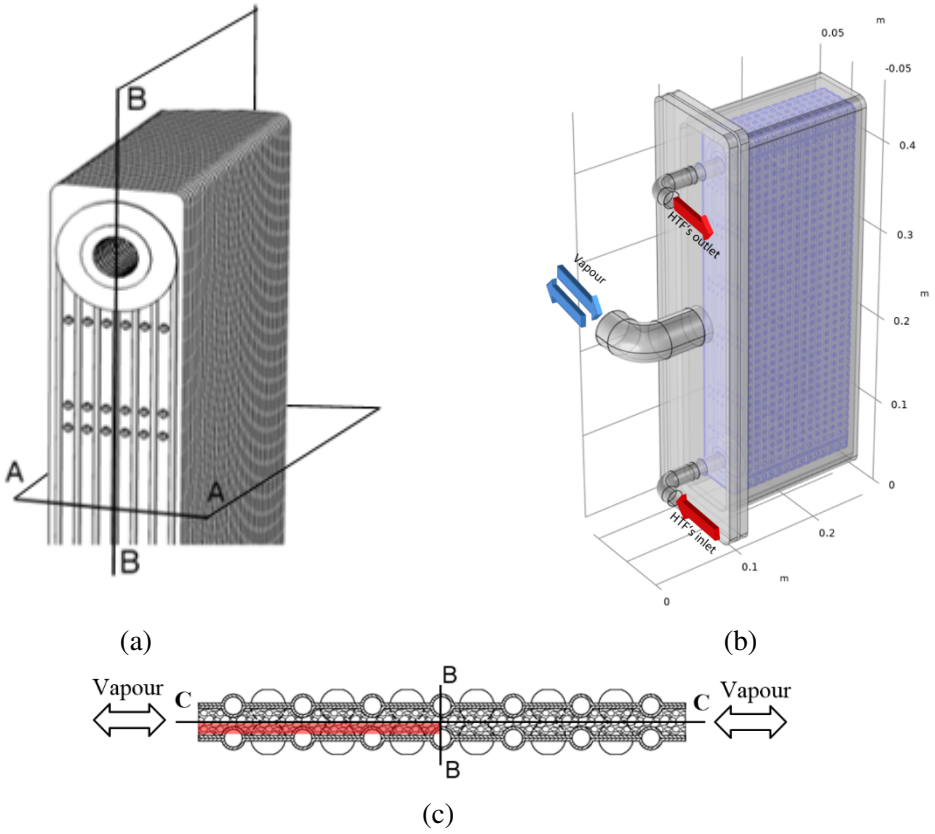

Fig. 5.1 The newly introduced adsober plate heat exchanger (APHE) [77] ; (a) a 3D-Segment showing the top end of the APHE, (b) the APHE inside the adsorber/desorber chamber and (c) a cross section in two successive plate pairs (A-A in Figure 5.1a) showing the open structure of the APHE.

5.2 Test frame and experimental work

Figure 5.1c illustrates the cross section A-A of Figure 5.1a of the APHE, which consists of identical plate-pairs.Water vapour, which fills the adsorber/desorber vacuum chamber shall flow from both sides of the stack into the adsorbent porous media filling the gap between each two successive plate-pairs during adsorption phase and leaves also from both sides of the stack during the desorption phase. It is, therefore, why the symmetrical axis B-B does exist for the mass transfer in the middle width of the plates. The second symmetrical axis C-C stays for heat transfer in the middle height of the adsorbent gap between each two successive plate pairs, as the porous media is equally cooled-down or heated-up by the two contacting plate pairs.

In case of testing AQSOA-Z02 in the V-LTJ kinetic setup installed in the LSP at OTH-Regensburg, the sample mass should be limited to 250 mg, in order to allow the adsorption or desorption measurements under quasi isobaric (Δp<2 mbar) conditions. In addition, the small-scale adsorbent sample should be in close agreement with the adsorbent bed of the APHE, in terms of the heat and mass transfer paths. The experimental setup enables exposing the sample to cooling/heating effect from only one side of the sample holder inside the measuring cell. Because of the symmetry of the adsorbent domain in the proposed APHE around the axis C-C, the heat transfer in a small-scale sample with a height equal to half of the adsorbent layer thickness and exposed to cooling/heating effect only from the bottom side shall be in close agreement with the heat transfer pattern in a half-adsorbent layer. The mass transfer symmetry around the axis B-B in Figure 5.1c enables cutting down the length of the adsorbent sample inside the test frame to half of the width of the APHE. Accordingly, the red segment in the lower left corner of Figure 5.1c must be sufficient to represent the heat and mass transfer behaviour of the APHE, provided that, the cooling pattern of the plate pairs is identical with that of the sample holder of the measuring cell, which has been already approved (see Figure 5.6).

Knowing the bulk density of dry AQSOA-Z02 pellets, in the tested grain-size's range of 0.61-0.7 mm, the corresponding width of the sample inside the test frame, through which water vapour shall flow is estimated to 11 mm. A dedicated test frame made of polyether ether ketone (PEEK) has been designed and realized by milling (see Figure 5.2), in which the adsorbent grain sample shall be placed. The frame has a slot on one side, which allows the water vapour to enter/leave the adsorbent domain through a fine stainless-steel sieve. The frame prevents the vapour to enter/leave the adsorbent domain from all other sides and allows the heat transfer only from/to the adsorbent mass through a piece of metal strip mounted at the frame's bottom side. The test frame, placed on the sample holder inside the measuring cell of the kinetic setup, is illustrated in Figure 5.2b. The corresponding height of the sample

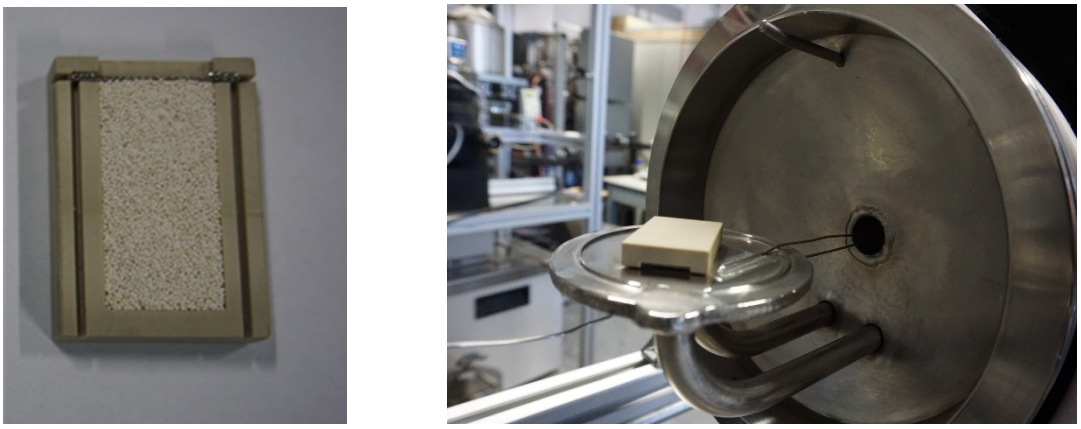

(a) (b)

Fig. 5.2 The frame prepared for testing the adsorption kinetics on a small scale adsorbent sample representing the behaviour of the whole APHE; (a) test frame filled in with loose grains and (b) test frame mounted on the surface of the sample holder of the V-LTJ kinetic setup

is 1.5 mm, half the thickness of an adsorbent layer in the proposed APHE. The adsorbent sample is cooled down or heated up during adsorption or desorption processes, respectively, allows realizing heat and mass transfer patterns inside the tested adsorbent sample, which are very close to the patterns occurring in the adsorbent domain of the proposed APHE. Two adsorption kinetic measurements at different evaporator-temperatures 5 and 10°C have been carried out at adsorption- and desorption-end temperatures of 35 and 90°C, respectively.

With the help of the available equilibrium data for water vapour adsorption on AQSOA-Z02 zeolite [18], the temperature at which the isobaric adsorption phase of an adsorption heat pump/chiller starts ($T_{ad-start}$) is determined. Thus, to realize water uptake at the beginning of the adsorption processes corresponding to condenser temperature of 35°C (adsorption-end temperature), driving source temperature of 90°C (desorption-end temperature), and evaporator temperatures of 5 and 10°C, $T_{ad-start}$ is determined to 56 and 61°C, respectively. The details of the V-LTJ kinetic setup, the experimental procedure and the evaluation of the instantaneous water uptake can be in Chapter 2. The accuracy of the applied individual sensors and the uncertainty analysis of the measurements are illustrated and discussed in Appendix A.

5.3 Mathematical modelling

The experimental activity carried out in this work on a representative segment of the OTH APHE does require modelling and simulation work for the subsequent design optimization and upscaling activities.

5.3.1 Estimation of the mass diffusion parameters

For the mathematical modeling of the APHE, it is necessary to determine the effective diffusion coefficient (D_{eff}) of the Linear Driving Force (LDF) model, Equation 4.7 (in this chapter denoted as Equation 5.1).

$$\frac{\partial w}{\partial t} = \frac{15 D_{eff}}{r_p^2}(w^* - w) \tag{5.1}$$

For the effective diffusion coefficient (D_{eff}), which appears in the LDF model (discussed in detail in Chapter 4), a new approach is considered for the AQSOA-Z02/water pair, for which the micro-pore diffusion is the dominating diffusion mechanism. Kärger and Ruthven [135] have introduced the following Equation 5.2 to account for the diffusion of a single component into the micro-pores of a porous adsorbent.

$$D_{eff} = D_o . \frac{dlnP}{dlnw}|_T \tag{5.2}$$

The effective micro pore diffusion coefficient D_{eff} or the "Fickian diffusivity" is thus the product of the self diffusion (mobility) coefficient D_o or the "corrected diffusivity" and the thermodynamic correction factor according to Darken [143]. The Darken factor $\frac{dlnP}{dlnw}|_T$ is the inverse of the slope of the equilibrium adsorption isotherm. In fact, except in dilute systems, the Fickian diffusivity is generally concentration dependent. Equation 5.2 shows that this dependence may arise from the concentration dependence of either D_o or $\frac{dlnP}{dlnw}|_T$. The concentration dependence of the thermodynamic correction factor is found to be much more pronounced than the concentration dependence of the corrected diffusivity [135].

The temperature dependence of the corrected diffusivity D_o is described in Equation 5.3 by an Arrhenius relationship as a function of the mico-pore diffusion coefficient at infinite temperature (D_∞) and the activation energy (E_a) along with the absolute adsorbent temperature.

$$D_o = D_\infty exp(-\frac{E_a}{R_m T}) \tag{5.3}$$

Dawoud et al. [94], applied the Darken-corrected micro-pore diffusion coefficient to model the adsorption kinetics of water vapour into a consolidated DDZ-70 zeolite layer, achieving a very good agreement between the experimental data and the simulation results.

The first part of the modelling work aims, therefore, at estimating the values of D_∞ and E_a for the water vapour diffusion on the investigated AQSOA-Z02 grains. To this aim, a transient 2-D mathematical model developed in Chapter 4 is applied to simulate the sorption behaviour of the adsorbent sample during quasi-isobaric processes, when the adsorbent sample is subjected to a sudden temperature drop. Recall that the model accounts for the combined heat and the mass transfer process inside the adsorbent sample. The experimentally recorded values for the instantaneous sample holder surface temperature and vapour pressure inside the measuring cell are fed into the model to account for the time-variant boundary conditions of the sample. By best fitting the model results with the experimental data, the mass diffusion parameters of water vapour in the AQSOA-Z02 grains (D_∞ and E_a) have been estimated.

5.3.2 Modelling of an intermediate section of the APHE

To properly apply the mathematical model developed in Chapter 4 for predicting the performance of the proposed APHE and, at the same time, consumes a reasonable computational time, an appropriate domain for the numerical study should be carefully selected. Since the introduced APHE consists of several identical plate-pairs, the adsorbent and the HTF domains between the successive plates are identical as well. Therefore, the numerical simulation of only an intermediate section can predict the performance of the whole APHE. Indeed, the adsorbent and HTF domains are symmetric around the axis B-B in Figure 5.1a, which divides it into two equivalent parts. For one representative plate-pair, half of the adsorbent domain thickness on each side, is sufficient to represent the whole APHE. Therefore, a section of the APHE composed of three contacted quarter parts of the domains of the adsorbent, the HTF and a plate-pair (metal) is selected to be the domain of the numerical study (see Figure 5.3).

5.3.3 Models' assumptions and governing equations

For both 2-D and 3-D mathematical models, the assumptions discussed previously in Chapter 4 are applied. In addition, for the 3-D model of the APHE's intermediate section, the pressure of the water vapour inside the adsorber chamber is assumed constant and equals the saturation pressure at the evaporator temperature.

The governing equations of the mathematical model have been already discussed in Chapter 4. However, it is important to mention that the equilibrium correlation between

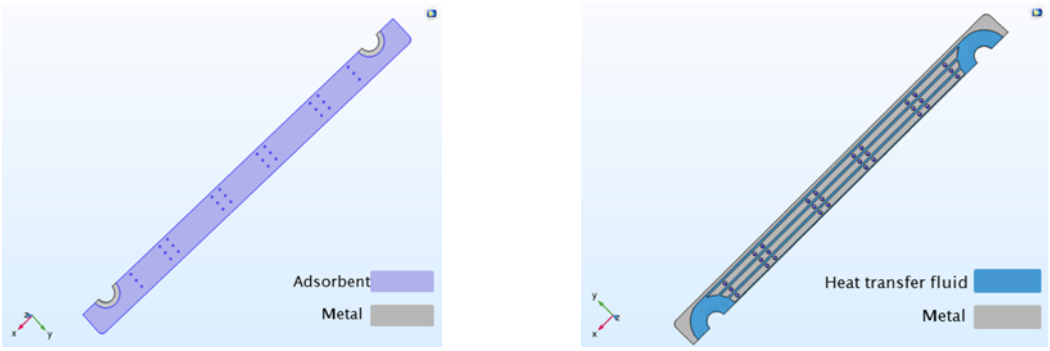

(a) (b)

Fig. 5.3 The intermediate representative segments of the APHE selected for the numerical simulation; (a) adsorbent-metal domain and (b) metal-HTF domain.

pressure, temperature and water uptake for AQSOA-Z02/Water pair is described by the Dubinin-Astakov relation (see Equation 5.4), where the parameters w_o, E and n have been taken from Ref. [18].

$$w^* = w_o \exp(-(\frac{A}{E})^n) \tag{5.4}$$

5.3.4 Initial conditions

The pressure, temperature, and adsorbate uptake distributions inside the experimentally tested adsorbent sample in the kinetic setup as well as the adsorbent domain of the newly introduced APHE are considered uniform at the initial state. The initial pressure of the water vapour inside the adsorbent is the saturation pressure corresponding to applied evaporator temperature. The initial temperature of the adsorbent is the corresponding adsorption start temperature ($T_{ad-start}$), which has been determined to 56 and 61°C for the evaporator temperatures of 5 and 10°C, respectively. For the metal and HTF domains of the selected domains for simulating the APHE, a uniform temperature distribution of $T_{ad-start}$ is assumed at the initial state.

5.3.5 Boundary conditions

For the numerical simulation of the experimentally tested adsorbent sample, the instantaneously recorded temperature of the sample holder and the pressure of the water vapour inside the measuring cell are utilized as the related boundary conditions for the adsorbent domain. Since the frame, where the sample is placed inside, allows the vapour to enter only from one side, the experimentally recorded pressure variation inside the measuring

cell is applied as the boundary condition at the sample vapour inlet, while zero normal pressure gradient ($\frac{\partial P}{\partial n}$=0) is assumed on all other boundaries. Moreover, the sample holder temperature recorded during the experimental work, from $T_{ad-start}$ to T_{ad-end}, is applied as the boundary condition at the lower surface of the adsorbent sample. For the other sides, insulation boundary conditions are applied ($\frac{\partial T}{\partial n}$=0).

For the selected domains to simulate the APHE, symmetric heat and mass transfer boundary conditions ($\frac{\partial T}{\partial n}$=0 and $\frac{\partial P}{\partial n}$=0) are applied at the symmetry planes described before. In addition, insulation boundary conditions ($\frac{\partial T}{\partial n}$=0) are applied at all outer sides of the adsorbent and metal domains. Different HTF-flow rates ($\dot{V}_{total}$) have been considered. At the HTF's inlet port, fully developed flow with flow rate of $\frac{\dot{V}_{total}}{4N_{plate-pairs}}$ and temperature of T_{ad-end} is assumed.

5.3.6 Implementation

As reported in Chapter 4, the commercial COMSOL Multiphysics® code is applied for all simulation tasks. Here, the same COMSOL modules that are also applied in the simulation models of the two APHEs investigated experimentally in Chapter 3 and numerically in Chapter 4 are applied. The physical properties of AQSOA-Z02/water pair required for the simulation work are taken from Refs. [18, 144]. The integrated optimization module in COMSOL is applied to estimate the parameters of the diffusion coefficient of water vapour into the zeolite pellets by best fitting the numerical results of the 2D model (simulation model of the adsorbent sample) to the experimental results obtained by the kinetic setup. The estimated values of D_∞ and E_a are fed to the "chemical reaction" module integrated in COMSOL to account for the mass diffusion resistance in the adsorbent grains. for the 3D model, the effect of the grid size and number of elements on the accuracy of the simulation results has been carefully investigated. To this aim, the number of grid elements has been changed from 265,601 to 2,136,471. It turned out, that a grid of 744,293 elements was adequate to obtain grid-independent results. The model has been solved in transient mode for 2000 s with a variant time step between 0.01 and 0.1 s. The relative tolerance has been set to 0.001.

5.4 Results

In this section, the adsorption kinetic results, obtained experimentally are presented and compared with some literature values. Moreover, the values estimated for the D_∞ and E_a by best fitting the obtained experimental data with numerical results using COMSOL's

optimization module are discussed. Finally, the results obtained from the 3D model developed to simulate the representative section of the APHE are presented and thoroughly discussed.

5.4.1 The representative adsorbent sample

Figure 5.4 presents the experimentally obtained water uptake at evaporator temperatures of 5 and 10° C starting at a water uptake of 7 g/100 g, which corresponds to a desorption temperature of 90°C and a condenser temperature of 35°C. The adsorption start temperatures amount to 56 and 61°C for the evaporator temperatures of 5 and 10°C, respectively. For both measurements, the adsorption-end temperature is 35°C. Based on the individual uncertainties of the applied measuring sensors listed in Table A.1 of Appendix A, the maximum error associated with measuring the temporal differential water uptake is estimated to $\pm$0.332 and $\pm$0.36 g/100 g in case of the adsorption at the evaporator temperature of 5 and 10°C, respectively. The continuous lines depict the simulated adsorption kinetics of the tested sample by the 2-D model. The best fitting between both experimental and simulated kinetic results has been achieved with a micro-pore diffusion coefficient at infinite temperature D_∞ of 2 E-4 $m^2.s^{-1}$ and an activation energy of 42.1 $J.mol^{-1}$.

It was reported in Ref. [142] that the effective diffusivity of the water vapour on the AQSOA-Z02 has not been measured before. Therefore, to account for the water vapour diffusion on the AQSOA-Z02 grains, Intini et al.[145] applied the D_∞ and E_a values estimated for the water vapour diffusion in standard zeolite 3 A [146]. For a grain diameter of 0.3 mm, Youssef et al. [147], have estimated the diffusion parameters for water vapour adsorption onto AQSOA-Z02 by best fitting the linear driving force model to the obtained isothermal kinetic data by a DVS instrument. They reported for D_∞ and E_a the pairs of 4.85E-9 $m^2.s^{-1}$ and 17709.8 $J.mol^{-1}$ as well as 2.77E-5 $m^2.s^{-1}$ and 44423.5 $J.mol^{-1}$, for the pressure ratio (P_r) between the bed (equilibrium pressure) and evaporator heat exchanger (saturation pressure) of > 0.1 and ≤ 0.1, respectively. Deviations between the measured and predicted temporal water uptake in the range of $\pm$ 15% have been obtained. It is important to mention that in the work of Youssef et al. [147], the Darken factor has not been applied. In Teo et al. [148], D_o was implicitly included in the adsorption rate coefficient (K_{ads}), which beside its dependency on both vapour pressure and temperature also depends on the activation energy E_a, which has been estimated to 52.250 $J.mol^{-1}$ for AQSOA-Z02.

The values of D_∞ and E_a obtained in this chapter (i.e. 2 E-4 $m^2.s^{-1}$ and 42.1 $J.mol^{-1}$, respectively) closely resemble those obtained in previous studies on water vapour adsorption in silica gel (specifically, Silica Fuji Davison type A and RD) reported in Refs. [149, 140].

Such a similarity between the water vapour diffusivities in silica gel and zeolite pellets has been reported on by Riffel et al. [150], who developed a transient mathematical model to

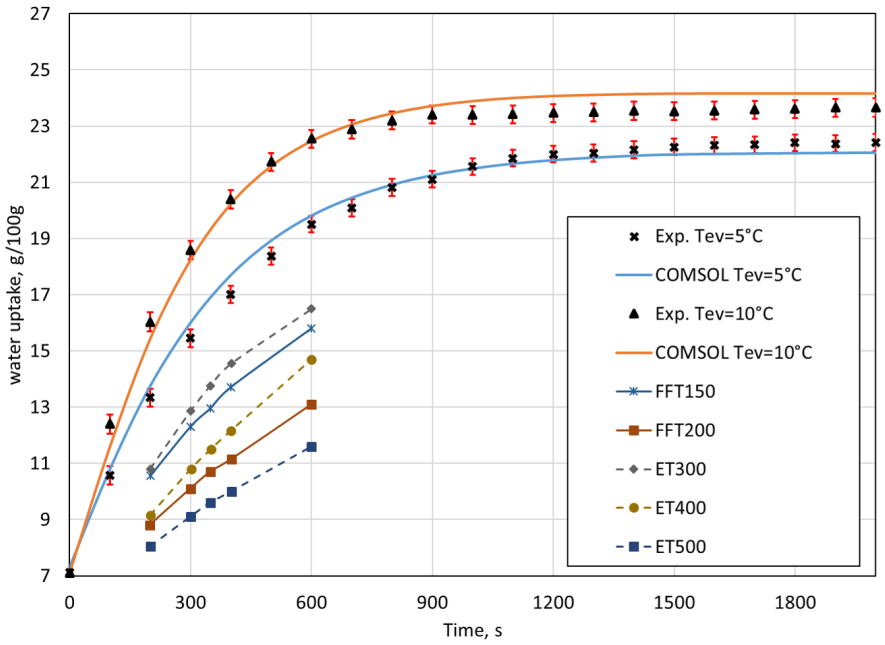

Fig. 5.4 Experimental and numerical water uptake of the investigated sample at two different evaporator temperatures compared with the adsorption kinetics of two different (FFT: Finned-Flat-Tube & ET: Extruded tube) coated adsorber heat exchangers [89]

simulate the performance of an adsorber heat exchanger. To account for the mass transfer, they used the definition of the time lag or the time constant (ζ) instead of the diffusion coefficient. Strictly speaking, Riffel et al. [150] has applied the following equation to describe the mass transfer or the time rate of pressure change inside the pores of the adsorbent grains ($\frac{dp}{dt}$) as a function of the temporal pressure difference between the vapour phase of the adsorber chamber (P_{ch}) and inside the adsorbent grains (p).

$$\frac{dP}{dt} = \frac{1}{\zeta}(P_{ch} - P) \tag{5.5}$$

By R^2-maximisation (coefficient of multiple determination), the time constants that best fit the model to the dynamic measurements of water vapour adsorption on silica gel and zeolite AQSOA-Z02 were estimated to ζ= 151.7 s for both adsorbents.

Figure 5.4 illustrates, in addition, the results obtained previously by Dawoud [95] upon investigating the adsorption kinetics of two different coated adsorber heat exchangers made of aluminium, which has been operated against a stagnant pool evaporator inside an adsorption heat pump module. The first adsorber heat exchanger was a finned flat-tube heat exchanger (FFT) made of brazed aluminium, while the second was an extruded-tube aluminium heat exchanger (ET). The numbers given aside to the abbreviations (ET or FFT) in Figure 5.4

correspond to the layer thickness in μm of the coated AQSOA-Z02 layers by Mitsubishi Plastic Incorporation. All five heat exchangers were investigated under evaporator, condenser and adsorber-end temperatures of 5 and 35 °C, respectively, while the desorption temperature amounted to 90°C. This allows the direct comparison with the results obtained at 5°C evaporator temperature for the representative test segment of the introduced APHE. From the heat capacity ratio point of view and, correspondingly, the COP point of view, the extruded tube aluminium heat exchanger coated with 500 μm (ET500) is comparable with the introduced APHE. The achieved differential water uptake with the introduced APHE at 300 and 600 s amount to 8.2 and 12.2 g/100 g, respectively. This corresponds to a remarkable enhancement of 310% (compared to 2 g/100 g) and 165% (compared to 4.6 g/100 g) at 300 and 600 s if compared with the ET500 adsorber heat exchanger.

5.4.2 Simulation results of the APHE

The values estimated before for D_∞ and E_a have been applied in the 3D simulations of the repeated segment of the APHE. Figure 5.5 illustrates a good agreement between the water uptake obtained from the numerical simulation of the APHE and that obtained from the experimental investigation of the representative segment depicted in Figure 5.2 at the evaporator temperatures of 5 and 10 °C.

The small deviation between the experimental and the numerical results is attributed to the applied boundary conditions (constant pressure for the APHE versus reduced pressure on the VLTJ-kinetic measurements) and the accuracy of the AQSOA-Z02/ water pair's equilibrium model, which is responsible for the small deviation in the final equilibrium uptake. Beside the thickness and the width of the space provided for placing the adsorbent material in the APHE, which are responsible for the mass transfer dynamics, a quick thermal response of the surface temperature of the plates to the sudden change in HTF's inlet temperature is also necessary to obtain sound combined heat and mass transfer characteristics from the adsorber heat exchanger. In order to achieve the later requirement, a uniform flow distribution of the HTF over all platepairs and inside each plate over all flow channels shall be guaranteed. In addition, the sum of the thermal capacities of the metal and the HTF of APHE related to the thermal capacity of the adsorbent must be minimized. The distribution of the HTF flow over the plate pairs and, in each, over the flow channels guarantees a low pressure loss and consequently a low parasitic energy consumption of the circulation pumps. Due to the low hydraulic diameter of the flow channels, a high convective heat transfer coefficient is realized, despite the resulted laminar flow regime.

Figure 5.6 presents the change in the measured temperature of the sample holder's surface of the kinetic setup (Figure 5.2b) and the numerical average surface temperature of one APHE

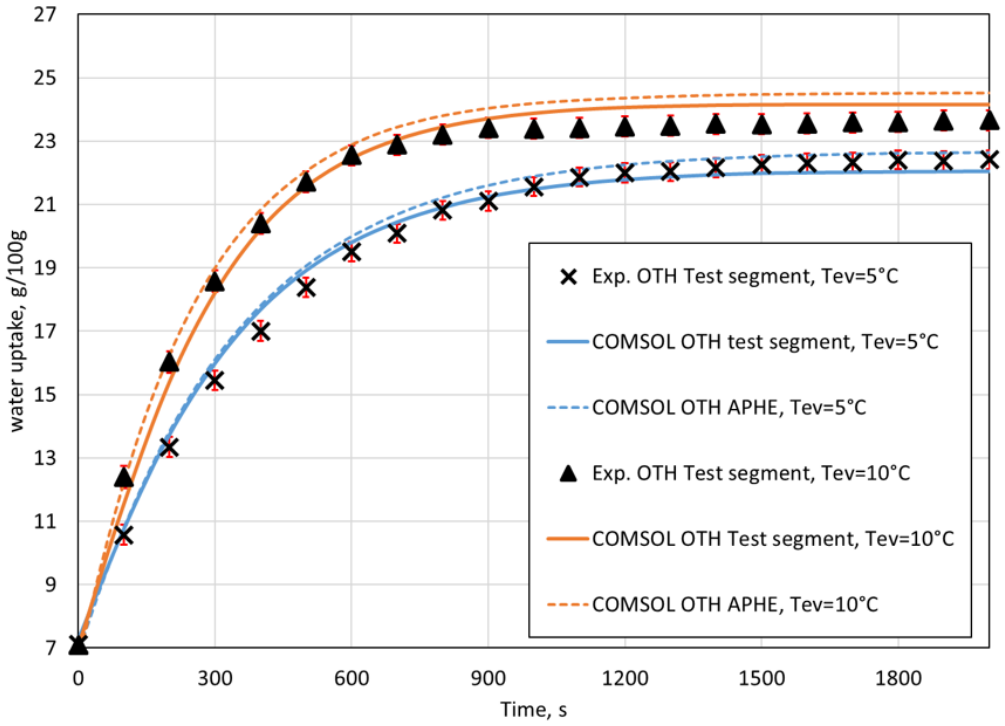

Fig. 5.5 Experimental and numerical water uptake of the investigated sample compared to the numerical average water uptake obtained from the APHE's simulation at two different evaporator temperatures.

plate, after the sudden change of the HTF's inlet temperature. In the experimental work, the sample holder temperature starts to decrease once the sample holder is connected to the thermal circulating bath set at $T_{ads-end}$. This is done by changing the position of the three way valves connecting the sample holder with the thermal circulating baths (Figure 2.10) [93, 125].

As shown in Figure 5.6 the rate of temperature decrease of both the surface of the sample holder and APHE's plates is almost identical over the first 20 s, during which the temperature is reduced to 38 °C. In the remaining time, the further reduction to 35 °C is faster in the kinetic setup as the sample mass is very low (250 mg) compared to the adsorbent mass on the adsorbent domain of the APHE. The comparison depicted in Figure 5.6 implies that the dynamic performance measured with the representative segment of the APHE is very much applicable to the dynamic performance of the real APHE.

5.4.3 Adsorber power output

Figure 5.7 illustrates the numerically estimated power output of the introduced APHE, which consists of 24 plate pairs offering an adsorbent volume of 1 L or 700 g AQSOA-Z02 at an

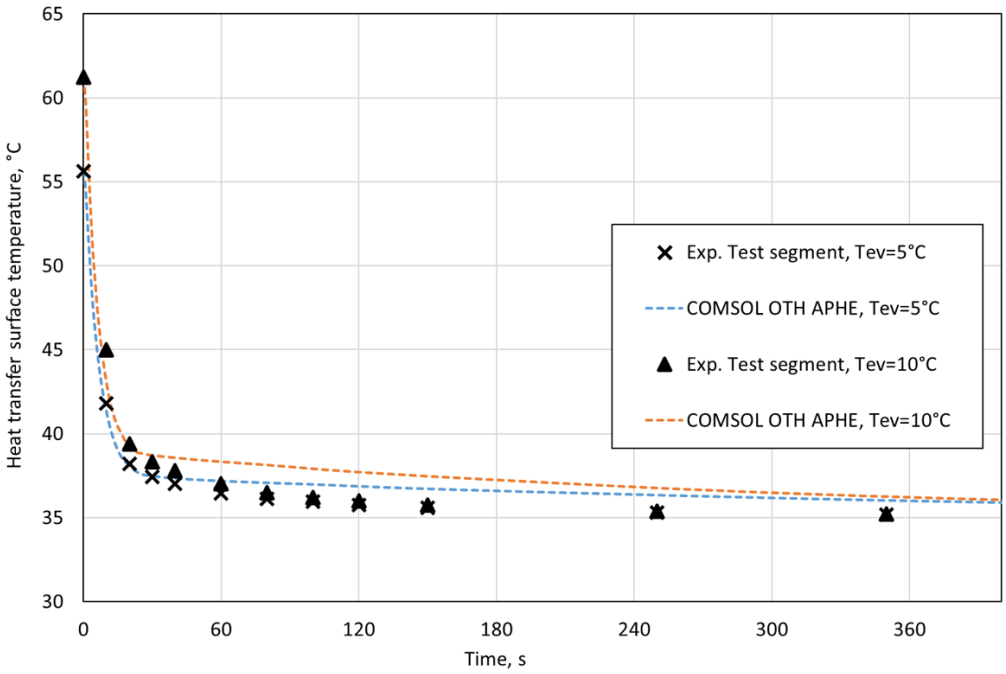

Fig. 5.6 Experimental sample holder's surface temperature and numerical average temperature of the metal plate's surface at two different evaporator temperatures.

evaporator temperature of 5 °C and a HTF flow rate of 6 LPM. Because of the simulated large temperature jump isobaric adsorption phase, the temporal adsorber power increases sharply and reaches up to 8.25 kW during the first few seconds. This is attributed to the step change in the HTF's inlet temperature. At the time of peak power, the HTF's outlet temperature is still very close to the APHE's initial temperature (56 °C), whereas the inlet temperature attains the adsorprion-end temperature (T_{ad-end}= 35°C). Afterwards, the power output decreases rapidly and gets lower than 3 kW after 15 s. After that time, the adsorber power continues to decrease, but with a clearly slower rate until it reaches almost zero power after 960 s. In order to evaluate the relative values of both sensible and adsorption heat amounts, a dedicated simulation run has been carried out without allowing the adsorption process to take place.

The power associated with removing the sensible heat stored in the APHE's material, HTF and the adsorbent, is presented by the dashed red line, which vanishes almost completely after 2 min. The solid blue line represents the overall power including that due to the release of the heat of adsorption. By subtracting the sensible heat related power (dashed red line) from the overall measured power (solid blue line), the power due to the release of the heat of adsorption has been evaluated and presented by the dashed brown line. The cross over between both contributions (cross point between both dashed red and brown lines) takes

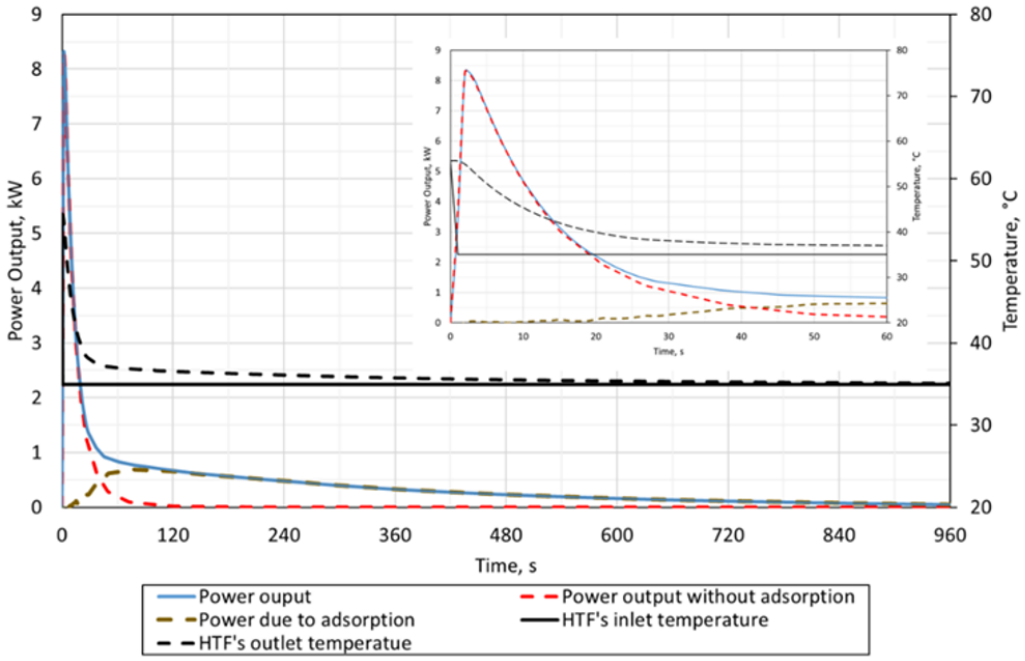

Fig. 5.7 APHE's power output and the contribution of the sensible heat stored in it along with the inlet and outlet temperatures of the HTF at the evaporator temperature of 5°C and HTF's flow rate of 6 LPM.

place after 42 s from the beginning of the adsorption process and, from there on, the release and removal of the heat of adsorption dominates the process dynamics.

As explained before, the lower the sensible heat stored in the metal and the HTF of the adsorber HX compared to the stored heat of adsorption, the higher the COP of the adsorption system. From the specific power (*SP*) point of view, this sensible heat has to be rapidly transferred to the HTF to allow a rapid and effective cooling of the adsorbent material and, consequently, a fast adsorption process leading to a high cooling capacity. The integration of the area under the curve of the power due to the release of the heat of adsorption or the integration of the area between the two power curves (with and without adsorption), over the process' time equals the released heat of adsorption. This concept has been introduced by Tokarev and Aristov [91] to estimate the temporal development of the uptake upon experimentally testing representative pieces of adsorber heat exchangers.

5.4.4 Effect of the HTF's flow rate

Figure 5.8 depicts the effect of the flow rate of the HTF on the adsorption kinetics. Increasing the flow rate of the HTF leads to enhancing the convective heat transfer coefficient on the HTF side. The overall heat transfer coefficient is dominated, however, by the heat transfer

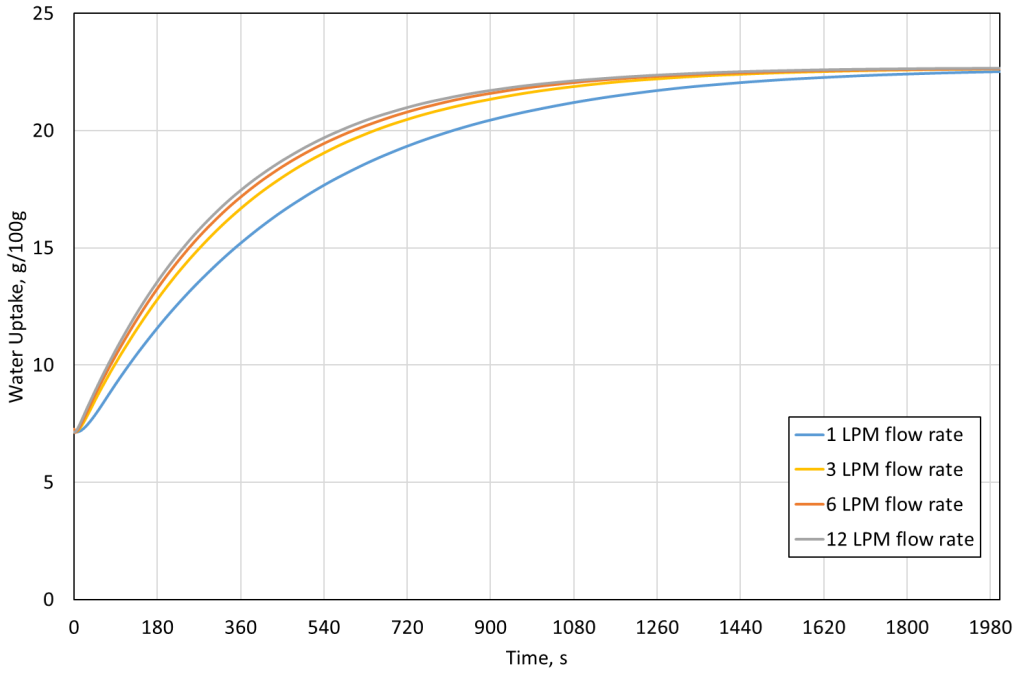

Fig. 5.8 Average water uptake dynamics of the introduced APHE at the evaporator temperature of 5 °C and different HTF's flow rates.

on the adsorbent side, due to its very low thermal conductivity. Increasing the HTF's flow rate above 3 l/min (LPM) for the encountered 24 plate pairs, is obviously not leading to a remarkable enhancement in the adsorption dynamics, compared to the dynamics increase between 1 and 3 LPM.

5.4.5 Effect of the construction material

The proposed APHE is decided to be made of stainless steel (SS) in order to completely avoid any corrosion potential against water or ethanol as refrigerants [57] or the application of selective water sorbents, which is formed by impregnating hygroscopic salts like LiBr or LiCl [8-10] inside the pores of mesoporous adsorbents. Figure 5.9 depicts the adsorption kinetics obtained numerically from the APHE's simulation at an evaporator temperature of 5 °C and the HTF flow rates of 1 and 6 LPM for both aluminium and SS as construction materials. According to the presented results, the construction material has a very limited effect on the performance of the introduced APHE. Among other factors, the adsorption dynamics of the APHE depend on the relative magnitudes of the thermal diffusivities of the construction material and the adsorbent. The thermal diffusivity of SS amounts to 3.8×10^{-6} $m^2 s^{-1}$, which is 18 times higher than the thermal diffusivity of the adsorbent (FAM-Z02).

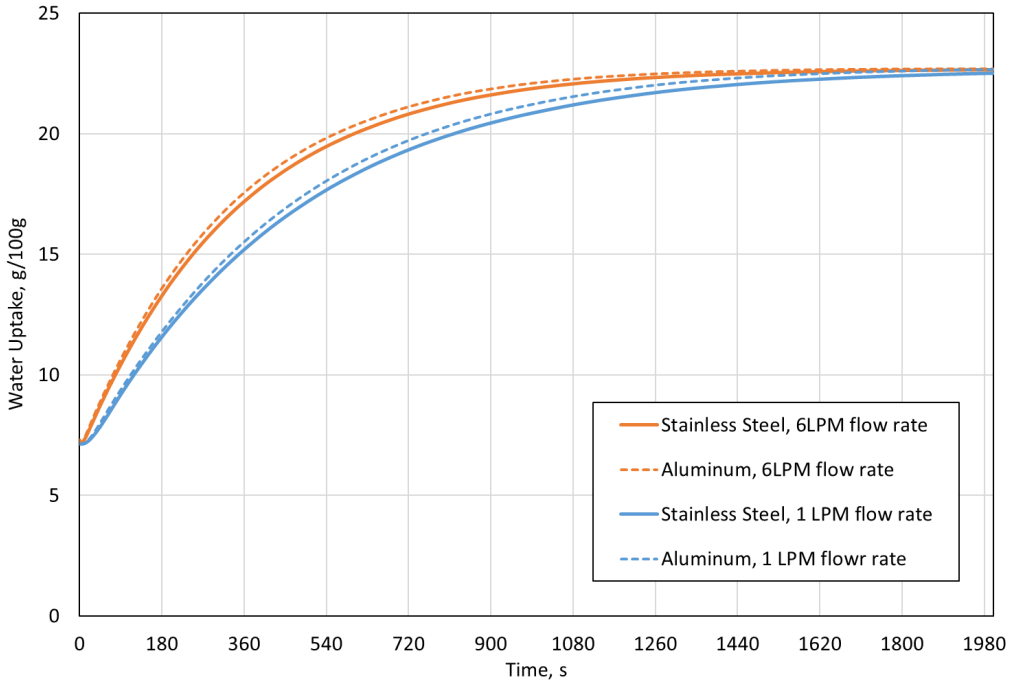

Fig. 5.9 Numerical water uptake dynamics of the introduced APHE with different construction materials at evaporator temperature of 5 °C and different HTF's flow rate.

This implies that the dynamics of adsorption is dedicated by the thermal diffusivity inside the adsorbent domain. The improvement of the thermal diffusivity of the construction material by making use of aluminium is, therefore, not leading to a remarkable enhancement on the adsorption dynamics.

5.5 Conclusion

An innovative plate heat exchanger is developed and introduced to act as a durable and high efficient adsorber in adsorption heat transformation processes like chillers, heat pumps as well as heat and cold storage. First experimental investigations on the adsorption dynamics of the introduced APHE have been carried out on a representative test frame, which has been constructed to simulate the heat and mass transfer characteristics of the introduced APHE. Experimental adsorption kinetic measurements on a small-scale adsorbent sample inside the test frame have been carried out at two different evaporator temperatures in a V-LTJ kinetic setup at OTH Regensburg.

In addition, a transient 2-D mathematical model developed previously (Chapter 4) is applied to simulate the combined heat and mass transfer encountered in the investigated adsorbent sample. The model has been implemented in a commercial simulation software

and its optimization module has been utilized to estimate the diffusion parameters. This methodology resulted in a mico-pore diffusion coefficient at infinite temperature (D_∞) of $2 \times 10^{-4}\ m^2 s^{-1}$ and an activation energy of 42.1 $kJ.mol^{-1}$. The mathematical model is further applied to simulate the introduced APHE. To this aim, a 3-D geometry comprising 3 domains, HTF, metal and the adsorbent/adsorbate is implemented in the commercial simulation software, which makes use of the obtained D_∞ and E_a from the previous activities. The results obtained from the investigation of the adsorbent sample demonstrated the superiority of the introduced APHE over an extruded aluminium heat exchanger coated with a 500 mm layer of the same adsorbent. Comparing the obtained results with the literature values for the extruded aluminium heat exchanger, differential water uptake obtained after 300 s of adsorption (8.2 g/100 g) implies a sound enhancement of 310%. This result proves the great potential of the introduced APHE to enhance remarkably the performance of adsorption heat transformation appliances.

Chapter 6

Effect of the heat and mass transfer characteristic lengths on the Adsorption and Desorption Dynamics

A new methodology for preparing small-scale adsorbent sample able to predict the performance of a real APHE has been introduced and validated experimentally in Chapter 3. Excellent agreements in the adsorption kinetics, at different testing conditions, have been obtained between commercially available PHEs (GLX30 and GL50, AlfaLaval©, Sweden) adapted to act as adsorbers/desorbers and small-scale adsorbent samples prepared to be representative of the investigated PHEs and tested in a volumetric large temperature jump (V-LTJ) kinetic setup [93]. Strictly speaking, an average relative deviation of only 12.3% has been obtained between the measured characteristic time constants (τ) of the adsorption kinetic measurements of the small-scale adsorbent sample and the full-scale GLX30 APHE. For the GL50 APHE, the matching between the small-scale and full-scale measurements was even much better with an average relative deviation of only 0.45%.

Although several studies addressed the influence of adsorbent bed thickness on the adsorption and desorption dynamics using small-scale adsorbent samples of loose grains or consolidated layers, no experimental study so far has treated the influence of the length of the refrigerant vapour diffusion path (MTCL) on the adsorption or desorption dynamics. This deems urgently required, if plate heat exchangers shall be designed and optimized for

---

Contents of this chapter have been reprinted from:
M. Mikhaeil, M. Gaderer and B. Dawoud."On the application of adsorber plate heat exchangers in thermally driven chillers; An experimental and analytical study". Applied Thermal Engineering 220 (2023), with permission from Elsevier.
Contributions of the author: Conceptualization, Methodology, Investigation, Formal analysis, Writing original draft.

Table 6.1 Specifications of the two investigated open-structured PHEs

Specification	**OTH APHE**	**GLX30**
HTF's inlet and outlet ports diameter (mm)	16	30
Thickness of one plate (mm)	0.3	0.35
gap between each two successive plate pairs (mm)	3	6
Width of the PHE (mm)	54	117
Volume of the adsorbent domain (L)	1.1	1.09
Volume of the HTF domain (L)	0.346	0.57
Mass of the heat exchanger (kg)	3.15	3.9

adsorption heat transformation processes. Recalling that the adsorption process is a combined heat and mass transfer process, the necessity for a comparative study on the influence of both HTCL and MTCL on the adsorption and desorption dynamics becomes obvious.

This chapter introduces, therefore, an experimental study on the effect of the adsorbent domain dimensions on the adsorption and desorption dynamics of representative samples of the adsorbent domains of two different, open-structured and asymmetric adsorber plate heat exchangers (APHE). Three dedicatedly designed test-frames will be used, which were constructed following the methodology introduced in Chapter 3 to allow the investigation of the influence of varying the HTCL at the same MTCL on the adsorption and desorption kinetics, and vice versa. The adsorption and desorption kinetic tests were performed according to the large-temperature-jump methodology in the constant volume kinetic setup (Chapter 2, Section 2.9.2). The tested samples are loose grains of silica gel Siogel®, Oker Chemie, Germany, in the range of 0.71 to 1.0 mm. The first test frame (TF1) corresponds to the OTH APHE depicted in Figure 6.1a (see Chapter 5), while the third (TF3) follows the design of the commercially available PHE depicted in Figure 6.1b (GLX30, AlfaLaval©, Sweden). TF2 has been prepared with the same heat transfer characteristic length (HTCL) of TF1 and the mass transfer characteristic length (MTCL) of TF3 as a variety of each PHE. The adsorption and desorption processes are conducted under different operating conditions of real adsorption chillers. Sensitivity analysis of the water uptake in the Siogel grains to the temperature and water vapour pressure is applied to interpret the effect of the HTCL and the MTCL on adsorption and desorption kinetics. Moreover, a simple mathematical model has been developed and introduced to estimate both *SCP* and *COP* associated with the application of the two investigated APHEs in a real adsorption chiller, out of the obtained experimental adsorption and desorption kinetic data. The obtained results have been compared with the values of an optimized extruded aluminium finned tube adsorber heat exchanger from the literature.

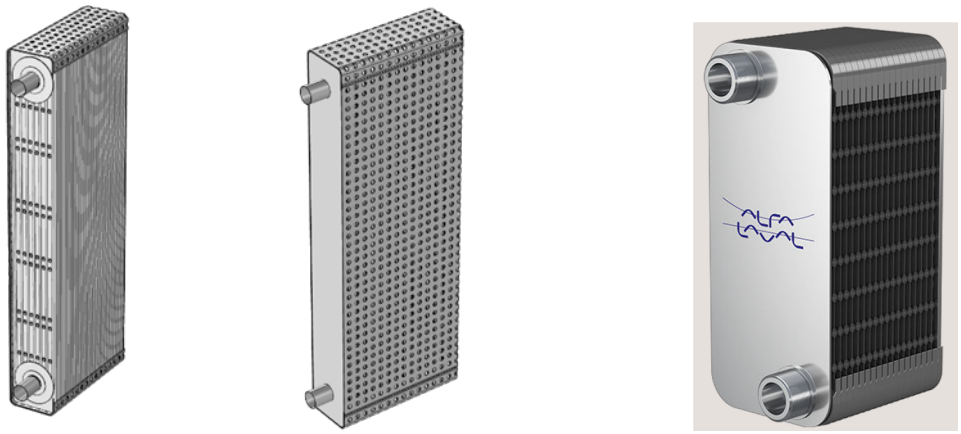

(a) OTH APHE (Chapter 5) (b) GLX30 PHE of Alfa Laval [151]

Fig. 6.1 OTH APHE and the GLX30 PHE

6.1 The representative test frames

The methodology applied in this chapter for preparing small-scale adsorbent samples able to predict the performance of the investigated APHEs is the one introduced and validated experimentally in Chapter 3. The methodology has been developed based on the following assumptions:

- The two investigated APHEs have a uniform temperature distribution over the surface of their plates. This means that both heat and mass transfer characteristics inside the adsorbent domain of the APHE are the dominant influencing parameters on its dynamic performance.
- The sudden change in surface temperature of the sample holder closely mimics the change in surface temperature of the investigated APHEs, upon conducting LTJ-adsorption or desorption process. Such assumption is based on previously findings discussed in Chapter 5, in which a very good agreement between the plates' surface temporal temperature of the OTH APHE and the surface of the sample holder of our V-LTJ kinetic setup, upon conducting sudden temperature decrease to initiate adsorption processes, has been demonstrated.
- The heat transfer in the adsorbent domain of the investigated APHEs is mainly in the normal direction to the surface of the APHE's plates.
- As each investigated APHE receives/delivers the refrigerant vapour mainly from two opposite side openings, it is assumed that the mass transfer (refrigerant vapour flow)

into the adsorbent domain occurs mainly in the normal direction to the two opposite side openings of the APHE.

- Indeed, the evaporator/condenser performance defines the temporal variation of the vapour pressure surrounding the APHE in its chamber upon the application in a real chiller, however, keeping the maximum pressure drop/jump of the vapour in the V-LTJ kinetic setup less than 2 mbar is low enough to replicate the pressure variation obtained upon applying an efficient evaporator/condenser in a real chiller (Chapter 3).

The dimensions and specifications of the representative adsorbent samples are determined based on the fact that each adsorbent subdomain of each APHE is surrounded by two HTF subdomains. Accordingly, a heat transfer symmetrical plan shall exist in the middle of the thickness of each adsorbent subdomain and will be in parallel to the plates' surface. It follows that the HTCL must equal to half of the gap between each two successive HTF-plate pairs. This means that the HTCLs of the OTH APHE (Chapter 5) and the GLX30 shall amount to 1.5 and 3.0 mm, respectively. Recalling that each of the investigated PHEs is open structured for a gas or vapour flow, the adsorbent domain is accessible from both sides by the refrigerant vapour. This implies that the mass transfer shall have a symmetrical plane in the middle width of each PHE. Accordingly, the MTCL of the newly introduced adsorber PHE and the GLX30 amounts to 27 and 58.5 mm, respectively.

By considering the prementioned assumptions and description, the adsorption and desorption dynamics of small-scale adsorbent samples with same HTCL and MTCL of the investigated APHEs can predict precisely their real dynamic performance.

Three test frames have been prepared for realizing three adsorbent samples of Siogel loose grains (0.71–1.0 mm) with HTCL and MTCL corresponding to the two investigated APHEs. The first test frame (TF1) corresponds to the OTH APHE, while the third (TF3) follows the design of a commercially available PHE (GLX30, AlfaLaval©, Sweden). TF2 has been prepared with the same HTCL of TF1 but with an identical MTCL of TF3 to offer the possibility of comparing the effect of two different MTCLs at one HTCL, and vice-versa, on the adsorption and desorption kinetics.

In order to guarantee quasi-isobaric ($\Delta P <$ 2 mbar) adsorption/ desorption processes in the Volumetric Large Temperature Jump (VLTJ) kinetic setup [93, 63], the dry sample mass of Siogel shall be limited to 320 mg. Accounting for the density of the investigated Siogel grains, the volume of each test frame shall equal to 526.5 mm^3. The width of each adsorbent domain inside the test frames ($TF1$, $TF2$ and $TF3$) is estimated, accordingly, to be 13, 6 and 3 mm, respectively.

All test frames have been made of Polyether Ether Ketone (PEEK) for its low thermal conductivity ($k = 0.25\ W.m^{-1}.K^{-1}$) and negligible outgassing characteristics. Each frame has a design enabling the refrigerant vapour (water vapour) to enter/leave the adsorbent sample placed inside the frame only from a small slot existing on one side of the frame. For preventing the heat transfer through the PEEK frame sides, the thickness of the frame (walls and ceiling) is determined to 5 mm. Figure 6.2 depicts the configuration of one of the three prepared test frames,namely $TF3$. The domain depicted in purple colour refers to the adsorbent sample. As shown in Figure 6.2, a piece of a stainless-steel sieve is mounted on the slot to prevent the grains from falling out. The stainless steel sieve is the same sieve applied for investigating the full-scale adsorber (Chapter 3) and it allows the vapour flow to enter the adsorbent sample from one side. At the downside of each frame, a stainless-steel substrate of 0.3 mm thickness is mounted to allow the heat transfer between the sample and the surface of the sample holder inside the measuring cell of the kinetic setup. The PEEK frames and the stainless steel substrates are sealed together by a special double-sided adhesive films of 0.5 mm thickness after inserting the adsorbent grains. For testing the adsorbent samples in their frames under the desired operating conditions, each sealed frame is fixed on the sample holder of the measuring cell using silicon-free thermal paste and the planned adsorption and desorption processes are performed. Figure 6.2 depicts the realized $TF3$ placed on the sample holder inside the measuring cell of the V-LTJ kinetic setup installed in the Laboratory of Sorption Processes (LSP) at OTH-Regensburg, Germany. More details on the test frames can be read in Chapters 5 and 3. Table 6.2 gives the dimensions of the adsorbent domains (depicted in purple colour in Figure 6.2) for the three prepared test frames.

The adsorption and desorption kinetic tests on the adsorbent samples inside the representative test frames $TF1$-$TF3$ have been carried out under the operating conditions of evaporator temperatures 5, 10 and 15°C, adsorber-end and condenser temperatures of 30 and 35°C, and a desorption-end temperature of 90 °C. The adsorption and desorption start temperatures, $T_{ads-start}$ and $T_{des-start}$, associated to the planned operating conditions are determined using the water-Siogel equilibrium model introduced in [17]. The thermostats feeding the oil circuit of the sample holder of the V-LTJ kinetic setup allow adjusting the sample holder temperature to the start temperature ($T_{ads-start}$ or $T_{des-start}$) and performing sudden temperature change to the sample holder surface until realizing the desired end temperature ($T_{ads-end}$ or $T_{des-end}$). The temporal change of sample holder temperature reaches 95 % of the final value in less than 2 min from the start of the cooling/heating process. The uncertainty analysis of the measured water uptake can be read in Appendix A. The uncertainty of the measured final differential water uptake $\sigma_{\Delta w_f}$ is reported in the results section (Tables 6.3 and 6.4).

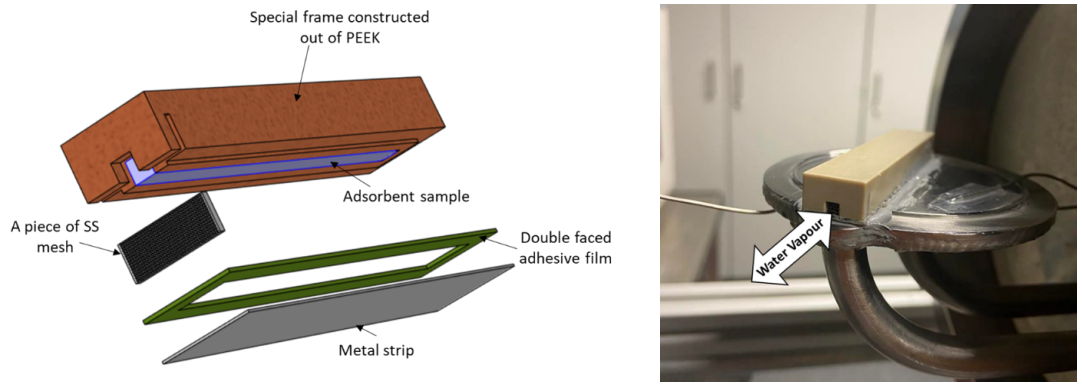

(a) (b)

Fig. 6.2 One of the three prepared test frame, namely $TF3$. (a) configuration of $TF3$ (b) realized $TF3$

Table 6.2 Fabricated test frames to investigate the adsorption/desorption kinetics of both open-structured PHE in a constant volume, large-temperature-jump kinetic setup (bold: MTCL, underlined: HTCL)

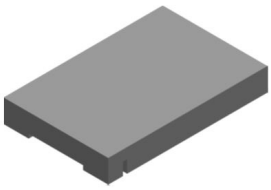	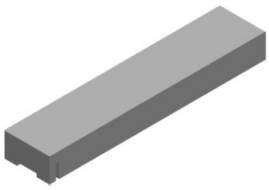	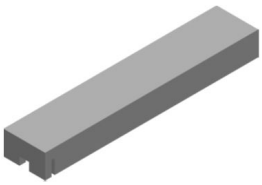
27 mm x <u>1.5 mm</u> x 13 mm	**58.5 mm** x <u>1.5 mm</u> x 6 mm	**58.5 mm** x <u>3 mm</u> x 3 mm
TF1	**TF2**	**TF3**

6.2 Evaluation of the adsorption and desorption kinetic performance

6.2.1 Exponential fitting

To define a criterion for evaluating the difference in the adsorption and desorption kinetics between the three adsorbent samples, all the experimental kinetic data have been fitted to the exponential form defined as

$$w(t) = w_o + \Delta w_f(1 - exp(-t/\tau)) \tag{6.1}$$

where $w(t)$ is the instantaneous water uptake inside the sample, w_o refers to the initial water uptake of the sample, Δw_f to the final or equilibrium differential water uptake ($w_f - w_o$), and τ is the characteristic time constant. To investigate the effect of the HTCL on the adsorption and desorption kinetics at different operating conditions, the ratio (r_{3-2}) between the characteristic time constants (τ) of the exponential forms of the test frames $TF3$ (τ_{TF3}) and $TF2$ (τ_{TF2}) is utilized, as $TF3$ and $TF2$ have equal MTCL and different HTCLs. For investigating the effect of the MTCL, r_{2-1} has been utilized, which is defined as the ratio between the time constants of the adsorbent samples inside $TF2$ (τ_{TF2}) and $TF1$ (τ_{TF1}), as they have the same HTCL but different MTCLs. Recalling that $TF1$ is representative to the OTH APHE in Chapter 5 and $TF3$ is representative to the GLX30 APHE investigated in Chapter 3, the ratio (r_{3-1}) is used to compare the dynamic performance of the same adsorbent (Siogel) inside the two APHEs.

6.2.2 Sensitivity analysis

Changing the HTCL and the MTCL affects the cooling/heating efficiency and the vapor pressure distribution in the adsorbent sample, respectively. In other words, the HTCL affects the average temperature of the adsorbent sample (T_{ads}) during the adsorption/desorption processes. Lower HTCL leads to lower T_{ads} during the adsorption and higher value during the desorption. On the other hand, higher MTCL leads to higher pressure drop in the adsorbent sample during the adsorption and, accordingly, lower average pressure in the adsorbent (P_{ads}). Contrary, in the desorption, higher MTCL leads to higher P_{ads}. Therefore, investigating the effect of changing T_{ads} and P_{ads} on the instantaneous water uptake (w) of the adsorbent samples shall be useful in the analysis of the data obtained from the experimental investigation of the HTCL and the MTCL effects on the adsorption and desorption dynamics.

To this aim, the sensitivities of w to T_{ads} and P_{ads}, $|\partial w/\partial T|$ and $|\partial w/\partial P|$, respectively, are driven from the equilibrium model developed in [17] for the Siogel/water pair, where w is given as a function in the adsorption potential.

$$w = w_o exp[-(\frac{F}{E})^{-1}], \tag{6.2}$$

Where w_o=0.38 g/g, E=220kJ/kg and n=1.1. F is the Dubinin-Polanyi potential or the adsorption potential, which can be calculated from the following equation.

$$F = -RT_{ads}.ln(P_{ads}/P_{sat}) \tag{6.3}$$

R is the gas constant of the water vapour ($0.461kJ/(kg.K)$). P_{sat} is the saturation pressure at T_{ads}, which can be given by Tetens equation [152].

$$P_{sat} = 6.1078exp(\frac{17.27T_{ads}}{T_{ads}+237.3}) \tag{6.4}$$

Where temperature T_{ads} is in (°C) and P_{sat} is in ($mbar$).

The sensitivity of w to T_{ads}, $|\partial w/\partial T|$=$-\frac{\partial w}{\partial T_{ads}}$ and the sensitivity of w to P_{ads}, $|\partial w/\partial P|$=$\frac{\partial w}{\partial P_{ads}}$ can be simplified to the following forms.

$$\frac{\partial w}{\partial T_{ads}} = \frac{\partial w}{\partial F}.\frac{\partial F}{\partial T_{ads}} \tag{6.5}$$

$$\frac{\partial w}{\partial P_{ads}} = \frac{\partial w}{\partial F}.\frac{\partial F}{\partial P_{ads}} \tag{6.6}$$

From the partial derivation of Equation 6.3 the followings have been obtained

$$\frac{\partial F}{\partial T_{ads}} = -R.ln(\frac{P_{ads}}{P_{sat}}) + R.\frac{T_{ads}}{P_{sat}}.\frac{\partial P_{sat}}{\partial T_{ads}} \tag{6.7}$$

$\frac{\partial P_{sat}}{\partial T_{ads}}$ shall be obtained from the derivation of Equation 6.4.

$$\frac{\partial P_{sat}}{\partial T_{ads}} = P_{sat}.[\frac{17.27}{T_{ads}+237.3} - \frac{17.27T_{ads}}{(T_{ads}+237.3)^2}] \tag{6.8}$$

$\frac{\partial F}{\partial P_{ads}}$ is also obtainable from the partial derivation of Equation 6.3

$$\frac{\partial F}{\partial P_{ads}} = -\frac{RT_{ads}}{P_{ads}} \tag{6.9}$$

$\frac{\partial w}{\partial F}$, which appears in Equations 6.5 and 6.6 can be obtained from the derivation of Equation 6.2

$$\frac{\partial w}{\partial F} = w.\frac{-n}{E^n}.F^{(n-1)} \tag{6.10}$$

By substituting Equations 6.7, 6.9 and 6.10 into Equations 6.5 and 6.6 the following relations can be realized

$$\frac{\partial w}{\partial T_{ads}} = w.\frac{-n.R}{E^n}.F^{(n-1)}[-ln(\frac{P_{ads}}{P_{sat}}) + \frac{T_{ads}}{P_{sat}}.\frac{\partial P_{sat}}{\partial T_{ads}}] \tag{6.11}$$

$$\frac{\partial w}{\partial P_{ads}} = w.\frac{-n.R}{E^n}.F^{(n-1)}[-\frac{T_{ads}}{P_{ads}}] \tag{6.12}$$

The variables F, w and $\frac{\partial P_{sat}}{\partial T_{ads}}$ shall be calculated from Equations 6.3, 6.2 and 6.8, respectively.

The results of the sensitivity analysis will be presented and discussed in the results section.

6.2.3 Estimation of the SCP and the COP

The obtained adsorption and desorption kinetic data of the adsorbent sample in each representative test frame have been utilized to estimate the specific cooling power (*SCP*) of an adsorption chiller employing the related PHE. Since the SCP of an adsorption chiller depends mainly on the differential water loading and the durations of both adsorption and desorption phases, the *SCP* associated with the application of the two investigated APHEs in a real chiller was evaluated at different adsorption durations (t_{ads} varies from 10 to 4800 seconds) and desorption durations (t_{des} varies from 10 to 1800 seconds). Indeed, the application of arbitrary (equal or different) adsorption and desorption durations in a real adsorption chiller shall result in a steady-state operation with equal differential water uptakes in the adsorption and desorption phases [42, 70, 127]. Based on that, an analytical algorithm was developed and implemented in Matlab© to determine the initial and final water uptake of the adsorption and desorption stages when different adsorption and desorption durations are applied, based on the experimentally measured and correlated adsorption and desorption kinetic data. The analytical model is described in the following paragraphs.

A typical periodical adsorption chiller cycle consists of four successive processes, namely preheating, desorption, precooling and adsorption processes. Figure 6.3 presents, in dashed lines, an ideal adsorptive cycle of an adsorption chiller on a Clapeyron diagram with quite long adsorption and desorption durations (t_{ads} and t_{des}) sufficient to reach thermal equilibrium between the adsorbent and the HTF flowing through the adsorber heat exchanger. The cycle presented in bold lines stays for optimized adsorption t_{ads} and desorption t_{des} durations to realize the maximum cycle's *SCP*. The preheating and precooling processes are assumed isosteric (w_1=w_2) and (w_3=w_4). The preheating and precooling phases taking place in a real adsorption chiller take quite short durations compared with the durations of the adsorption and desorption phases and depend mainly on the management of the adsorption machine. The algorithm presented in this work assumes 10 s for each phase according to [153], i.e., $t_{precool.}$+$t_{preheat.}$=20 s.

Figure 6.4 presents a pair of exponentially fitted water uptake kinetic curves for a given set of operating conditions (i.e. T_{ev}/T_{cond}/T_{des}) according to Equation 6.1. The blue curves represent adsorption and the red curves represent desorption kinetics. The principle of the developed algorithm is also illustrated in Figure 6.4. In the zeroth iteration, the algorithm sets the initial point on the adsorption curve (w_4=w_{min}) as the starting uptake value for the adsorption phase. The exponential fit form of the adsorption kinetic curve is used to calculate

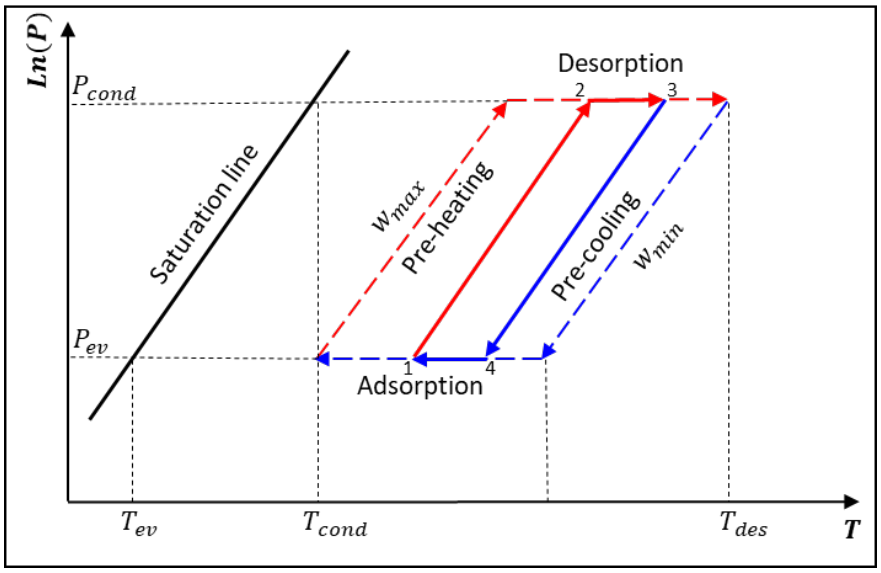

Fig. 6.3 Ideal adsorptive cycles of an adsorption chiller/heat pump, the cycle presented in dashed lines has infinite adsorption and desorption durations (t_{ads} and t_{des}) sufficient to reach thermal equilibrium with the HTF flowing through the adsorber heat exchanger, while the cycle presented in bold lines has optimized t_{ads} and t_{des} to get maximum cycle's *SCP*.

w_1 at the end of the adsorption phase, means at t_1=t_4+t_{ads}. The algorithm then equates the initial w of the desorption stage (w_2) with the calculated final w of the adsorption stage (w_1) and estimates the time (t_2). Based on the internal value of t_{des} the time t_3=t_2+t_{des} is calculated. The final uptake w_3 of the desorption stage is then estimated using the exponential fit form of the desorption kinetic curve at the corresponding operating condition. The algorithm compares now between w_4 and w_3. If the difference between them is smaller than 0.0001, the obtained initial and final uptake values are considered final for calculating the differential adsorption/desorption water uptake (Δw=w_1-w_4=w_2-w_3). Otherwise, the algorithm equates w_4 to the last estimated uptake value of w_3 and performs a new iteration. The final obtained Δw is applied to calculate the specific cooling power *SCP*. Figure 6.5 depicts the flow chart of the developed algorithm.

The implementation of the algorithm for each adsorbent sample at every set of operating conditions results in the values of the differential adsorption/desorption water uptake (Δw), which shall be applied in the following equation to calculate the *SCP* of an intermittent adsorption chiller having only one adsorber-desorber.

$$SCP = \frac{\Delta w}{t_{ads} + t_{des} + t_{precool.} + t_{preheat.}} . h_{fg}(T_{ev}) \tag{6.13}$$

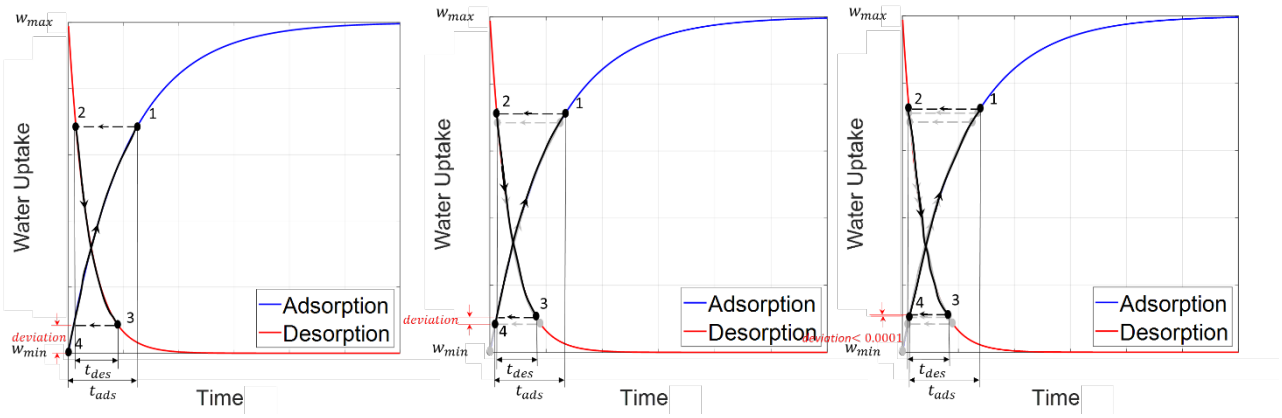

(a) (b) (c)

Fig. 6.4 Iterative principle of the developed algorithm; (a) zero-iteration, (b) first iteration, and (c) last iteration.

$h_{fg}(T_{ev})$ is the latent heat of the water evaporation at the investigated evaporator temperature (T_{ev}).

The mass-specific (per kg of adsorbent) heat added to the adsorber heat exchanger (q_{in}) during the preheating and desorption phases can be calculated from:

$$q_{in} = \Delta w.\Delta h_{ads} + q_{s,AdHEx} \tag{6.14}$$

Herein Δh_{ads} is the isosteric heat of water adsorption in Siogel (50.5 kJ/mol [17]) . In addition, $q_{s,AdHEx}$ stays for the specific (per kg adsorbent) sensible heat added to adsorber heat exchanger components (metal and HTF), which can be evaluated from the following equation:

$$q_{s,AdHEx} = \frac{1}{m_{ads}}(m_{metal}.c_{metal} + m_{HTF}.c_{HTF}).(T_{des} - T_{ads}) \tag{6.15}$$

m_{ads} is the mass of the Siogel filling the investigated AdHEx. The GLX30 APHE has been filled experimentally with 842 g of Siogel as reported in Chapter 3. The APHE introduced in Chapter 5 can be filled with the same amount, as the volume of its adsorbent domain is equal to the one of the GLX30 APHE.

The *COP* of the intermittent adsorption chiller can be calculated as follows:

$$COP = \frac{SCP}{q_{in}} \tag{6.16}$$

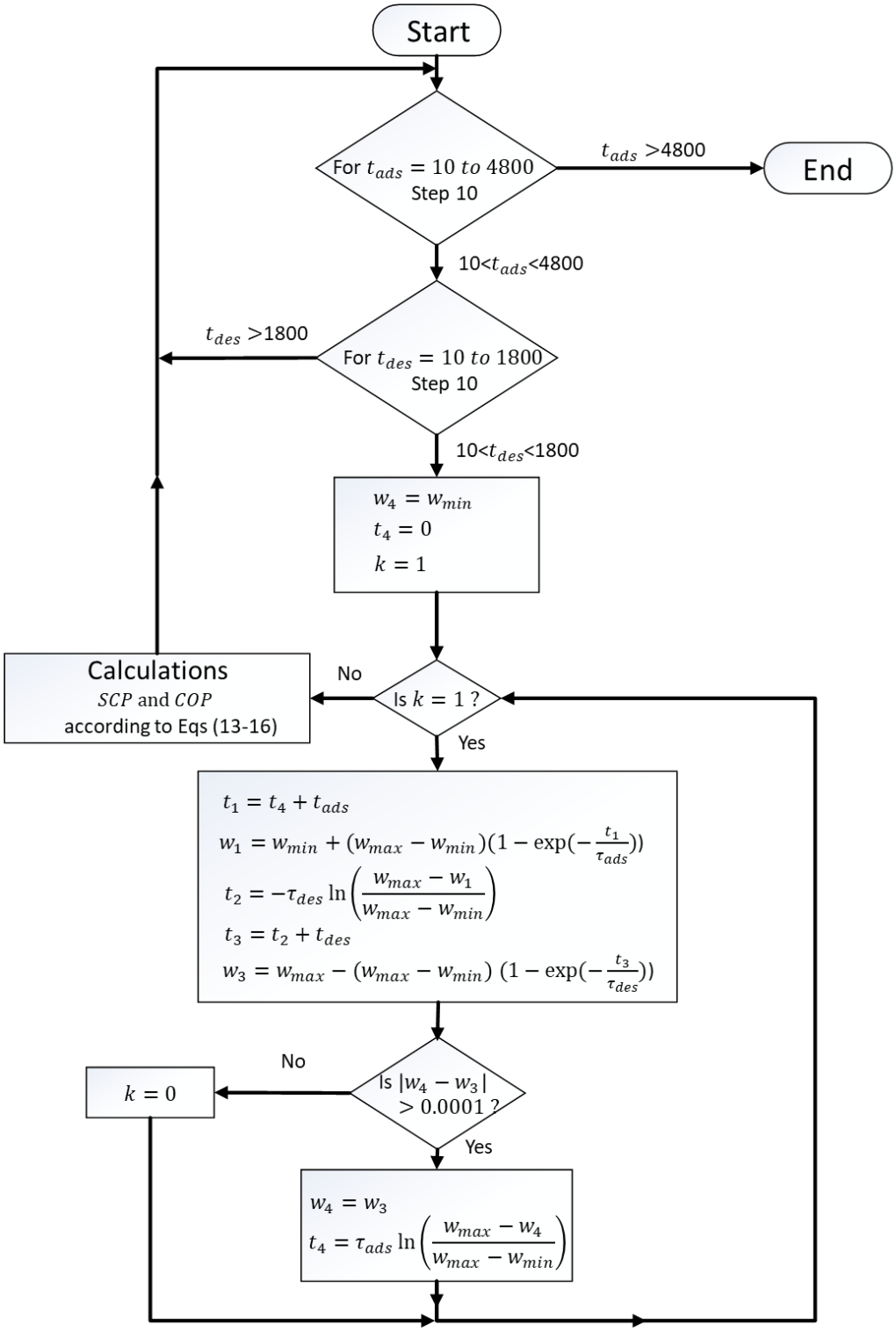

Fig. 6.5 Flow chart of the algorithm developed to calculate the adsorption system performance at different pairs of t_{ads} and t_{des}

6.3 Results and discussion

In this section, the original kinetic measurements and their correlations to Equation 6.1 will be presented and then utilized to investigate the effects of the HTCL and the MTCL on the adsorption and desorption kinetics. In addition, the cycle *SCPs* and the *COPs* obtained upon applying both plate heat exchangers illustrated in Figure 6.1 to act as an adsorber/desorber for an adsorption chiller will be estimated and presented against varying adsorption and desorption durations for all investigated operating conditions. Finally, the obtained values for the *SCP* and the related *COP* will be compared to the values of an optimized extruded aluminium finned tube adsorber heat exchanger from the literature.

6.3.1 Adsorption and desorption kinetic measurements

Figures 6.6 and 6.7 depict the measured and the exponential fitting curves according to Equation 6.1 of the water uptake obtained during the adsorption and desorption processes, respectively, which were conducted on loose Siogel grains inside the three test frames TF1-TF3 illustrated in Table 6.2 at all applied operating conditions.

The detail results of the measuring campaign and the values of the time constants (τ) and the coefficient of determination (R^2) are presented in Tables 6.3 and 6.4 for the adsorption and desorption processes, respectively. The lowest R^2 value for the adsorption processes amounts to 0.9890 and is obtained for TF3 at operating conditions of 15/30/90°C, while the lowest R^2 value for the desorption processes is obtained for TF2 at operating conditions of 5/30/90°C and amounts to 0.9494. It can be concluded that, all adsorption and desorption kinetic curves for the Siogel samples inside the three test frames do follow the exponential relationship described in Equation 6.1.

6.3.2 Effect of the HTCL; Comparison between TF2 and TF3

Increasing the thickness of the adsorbent domain (HTCL) from 1.5 to 3.0 mm (TF2 vs. TF3) while keeping the MTCL equal to 58.5 mm corresponding to the GLX30 PHE, results in a slight change in the adsorption kinetic, i.e. limited change in the value of τ by almost zero % at the operating condition of 15/35/90 °C and 10/30/90 °C to a maximum percentage of 19% at operating conditions of 10/35/90°C. This implies that the effect of doubling the HTCL of the adsorbent domain on the adsorption dynamics is quite low as long as the MTCL is in the order of 58.5 mm. In other words, at such high MTCL, the influence of the HTCL, within the investigated range in this chapter, is less pronounced on the adsorption characteristic time τ.

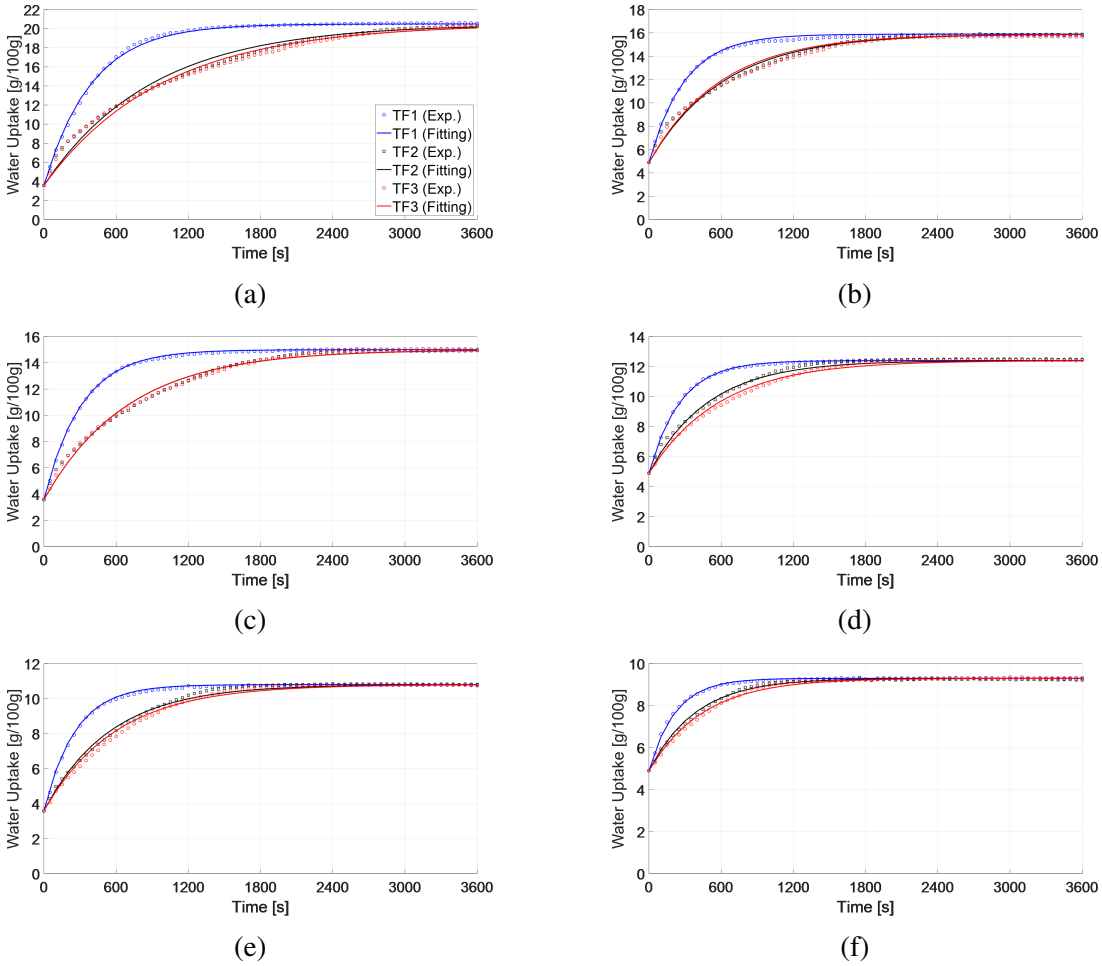

Fig. 6.6 Adsorption kinetic curves for loose grains of Siogel inside the three test frames depicted in Table 2 at evaporator, condenser/adsorption-end and desorption temperatures of a) 15/30/90 °C , b) 15/35/90°C, c) 10/30/90°C, d)10/35/90°C, e) 5/30/90°C and f) 5/35/90°C.

It can be further observed that, the effect of doubling the HTCL between TF2 and TF3 on changing the adsorption characteristic time becomes slightly pronounced at severer operating conditions, at which the differential water uptake becomes smaller (low evaporator temperatures (10 and 5°C) and/or higher condenser and adsrober-end temperatures (35°C)).

Contrary to that, doubling the HTCL (TF2 vs. TF3) has a pronounced influence on the desorption kinetic. The desorption characteristic times are significantly higher for the thicker adsorbent sample (TF3) compared to TF2. Strictly speaking, doubling the HTCL results in changing the value of the desorption characteristic time by 24% at operating condition of 10/30/90°C to a maximum percentage of 52% at operating conditions of 5/30/90°C. This implies that the influence of changing the HTCL is more pronounced on the desorption

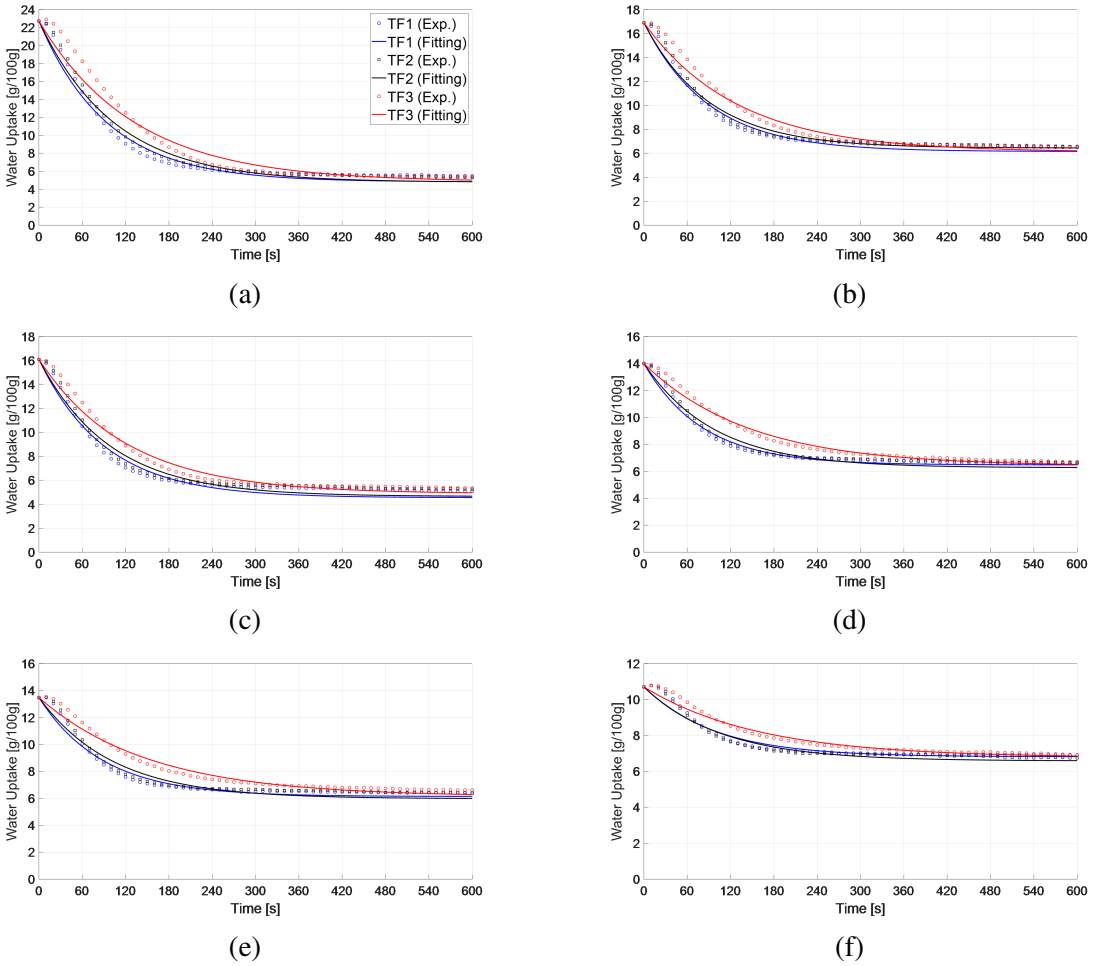

Fig. 6.7 Desorption kinetic curves for loose grains of Siogel inside the three test frames depicted in Table 2 at evaporator, condenser/adsorption-end and desorption temperatures of a) 15/30/90 °C , b) 15/35/90°C, c) 10/30/90°C, d)10/35/90°C, e) 5/30/90°C and f) 5/35/90°C.

kinetics than on the adsorption kinetics inside adsorber plate heat exchangers within the tested range of design conditions (Tables 6.3 and 6.4).

6.3.3 Effect of the MTCL; Comparison between TF1 and TF2

Indeed, both TF1 and TF2 have the same HTCL (1.5 mm) and, accordingly, the same S/m ratio. According to the existing experiences in the literature [99, 96, 100], they should have the same kinetic performance. The obtained results in Figure 6.6 puts in evidence that the MTCL does have a major role on the adsorption kinetics for the same HTCL or S/m ratio. Strictly speaking, the adsorption characteristic times of the adsorbent sample inside TF2 are much higher than those of the sample inside TF1 (178 to 228 % higher value of the

Table 6.3 Adsorption start temperature ($T_{ads-start}$), initial water uptake (w_o), final differential water uptake (Δw_f), measurement uncertainty of Δw_f ($\sigma_{\Delta w_f}$), time constant of the exponential fitting (τ) and its (R^2), ratios of τ (r_{2-1},r_{3-2} and r_{3-1}) at each operating condition for the three tested frames

Operating Condition $T_{ev}/T_{cond}/T_{des}$[°C]	$T_{ads-start}$ °C	w_o g/100g	Δw_f g/100g	$\sigma_{\Delta w_f}$ g/100g	TF #	τ s	R^2	$r_{2-1} = \frac{\tau_{TF2}}{\tau_{TF1}}$	$r_{3-2} = \frac{\tau_{TF3}}{\tau_{TF2}}$	$r_{3-1} = \frac{\tau_{TF3}}{\tau_{TF1}}$
15/30/90	70.5	3.6	16.9	±0.45	1	394.6	0.9984	2.28	1.09	2.47
					2	898.3	0.9894			
					3	975.6	0.9890			
15/35/90	62.4	4.9	11.0	±0.46	1	292	0.9982	2.11	0.96	2.03
					2	614.7	0.9905			
					3	591.3	0.9894			
10/30/90	66.1	3.6	11.4	±0.33	1	310.5	0.9968	2.25	1.00	2.25
					2	698.5	0.9936			
					3	700	0.9923			
10/35/90	58.7	4.9	7.5	±0.34	1	257.2	0.9957	1.91	1.19	2.28
					2	492.1	0.9945			
					3	586.1	0.9913			
5/30/90	58.5	3.6	7.2	±0.23	1	258.7	0.9927	2.12	1.09	2.30
					2	548.8	0.9931			
					3	595.7	0.9906			
5/35/90	53.2	4.9	4.4	±0.24	1	218	0.9960	1.78	1.16	2.06
					2	387.3	0.9944			
					3	449.3	0.9937			

adsorption characteristic time of the sample inside TF2 if compared to sample inside TF1). In addition, the ratio of τ (r_{2-1} in Table 6.3) decreases if the overall mass transfer (the differential water uptake) is reduced (at the operating conditions of 10/35/90 and 5/35/90 °C). Reducing the evaporator temperature from 15 down to 10 and 5 °C at 30 °C adsorption-end and condenser temperature results in reducing the differential water uptake from 16.5 down to 11.4 and 7.2 g/100g, which is associated with decreasing r_{2-1} from 2.28 down to 2.25 and 2.12, respectively. The same is valid and more pronounced at the more severe operating condition of 35°C for the adsorption-end and condenser temperatures.

In contrast, by excluding the effect of HTCL and investigating only the effect of the change in the MTCL on the desorption kinetic, from 27 mm (TF1) to 58.5 mm (TF2), a smaller effect of the MTCL on the desorption kinetics has been found compared to the

Table 6.4 Desorption start temperature ($T_{des-start}$), initial water uptake (w_o), final differential water uptake (Δw_f), measurement uncertainty of Δw_f ($\sigma_{\Delta w_f}$), time constant of the exponential fitting (τ) and its (R^2), ratios of τ (r_{2-1},r_{3-2} and r_{3-1}) at each operating condition for the three tested frames

Operating Condition $T_{ev}/T_{cond}/T_{des}$,°C	$T_{des-start}$ °C	w_o g/100g	Δw_f g/100g	$\sigma_{\Delta w_f}$ g/100g	TF #	τ s	R^2	$r_{2-1} = \frac{\tau_{TF2}}{\tau_{TF1}}$	$r_{3-2} = \frac{\tau_{TF3}}{\tau_{TF2}}$	$r_{3-1} = \frac{\tau_{TF3}}{\tau_{TF1}}$
15/30/90	44.5	22.7	-17.9	±1.27	1	94.3	0.9735	1.11	1.27	1.41
					2	104.5	0.9826			
					3	132.9	0.9756			
15/35/90	55.1	16.9	-10.5	±1.63	1	88.9	0.9720	1.01	1.44	1.46
					2	90.0	0.9805			
					3	129.7	0.9787			
10/30/90	50.5	16.1	-11.4	±1.24	1	91.9	0.9531	1.08	1.24	1.34
					2	98.8	0.9550			
					3	122.9	0.9752			
10/35/90	58.8	14.0	-7.6	±1.62	1	81.1	0.9834	1.20	1.49	1.79
					2	97.4	0.9591			
					3	145.5	0.9813			
5/30/90	57.1	13.5	-7.4	±1.23	1	87.5	0.9497	1.18	1.52	1.80
					2	103.0	0.9494			
					3	156.4	0.9729			
5/35/90	68.4	10.7	-4.0	±1.61	1	98.6	0.9605	1.09	1.48	1.61
					2	107.7	0.9577			
					3	158.8	0.9774			

effect of the HTCL. The ratio r_{2-1} in Table 6.4, which reflects the effect of the MTCL on desorption kinetics, implies an increase in the desorption τ-value ranging between 1%, obtained at operating condition of 15/35/90°C and 20%, at operating condition of 10/35/90°C, upon changing the MTCL from 27 mm to 58.5 mm.

6.3.4 Effect of both HTCL and MTCL; Comparison between TF1 and TF3

The comparison between the adsorption and the desorption kinetics of the same adsorbent inside TF1 and TF3 (the ratio r_{3-1} of their τ in Tables 6.3 and 6.4, respectively), reveals that the performance of commercially available heat exchanger (GLX30), as an adsorber heat

exchanger, is quite poor if compared with dedicatedly designed heat exchanger (i.e OTH APHE introduced in Chapter 5). It can be concluded, therefore, that the MTCL and the mass transfer resistance inside the adsorbent domain must be taken into account together with the HTCL or the S/m ratio, for designing effective adsorber plate heat exchangers.

6.3.5 Interpretation of the experimental results through the sensitivity analysis

Adsorption results

Figure 6.8 shows the variation of $|\partial w/\partial T|$ and $|\partial w/\partial P|$ against P_{ads} and T_{ads} on their ranges during the investigated adsorption processes. The maximum P_{ads} in the conducted experiments is $\approx$ 17 mbar and T_{ads} ranges from a minimum value of 30°C, to maximum value of $\approx$ 70°C . As shown in the figure, at each value of T_{ads}, the sensitivity of w to T_{ads} , i.e. $|\partial w/\partial T|$, tends to decrease significantly with the reduction in P_{ads}. This means that for a higher MTCL and due to the high inter-particle mass transfer resistance, a significant reduction in P_{ads} is expected and, accordingly, a significant reduction in the sensitivity of w to T_{ads}. In other words, improving the heat transfer in this case will not improve significantly the adsorption dynamics. It can be concluded that decreasing the HTCL with keeping the MTCL high will not lead to a significant improvement in the adsorption dynamics due to the explained slight dependency of w on T_{ads}.

On the other side, as Figure 6.8 depicts, the sensitivity of w to P_{ads} , i.e. $|\partial w/\partial P|$, increases significantly with decreasing P_{ads} within the adsorption operation range. This implies that, every measure to enhance the mass transfer shall improve the adsorption dynamics. The above discussion interprets clearly, why TF2 and TF3, which have a high MTCL, demonstrate similar low adsorption dynamics despite the inequality in the HTCL. This explains also, why TF1, which has the least MTCL, demonstrates quite better adsorption dynamics than TF2 with both having the same HTCL.

Desorption results

Figure 6.9 presents the sensitivity of w to both T_{ads} and P_{ads} within their ranges of operation during the investigated desorption processes. The minimum P_{ads} in the conducted desorption experiments is $\approx$ 42 mbar and T_{ads} ranges from a minimum value of $\approx$ 45 °C, to a maximum of 90 °C. As shown in the figure, at each value of T_{ads}, the sensitivity of w to T_{ads} i.e., $|\partial w/\partial T|$, tends to increase with the increase of Pads, which is expected during the desorption processes of the test frames with the higher MTCL i.e., TF2 and TF3.

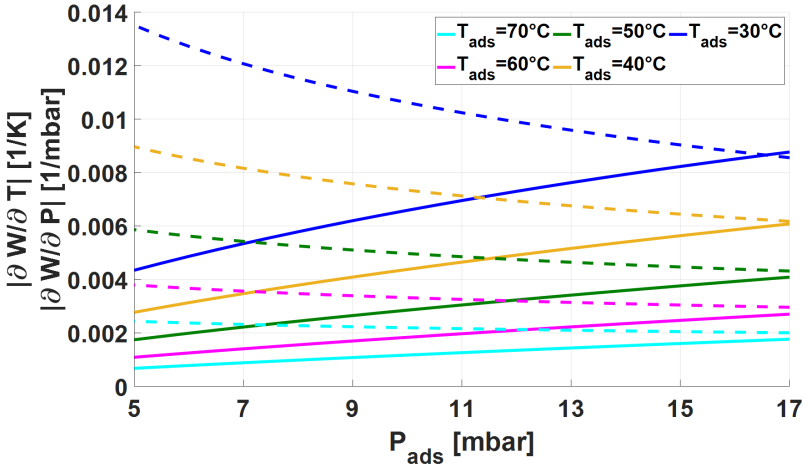

Fig. 6.8 Sensitivity of w to T_{ads}, i.e. $|\partial w/\partial T|$ (solid lines) and sensitivity of w to P_{ads} , i.e. $|\partial w/\partial P|$ (dashed lines) in the adsorption processes' ranges

The variation of the sensitivity of w to P_{ads}, i.e. $|\partial w/\partial P|$ against P_{ads}, especially at higher adsorbent temperatures ($T_{ads} > 70°C$) interprets quite clearly why the desorption dynamic is not affected by the MTCL (see Section 6.3.3). As depicted in the figure, $|\partial w/\partial P|$ has the lowest and almost invariant values for all values of Pads illustrated in the figure. The invariance of $|\partial w/\partial P|$ against P_{ads}, is highly pronounced at the higher values of T_{ads}. This discussion elucidates clearly, why TF1 and TF2, which have the same HTCL and different MTCL, demonstrate quite similar desorption dynamics.

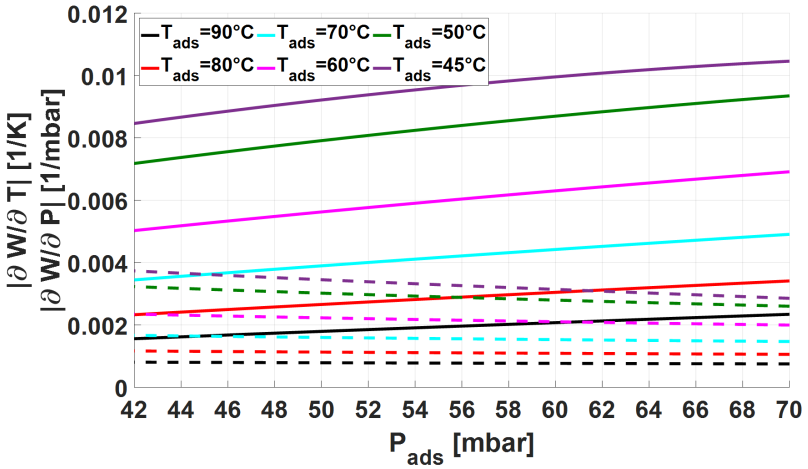

Fig. 6.9 Sensitivity of w to T_{ads}, i.e. $|\partial w/\partial T|$ (solid lines) and sensitivity of w to P_{ads} , i.e. $|\partial w/\partial P|$ (dashed lines) in the desorption processes' ranges

6.3.6 Impact of applying the investigated APHEs in an adsorption chiller

The described analytical algorithm developed to predict the performance of a real adsorption chiller comprising the two investigated APHEs, has been implemented in a MATLAB code with the application of T_{ev} equal to 5, 10 and 15° C against condenser temperature (T_{cond}) of 30 and 35° C. Figure 6.10 depicts the impact of applying the OTH APHE (Chapter 5) on the *SCP* and the *COP* of a single-bed adsorption chiller at all applied operating conditions. The change step on the *SCP* on each chart equals 50 $W.kg^{-1}$. The value of the *SCP*-contours increases towards the lower-left corner of each chart. The step between the *COP* dashed lines on the charts amounts to 0.1. The value of the *COP* contours increases towards the upper-right corner of each chart. In addition, the maximum possible *COP* for each boundary condition at the highest possible adsorption and desorption times is also plotted in each chart.

The illustrated results show that the application of the OTH APHE in a single-bed adsorption chiller with loose grains of Siogel as an adsorbent can produce a specific cooling power (*SCP*) up to 453.6 $W.kg^{-1}$, and a *COP* up to 0.614. The results indicate that the *SCP* as well as the *COP* increase with increasing the value of T_{ev} and decreasing T_{cond}, which can be attributed to the increase in the differential water uptake and the increased dynamics of both adsorption and desorption phases. For all applied operating conditions, short adsorption and desorption durations, t_{ads}<200s and t_{des}<100s, results in the highest obtainable *SCP* (SCP_{max}). In contrary, applying long adsorption and desorption durations leads to highest possible *COP*, which is directly proportional to the differential water uptake, which approaches its maximum or equilibrium values as the time does excessively increase.

Figure 6.11 compares between the three investigated APHEs, represented by the test frames (TF1-TF3), at the operating condition of 15/30/90 °C. The results show the clearly higher performance of the OTH APHE represented by TF1 over the APHEs represented by TF2 and TF3, in terms of both *SCP* and *COP*. The higher *SCP* for TF1 can be attributed mainly, based on the discussion in Sections 6.3.2, 6.3.4 and 6.3.3, to its short MTCL compared to the GLX30-APHE. On the other hand, the better *COP* can be referred to the extremely reduced volume of the HTF and metal domains of the OTH APHE compared to the GLX30 APHE, see Table 6.1. To keep the *SCP* of TF1 equal or higher than 90% of the SCP_{max}, both t_{ads} and t_{des} should be kept in the range, 60 to 470 s for t_{ads} and 30 to 230 s for t_{des}. To achieve a *COP* of 0.5 under the operating condition 15/30/90 °C, the OTH APHE can realize a *SCP* of 423.3 $W.kg^{-1}$ while the GLX30 APHE a *SCP* of 162.1 $W.kg^{-1}$.

Figure 6.12 presents a comparison between the three test frames in terms of the maximum obtainable *SCP* (Figure 6.12a) and the associated *COPs* (Figure 6.12b) under each operating condition. The TF1 representing the OTH APHE [82] demonstrates the highest SCP_{max} and

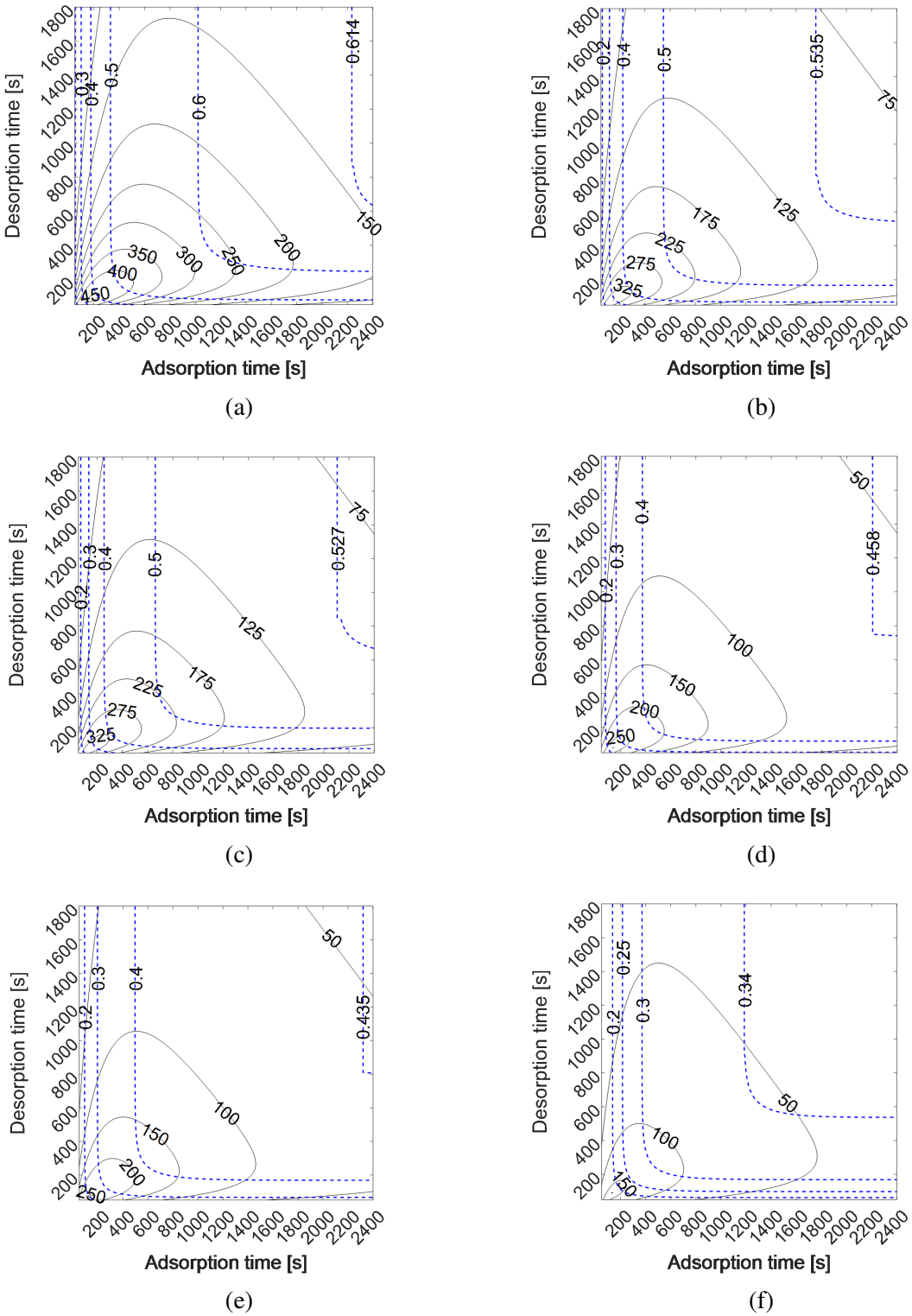

Fig. 6.10 The *SCP* (black continuous lines) and *COP* (blue dashed lines) calculated for the test frame representative to OTH APHE introduced in Chapter 5, a) 15/30/90 °C , b) 15/35/90°C, c) 10/30/90°C, d)10/35/90°C, e) 5/30/90°C and f) 5/35/90°C.

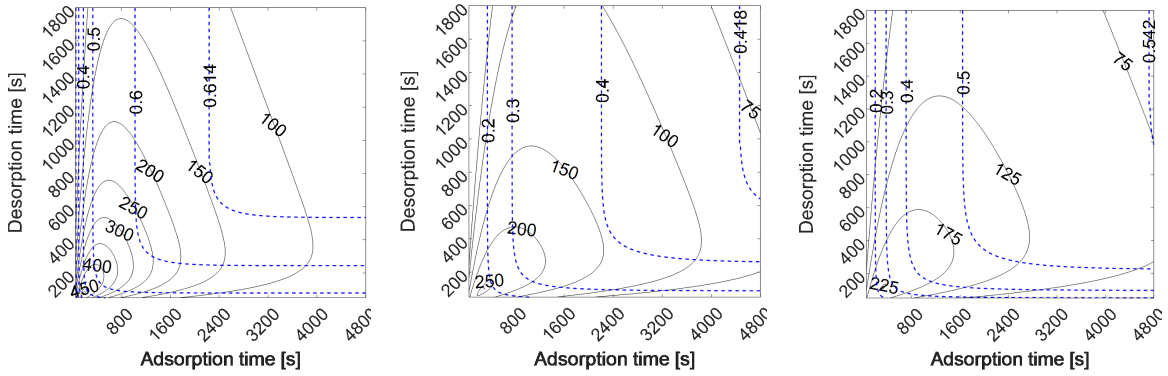

Fig. 6.11 The *SCP* (black continuous lines) and *COP* (blue dashed lines) calculated at T_{ev}=15°C, T_{cond}= 30°C and T_{des}=90°C for the three test frames (TF1-TF3), (a) TF1, (b) TF2 and (c) TF3

COP at all applied operating conditions (the blue bars). The SCP_{max} of TF1 ranges between 157.6 $W.kg^{-1}$, obtained at 5/35/90°C, t_{ads}=140 s and t_{des} =90 s, and 453.6 $W.kg^{-1}$ obtained at 15/30/90 °C and t_{ads} / t_{des} of 190 / 90 s, respectively. The SCP_{max} of TF3, which represents the GLX30 APHE, ranges between 87.8 $W.kg^{-1}$, at 5/35/90°C, t_{ads}=210 s and t_{des}=120 s, and 225.4 $W.kg^{-1}$, at 15/30/90 °C, t_{ads}= 310 s and t_{des} = 110 s. It can be concluded that changing the MTCL from 58.5 to 27 mm while keeping the HTCL equal to 1.5 mm (i.e. TF1 vs TF2) leads to improvement in the SCP_{max} by 44.2% (at 5/35/90°C) up to 78.9% (at 15/30/90°C). On the other hand, decreasing the HTCL from 3 to 1.5 mm while keeping the MTCL=58.5 mm (i.e. TF2 vs TF3) leads to a slight improvement in the SCP_{max} by 6.0% (at 10/30/90°C) to 26.1% (at 10/35/90°C).

6.3.7 Comparison with a finned tube adsorber heat exchanger

To evaluate the performance of the two investigated APHEs compared to the performance of a finned tube adsorber heat exchanger investigated under similar operating conditions and with silica gel/water as a working pair, the adsorber heat exchanger presented in [26] and experimentally investigated in [153] using a small representative piece filled with loose grains of silica gel 123 in size range of 0.9 mm and with the application of water as a refrigerant has been selected. In their work, Lanzerath et al. [26] introduced an extruded aluminum, tube heat exchanger designed dedicatedly for the application as an adsorber/desorber in thermally driven adsorption machines. The tubes of this adsorber heat exchanger have a special finned structure on both internal and external surfaces to enhance the overall heat transfer. Table 6.5 gives some data of this adsorber heat exchanger according to [70, 154, 139]. In [153], the

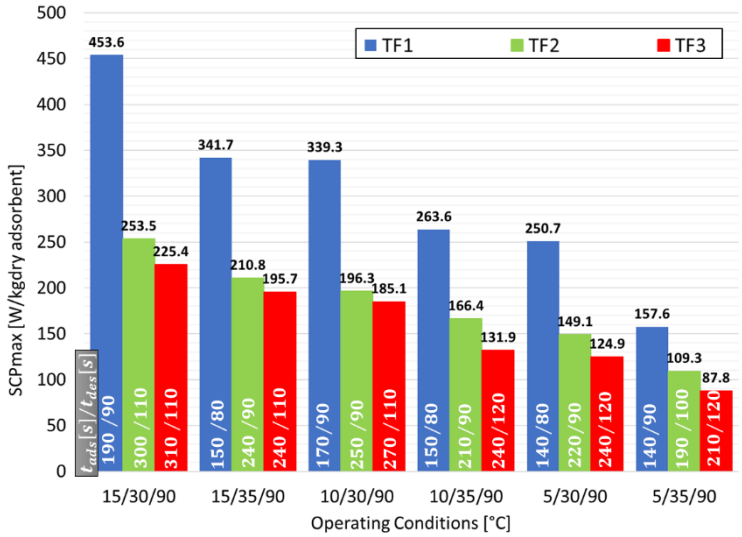

(a)

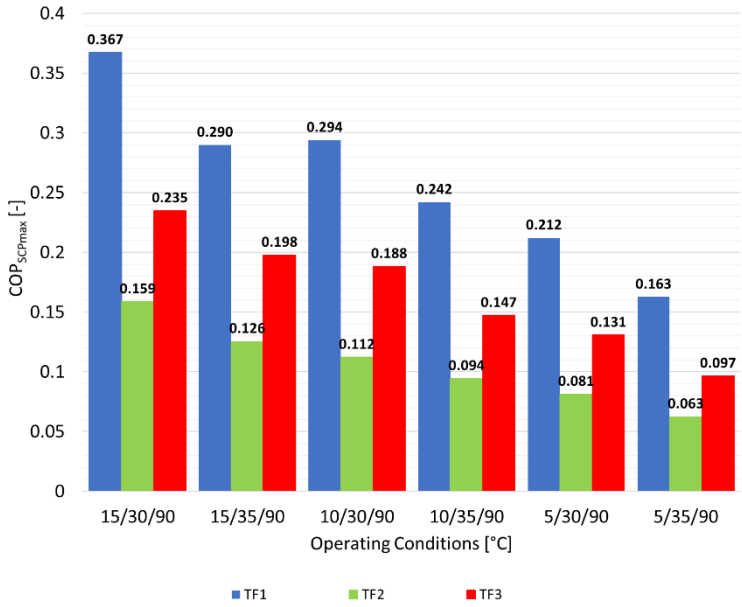

(b)

Fig. 6.12 Cycle's maximum specific cooling power (SCP_{max}) and the associated COP obtainable from the three investigated test frames at each operating condition, (a) SCP_{max} $W/kg_{adsorbent}$, (b)$COP_{SCP_{max}}$

adsorption and desorption kinetics of a small piece, representative for this adsorber heat exchanger have been investigated in a gravimetric large temperature jump (G-LTJ) kinetic setup [96]. Only the temporal water uptake variation of the adsorption and desorption processes conducted at 10/35/90°C are presented in [153]. To compare between the two APHEs investigated in this work and the adsorber heat exchanger of [26],the adsorption and desorption kinetic data presented in [153] have been fitted into the exponential form of Eq. 6.1. Table 6.6 compares between the two investigated APHEs and the adsorber heat exchanger of [26] in terms of τ obtained for the adsorption and desorption processes conducted at 10/35/90 °C. Indeed, the finned tube adsorber heat exchanger [26] demonstrates a bit higher adsorption kinetics (τ=243.5 s), if compared with the OTH APHE (τ=257.7 s). It is also evident that, the OTH APHE demonstrates the highest desorption kinetics (τ=81.1 s) among all three heat exchangers.

In addition, the comparison between the two investigated APHEs and the finned tube adsorber heat exchanger of [26] has been made in terms of the maximum specific cooling power (SCP_{max}) and the associated COP value. In [153] a calibrated mathematical model to simulate an adsorption chiller applying the finned tube adsorber heat exchanger of [26] was introduced. The model was used to optimize the adsorption and desorption durations to get the highest possible SCP, which amounts to 268.0 $W.kg^{-1}$ upon applying adsorption and desorption durations of 200 and 125 s, respectively. The time of the preheating and precooling phases were assumed to be 10 s each. The SCP_{max} of the OTH APHE at 10/35/90 °C amounts according to Figure 6.12a to 263.6 $W.kg^{-1}$, upon applying t_{ads} and t_{des} of 150 and 80 s, respectively. The GLX30 APHE provides a much lower SCP_{max} compared to the two other adsorber heat exchangers, namely 131.9 $W.kg^{-1}$, upon applying t_{ads} and t_{des} of 240 and 120 s, respectively.

Beside the differences in the equilibrium differential water uptakes between the two applied adsorbents, (Siogel in the current study versus silica gel 123 in [153], it is important to mention that the G-LTJ kinetic setup applied in [153] differs from the V-LTJ kinetic setup applied in the current study in the principle of water uptake measurement. In the G-LTJ kinetic setup, direct measurement for the temporal mass change of the tested adsorbent sample is applied. Indeed, the pressure of the refrigerant vapour surrounding the tested sample in the G-LTJ kinetic setup could change during the adsorption and the desorption processes, based on the performance of the applied evaporator/condenser unit, however the difference between the initial and final pressure of the refrigerant vapour surrounding the tested sample equals almost zero [96]. This leads to a slight difference between Δw_f obtained at 10/35/90 °C using the V-LTJ kinetic setup (see Tables 6.3 and 6.4) and the Δw_f obtained using a G-LTJ kinetic setup at the same operating conditions [153]. Strictly speaking, Δw_f

Table 6.5 Specifications of the adsorber heat exchanger introduced in [34]

Specification	value
Number of fins	14
Thickness of fin, mm	1.42
Height of the outer fins, mm	9.85
Length of the tube, m	7.355
Inner diameter of the tube, mm	12.85
Outer diameter of the tube, mm	15.71
Volume of the adsorbent domain, l	3.1
Volume of the HTF domain, l	0.9538
Mass of the heat exchanger, kg	4.212

obtained using V-LTJ setup with Siogel amounts to 7.5 g/100g, while the one obtained using G-LTJ with silica gel 123 amounts to 8.9 g/100g [153]. Such a difference of around 19% does have a large impact on both *SCP* (Equation 6.13) and *COP* (Equations. 6.13-6.16) of both APHEs. To have a fair comparison, the same differential water uptake of 8.9 g/100g have been applied to estimate the modified performance indicators of both plate heat exchangers for the operation with silica gel 123. Figure 6.13 presents the modified performance charts (the charts of SCP^* and COP^*) of the OTH APHE and the GLX30 APHE at 10/35/90°C, upon applying the silica gel 123. The maximum specific cooling power (SCP^*_{max}) of the OTH APHE amounts to 308.6 $W.kg^{-1}$, while the SCP^*_{max} of the GLX30 APHE amounts to 154.5 $W.kg^{-1}$ (see the red circular marks "•" on Figure 10a and b). Moreover, the modified obtainable *COP* at the maximum *SCP* ($COP^*_{SCP^*_{max}}$) of the OTH APHE amounts to 0.271, while the one of the GLX30 APHE amounts to 0.168. These data are summarized also in Table 6.6. If the target SCP^* for the OTH APHE is reduced to the same value of the extruded aluminum heat exchanger; namely, to 268 $W.kg^{-1}$, the obtainable COP^* is estimated to 0.42, which is only 9 points less that the obtainable *COP* of the extruded aluminum adsorber heat exchanger. Such an operation can be realized with adsorption and desorption times of 380 and 180 s, respectively, the red cross point in Figure 6.13a.

Indeed, the aluminum finned tube adsorber heat exchanger presented in [26] demonstrated a bit higher *COP* than the investigated OTH plate heat exchanger in Chapter 5 at the same *SCP*. On the other hand, aluminum is subjected to corrosion with almost all typical refrigerants like water, ethanol and methanol [63, 64, 57]. The absolutely durable operation associated with applying the nickel-brazed, stainless steel adsorber plate heat exchangers in adsorption systems allows, accordingly, further design optimizations and experimental investigations of such a promising technology.

Table 6.6 Comparison between the performance of the two investigated APHEs and the finned tube adsorber plate heat exchanger introduced in [34] at operating conditions of 10/35/90°C

	Newly Introduced APHE	**GLX30 APHE**	**Finned tube adsorber heat exchanger**
τ_{ads}, s	257.7	586.1	243.5
R^2	0.9957	0.9913	0.9908
τ_{des}, s	81.1	103.0	105.5
R^2	0.9834	0.9813	0.9942
Optimum t_{ads}, s *and* t_{des}, s	150, 80	240,120	200, 125
SCP_{max}, $W{\cdot}kg^{-1}$	263.6	131.9	268.0
$COP_{SCP_{max}}$	0.242	0.147	0.51
SCP^{*}_{max}, $W{\cdot}kg^{-1}$	308.6	154.5	268.0
$COP^{*}{}_{SCP^{*}_{max}}$, -	0.271	0.168	0.51
target SCP^{*}, $W{\cdot}kg^{-1}$	268.0	268.0 can't be realized	268.0
$COP^{*}{}_{target\ SCP^{*}}$, -	0.42		0.51
t_{ads}, s *and* t_{des}, s *at target* SCP^{*}	380, 180		200, 125

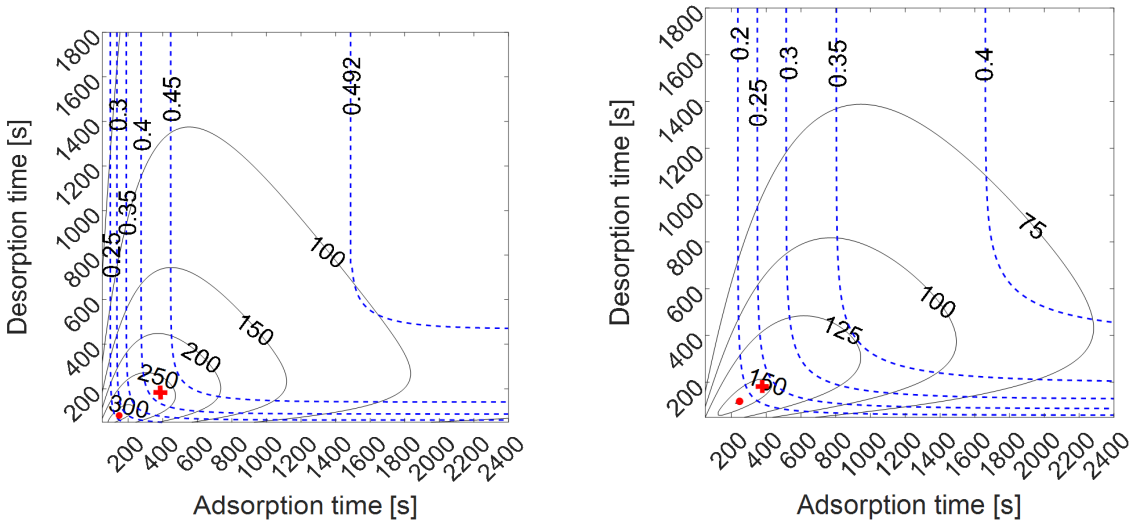

(a) (b)

Fig. 6.13 The modified *SCP* (*SCP**) (black continuous lines) and the modified *COP* (*COP**) (blue dashed lines) calculated for, (a) the OTH APHE and (b) the GLX30 APHE. The SCP^*_{max} and its associated *COP** marked with "•". The *SCP** and *COP** obtainable at t_{ads} and t_{des} of 380 and 180 s, respectively are marked with "+"

6.4 Conclusion

In this chapter, three different test frames (TF1-TF3) are prepared to realize adsorbent samples representative to different adsorbent domains inside open-structured adsorber plate heat exchangers (APHEs).Accordingly, the prepared adsorbent samples have different thicknesses and lengths, termed in this chapter as the heat and mass transfer characteristic lengths (HTCL and MTCL), respectively. Sensitivity analysis of the water uptake to the temperature and vapour pressure in the adsorbent domain is applied to interpret the experimental kinetic results. In addition, a new methodology has been introduced to assess the obtained kinetic data in terms of the obtainable *SCP* and the *COP* at different durations for the adsorption-evaporation and desorption-condensation phases in a real intermittent adsorption machine applying the investigated APHEs. Finally, the performance of the investigated APHEs have been compared with an optimized extruded aluminum finned tube adsorber heat exchanger. The main outcomes of this chapter are summarized below:

- All obtained adsorption and desorption kinetic curves could be described with one time constant for each tested boundary condition and frame with a better coefficient of determination (R^2) than 0.989 for adsorption and 0.949 for desorption.

- Doubling the half thickness of the adsorbent domain from 1.5 to 3 mm at a MTCL of 58.5 mm (TF2 to TF3) resulted in a slight increase in the characteristic time (τ) of the adsorption, less than 19%. This small effect implies that such a MTCL is quite high, so that the mass transfer resistance becomes more dominant than the heat transfer resistance.

- In contrast, doubling the half thickness of the adsorbent domain from 1.5 to 3 mm at a MTCL of 58.5 mm (TF2 to TF3) resulted in a significant increase in the characteristic time (τ) of the desorption, up to 52% at the tested boundary conditions.

- At the same HTCL of 1.5 mm (means the same S/m ratio), increasing the MTCL from 27 mm (TF1) to 58.5 mm (TF2) results in much slower adsorption kinetics and a slight influence on the desorption kinetics. The characteristic time τ of adsorption increases by 78% and 128% at the operating conditions 5/35/90 and 15/30/90 °C, respectively, while the characteristic time τ of the desorption increases by less than 20%. These results contradict the known results so far; namely to expect the same adsorption dynamics for samples having the same S/m ratio.

- The obtained results put in evidence the importance of considering the MTCL beside the HTCL upon designing the adsorber heat exchangers.

- The introduced OTH APHE (Chapter 5) offers up to 2.0 times higher *SCP* if compared with the GLX30, which is available in the market as a unique crossflow, gas-liquid plate heat exchanger.

- The optimal *SCP* of the OTH APHE (Chapter 5) ranges between 157.6 $W.kg^{-1}$, obtained at 5/35/90°C, t_{ads}=140 s and t_{des}=90 s, and 453.6 $W.kg^{-1}$ obtained at 15/30/90 °C and t_{ads} and t_{des} of 190 and 90 s, respectively.

- The OTH APHE (Chapter 5), performs quite comparably to an optimized extruded aluminium finned-tube heat exchanger [26]. However, the OTH heat exchanger has the advantage of highest resistivity against corrosion, which takes place if aluminium is applied as a construction material with all known refrigerants for TDAd systems.

If remarkable achievements concerning the market penetration of sustainable adsorption heat transformation appliances are targeted, dedicatedly designed, and optimized plate heat exchangers are needed. To maximize both *SCP* and *COP* at the nominal design condition(s), both heat and mass transfer characteristic lengths should be taken into account, which is going to be the subject of the next chapter.

Chapter 7

Introduction and design assessment of a new closed structured asymmetric APHE

The appropriateness of applying stainless steel plate heat exchangers in adsorption systems as adsorbers/desorbers has been proven in the previous chapters. The investigation showed that in particular, the application of the closed structure plate heat exchangers seems very promising as it can bring several advantages in terms of compactness of the system and, accordingly, the specific power density of the system. In addition, the construction cost of the adsorption system can be significantly reduced since the adsorber/desorber does not need to be housed in a vacuum-tight chamber, which is quite bulky and costly. Extremely long-life operation due to the lack of corrosion potential is a particular additional advantage.

As mentioned earlier, to our knowledge there is no stainless steel plate heat exchanger in the market specifically designed for use in adsorption systems. In the literature, there is only one open structured PHE investigated numerically as adsorber/desorber of an adsorption chiller [81]. In [81], the application of an embossed plate heat exchanger made of copper to act as an adsorber heat exchanger has been suggested. A numerical parametric study with the application of the SWS-1L and water as an adsorbent-adsorbate pair has been conducted. However, the authors in [81] did not discuss the manufacturing of their suggested embossed plate heat exchanger. In addition, there is a high potential of corrosion that their PHE would be facing if it is made of copper, as reported, and some salt leaks from the SWS-1L[1] [65].

In this dissertation, two innovative plate heat exchangers with different structures are presented for application as adsorbers/desorbers in adsorption systems. In Chapter 5, the OTH's innovative adsorber plate heat exchanger (OTH APHE), which has open structure, is presented and investigated experimentally and numerically. In this chapter, an innovative

[1] a composite adsorbent obtained by impregnating mesoporous silica gel with CaCl2

closed structured APHE will be introduced and investigated numerically. The configuration and the design optimization in terms of the HTCL and MTCL of the adsorbent domain inside the new APHE will be discussed. finally, the estimated performance indicators (SCP and COP) of a single bed adsorption chiller employing the introduced closed structured APHE will be presented and discussed.

7.1 Key design parameters

The commercially available PHEs investigated in Chapter 3 as adsorbers/desorbers had the advantage of having a uniform temperature distribution over their plates' surface. In fact, most of the PHEs available in the market have this advantage. Usually in 2-3 minutes, a uniform temperature distribution over the plates surface can be realized. However, only the uniformity of the temperature distribution over the plates cannot guarantee good performance for the APHE. There are two aspects, which should be considered upon designing an effective APHE:

- Due to the intermittent nature of the adsorber/desorber heat exchanger operation in adsorption systems, high attention must be paid to the sensible heat capacity of the adsorber heat exchanger components. As explained before (see Chapter 5), the lower the sensible heat stored in the metal and the HTF of the adsorber HEX compared to the stored heat of adsorption, the higher the COP of the adsorption system. From the specific power (SP) point of view, this sensible heat has to be rapidly transferred to the HTF to allow a rapid and effective cooling and heating of the adsorbent material and, consequently, a fast adsorption and desorption processes leading to a high SP. Therefore, an extremely reduced volume of the heat transfer fluid (HTF) domain compared to the adsorbent domain, while keeping the uniformity of the temperature distribution over the heat exchanger's plates must be one key design parameter of the closed structured APHE introduced in this chapter.

- Both heat and mass transfers characteristics of the adsorbent placed on the plates are the major influencing parameters on the performance indicators of an APHE. Thus, to realize an efficient APHE, attention has to be paid to the dimensions of the adsorbent domain inside the APHE. Strictly speaking, the thickness of the adsorbent domain is the most important for the heat transfer and the length or the diffusion path length of the adsorbent domain in the direction of the adsorbate flow is the most important for the mass transfer.

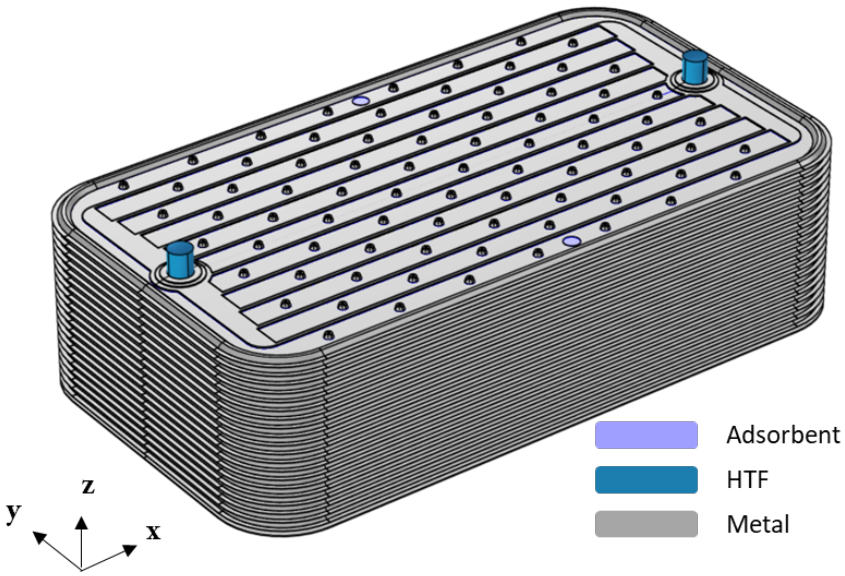

Fig. 7.1 The stack of the plate-pairs of the new APHE. The metal, the HTF and the adsorbent are depicted in different colors. The adsorbent and HTF subdomains do not appear in the figure because they are located between the plates. Only the HTF at its inlet and outlet ports and the adsorbent at the filling ports appear in the figure.

7.2 Design concept

To avoid the necessity of housing the APHE in a vacuum chamber where the refrigerant vapor accumulates during the system operation, the new APHE shall be designed as a closed stack of multi-nickel-brazed parallel plate-pairs made of stainless steel 316l, wherein each plate-pair consists of two identical stamped plates brazed together and enclosing a space for a HTF with an inlet and an outlet port. Figure 7.1shows the stack of the plate-pairs of the new APHE.

For the new APHE introduced in this chapter, the dimensions of one plate are 500 mm in length and 280 mm in width. The plate thickness amounts to 0.3 mm. The new APHE is intended to be filled with about 10 kg of Siogel adsorbent (particle size: 0.71-1.0 mm). Table 7.1 provides some specifications of the new design. The size of the new APHE can be scaled up or down by changing the number of the plate-pairs. Each plate has inlet and outlet ports of 18 mm diameter for the HTF (see Figure 7.2a). The plates shall be formed by stamping, i.e pressing by dies, to realize a special profile on the plates allowing, after arranging the plates and brazing them together, the realization of a PHE of closed sides, in which there is a set of identical spaces (subdomains) for the HTF, i.e HTF domain, and another set of spaces (subdomains) for the adsorbent material (adsorbent domain).

Table 7.1 Specifications of the new APHE, designed for 10 kg of Siogel grains

Specification	value
HTF's inlet and outlet ports diameter (mm)	18
Thickness of one plate (mm)	0.3
Thickness of end plates (mm)	2
Number of plate-pairs, in case of gap between each two successive plate-pairs = 6 mm	20
Width of the PHE (mm)	280
Length of the PHE (mm)	500
Volume of the adsorbent domain (L), with gap between each two successive plate-pairs = 6 mm	13.16
Volume of the HTF domain (L)	0.808
Volume of the metal domain, with end plates (L)	2.337

To minimize the volume of the HTF domain while keeping the uniformity of the temperature distribution over the plates of the heat exchanger, the concept of distributing the HTF in the open-structured APHE presented in Chapter 5 is followed with some modifications. Thus, for each plate-pair in the new APHE, the HTF is to flow through a set of parallel channels (10 channels with 24 mm spacing) created by stamping, arranging, and brazing the plates together. Figure 7.2a shows the HTF inlet and outlet ports of one plate and Figure 7.2b shows the HTF subdomain confined in a plate-pair of the new APHE. The channels in each plate-pair of the new APHE connect the inlet port to the outlet port of that plate-pair. Each channel has a square cross-section with inner sides of 2 mm. Since the width of the plate pairs is large, the HTF enters each plate-pair through its inlet port and is then distributed by a ring to two identical branches. Thanks to the gradually decreasing cross-sectional area of the branches, the HTF flowing through the branches is distributed quasi-uniformly to the parallel channels.

Upper and down end-plates of thickness 2 mm are brazed to the stack of the parallel plate-pairs described above. The down end-plate is blind, while the upper end-plate is equipped with one big port (d= 50 mm) in the middle of the plate for transferring the refrigerant vapour to/from the APHE during the adsorption/desorption processes, two ports (d= 18 mm) for the HTF (inlet and outlet ports) and two small ports (d= 10 mm) for filling the APHE with the adsorbent (in granular form).

In an adsorption process, the refrigerant vapor entering the new APHE should be evenly distributed to the identical adsorbent subdomains existing between the successive plate-pairs in the APHE. In a desorption process, the refrigerant vapour desorbed from each adsorbent subdomain should find a way to exit the APHE. Moreover, the refrigerant vapour in each

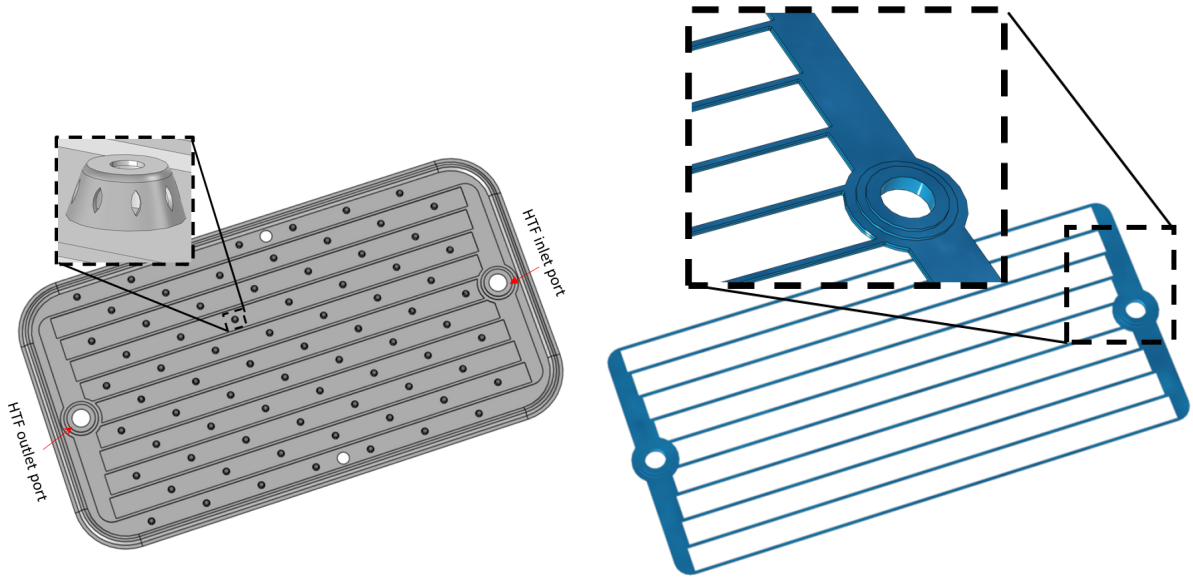

(a) (b)

Fig. 7.2 (a)a plate-pair of the new APHE, (b) HTF subdomain confined in a plate-pair

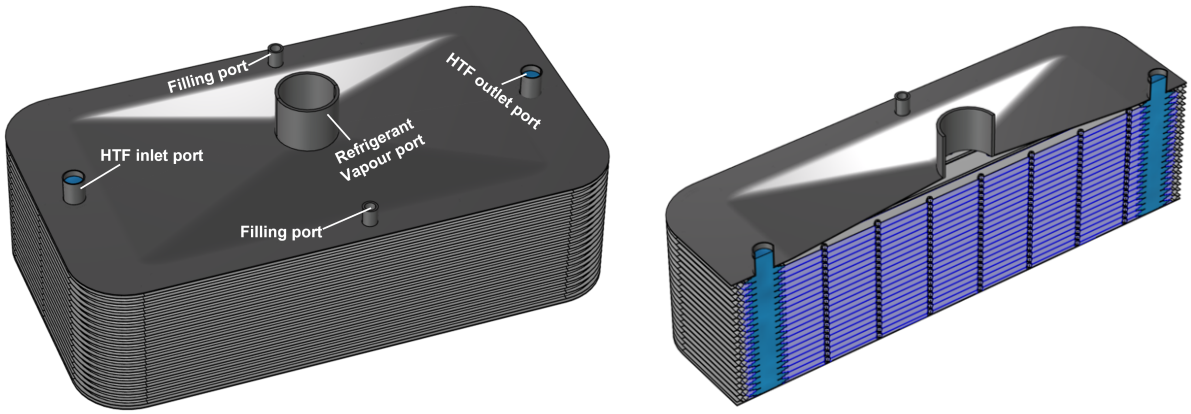

(a) (b)

Fig. 7.3 The new closed structured APHE (a) outer design (b) full section

adsorbent subdomain should encounter a rather limited mass transfer resistance to avoid a sharp pressure drop during the adsorption and a high pressure rise during the desorption, which degrade the adsorption and desorption kinetics, respectively, and accordingly reduce the achievable SP of the adsorption system.

Therefore, special attention has been paid to the distribution of the refrigerant vapour in this new APHE. The idea for this is to create a number of perforated dimples in shape of hollow truncated cones on each plate.

A plate with perforated dimples similar to the one shown in the Figure 7.2a can be made by stamping a perforated flat plate (see Figure 7.4a and Figure 7.4b) with a truncated cone-shaped punches (Figure 7.4c). To form one perforated dimple, a truncated cone-shaped punch is pressed onto the flat perforated plate with the centerline of the punch coinciding with the centerline of the set of holes shown in Figure 7.4b (one center hole (d=2 mm) and 8 small holes (d=1 mm)) distributed on a circle of diameter 5.4 mm.

The dimples on each plate shall be in a segregated arrangement as depicted in Figure 7.2a. The dimples are to be interfaced with the adsorbent sub-domains on their outer surfaces. Each dimple has a central large hole on the top for receiving/delivering the vapour and small holes on the inclined walls for delivering/receiving the vapour to/from the adsorbent surrounding the dimple (see Figure 7.4d). Since the plates are identical, when the plates are assembled and brazed together, the successive dimples form vertical distributors for the refrigerant vapour in the APHE. Figure 7.5 shows a section of the stack of the plate-pairs (without both the upper end-plate and first thin plate). It can be observed how the refrigerant vapour can be distributed to the adsorbent subdomains via the vertical distributors. The large port on the upper end-plate is the only vapour port of the new APHE. Therefore, another vapour distributor (horizontal distributor) is required to distribute the vapour to the vertical distributors formed by the successive interfaced dimples. Thus, the space between the upper end-plate and the first plate pair in the stack of the APHE is not filled with the adsorbent, but serves as a horizontal vapour distributor for the vertical distributors. Therefore, in this chapter, the horizontal distributor is referred to as primary distributor and the vertical distributors are referred to as secondary distributors. Figure 7.6 shows how the vapour is distributed horizontally and then passes through the vertical distributors. It is important to mention that the primary (horizontal) vapour distributor is not reachable from the two small ports on the upper end-plate designated for filling the APHE with a granular adsorbent. The first space reachable from the filling ports is the one existing between the first two successive plate-pairs (i.e. the first adsorbent subdomain), See Figure7.7b.

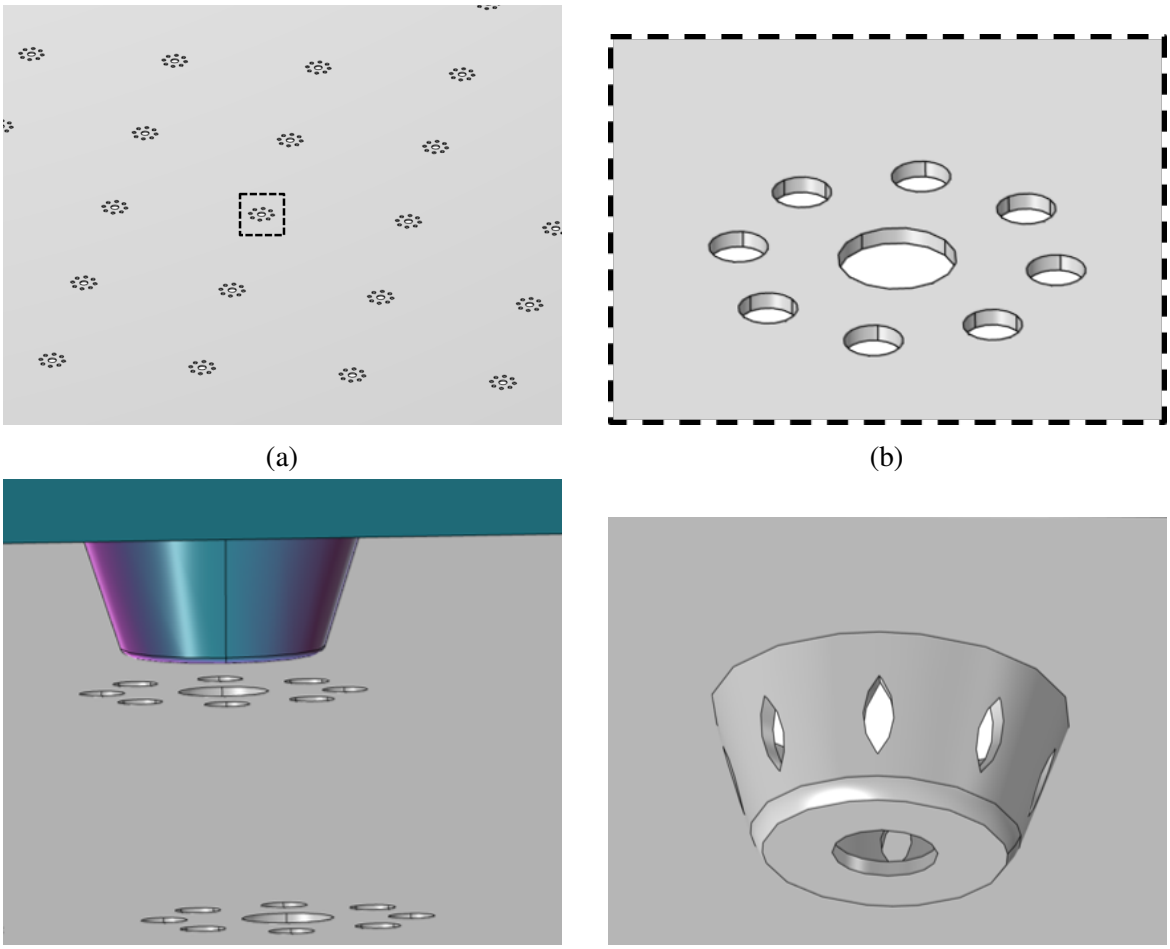

Fig. 7.4 The forming process of the perforated dimples, (a) perforated thin flat plate, (b) one set of holes, (c) truncated cone-shaped punch, (d) perforated dimple

It is now obvious to the reader that the HTCL and MTCL of the adsorbent domain in the new APHE can be defined by the height of the dimples and the distance between them in any of the adsorbent subdomains in the APHE, respectively.

7.3 Examination of the HTF distribution

The HTF distribution in the new APHE should be examined numerically in terms of the pressure drop and the degree of uniformity of the temperature distribution on the plates' surface. As done for the APHE presented in Chapter 5, the simulation model developed in Chapter 4 is applied to only one quarter part of one plate-pair of the new APHE. Note that each pair of plates of the new APHE is symmetric about two perpendicular planes, one of

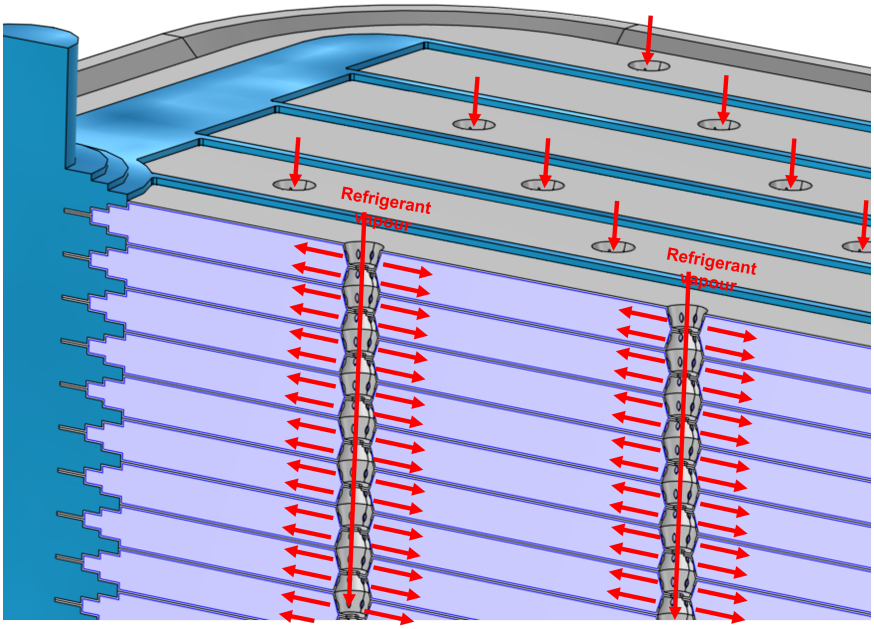

Fig. 7.5 Vertical refrigerant vapour distributors

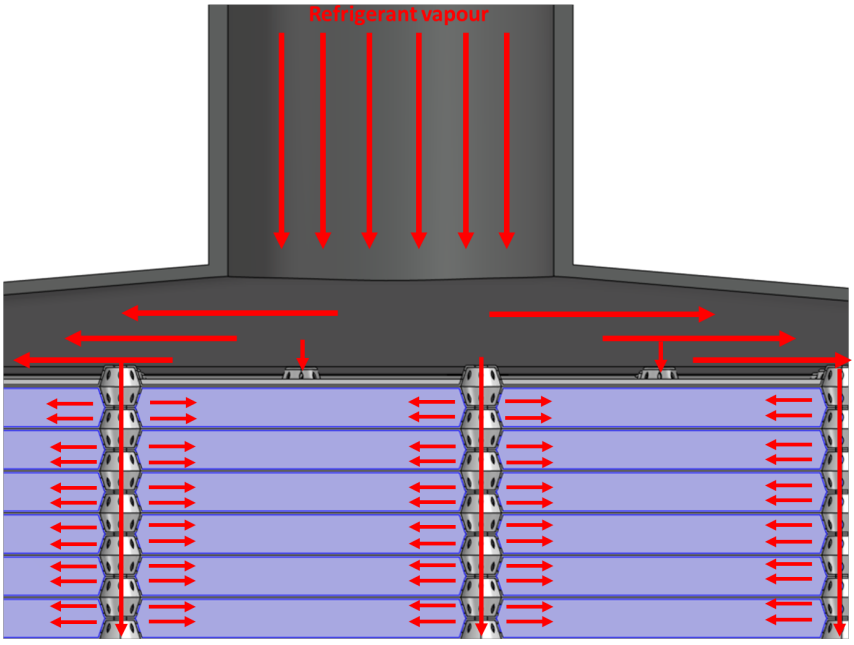

Fig. 7.6 Horizontal refrigerant vapour distributor

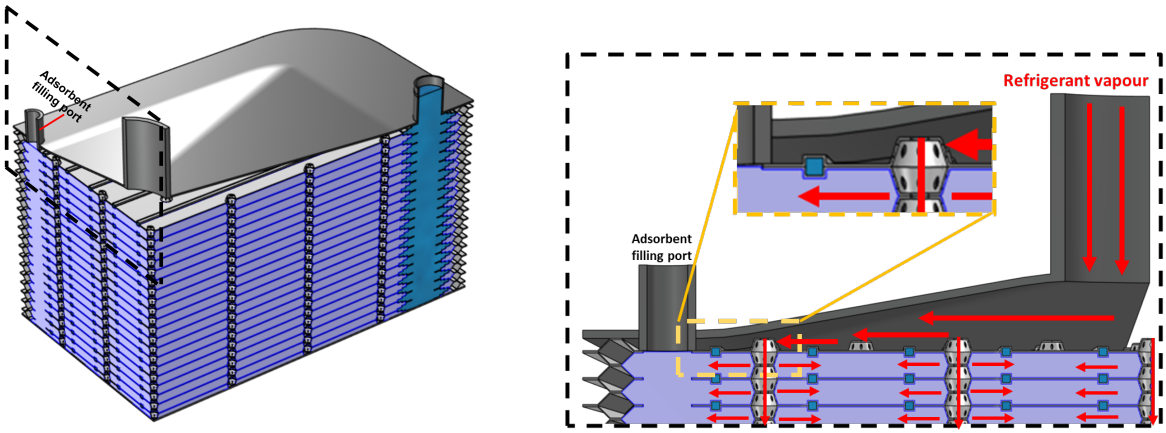

(a) (b)

Fig. 7.7 Preventing the adsorbent grains from reaching the primary refrigerant vapour distributor

which is parallel to the surface of the plates and passes through the interfacial surface where the two plates forming the plate-pair are brazed together, and the other perpendicular to the surface of the plates and passes through the centerlines of the HTF ports. The simulation model shall be implemented in COMSOL Multiphysics without including the adsorbent domain and its related equations in the model implementation.

The HTF inlet temperature experimentally applied in the adsorption and desorption processes conducted on the two APHEs investigated in Chapter 3 and associated to operating conditions 10/30/90°C and 10/35/90°C are applied here as thermal boundary conditions at the inlet port of the HTF of the new APHE. The flow rates applied are to 1, 1.8 and 2 LPM/plate-pair. The other boundary conditions applied in this simulation are the same as those applied to the metal and HTF domains in the simulation of the quarter part of a plate-pair of the APHE presented in Chapter 5.

7.4 Representative section of the new APHE

To assess the HTCL and the MTCL of the adsorbent domain inside the new APHE and then predict the APHE's performance upon applying relevant operating conditions of an adsorption appliance, an appropriate (representative) section of the new APHE should be carefully selected for the numerical investigation. High attention should be paid to the size of the representative section for consuming a reasonable computational time during both assessment and the performance prediction of the APHE. The previously developed mathematical model shall be applied for the aforementioned purposes.

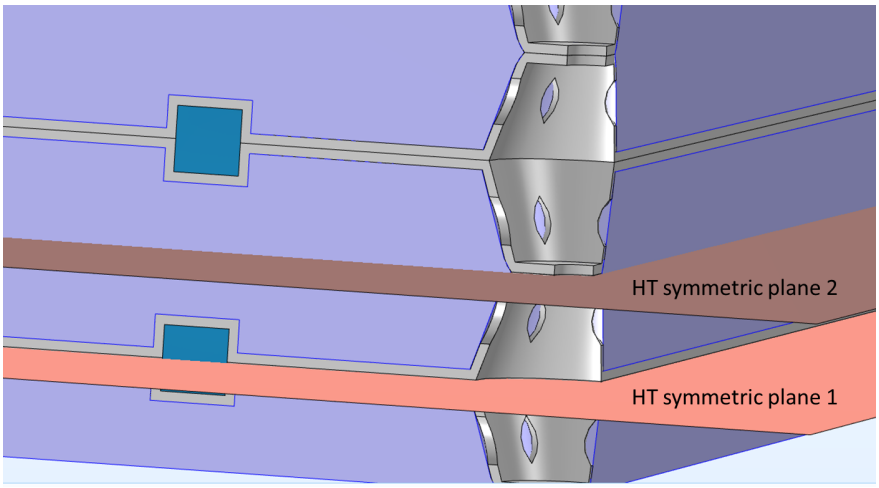

Fig. 7.8 Heat transfer symmetric planes of a plate-pair and an adsorbent subdomain

Since the new APHE consists of several identical plate-pairs, the adsorbent and the HTF subdomains between the successive plates are identical as well. So, a representative section of the new APHE could be a piece of a plate-pair (metal) in contact with pieces of the HTF and the adorbent domains. It is obvious that each plate-pair of the new APHE is symmetrical around a plane parallel to the surface of the plates and passing through the interfacial surface where the two plates forming the plate-pair are brazed together. This described symmetric plane is referred to as "HT symmetric plane 1", see Figure 7.8. Moreover, as each adsorbent subdomain of the new APHE is surrounded by two plate-pairs. Accordingly, a heat transfer symmetrical plane parallel to the plate's surface shall exist in the middle of the thickness of each adsorbent subdomain, i.e. passes through the interfacial surface at which the opposite dimples are brazed together. This described symmetric plane is referred to as "HT symmetric plane 2", see Figure 7.8.Thus, from the perspective of the heat transfer in the direction normal to the surface of the plates, the selected representative section should extend from the "HT symmetry plane 1" to the "HT symmetry plane 2". The height of the adsorbent in the representative section is defined as the HTCL of adsorbent domain inside the new APHE, which corresponds to the height of the dimples.

As shown in Figure 7.5, for each adsorbent subdomain, the upper and the down dimples are identical, therefore the plane passing through the interfacial surface at which the opposite dimples are brazed together can be considered as a mass transfer symmetry plane. In other words, concerning the mass transfer in the adsorbent domain, each adsorbent subdomain is symmetric around a plane parallel to the plate's surface and existing in the middle of the thickness of the adsorbent subdomain. For considering the mass transfer in the representative section, two sets of parallel planes normal to each other and passing through the centerlines

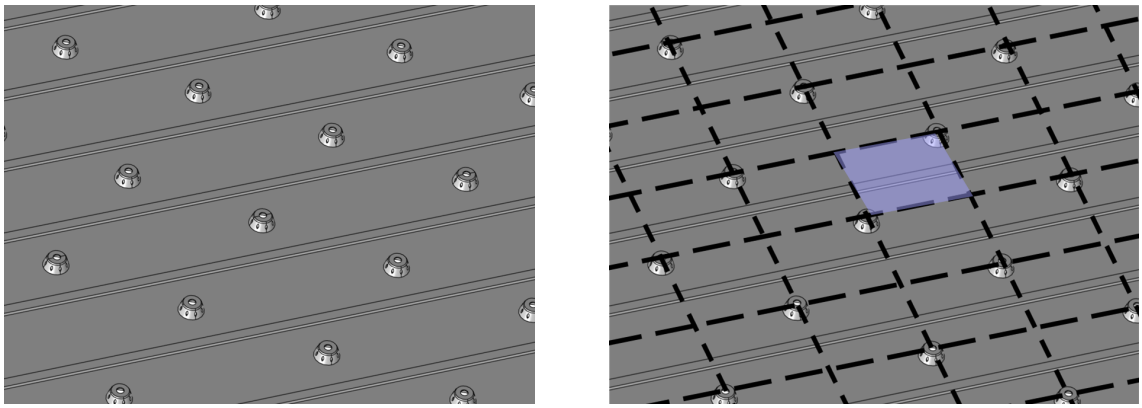

(a) (b)

Fig. 7.9 Designation for the representative section of the new APHE, (a) surface of a plate of the new APHE (b) heat and mass transfer symmetry planes normal to the surface of the plate

of the dimples and normal to the surface of the plates are assumed. In other words, for every dimple, two planes normal to each other and passing through its centerline are assumed. Thus, all those planes can be considered as mass and heat transfer symmetry planes for the adsorbent placed on the surface of a plate-pair.

As shown in Figure 7.9 the two sets of the planes mentioned above divide the plate into identical sections. Thus, one of those sections can be representative to the APHE. This representative section shall be examined for determining the MTCL of the APHE. Figure 7.10a shows one of the identical sections of the plate (representative section). The adsorbent material placed on this section of the plate appears in Figure 7.10b. As shown in the figure, the adsorbent material of the representative section receives/delivers the refrigerant vapour from/to two dimples placed in two opposite corners of the section. As depicted in Figure 7.10b, heat and mass transfer symmetry boundary conditions are assumed on five sides of the representative section.

As the distance between the two dimples in the representative section defines the inter-particle mass transfer resistance in the adsorbent domain, this distance shall be defined as the MTCL of the new APHE. Figure 7.11 depicts the HTCL and MTCL of the representative section of the new APHE.

To sum up, in the new APHE, the HTCL is defined by the height of the dimples and the MTCL is defined by the distance between two successive dimples lying on a diagonal line.

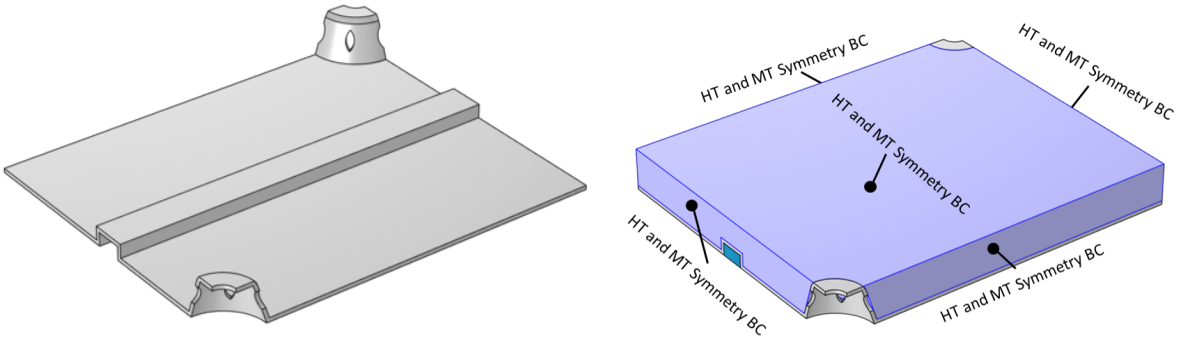

(a) (b)

Fig. 7.10 The representative section of the new APHE,(a) metal domain of the representative section, (b) boundary conditions of the adsorbent domain of the representative section

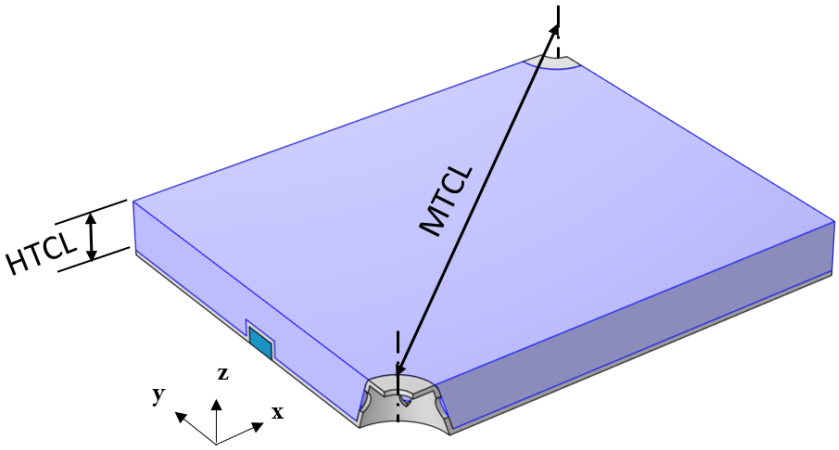

Fig. 7.11 The HTCL and the MTCL of the new APHE

7.5 HTCL and MTCL assessment

It is obvious that the lower the HTCL and MTCL, the higher the adsorption and desorption dynamics of the APHE and, accordingly, the higher the SP of the adsorption system. In fact, optimizing the HTCL and the MTCL only with respect to SP leads to zero values for both. However, extremely low HTCL and MTCL result in a quite low adsorbent to heat exchanger (metal+HTF) mass ratio and, accordingly, a quite low COP value. For instance, if the HTCL, i.e. the dimple height, is reduced to half, the adsorbent to heat exchanger mass ratio doubles and the COP value drops significantly, especially when long adsorption and desorption times are applied.

As illustrated in Chapter 6, the MTCL dominates the adsorption dynamics of the APHEs, while the HTCL dominates the desorption dynamics. In Chapter 3 and Chapter 6, it is also illustrated that for an APHE, the desorption dynamics are on average three times higher than the adsorption dynamics. Therefore, in this chapter, special attention is paid to the investigation of the effect of MTCL on the adsorption dynamic of the new APHE.

For this purpose, the adsorption dynamic of the representative section described above are numerically evaluated upon applying different MTCL values (ranging from 90 to 25 mm) with Siogel/water as a working pair and applying different operating conditions of the adsorption chillers, namely 10/30/90 °C and 10/35/90 °C. To change the MTCL of the representative section shown in Figure 7.11 without changing the spacing between the HTF channels, the width of the section, in y-direction, has to remain fixed, while the length of the section, in x-direction, has to be changed. Regarding the effect of HTCL on the adsorption and desorption dynamics of the new APHE, two HTCL values, namely 1.5 mm and 3 mm, are investigated at the previously mentioned operating conditions and with the application of the optimized MTCL.

As will be presented later (in the results section), the temperature distribution over the plates surface of the new APHE upon applying HTF's flow rate equal or higher than 1 LPM/plate-pair is quite uniform. Based on this, and to minimize the computational time, the simulation model is applied only to the adsorbent domain of the representative section of the new APHE, i.e., excluding the metal and HTF domains and the associated energy and mass conservation equations. Instead of including the energy and mass conservation equations of the metal and HTF in the simulation, a thermal boundary condition is applied to the surface of the adsorbent domain at the interface with the metal domain of the representative section of the APHE. Strictly speaking, the time-average temperature of the active area of the plate given the HTF flow rate of 1.8 LPM/plate pair is applied as the boundary condition of the interfaces between the adsorbent and the metal plate.

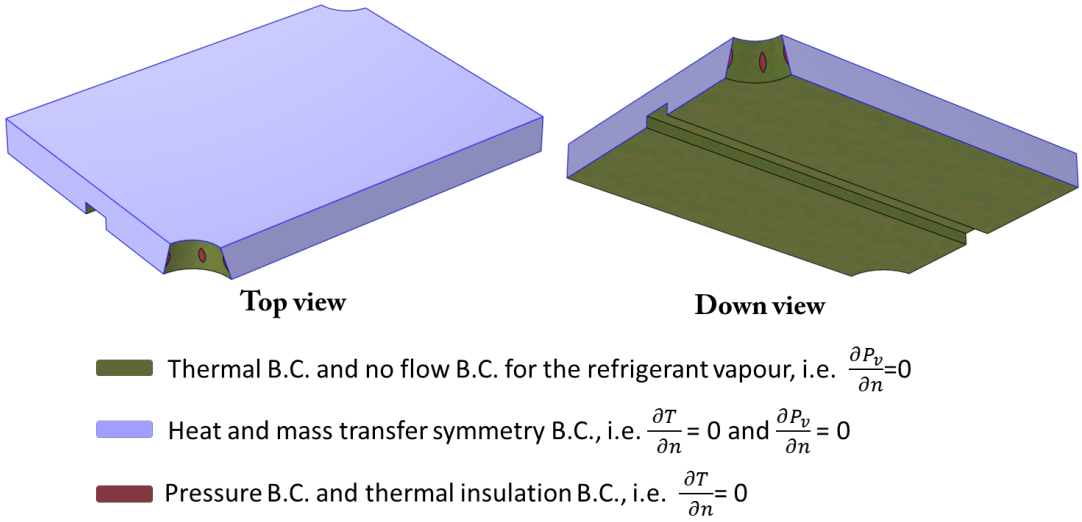

Fig. 7.12 The adsorbent domain of the representative section with illustration of all applied boundary conditions

Figure 7.12 shows the adsorbent domain of the representative section with illustration of all applied boundary conditions. As shown in the figure, pressure boundary conditions are applied to the projection areas of the dimples' holes on the round surfaces of the adsorbent area, where the adsorbent interfaces the two opposite dimples in the representative section of the APHE. The pressure values applied as boundary conditions here is the temporally variant pressure values recorded in the experimental investigation of the GL50 APHE (see Chapter 3). Recall that the GL50 PHE is a closed structured one which was investigated experimentally as adsorber/desorber (with Siogel/water as working pair) against an identical GL50 PHE acting as evaporator/condenser. Thereby, the effect of the evaporator/condeser performance on the adsorption and desorption kinetics is properly considered in the current simulation.

To define a criterion for evaluating the effect of the MTCL as well as the HTCL on the adsorption and desorption dynamics, all the numerical results shall be fitted to exponential form.

$$w(t) = w_o + \Delta w_f(1 - exp(-t/\tau)) \tag{7.1}$$

where $w(t)$ is the instantaneous water uptake, w_o refers to the initial water uptake, Δw_f to the final equilibrium differential water uptake $(w_f - w_o)$, and τ is the characteristic time constant.

In addition, the simple mathematical model developed and introduced in Chapter 6 for estimating SCP and COP is applied to estimate both performance indicators upon utilizing the new APHE in a real adsorption chiller and applying the previously mentioned working pair and operating conditions, and the results will be discussed.

7.6 Results and discussion

7.6.1 Temperature distribution on the plates' surface

Figure 7.13 shows the temporal and spatial distribution of the temperature on the surface of a half-plate of the new APHE. The results are obtained upon applying HTF inlet temperature associated to an adsorption process at operating conditions of 10/30/90°C and HTF flow rate of 1 LPM/plate-pair. As can be seen in the figure, almost uniform temperature distribution over the active surface of the plate pair is achieved within two minutes (Figure 7.13b). The active area of the plate pair refers to the area of the plates adjacent to the adsorbent domain, i.e. the area of the plates excluding the area of their edges. The obtained total pressure drop of the HTF due to hydraulic resistance within a plate pair at 1 LPM/plate pair amounts 8.0 mbar.

Figure 7.14 compares the time variation of the HTF at the inlet port of the plate pair (as a boundary condition) with the time variation of the average temperature of the active surface of the plates at different flow rates of the HTF. The figure shows that increasing the flow rate from 1.2 LPM/plate-pair ($\dot{V}_{total}$=24.0 LPM) to 1.8 LPM/plate pair ($\dot{V}_{total}$= 32.0 LPM) results in a slight improvement in convective heat transfer between the HTF and the metal plates and, accordingly, higher temporal variation of the plates' surface. Increasing the flow rate to 2.4 LPM/plate-pair ($\dot{V}_{total}$= 48.0 LPM) does not result in a noticeable improvement in the temporal variation of the plate average surface temperature. However, it does result in a noticeable increase in the pressure drop of the HTF, from 18.5 mbar at 1.8 LPM/plate pair to 28.2 mbar at 2.4 LPM/plate-pair.

7.6.2 MTCL assessment

Figures 7.15a and 7.15b show the effect of the MTCL on the adsorption kinetics of the new APHE at 10/30/90°C and 10/35/90°C, respectively. For both applied operating conditions, the HTCL remains fixed at 3 mm. The black curve in each figure presents the adsorption kinetic of the new APHE with negligible mass transfer resistance between particles, i.e., with quite low MTCL, meaning quite short distances between dimples. This has been considered in the simulation by setting the interparticle mass transfer resistance to zero. As can be seen

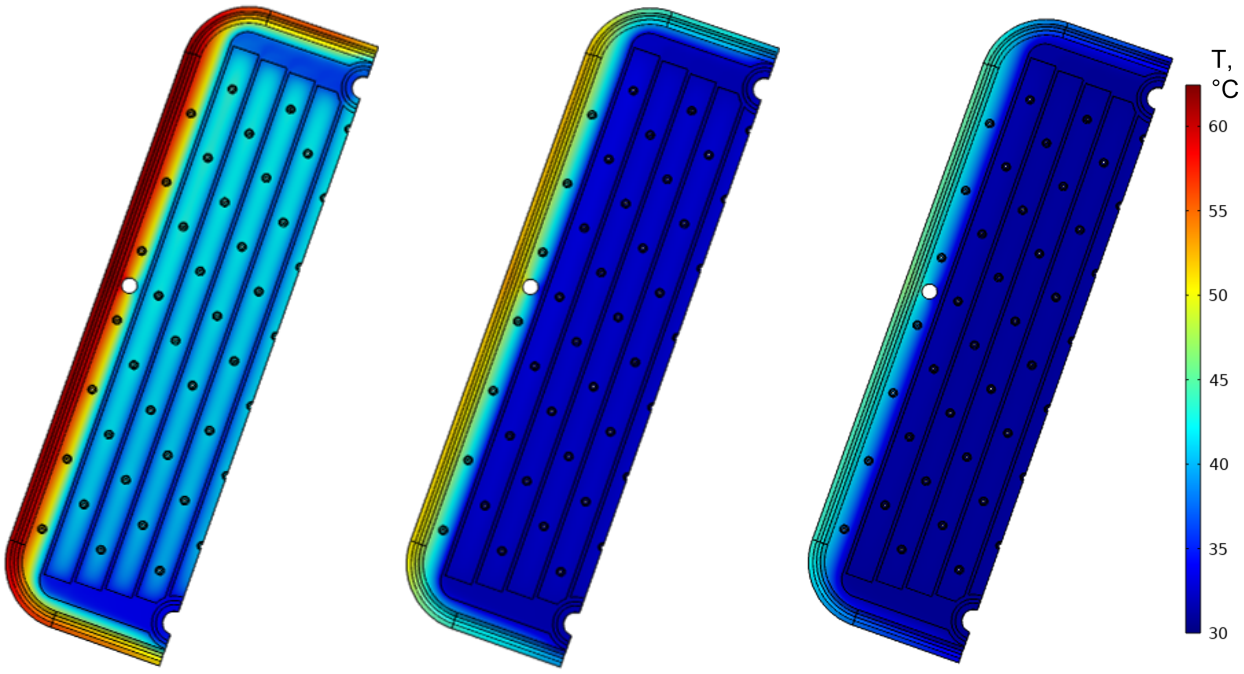

Fig. 7.13 The temporal and spatial distribution of the temperature on the surface of the half-plate of the new APHE upon applying HTF's flow rate of 1 LPM/plate-pair, (a) time= 60 s, (b) time= 120 s, (c) time= 180 s

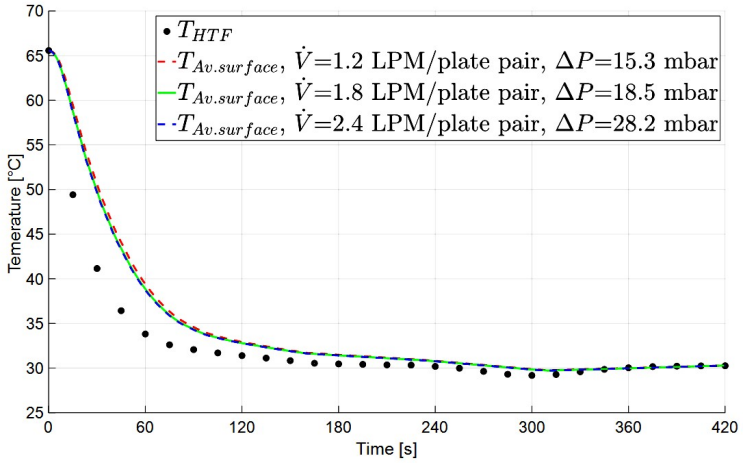

Fig. 7.14 Temporal variation of the average temperature over the active area of a plate-pair

Table 7.2 Characteristic time constant (τ) of the exponential fitting of the adsorption results corresponding to different MTCL of the representative section with applying the boundary conditions of 10/30/90 °C and 10/35/90 °C

MTCL, mm			Negligible	25	30	40	50	60	70	80	90
Operating Conditions, °C	10/30/90	τ	447.0	462.0	491.6	539.0	594.7	644.9	715.0	772.7	833.5
		R^2	0.9954	0.9963	0.9968	0.9972	0.9975	0.9978	0.998	0.9983	0.9983
	10/30/90	τ	373.9	383.5	406.3	441	472.2	505.4	546.7	583.8	635.2
		R^2	0.9947	0.9949	0.9954	0.9962	0.9962	0..9964	0.9967	0.9969	0.9972

from the figures, the adsorption kinetics obtained at a MTCL of 30 mm or less are very close to the highest kinetics obtained at negligible mass transfer resistance between particles, i.e. MTCL=zero.

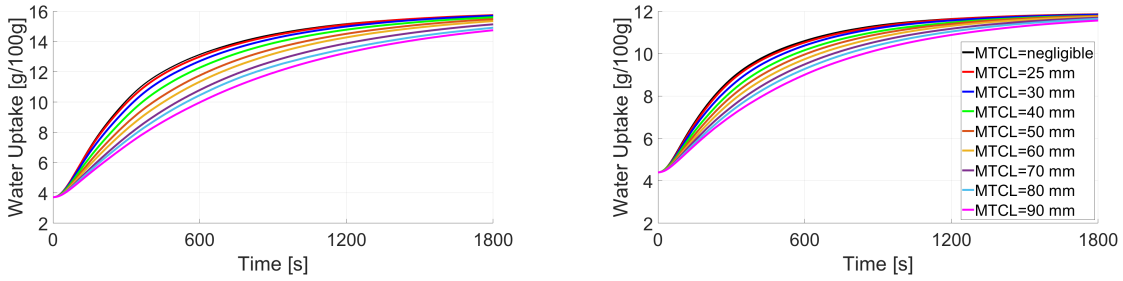

(a) (b)

Fig. 7.15 Effect of the MTCL on the adsorption kinetics,(a) 10/30/90°C, (b) 10/35/90°C

Figure 7.16 shows the relation between the characteristic time constant (τ) of the exponential fitting of the kinetic results depicted in Figure 7.15 and the MTCL of the new APHE. Table 7.2 gives the values of τ depicted in Figure 7.16 and their R^2-values. As can be seen in Figures 7.15 and 7.16, the adsorption kinetics obtained at a MTCL of 30 mm or less are very close to the highest kinetics obtained at negligible interparticle mass transfer resistance. As shown in Figure 7.16 τ value at MTCL of 30 mm is higher than the τ at negligible interparticle mass transfer resistance by less than 9% for 10/30/90 °C and 8% for 10/35/90°C. In order to make the spacing between the dimples in x-direction not less than 18 mm, a MTCL of 30 mm is considered optimal for the new APHE.

7.6.3 HTCL assessment

Figure 7.17 shows the adsorption and desorption kinetics of the representative section with MTCL equal to 30 mm and two different values for the HTCL, namely 1.5 and 3 mm. This is in agreement with the results of the sensitivity analysis of w to T_{ads} and P_{ads} presented in Section 6.3.5. As discussed in Section 6.3.5, the influence of the HTCL on the adsorption

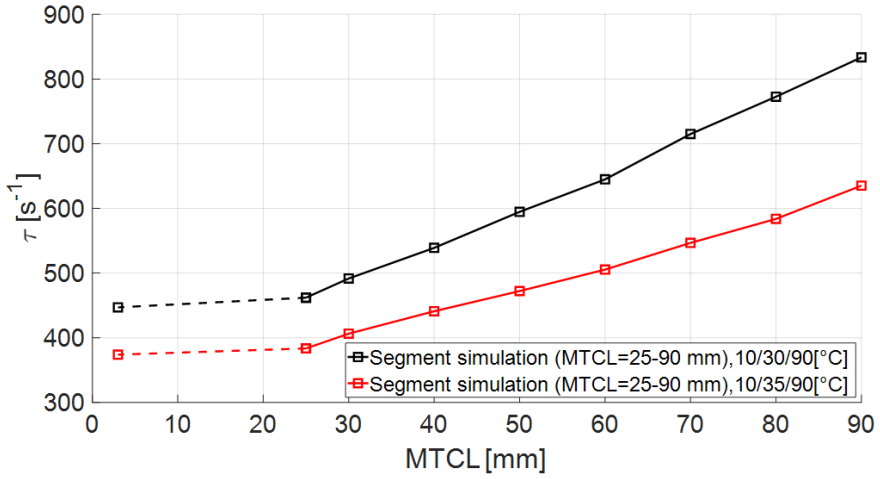

Fig. 7.16 MTCL vs τ, for the representative section with applying the boundary conditions of 10/30/90 °C and 10/35/90 °C

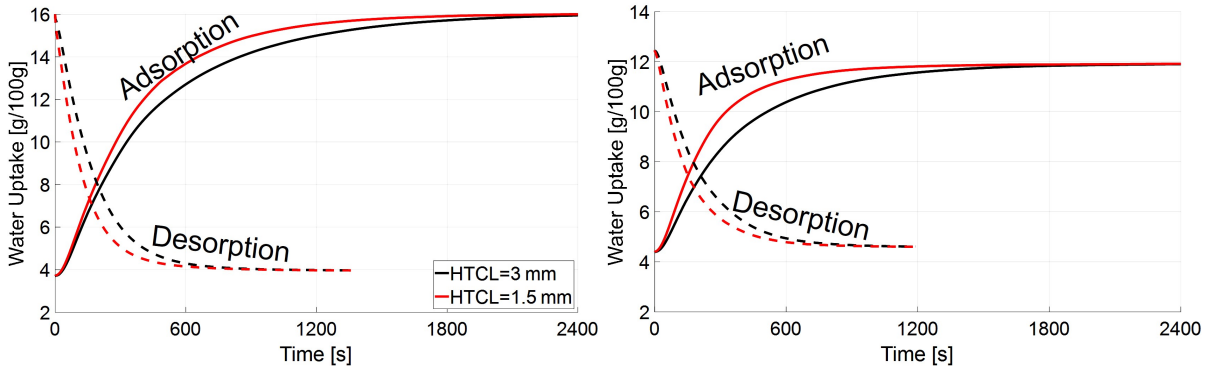

Fig. 7.17 Effect of the HTCL on the adsorption and desorption kinetics with applying MTCL of 30 mm, (a) 10/30/90°C, (b) 10/35/90°C

dynamics is pronounced only for low values of the MTCL. This is the case for the new APHE with a MTCL of 30 mm. Table 7.3 gives the τ and R^2 values of the adsorption and desorption curves depicted in Figure 7.17. Those values shall be used in the estimation of the performance indicators, i.e. *SCP* and *COP*, of an adsorption chiller in which the new APHE is integrated.

7.6.4 SCP and COP of the new APHE

The simple mathematical model developed and presented in Chapter 6, section 6.2.3, was used to estimate both *SCP* and *COP* of a single-bed (intermittent) adsorption chiller utilizing the new APHE. Figures 7.18 and 7.19 show the SCP and COP associated to the application of

Table 7.3 Characteristic time constant (τ) of the exponential fitting of the adsorption and desorption results corresponding to different HTCL of the representative section with applying MTCL= 30 mm and boundary conditions of 10/30/90 °C and 10/35/90 °C

HTCL, mm			1.5		3	
			Adsorption	Desorption	Adsorption	Desorption
Operating Conditions, °C	10/30/90	τ	401.9	125.7	491.6	186.9
		R^2	0.9953	0.9997	0.9968	0.9975
	10/35/90	τ	284.2	162.2	406.5	221.6
		R^2	0.9923	0.998	0.9954	0.9939

the new APHE at 10/30/90°C and 10/35/90°C, respectively. Assuming that 0.5 is the target COP of the new APHE, the new APHE with HTCL=1.5 mm can provide a *SCP* of 272.6 $W.kg^{-1}$ at 10/30/90°C when t_{ads} and t_{ads} of 360 and 180 s are applied, respectively. The *SCP* of the new APHE with a HTCL of 3 mm, at the same operating conditions, decreases to 219.5 $W.kg^{-1}$, which can be achieved by applying t_{ads} and t_{ads} of 210 and 130 s, respectively.

At 10/35/90°C, for a target COP of 0.5, the new APHE with HTCL=1.5 mm can provide 158.6 $W.kg^{-1}$ when t_{ads} and t_{ads} of 510 and 350 s, respectively, are applied. For the design with HTCL=3 mm, the achievable *SCP* decreases to 138.3 $W.kg^{-1}$, when t_{ads} and t_{ads} of 290 and 190 s, respectively, are applied.

It should be recalled that the open-structured APHE presented in Chapter 5 (OTH APHE), which was didactically designed for the application in the adsorption machines, demonstrated comparable performance to an optimized aluminum adsorber heat exchanger with extruded finned tubes [26] (see Section 6.3.7 in Chapter 6). Indeed, with the application of Siogel-water as a working pair and at the same operating conditions, the maximum *SCP* (SCP_{max}) of the open-structured APHE (OTH APHE) is higher than the SCP_{max} of the closed APHE presented in this chapter (see the results of the OTH APHE with Siogel-water as working pair in Chapter 6). However, the closed APHE presented here outperforms the OTH APHE if a target COP of 0.5 is considered. Strictly speaking, at a target *COP* of 0.5, the new closed structured APHE with HTCL=1.5 m demonstrated a *SCP* that is 18.2% higher than the OTH APHE at 10/30/90°C. At the 10/35/90°C operating conditions, the new closed-structured APHE provides 158.6 $W.kg^{-1}$ at the target *COP*, while the OTH APHE introduced in Chapter 5 could not achieve a *COP* higher than 0.458. At this highest COP, the OTH APHE can only produce about 75 $W.kg^{-1}$ as *SCP*.

It is worth noting that the application of the new APHE in an intermittent adsorption chiller can result in a COP of up to 0.73 (see Figure 7.18b). To the best of our knowledge, no higher COP values have been previously published for an intermittent adsorption chiller (single-bed adsorption chiller). At a target COP of 0.6, the new APHE can achieve a SCP

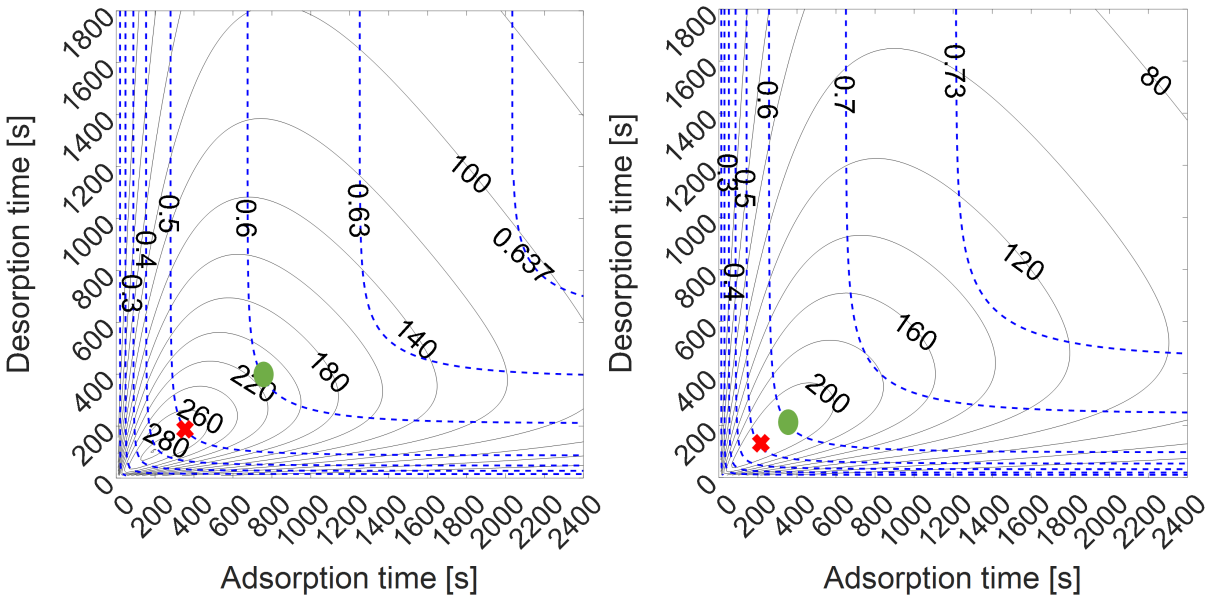

(a) (b)

Fig. 7.18 The SCP (black solid lines) and COP (blue dashed lines) calculated for the representative section of the new APHE at 10/30/90 °C, (a) HTCL=1.5 mm, (b) HTCL=3 mm. The red cross symbols refer to the operating points at a COP target of 0.5. The green point refers to the operating points at a COP target of 0.6

of up to 215.0 $W.kg^{-1}$ at 10/30/90 °C and 127.0 $W.kg^{-1}$ at 10/35/90 °C, see green points in Figures 7.18 and 7.19. In addition, the COP can be significantly improved by up to 38% by applying heat recovery [22] when the new APHE is applied in a multi-bed adsorption chiller.

7.7 Conclusion

This chapter presents a new closed asymmetric stainless steel plate heat exchanger for the application as adsorber/desorber in adsorption appliances. In fact, it is the first ever specially developed closed structured APHE. Besides the corrosion-free advantage of a stainless steel APHE, the most attractive advantage of using a closed-structured APHE is that it does not have to be housed in a vacuum chamber. Concerning the dynamic performance of the closed structured APHE presented in this chapter, a design optimization was performed based on the simulation model presented and validated in Chapter 4. The design optimization leads to a superior performance of the presented closed-structured APHE compared to all adsorber heat exchangers numerically and experimentally investigated in this dissertation. The main outcomes are summarized below:

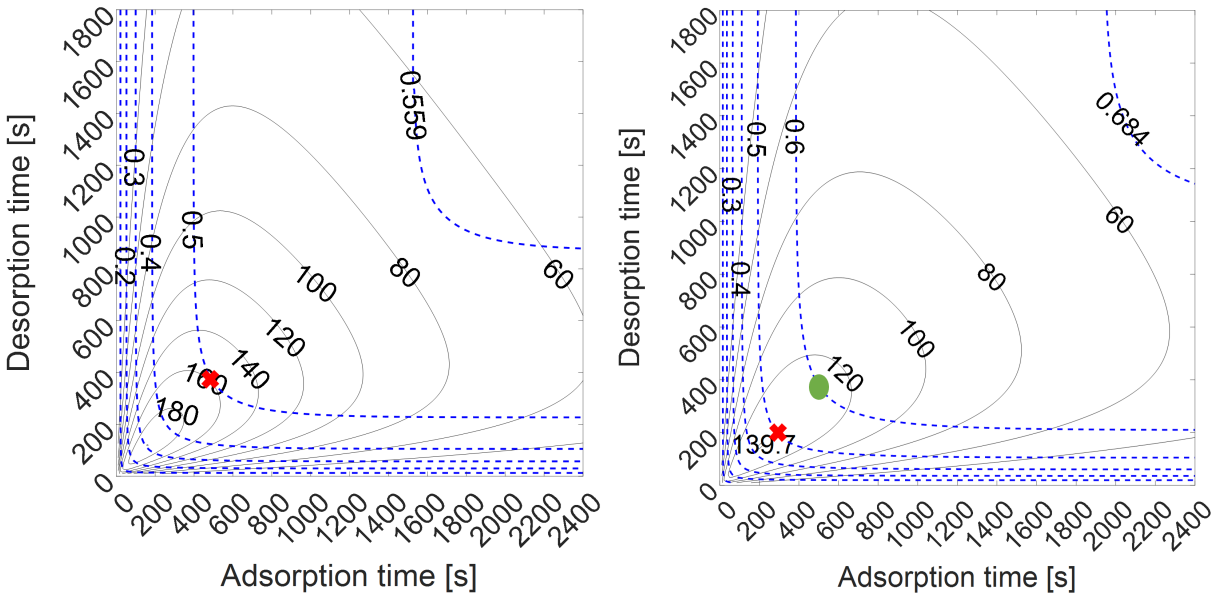

(a) (b)

Fig. 7.19 The SCP (black solid lines) and COP (blue dashed lines) calculated for the representative section of the new APHE at 10/35/90°C, (a) HTCL=1.5 mm, (b) HTCL=3 mm. The red cross symbols refer to the operating points at a COP target of 0.5. The green points refer to the operating points at a COP target of 0.6

- A quite uniform temperature distribution over the active surface of the plate pairs of the APHE is achieved within two minutes (Figure 7.13b) after the start of the sudden temperature change of the HTF inlet temperature.
- The obtained total pressure drop of the HTF due to hydraulic resistance within a plate pair ranges between 15.3 and 28.2 mbar at a flow rate of 1.8 to 2.4 LPM/plate-pair (i.e. total volume flow rate ($\dot{V}_{total}$) ranges between 24.0 and 48.0 LPM).
- Increasing the flow rate from 1.8 to 2.4 LPM/plate-pair (i.e. $\dot{V}_{total}$ from 36.0 to 48.0 LPM) does not result in a noticeable improvement in the temporal variation of the plate average surface temperature . However, it does result in a noticeable increase in the pressure drop of the HTF, from 18.5 mbar at 1.8 LPM/plate pair to 28.2 mbar at 2.4 LPM/plate pair.
- The optimal MTCL for the new closed structured APHE is defined as 30 mm.
- At a target *COP* of 0.5, the new closed structured APHE with HTCL=1.5 m demonstrated a *SCP* of 272.6 $W.kg^{-1}$ which is 18.2% higher than the open structured APHE (the OTH APHE introduced in Chapter 5) at 10/30/90°C (230.6 $W.kg^{-1}$).

- At the 10/35/90°C operating conditions, the new closed-structured APHE provides 158.6 $W.kg^{-1}$ at the target COP, while the open structured APHE of OTH could not achieve a COP higher than 0.458.

Chapter 8

Application of closed structured asymmetric plate heat exchanger as evaporator/condenser

AS shown in Chapter 3 the dynamics of the adsorption-evaporation processes are quit low compared to the desorption-condensation processes. For an adorptive cycle, it was found, as explained in Chapter 3, that the desoprtion-condensation process is in average three times faster than the adsorption-evaporation. Therefore, This Ph.D study pays more attention to the adsorption-evaporation processes. In the last chapters, the performance of different APHEs has been thoroughly investigated with focus on the adsorption-evaporation processes. As the evaporator plays a significant role in the adsorption-evaporation dynamics, this chapter presents an experimental and analytical study on the evaporation mechanism in a closed-structured asymmetric plate heat exchanger (PHE) employed as a stagnant water evaporator for the application in an adsorption chiller.

To this aim, the experimental setup presented in Chapter 3 for investigating the application of the GL50 PHE as adsorber/desorber is utilized, with endoscopes inserted into the evaporator/condenser heat exchanger. Recall that the GL50 experimental setup comprises two identical GL50 PHEs, one acting as an adsorber/desorber and the second, as an evaporator/condenser. Two endoscopes are mounted inside the investigated evaporator to visualize the evaporation mechanism when performing adsorption evaporation processes

---

Contents of this chapter have been reprinted from:
M. Mikhaeil, S. Nowak, V. Palomba, A. Frazzica, M. Gaderer and B. Dawoud."Experimental and analytical Investigation of applying an asymmetric plate heat exchanger as an evaporator in a thermally driven adsorption appliance". Applied Thermal Engineering, 228 (2023), with permission from Elsevier.
Contributions of the author: Conceptualization, Methodology, Investigation, Formal analysis, Writing original draft.

Table 8.1 Geometric parameters of the GL50 PHE as an evaporator

Parameter	Value
Number of plates	20
Overall dimensions	278 [mm] x 123 [mm] x 83 [mm]
Heat transfer surface per plate	0.0393 [m^2]
Empty weight	3.4 [kg]
Volume refrigerant side	1.5 [L]
Volume HTF side	0.9 [L]
Plate thickness	0.35 [mm]

under different boundary conditions. It turned out that the evaporation mechanism is a partially covered, thin film evaporation.

A heat transfer analysis is performed to evaluate the heat transfer coefficient of the thin film evaporation (h_f) inside the investigated evaporator. Moreover, the obtained h_f at different operating conditions is correlated to the film thickness δ and the wetted area (A_w) of the evaporator. In addition, an analytical model is developed and introduced to correlate the overall evaporator heat transfer coefficient with the adsorption potential and the time rate of change of the water uptake.

8.1 Experimental setup and test procedure

8.1.1 Test unit

The experimental setup (see Figure 8.1) built to investigate the application of the GL50 PHE as adsorber/desorber and as evaporator/condeser has been described in detail in Section 3.1.1. Table 8.1 presents the specifications of the GL50 PHE. For the visualized investigation, two different endoscope video cameras (BS-3.9/1m QVGA and BS-350XIPSD, from VOLTCRAFT®) are used for the visualization of the evaporation process inside the investigated evaporator heat exchanger. The main characteristics of the endoscopes are listed in Table 8.2. The endoscopes are inserted into the evaporator heat exchanger using an electrical vacuum feedthrough (MIL-C-24308) on a KF40 flange (VACOM®), as shown in Figure 8.2. The installation positions of the endoscopes inside the evaporator heat exchanger are schematically illustrated in Figure 8.3, where it can be seen that one endoscope, namely endoscope (1), is positioned inside the fifth refrigerant channel to visualize the evaporation mechanism. Endoscope (2) is positioned in one of the two refrigerant vapour manifolds of the evaporator heat exchanger to observe the bottom of the manifold as well as the inlet of the refrigerant channels interfaced with the vapour manifold.

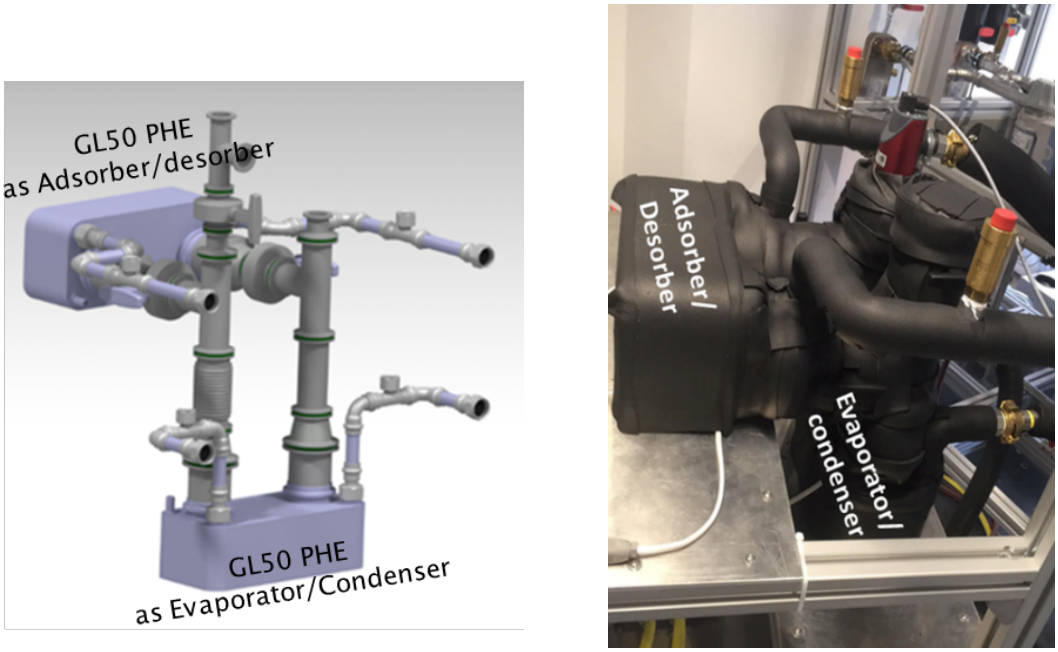

(a) (b)

Fig. 8.1 GL50 experimental test setup, (a) 3D-drawing , (b) realized setup

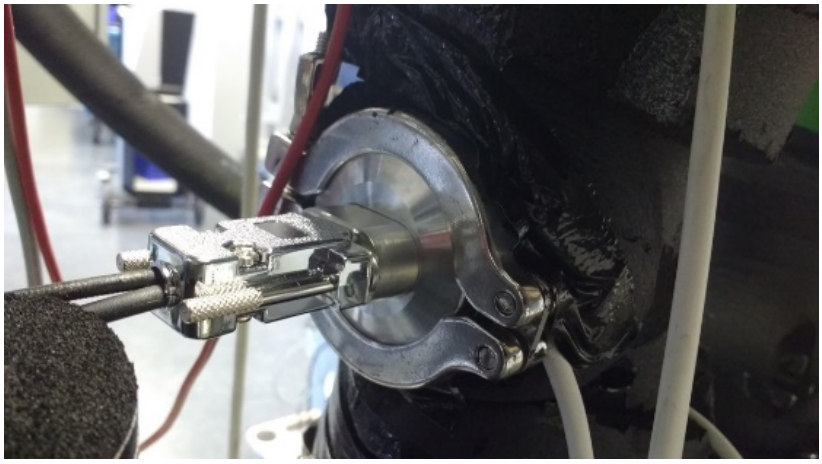

Fig. 8.2 Vacuum feedthrough of the two endoscope cameras into the test unit

Table 8.2 Properties of the used endoscope video cameras

Parameter	**Endoscope (1)**	**Endoscope (2)**
Model	BS-3.9/1m QVGA	BS-350XIPSD
Position	refrigerant channel	manifold
Diameter	3.9 [mm]	8 [mm]
Resolution	320x240	640x480
Focusing	10 [mm] to 50 [mm]	30 [mm] to 60 [mm]
Field of vision	54°	54°

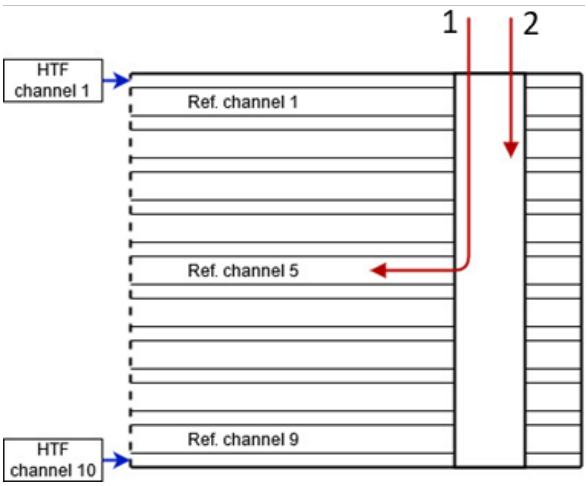

Fig. 8.3 Schematic drawing for illustrating the position of enoscopes (1) and (2) inside the evaporator heat exchanger

8.1.2 Test conditions and experimental procedure

Throughout the course of investigating the GL50 PHE as an evaporator, the adsorption-evaporation processes have been conducted following the Large Temperature Jump (LTJ) technique under different operating conditions of a real adsorption chiller. Figure 8.4 presents the ideal adsorption chiller process (in black) versus those taking place in a real adsorption chiller (in red). As the evaporator-condenser heat exchanger is not of infinite size, the pressure can't be kept constant. At the beginning of each process, the adsorption or desorption sucks or drives out more water vapour than that producible by the evaporator or condensable by the condenser. As the adsorption unit represent thermodynamically a closed system, the pressure shall decrease/increase at the beginning of the adsorption/desorption process, respectively, the case of the red lines 4-1 for adsorption and 2-3 for desorption in Figure 8.4. Approaching the final equilibrium state, the rate of adsorption/desorption decreases, so that the size of the evaporator/condenser becomes big enough to retain the initial pressure level according to the inlet temperature into the heat exchanger.

The LTJ adsorption-evaporation processes have been conducted at evaporator temperatures (T_{evap}) of 15 and 10°C, condenser (adsorption-end) temperatures (T_{cond} =$T_{ads-end}$) of 30 and 35°C and driving heat source (desorption-end) temperature (T_h) of 90°C. The adsorption-start temperature (ads-start), i.e., the temperature of state 4 (T_4) has been determined using the equilibrium model developed in [17] for water adsorption in Siogel at all defined sets of operating conditions and listed in Table 8.3. Two selected sets of operating conditions, namely 15/30/90°C and 10/35/90°C, have been conducted 3 times to check the repeatability of the measurements.

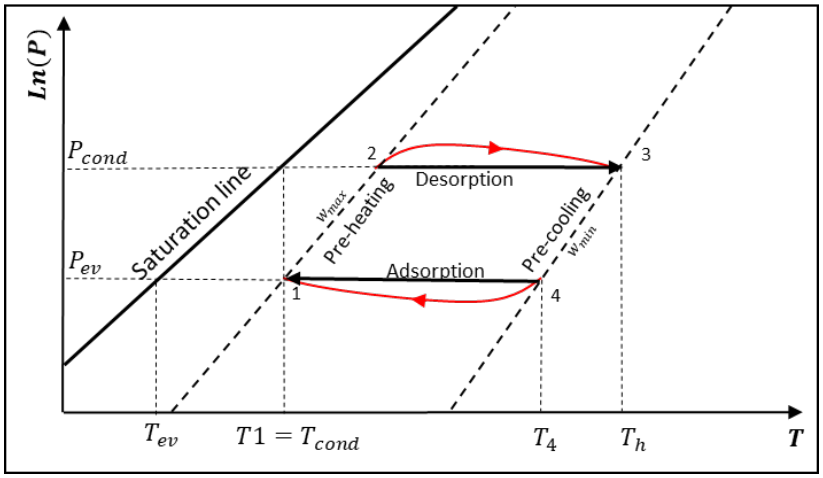

Fig. 8.4 Schematic representation of both ideal and real adsorption and desorption processes of an adsorption chiller in a Clapeyron diagram

Table 8.3 Boundary conditions of the conducted adsorption-evaporation processes

Process	$T_{evap}/T_{cond}/T_h$ **°C**	$T_{ads-start}$, T_4**°C**	$T_{ads-end}$ **or** T_{cond}, T_1**°C**
1	15/30/90	70.5	30.0
2	15/35/90	62.4	35.0
3	10/30/90	66.1	30.0
4	10/35/90	58.8	35.0

The test procedure of a LTJ adsorption-evaporation process consists of the following two phases, during which the gate valves (V2.1 and V2.2) connecting the adsorber to the evaporator are kept open (Figure 3.5a):

1. The preparation phase, which aims at realizing the adsorption start condition. This is done by setting the adsorber heat exchanger to the adsorption start temperature (T_4) and, at the same time, setting the temperature of the evaporator heat exchanger to the required evaporation temperature (T_{evap}). This preparation phase takes 2 hours to ensure reaching the equilibrium state 4.

2. The second phase is the LTJ-quasi-isobaric adsorption phase, in which the temperature of the HTF feeding the adsorber experiences a step-change to the adsorption-end temperature (T_1). The LabVIEW code written to control the whole set-up allows setting the desired end-temperature and realizing it at the inlet of the adsorber heat exchanger in about 2 minutes after finishing phase one. The adsorption phase is measured over 2 hours to ensure reaching the equilibrium state (state 1) at the end of the process.

8.1.3 Evaluation of the evaporator performance

A MATLAB® code has been developed to estimate the evaporator power out of the recorded experimental data, the overall and the individual heat transfer coefficients of the investigated evaporator heat exchanger for all conducted adsorption-evaporation processes (see Table 8.3). The achieved evaporator power has been calculated according to Equation 8.1,

$$\dot{Q}_{evap} = \dot{V}_{HTF}.\rho_{HTF}.C_{p_{HTF}}.(T_{HTF,in} - T_{HTF,out}) \tag{8.1}$$

Where $\dot{Q}_{evap}$, W, is the evaporator power, $\dot{V}_{HTF}$, $m^3.s^{-1}$, is the measured volume flow rate of the heat transfer fluid (HTF), ρ_{HTF}, $kg.m^{-3}$ is the density of the HTF, $C_{p_{HTF}}$, $J.kg^{-1}.K^{-1}$, is its specific heat capacity and $T_{HTF,in}$, °C, and $T_{HTF,out}$, °C, are the measured inlet and outlet temperature of the HTF. The thermodynamic properties of the HTF (water) have been determined at the mean temperature between the inlet and outlet of the HTF passing through the evaporator heat exchanger using the thermophysical property database CoolProp, which is coupled to MATLAB®.

Having calculated the evaporator power, the overall heat transfer coefficient U, $W.m^{-2}.K^{-1}$, in the evaporator can be estimated by the following equation.

$$U = \frac{\dot{Q}_{evap}}{A_{total} LMTD} \tag{8.2}$$

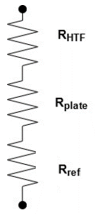

Fig. 8.5 Thermal resistances of the evaporator HEx

Where, A_{total}, m^2, is the heat transfer area of the evaporator and $LMTD$, K, is the logarithmic mean temperature difference, which is defined by Equation 8.3.

$$LMTD = \frac{T_{HTF,in} - T_{HTF,out}}{ln\frac{T_{HTF,in} - T_{ref}}{T_{HTF,out} - T_{ref}}} \tag{8.3}$$

T_{ref} is the saturation temperature of the refrigerant (water) corresponding to the measured vapour pressure inside the evaporator (P_{evap}). The total thermal resistance of the evaporator heat exchanger can be represented as a series connection of three resistances as shown in Figure 8.5. Accordingly, the overall thermal resistance R_{total}, $K.W^{-1}$, can be expressed as:

$$R_{total} = R_{ref} + R_{plate} + R_{HTF} \tag{8.4}$$

Where R_{ref}, $K.W^{-1}$, is the thermal resistance of the evaporating water from the channel's wall, R_{HTF}, $K.W^{-1}$, is the convective heat transfer resistance between the HTF and the channel's wall and R_{plate}, $K.W^{-1}$, is the conductive thermal resistance through the channel's wall.

Based on the basic heat transfer relationship (Equation 8.5), between the overall heat transfer coefficient and the total thermal resistance, the unknown evaporative heat transfer coefficient on the refrigerant (water) side h_{ref}, $W.m^{-2}.K^{-1}$ can be determined by Equation 8.6.

$$U.A_{total} = \frac{1}{R_{total}} \tag{8.5}$$

$$h_{ref} = (\frac{1}{U} - \frac{1}{h_{HTF}} - \frac{1}{h_{plate}})^{-1} \tag{8.6}$$

where the heat transfer coefficient h_{plate}, $W.m^{-2}.K^{-1}$, represents the conduction through the wall (see Equation 8.7) and h_{HTF}, $W.m^{-2}.K^{-1}$, is the convective heat transfer coefficient between the wall and the HTF (cf. Equations 8.8 and 8.9).

$$h_{plate} = \frac{k_{plate}}{L_{plate}} \tag{8.7}$$

Where k_{plate} is the thermal conductivity of the plate, amounts 15 $W.m^{-1}.K^{-1}$ and L_{plate}, m, is the plate thickness, amounts to 0.35 mm.

The heat transfer coefficient h_{HTF} between the wall and the HTF is determined using the correlation proposed by Gnielinski [155]:

$$Nu = 0.664.Re_{HTF}^{1/2}.Pr^{1/3} \tag{8.8}$$

$$h_{HTF} = 1.5Nu\frac{k_{HTF}}{d_{h,HTF}} \tag{8.9}$$

Where Nu is the Nusselt number, Re is the Reynolds number of the HTF and Pr its Prandtl number. K_{HTF}, $W.m^{-1}.K^{-1}$, is the thermal conductivity of the HTF and $d_{h,HTF}$, m, the hydraulic diameter of the HTF channel. $d_{h,HTF}$ is estimated using the 3D drawings of the "GL50" plates and equals 7.5E-3 m. The factor 1.5 is to account for the effect of the dimples on the h_{HTF} [112, 111, 114].

8.1.4 Uncertainty of the measurements

The uncertainty of the overall heat transfer coefficient (σU) is calculated by means of the law of error propagation for Equation 8.10, leading to the following expression,

$$\sigma U = \sqrt{(\frac{\partial U}{\partial \dot{Q}_{evap}}.\sigma \dot{Q}_{evap})^2 + (\frac{\partial U}{\partial LMTD}.\sigma LMTD)^2 + (\frac{\partial U}{\partial A}.\sigma A_{total})^2} \tag{8.10}$$

With $\sigma \dot{Q}_{evap}$, $\sigma LMTD$ and σA_{total} being the uncertainty of the evaporator power, the logarithmic mean temperature difference ($LMTD$) and the overall heat transfer area, respectively. $\sigma \dot{Q}_{evap}$ and $\sigma LMTD$ are determined by means of the law of error propagation for Equation 8.1 and 8.3, respectively. σA_{total} is estimated based on the uncertainty of the plate dimensions given by the "GL50" PHE's manufacturer [151] and found about ±1.55%.

$$\sigma \dot{Q}_{evap} = \sqrt{(\frac{\partial \dot{Q}_{evap}}{\partial T_{HTF,in}}.\sigma T_{HTF,in})^2 + (\frac{\partial \dot{Q}_{evap}}{\partial T_{HTF,out}}.\sigma T_{HTF,out})^2 + (\frac{\partial \dot{Q}_{evap}}{\partial \dot{V}_{HTF}}.\sigma \dot{V}_{HTF})^2} \tag{8.11}$$

The uncertainty of ρ_{HTF} and $C_{p_{HTF}}$, i.e., $\sigma \rho_{HTF}$ and $\sigma C_{p_{HTF}}$ have been neglected.

$$\sigma LMTD = \sqrt{(\frac{\partial LMTD}{\partial T_{HTF,in}}.\sigma T_{HTF,in})^2 + (\frac{\partial LMTD}{\partial T_{HTF,out}}.\sigma T_{HTF,out})^2 + (\frac{\partial LMTD}{\partial T_{ref}}.\sigma T_{ref})^2} \tag{8.12}$$

The uncertainty expected by the estimation of the film heat transfer coefficient (σh_f) is calculated according to Equation 8.13 based on Equation 8.6

$$\sigma h_{ref} = \sqrt{(\frac{\partial h_{ref}}{\partial U}.\sigma U)^2 + (\frac{\partial h_{ref}}{\partial h_{plate}}.\sigma h_{plate})^2 + (\frac{\partial h_{ref}}{\partial h_{HTF}}.\sigma h_{HTF})^2} \tag{8.13}$$

Where; σh_{plate} and σh_{HTF} are the uncertainty of h_{plate} and h_{HTF}, respectively.

8.2 Analytical investigation

8.2.1 Thin film evaporation; a theoretical background

During evaporation in a stagnant evaporator, the heat flux densities required for nucleate boiling are not achieved at the prevailing evaporator pressures. Convective boiling is also not to be expected due to the large temperature differences required between the surfaces of the water layer to be evaporated. Furthermore, the filling quantity of the evaporator in such an intermittent adsorption appliance shall be reduced to the minimum required level, in order to minimize the pre-heating and pre-cooling losses. Accordingly, the filling levels of the water required for convective boiling are not available. For the explained reasons, the expected evaporation mechanism is heat conduction through a thin film.

The applied asymmetric plate heat exchanger shall offer the required large heat transfer surface area, in order to realize an effective thin film evaporation. Lang [156] and Westerfeld [157] have introduced and analyzed a set of finned-tube evaporator and adsorber heat exchangers for intermittent adsorption heat pumps. Sato and Niceno [158] have studied nucleate boiling and its transition to film boiling on horizontal surfaces. They reported that, in case the length of the liquid-vapour interface is smaller than the so-called “critical wavelength (λ_C) defined by Equation 8.14, the interface becomes stable resulting in a stable film boiling. Otherwise, the interface becomes unstable and nucleate boiling is the dominating evaporation mechanism. The critical wavelength can be considered as the instability limit according to the Rayleigh-Taylor instability as introduced in [159, 160].

$$\lambda_C = 2\pi.\sqrt{\frac{\sigma}{(\rho_l - \rho_v).g}} \tag{8.14}$$

For the tested water evaporation at 10 to 15 °C, the critical wavelength amounts to 17.3 mm. The applied asymmetric plate heat exchanger is equipped with dimples with a maximum diameter of less than 9 mm and a maximum flat surface distance between two successive dimples of less than 12 mm. Accordingly, a stable thin film evaporation is expected to take place inside the introduced PHEx. To achieve a good heat transfer coefficient h_f, with the low thermal conductivity of water (λ_w) of 0.57 $W.m^{-1}.K^{-1}$, thin layers of the liquid film are required, which depends on the surface tension of the liquid water (σ) and the surface forces between the phases in contact. Wolf [161] gives the following relationship (Equation 8.15) for the minimum or critical layer thickness, δ_{min} or δ_c, of a liquid film on a flat solid surface:

$$\delta_{min} \text{ or } \delta_c = \sqrt{\frac{2\sigma}{\rho \cdot g}(1 - cos\theta)} \tag{8.15}$$

The critical layer thickness is, obviously, a function of the contact angle, which in turn depends on a large number of influencing factors. Upon wetting metallic surfaces with water, contact angles of almost zero degree can generally be achieved [162, 163]. In technical applications, however, the contact angle can be higher due to the contamination of the surfaces with wetting-inhibiting substances. Measures to increase wetting, such as the application of a capillary structure on the metal surface by sandblasting or etching, in turn, lead to a sharp reduction in the contact angle [164]. Furthermore, a distinction must be made as to whether the liquid spreads over the surface to be wetted, in which case the contact angle is termed as the advancing contact angle. In case the liquid film contracts over the surface, which is the expected case in our stagnant film evaporator during the adsorption-evaporation process, the contact angle is termed as the receding contact angle [165, 166].

A precise statement about the contact angle is difficult due to the complex relationships, since the values contained in the literature for metal-water pairings under vacuum and in the temperature range under study are quite scarce. Hobler [167] gives a value of = 37.7° for the pair aluminum-water, without specifying whether it is an advancing or receding angle. Harmati [164] determined an advance angle of = 39° in spray tests.

To minimize the wetting angle and thus the minimal water layer thickness in the evaporator of adsorption appliances, the evaporator surfaces shall be sandblasted and cleaned in an ultrasonic bath [156]. The experimental observations during the evaporation process of [156] revealed that, with carefully pretreated, clean evaporator surfaces, minimal layer thicknesses of well below 1 mm can be achieved. As the investigated asymmetric plate heat exchanger is a nickel-brazed heat exchanger, the surface of each plate can be simply assumed to be perfectly clean as the brazing process takes place inside a vacuum oven at around 1100 °C. The residuals of the nickel foils can be seen on the surface of the brazed plates with a simple

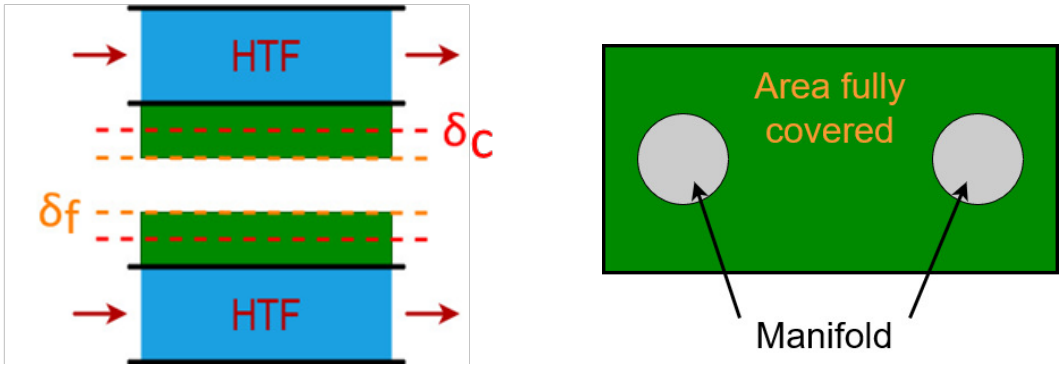

(a) (b)

Fig. 8.6 Scenario 1 of the thin film evaporation. (a) Side view of a volume element, (b) Top view of a plate

endoscope, which are expected to reduce the contact angle very much (doing the same effect like sandblasting, however in a much cleaner way).

The obtained results of the experimental investigations of the currently studied evaporator shall be applied to derive a relation between the liquid film thickness (δ), the active (wetted) area of the evaporation (A_{wet}) and the film evaporation heat transfer coefficient (h_{ref}). The following paragraphs present the analytical model to account for film evaporation at layer thicknesses greater or equal to the critical film thickness.

8.2.2 Development of the h_f-δ-A_{wet} correlations

Upon developing a correlation between the thin-film heat transfer coefficient (h_f), the film thickness (δ) and the wetted evaporator area (A_{wet}), a distinction must be made between three expected evaporation scenarios. In the first scenario (Scenario 1), the thickness of the liquid water film is higher than a critical liquid film thickness (δ_c) (as defined by Equation 8.15), see Figure 8.6. Hereby the thickness of the liquid film decreases homogenously with ongoing time (Figure 8.6a), whereas the whole plate's area remains fully wetted with liquid (Figure 8.6b).

Once the liquid film thickness reaches its critical value δ_c, due to the continuous evaporation of the water, the evaporation mechanism changes, and one of the two following scenarios (Scenarios 2 and 3) shall be encountered. In Scenario 2, see Figure 8.7, the liquid film thickness cannot decrease below a critical value and thus remains constant at δ_c over time (Figure 8.7a), but the wetted area covered with water starts to shrink continuously as long as the evaporation is still ongoing (Figure 8.7b). In other words, the plate's area is partially wetted, and the wetted area is decreasing with time at a constant critical film thickness. In

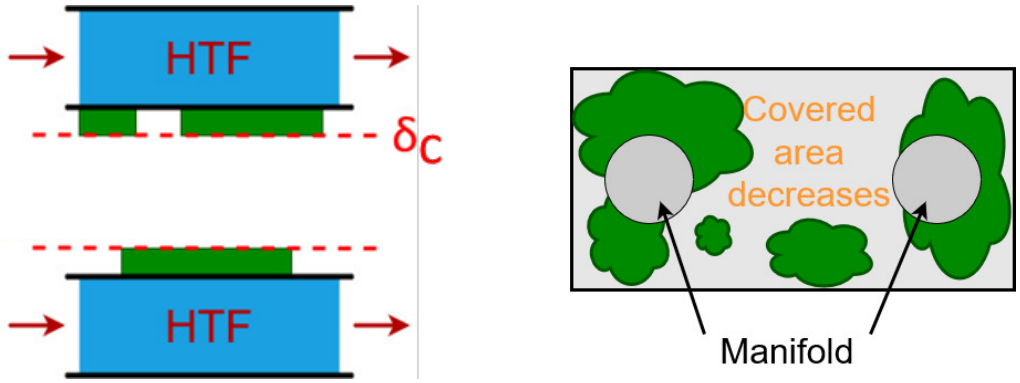

(a) (b)

Fig. 8.7 Scenario 2 and 3 of the thin film evaporation. (a) Side view of a volume element, (b) Top view of a plate

Scenario 3, the value of the critical liquid film thickness δ_c is variable (δ_c=$f(t)$) due to the existence of the dimples and, consequently, both the wetted area and the film thickness shall change continuously as long as the evaporation is still ongoing.

Based on the above discussion for Scenarios 2 and 3, it can be considered that Scenario 3 is a general case for any non-fully covered thin film evaporation, while Scenario 2 represents a special case of Scenario 3, in which the liquid film thickness does not decrease below the critical or minimum value.

Based on the previous discussion of the three scenarios, the correlated film heat transfer coefficient $h_{f,corr}$ can be expressed as:

$$h_{f,corr} = \frac{k_l}{\delta(t)} \frac{A_{wet}(t)}{A_{total}} \tag{8.16}$$

Where k_l, $W.m^{-1}.K^{-1}$, is the thermal conductivity of the liquid water, $A_{wet}(t)$, m^2, is the wetted or the active evaporation area, and $\delta(t)$, m, is the instantaneous film thickness. Depending on whether A_{wet}, m^2, is equal to A_{total}, m^2, (Scenario 1) or less (Scenarios 2 and 3), the following equation is developed for the calculation of δ, m.

$$\delta(t) = \begin{cases} \delta_f(t), & A_{wet} = A_{total} \text{ (Scenario 1)} \\ \delta_c = constant, & A_{wet} < A_{total} \text{ (Scenario 2)} \\ \delta(t), & A_{wet} < A_{total} \text{ (Scenario 3)} \end{cases} \tag{8.17}$$

$\delta_f(t)$, m, is the liquid film thickness if the film is fully covering the evaporator area, i.e., if the liquid film does cover the whole plates' area. Equation 8.18 accounts for $\delta_f(t)$

$$\delta_f(t) = \frac{V_l(t)}{A_{total}} \tag{8.18}$$

where $V_l(t)$ is the liquid water volume in the evaporator heat exchanger (Equation 8.19). The realization of a liquid film with a thickness of δ_f is not inevitable during an evaporation process as the evaporation process can start with non-fully covered liquid film. In this case, the actual initial thickness of the liquid film will equal δ_c and shall either remain invariant during the whole evaporation time (Scenario 2) or may increase during the evaporation because of the collection of the water in the concave, downward-oriented dimples (Scenario 3). However, the wetted area of the plates in both scenarios (2 and 3) shall shrink with the ongoing time of the evaporation process. The water volume as a function of time can be obtained from the following equation.

$$V_l(t) = V_l(t=0) - \frac{t}{\rho_l.h_{fg}} \int_0^t \dot{Q}_{evap}.dt \tag{8.19}$$

Hereby h_{fg}, $J.kg^{-1}$, is the water's latent heat of vaporization and ρ_l, $kg.m^{-3}$, is the density of liquid water.

The ratio A_{wet}/A_{total} appearing in Equation 8.16 is to account for the influence of the active or wetted evaporator area A_{wet}, m^2, on $h_{f,corr}$, as $h_{f,corr}$ shall be associated to A_{total} as done with the evaporation heat transfer coefficient obtained experimentally, i.e. h_f (cf. Equations 8.5 and 8.6). The active or wetted area during thin film evaporation A_{wet}, m^2, can be determined knowing the current water volume $V_l(t)$ in the evaporator heat exchanger:

$$A_{wet}(t) = \frac{V_l(t)}{\delta(t)} \tag{8.20}$$

From Equations 8.16 and 8.20 the following equation for the correlated thin-film evaporative heat transfer coefficient can be derived.

$$h_{f,corr}(t) = \frac{k_l}{\delta(t)^2} \frac{V_l(t)}{A_{total}} \tag{8.21}$$

A sensitivity analysis is conducted for every applied set of operating conditions to find the instantaneous film thickness $\delta(t)$ that best fits $h_{f,corr}$ to the experimentally obtained value of h_f for each time point (t). The best fitted film thickness at a certain time point, $\delta(t)$, is the one that minimizes the sum of the absolute differences between $h_{f,corr}$ and h_f over a time duration $t-\Delta t$ to $t+\Delta t$. For each couple of the residuals (instantaneous values) of the $h_{f,corr}$ and h_f, the following equation is applied to get the instantaneous δ value, $\delta(t)$.

$$\min_{\delta(t)} \sum_{t-\Delta t}^{t+\Delta t} |h_{f,corr}(\delta(t)) - h_f(t)| \tag{8.22}$$

After getting the instantaneous $\delta(t)$ values, Equation 8.20 shall be applied to estimate the instantaneous wetted area $A_{wet}(t)$.

8.2.3 Correlating the Evaporator and the Adsorber performances

It is well-known, that the prime mover for the evaporation process in an adsorption chiller, heat pump or storage unit is the adsorber performance. Indeed, the size and performance matching between both adsorber and evaporator heat exchanger dictate the temporal behaviour of the encountered combined heat and mass transfer process. If the adsorber HEX is more effective than the evaporator HEX, the pressure is expected to decrease very much, which implies a non-isobaric adsorption process. Indeed, the adsorption potential of the adsorbent and the high heat and mass transfer characteristics of the adsorber HEX results in a high adsorption rate (high time rate of change of the water uptake). If the evaporator is not able to supply the water vapour at the dictated rate, based on the adsorber performance, the pressure shall decrease and, consequently the temperature of the evaporated water is going to decrease compared to the heat transfer fluid temperature. The instantaneous value of the overall evaporator heat transfer coefficient (U) depends, consequently, on the measured evaporator power according to equation 8.1 and the logarithmic mean temperature difference ($LMTD$) as defined by equations 8.2 and 8.3. Under extremely good operating conditions for the adsorber (high evaporator and low adsorption-end temperatures) the expected time rate of change of the water uptake is quite high and, in turn, the pressure reduction. This implies an increase in the $LMTD$ and not necessarily an increase in U. On the contrary, moderate operating conditions would imply moderate pressure reduction and, consequently lower $LMTD$ leading to a higher overall evaporator heat transfer coefficient. In the following paragraphs, an attempt to explore the dependency of the evaporator's overall heat transfer coefficient on the adsorption potential and the time rate of change of the water uptake is introduced.

As depicted in Equation 8.2, the overall heat transfer coefficient in the evaporator (U) is proportional to the evaporator power divided by the logarithmic mean temperature difference ($LMTD$), where the proportional factor is the reciprocal value of the total heat transfer area.

$$U \propto \frac{\dot{Q}_{evap}}{LMTD} \tag{8.23}$$

As the amount of the evaporated water from the evaporator equals to the amount adsorbed in the adsorber, the evaporator power $\dot{Q}_{evap}$, W, can be also expressed by the following equation.

$$\dot{Q}_{evap} = m_{ads}.\frac{dw(t)}{dt}.h_{fg} \tag{8.24}$$

Herein, m_{ads}, kg, is the mass of the dry adsorbent filled inside the adsorber heat exchanger, $\frac{dw(t)}{dt}$, s^{-1}, is the time rate of change of the instantaneous water uptake, which is dictated by the adsorber HEX, h_{fg}, $J.kg^{-1}$, is the latent heat of evaporation corresponding to the prevailing evaporator temperature T_{evap}. From the above equation, the following relationship can be formulated.

$$\dot{Q}_{evap} \propto \frac{dw(t)}{dt} \tag{8.25}$$

As depicted in Equation 8.3, the $LMTD$ is a function in $T_{HTF,in}$, $T_{HTF,out}$ and T_{ref}. The instantaneous change in the $LMTD$ value is mainly due to the change in the T_{ref}. Recalling that $T_{HTF,in}$ is constant during each conducted adsorption-evaporation process. Due to the suction of water vapour by the adsorber, the evaporation process in the evaporator is induced leading to a temporal drop in T_{ref} and, consequently, a drop in $T_{HTF,out}$. It can, therefore, be considered that the $LMTD$ is mainly a function in T_{ref}.

$$LMTD = f(T_{HTF,in}, T_{HTF,out}, T_{ref}) = f(T_{ref}) \tag{8.26}$$

T_{ref} is measured implicitly during the conducted adsorption-evaporation processes by means of measuring the temporal vapour pressure in the evaporator (P_{evap}). Tetens equation is used to estimate the temporal T_{ref} out of the measured pressure inside the evaporator [152] as presented in Equation 8.27.

$$T_{ref}(t) = T_{sat}(P_{evap}(t)) = -237.3(\frac{ln(P_{evap}(t)/6.1078)}{ln(P_{evap}(t)/6.1078) - 17.27}) \tag{8.27}$$

In Equation 8.27, P_{evap} is in $mbar$ and the obtained T_{ref} is in C. From Equations 8.26 and 8.27,

$$LMTD = f(P_{evap}) \tag{8.28}$$

The Linear Driving Force (LDF) model [133, 150] gives a relationship for $\frac{dw}{dt}$ as a function in the instantaneous water uptake ($w(t)$), the evaporator pressure P_{evap}, the instantaneous vapor pressure inside the adsorbent (P_{ad}) and the instantaneous adsorbent temperature T_{ad}. The following relationship for P_{evap} can, therefore, be considered.

$$P_{evap} = f(P_{ad}, T_{ad}, \frac{dw}{dt}) \tag{8.29}$$

At the same time, the adsorption potential or the so-called "Dubinin-Polanyi" potential (A), $J.kg^{-1}$,[168] also represents a relation between P_{ad} and T_{ad} as follows.

$$A = -R.T_{ad}.ln(\frac{P_{ad}}{P_{sat}}) = f(P_{ad}, T_{ad}) \tag{8.30}$$

Hereby R, $kJ.mol^{-1}.K-1$, is the universal gas constant and P_{sat}, Pa, is the saturated vapour pressure corresponding to the instantaneous adsorbent temperature T_{ad}. Eliminating T_{ad} and P_{ad} from the relationships 8.29 and 8.30, the following functional relationship can be formulated to couple the $LMTD$ (Equation 8.28) and both the adsorption potential and the time rate of change of the water uptake.

$$LMTD = f(A, \frac{dw}{dt}) \tag{8.31}$$

From the relationships 8.23, 8.25 and 8.31, the following dependency is expected for the overall evaporator heat transfer coefficient on the adsorption potential and the time rate of change of the water uptake inside the adsorbent.

$$U \propto \frac{\frac{dw}{dt}}{f(A, \frac{dw}{dt})} \approx f(A, \frac{dw}{dt}) \tag{8.32}$$

As T_{ad} cannot be directly measured, the instantaneous values of the adsorption potential (A), $kJ.kg^{-1}$, are estimated out of the equilibrium function for the water uptake, w of the utilized adsorbent (Siogel) inside the adsorber heat exchanger [17].

$$A = E.(-ln(\frac{w}{w_o}))^(\frac{1}{n}) \tag{8.33}$$

Where w_o=0.38 $kg.kg^{-1}$, E=220 $kJ.kg^{-1}$ and n=1.1.

In the result section, the type of the function, which best describe the developed functional relationship 8.32 will be presented and the obtained results will be discussed.

8.3 Results and discussion

8.3.1 Visualized investigation on the evaporation mechanism

The visualization of the water evaporation on the surface of one of the refrigerant channels and one of the two refrigerant vapour manifolds inside the investigated evaporator plate

heat exchanger is utilized to determine the evaporation mechanism prevailing during the conducted adsorption-evaporation processes. A number of screenshots taken from the video film recorded by endoscope (1) during the adsorption-evaporation process under the operating condition of 15/30/90 C are presented in Figure 9, showing the vision of endoscope (1) between two successive HTF channels. Six inclined surfaces of different dimples and the flat horizontal surfaces connecting them can be distinguished [169]. The dimples appearing in the vision of endoscope (1) are categorized into (i) two opposite, deep and concave dimples, (ii) two opposite, shallow and concave dimples, and (iii) two opposite and convex dimples brazed together at their interfacial surface. As the thin liquid film is transparent, the visualization of the free surface of the liquid film in the refrigerant channel cannot be clearly observed by the illustrated screenshots. Therefore, red, and blue contours on the boundary of the liquid film covering the surface of the deep and shallow dimples, respectively, have been added to all screenshots illustrated in Figure 8.8. In addition, a short video (**Video 1**) from the recording of endoscope (1) is attached. The video shows the movement (shrinking) of the liquid film during the evaporation, which is detectable by the change in the brightness of the liquid film.

It can be noticed that, at the beginning of the evaporation process (Figure 8.8a) the dimples were covered with a liquid film. After about 5 minutes of evaporation, a small amount of liquid was evaporated, and the liquid film start to shrink. With ongoing time, the liquid film especially in the upper deep concave dimple shrinks noticeably and disappeared completely (Figure 8.8b). Lastly, the liquid film in the lower deep concave dimple evaporated completely and the area appearing in the vision of endoscope (1) became dry at the end of the evaporation process (Figure 8.8c). Indeed, the test unit is filled with 225 g of degassed water, which is higher than the total water amount that can be exchanged between the adsorber and evaporator under the most severe applied operating condition (T_{evap}=15 C and $T_{ads-end}$=T_{cond} = 30 C). This means that the visualization of a totally dry area in a refrigerant channel as depicted by the viewed segment of endoscope (1) and (Figure 8.8c), does not imply that the whole evaporator shall be empty at the end of the evaporation process. Based on the above discussion and, most specifically, the observed film shrinking in all investigated videos from the beginning till the end of the conducted adsorption-evaporation processes, it can be concluded that partially covered (discontinuous) thin film evaporation is the evaporation mechanism taking place in the investigated asymmetric plate heat exchanger acting as a horizontally placed, stagnant evaporator for the adsorption chilling unit presented in Figure 8.1.

Figure 8.9 depicts two screenshots taken from a video film of endoscope (2), which has been recorded simultaneously with the video film of endoscope (1). A short video (**Video 2**))

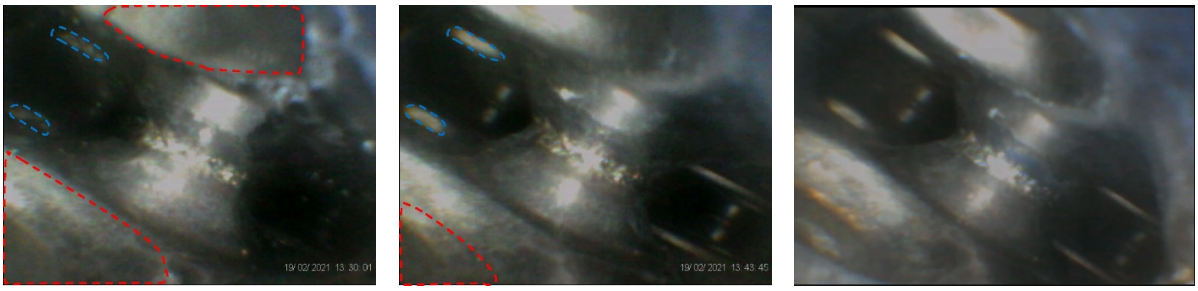

(a) (b) (c)

Fig. 8.8 Screenshots from endoscope (1) between the plates. (a) at the start of the evaporation, (b) upper deep and concave dimple becomes almost dry, (c) at the end of the evaporation

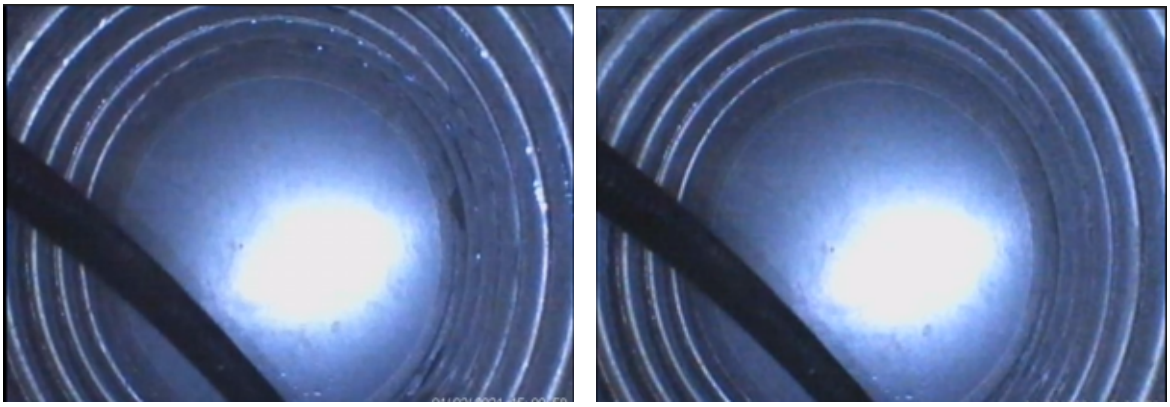

(a) (b)

Fig. 8.9 Screenshots from endoscope (2) in the manifold. (a) at the start of the evaporation, (b) at the end of the evaporation

from the recording of endoscope (2) is attached as well. The visualization of endoscope (2) presented in Figure 8.9a illustrates that from the start of the adsorption-evaporation process the bottom of the manifold is almost dry. However, during the first few seconds after the start of the adsorption-evaporation process, the free water surface at the entrance into all parallel evaporation domains are very much disturbed (Figure 8.9a). This is attributed to the high adsorption rate at the beginning of the adsorption-evaporation process. With ongoing time, the amount of the liquid water existing at the inlet of the refrigerant channels is reduced very much and quite thin liquid film on the edges of the refrigerant channels' inlet was realized. Finally, this thin liquid film on the edges of the refrigerant channels' moves (shrinks) into the inside of the successive evaporation domains (see Figure 8.9b and Video 2). Similar results were obtained in the tests at the other boundary conditions.

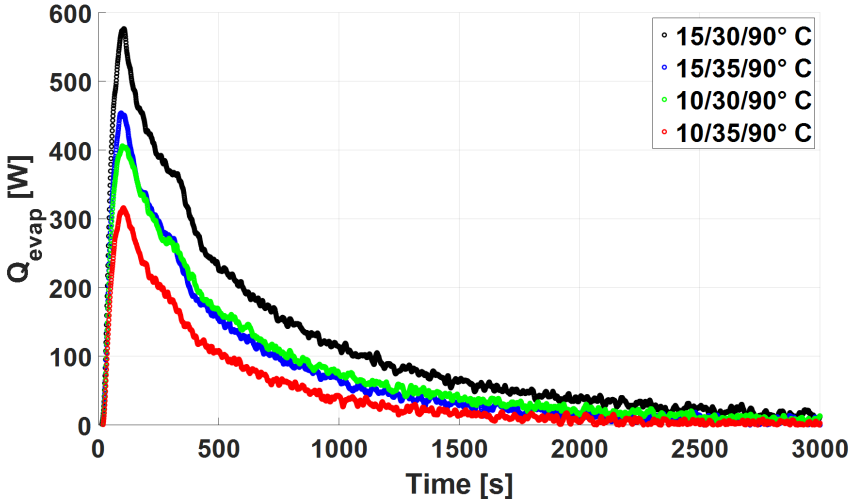

Fig. 8.10 Calculated evaporator power for all applied operating conditions.

8.3.2 Evaporator power and its overall heat transfer coefficient

The measured temporal evaporator powers of all conducted adsorption-evaporation processes are depicted in Figure 8.10. The uncertainty analysis of the obtained $\dot{Q}_{evap}$-values ($\sigma\dot{Q}_{evap}$) according to Equation 8.11 in Section 8.1.4 results in a maximum relative error of $\pm 2\%$. The evaporator power obtained from the adsorption-evaporation process conducted at 15/30/90 °C is nearly twice as high as that conducted at 10/35/90 °C, whereas the evaporator power obtained at 15/35/90 °C is almost equal that obtained at 10/30/90 °C. This implies that the time rate of change of the water uptake at the condition 15/30/90 °C is almost twice as high as that at 10/35/90 °C operating condition. The cooling effect, which is the time integral of the evaporator power as described by Equation 8.25 is directly proportional to the differential water uptake, Δw, $kg.kg^{-1}$, of the adsorbent. Strictly speaking, Δw equals 0.182 $kg.kg^{-1}$ at 15/30/90 °C , and 0.094 $kg.kg^{-1}$ at 10/35/90 °C [17]. At the operating conditions 15/35/90 °C and 10/30/90 °C, almost the same differential water uptakes (Δw) have been obtained; namely, 0.129 $kg.kg^{-1}$ and 0.123 $kg.kg^{-1}$, respectively. The measured evaporator power curves at both boundary conditions (green and blue curves in Figure 8.10) are almost identical, which implies similar temporal course of variation of their respective $\frac{dw}{dt}$.

Figure 8.11 presents the test results to investigate the repeatability of the obtained results out of the experimental setup. Indeed, almost identical evaporator power curves have been measured upon repeating the adsorption-evaporation process at 15/30/90°C (Figure 8.11a) and at 10/35/90 °C (Figure 8.11b). The maximum deviation between the measured curves is less than $\pm$ 0.3%, which proves the repeatability of the experimental setup and the measuring devices.

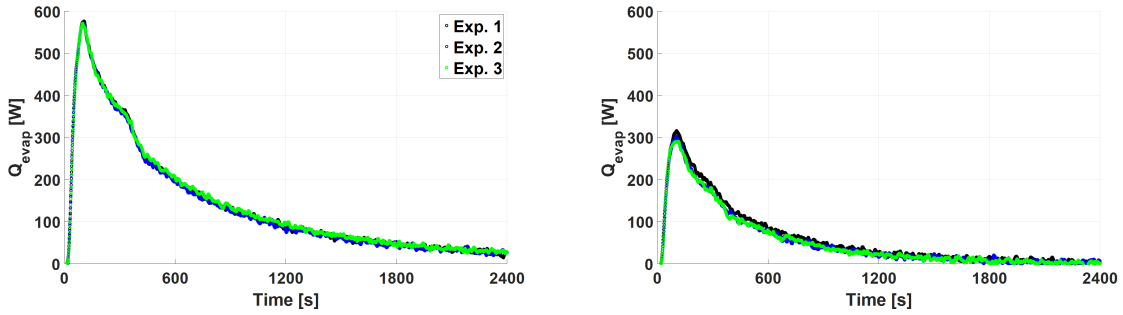

(a) (b)

Fig. 8.11 Calculated evaporator power for repeated adsorption evaporation processes at two different operating conditions. (a) 15/30/90°C, (b) 10/35/90°C

Figure 8.12 shows the estimated evaporator's overall heat transfer coefficient according to Equation 8.2 for repeated adsorption-evaporation processes, at 15/30/90 °C (Figure 8.12a) and at 10/35/90°C (Figure 8.12b). Here also quite similar U curves have been obtained for every applied set of operating condition. This indicates a high stability of the established experimental setup. Since the experimental data of $\dot{Q}_{evap}$ and the $LMTD$ obtained at the beginning of the adsorption-evaporation processes are close to zero, the calculated U-values are characterized by fluctuations with a higher level of uncertainty. The same is valid after 2400 s from the beginning of each process, where the equilibrium condition is approached and, consequently, the temperature difference becomes so low that the uncertainty in measuring that temperature difference and, accordingly, the U-value does remarkably increase. Therefore, the analysis of the experimental results is done for the period between 60 s and 2400 s. In the fixed time range for the analysis, the uncertainty of $\dot{Q}_{evap}$ and the $LMTD$, i.e. $\sigma\dot{Q}_{evap}$ and $\sigma LMTD$ are less than $\pm 2\%$ and $\pm 14\%$, respectively. The corresponding uncertainty of U (σU) is estimated to be less than $\pm 20\%$.

8.3.3 Individual contributions to the overall heat transfer coefficient

Applying Equations 8.1 to 8.9, the contribution of each individual heat transfer coefficient to the overall heat transfer coefficient under the operating condition 15/30/90°C are estimated and presented in Figure 8.13. It is a basic heat transfer knowledge that the overall heat transfer coefficient (U) shall be less than the least heat transfer coefficient in the serial connection according to Figure 8.5, for which the total heat transfer resistance is expressed by Equation 8.4.

It is clearly visible that the film evaporation heat transfer coefficient on the refrigerant side h_f is the one with the major influence on U, followed by the heat transfer coefficient on the

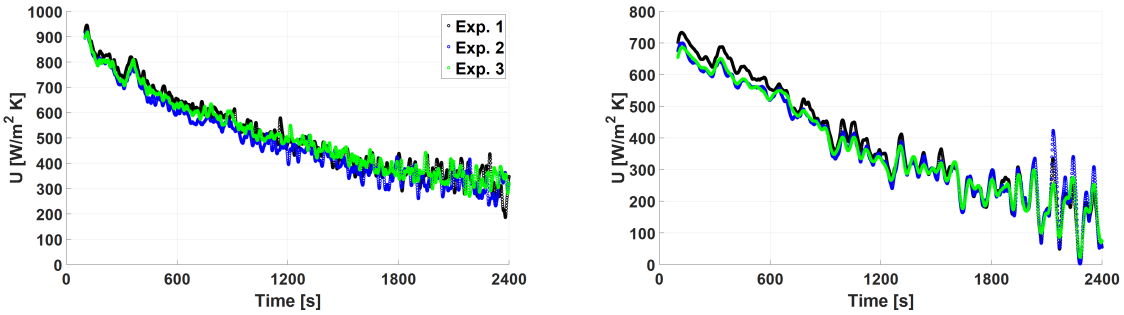

Fig. 8.12 Calculated overall heat transfer coefficient (U) of the evaporator for repeated adsorption evaporation processes at two different operating conditions. (a) 15/30/90°C, (b) 10/35/90°C

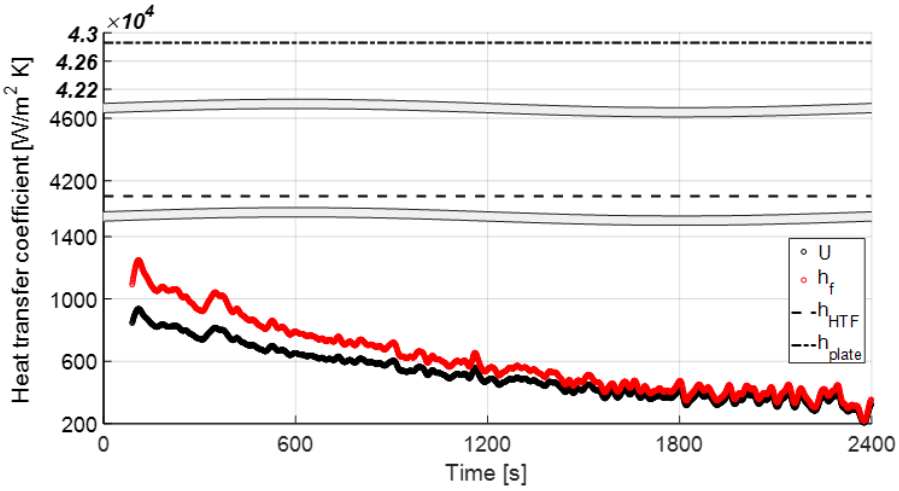

Fig. 8.13 Contributions to the overall heat transfer coefficient

HTF side (h_{HTF}) and the heat transfer coefficient due to conduction through the plate's wall h_{plate}. Based on Equation 8.6, the observed temporal fluctuation appearing in h_f are mainly caused by those existing in U, which are attributed to the main uncertainty in estimating the $LMTD$ as described before. The uncertainty in h_f (σ_{h_f}) based on Equation 8.13 is estimated to be less than $\pm 20\%$ in the determined time range for the analysis.

8.3.4 Fitting $h_{f,corr}$ to $h_{f,exp}$

Figure 8.14 illustrates the temporal courses of; (i) the experimentally obtained overall heat transfer coefficient U of the evaporator (in black), (ii) the experimentally obtained thin film evaporation heat transfer coefficient $h_{f,exp}$ (in red out of Equation 8.6), and (iii) the analytically obtained thin film evaporation heat transfer coefficient $h_{f,corr}$ (in blue according to Equations 8.16-8.21 that best fit the experimentally obtained results at all applied sets of operating conditions.

As shown in Figures 8.14a-8.14d, the value of h_f over the whole investigated boundary conditions decreases from an initial value in the range of 1330 ± 260 down to 160 ± 32 $W.m-2.K^{-1}$ upon approaching the equilibrium condition, at the end of each process. As illustrated in Figures 8.14a-8.14d, both U and h_f values do decrease from a higher value, at the beginning of each process, with time. This implies that each investigated process does start with a partially covered thin film (A_{wet}<A_{total}), which excludes Scenario 1 from the further analysis (cf. Equation 8.17). The obtained values of h_f are very close to the range of the evaporation heat transfer coefficient found for a finned tube flooded evaporator [118], which varies between 465 and 1390 $W.m^{-2}.K^{-1}$ in the evaporator temperature range between 5 and 20°C. In addition, the evaporation heat transfer coefficient measured for a capillary-assisted evaporator with fine fins on the tube's outer surface [170], has been found in range between 500 and 1000 $W.m^{-2}.K^{-1}$, which is not far from the measured range of h_f inside the investigated plate heat exchanger. In [119, 120], capillary assisted evaporator tubes have been investigated against a vacuum pump and a condenser, respectively, showing a very promising performance. Strictly speaking, evaporator U-values up to 5 $KW.m^{-2}.K^{-1}$ have been measured resulting in thin-film evaporative heat transfer coefficients of up to 11300 $W.m^{-2}.K^{-1}$. Because of the applied constant rate of evaporation, dictated by the vacuum pump [119] and the condenser at a lower temperature [120], both overall evaporator and thin film evaporation heat transfer coefficients do increase with time, in contrast to the behaviour obtained in this work, in which the evaporator works against a real adsorber heat exchanger. The presented temporal courses of U and h_f in Figures 8.13 and 8.14 decrease with time because the driving force of evaporation; namely, the adsorption rate decreases with time approaching the equilibrium state at each operating condition. Indeed,

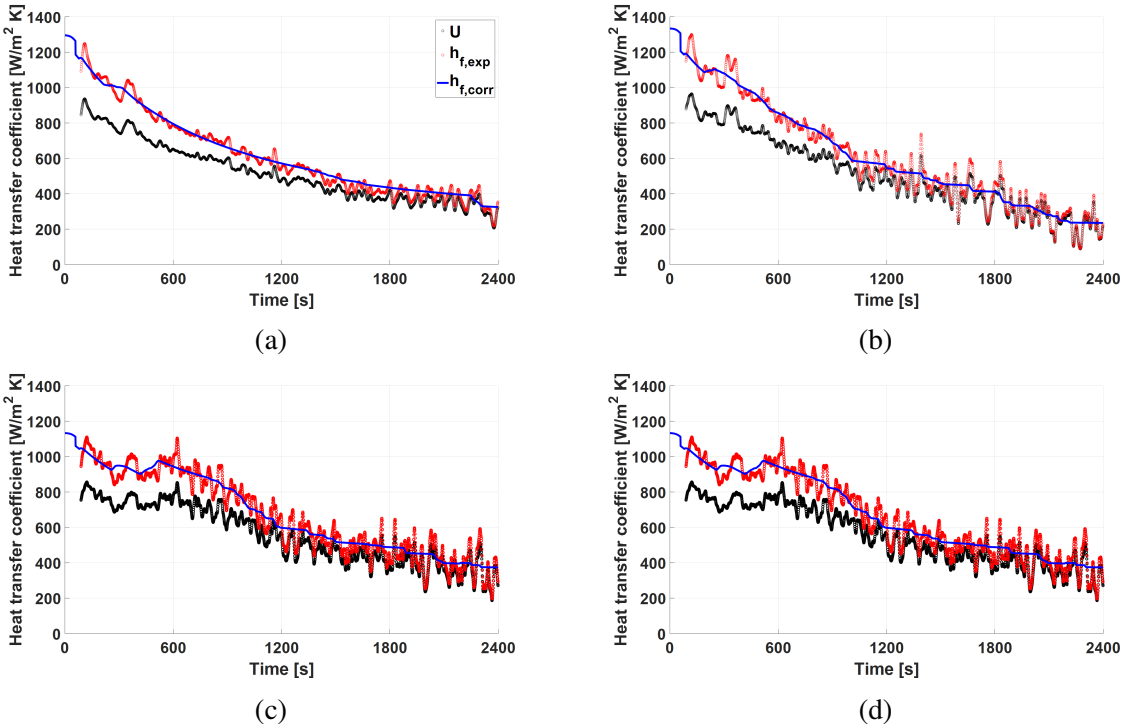

Fig. 8.14 Experimentally obtained U and $h_f(h_{f,exp})$ Together with the correlated thin film heat transfer coefficient ($h_{f,corr}$) at all applied sets of operating conditions, (a) 15/30/90°C, (b) 15/35/90°C, (c) 10/30/90°C and (d) 10/35/90°C

the evaporator performance is highly dependent on the adsorber performance, as already explained in Section 8.2.3 and will be presented in Section 8.3.6. The extremely good values presented in [119, 120] stay, therefore, as upper limits, until the proposed evaporator heat exchangers will be applied and measured against an adsorber heat exchanger.

8.3.5 Correlating the film evaporative heat transfer coefficient h_f to δ and A_{wet}

Figure 8.15 depicts the temporal development of the film thickness δ (in black) and the active or wetted to total area ratio A_{wet}/A_{total} (in red) of the thin liquid film covering the plates' surface in the evaporator at all applied sets of operating conditions. As illustrated in Figure 8.15a, the variation of the liquid film thickness δ is very limited at the operating condition of 15/30/90°C. The film starts with a thickness of δ=0.35 mm, which remains constant within $\pm$0.01 mm over the whole adsorption evaporation time. This implies a constant film thickness, while the wetted to total area ratio decreases continuously with time. This case matches exactly Scenario 2 as described in detail in Section 8.2.2. The quite low

film thickness of 0.35 *mm* can be attributed to the very clean surface due to vacuum brazing and the sandblasting like effect by the residuals of the nickel foils, which are observable on the evaporator surface.

The temporal developments of δ (in black) and A_{wet} (in red) obtained at all other applied sets of operating conditions, depicted in Figures 8.15a-8.15d, are in accordance with Scenario 3, in which both the δ and A_{wet} do vary with time. It can be even observed that, during the first 10 minutes of each process, the film thickness remains constant while A_{wet}/A_{total} decreases, which implies that Scenario 2 is valid over that period. After that time Scenario 3 is realized and continues till the end of the evaporation process. It is worth to notice that the value of δ tends to increase for the three above mentioned sets of operating conditions, as depicted in the Figures 8.15a-8.15d. As mentioned in Section 8.2.2, in case of realizing partially covered, thin film evaporation on a flat surface, a constant and uniform film thickness equal to a minimum or critical value (δ_{min} or δ_c) shall be encountered (Scenario 2). However, the existence of the different dimples on each plate of the studied plate heat exchanger can lead to spatial and temporal variation in the thickness of the partially covered film. In other words, realizing constant film thickness in only a special case, at 15/30/90 °C, while increasing film thickness in the other cases can be interpreted by the effect of the dimples. It is important to emphasize that the temporal film thickness discussed through this work ($\delta(t)$) refers to the instantaneous average thickness of the liquid film, which partially covers the plates' surface of the evaporator. This means that a spatial distribution of the film thickness is expected. Due to the gravity effect, it is expected that on the lower plate of a refrigerant channel, the thickness of the liquid film covering the bottom of the concave, deep and shallow, dimples is higher than the thickness of the film covering the flat surfaces between the dimples of this plate. In fact, the liquid film thickness should be thinner on the flat surfaces between the dimples and increase gradually along the inclined surfaces of the concave dimples towards their centerlines, as observed upon investigating a thin film of water evaporation on spherical, concave and downward oriented surfaces [171]. Concerning the upper plate, the film thickness distribution shall be the opposite case compared to the one described for the lower plate. This means that the liquid film thickness should be thinner on the top plates' concave dimples and increase gradually along the inclined surfaces towards the flat surfaces between the dimples.

The evaporation and, consequently, the shrinking of the thin liquid film leads to tearing the film in several segments. The collection, even partially, of the separated film segments in the lower concave dimples, due to the gravity effect, leads to a continuous increase in film thickness in the lower dimples. This explains the slight increase in the average film thickness observed in Figure 16.b-d after the first 10 to 15 minutes. The high rate of adsorption,

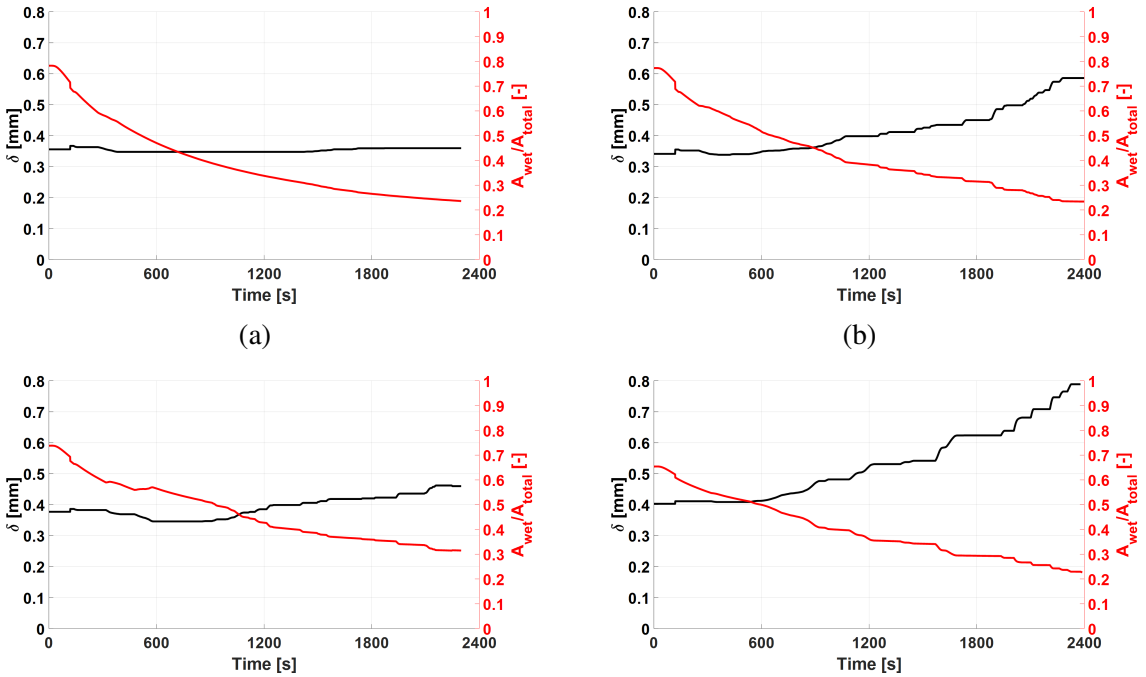

Fig. 8.15 Temporal development of the thin film thickness (δ) and the wetted area to total area ratio (A_{wet}/A_{total}), at all applied sets of operating conditions, (a) 15/30/90°C, (b) 15/35/90°C, (c) 10/30/90°C and (d) 10/35/90°C

Table 8.4 $Slope$ and R^2 values of the linear fittings, U vs $\sqrt{\frac{dw/dt}{A}}$

Process	$T_{evap}/T_{cond}/T_h$ **°C**	$Slope$ $J.m^{-1}.kg^{-0.5}.K^{-0.5}$	R^2
1	15/30/90	1.023E+6	0.9794
2	15/35/90	1.168E+6	0.9545
3	10/30/90	1.045E+6	0.9101
4	10/35/90	1.123E+6	0.9469

which dictates a high evaporation rate may change the situation and results in an invariant film thickness. The above interpretation probably explains why the high evaporation rate associated with the operating condition 15/30/90 °C has resulted in an almost invariant average film thickness as depicted in Figure 8.15a at the operating condition 15/30/90 °C.

Indeed, the existence of a complex topology (such as dimples) on the plates' surface does increase the heat transfer area of the evaporator and enhance the convective heat transfer on the HTF side. However, the above discussion shows the necessity for more dedicated investigations and for a careful design of the plates' topology. Based on Equation 8.15 and the presented results of the film thickness in Figure 8.15, the contact angle (θ) lies between 11° and 16° for water on the tested heat exchanger (Nickel-brazed stainless steel) under the listed operating conditions in Table 8.3. As the liquid film contracts with time over the evaporator's surface, the estimated contact angles are receding contact angles as defined in [165, 166]. The quite low contact angles are attributed to the very clean evaporation surface because of the applied vacuum brazing process.

8.3.6 Adsorber-Evaporator performance correlation

Based on the discussion in Section 8.2.3 and, most specifically Equation 8.32, the "curve fitting" facility built in MATLAB® has been used to find the most suitable functional relationship between the evaporator's overall heat transfer coefficient (U) and the adsorption potential (A) and the time rate of change of the water uptake ($\frac{dw}{dt}$) of the adsorber. The following relation has been found,

$$U \propto (\frac{dw/dt}{A})^n \tag{8.34}$$

With n equal to 0.5, a linear relation between U and $\sqrt{\frac{dw/dt}{A}}$ is observed. Table 8.4 gives the slopes obtained for the four applied sets of operating conditions. The coefficient of determination (R^2) values are also presented in Table 8.4.

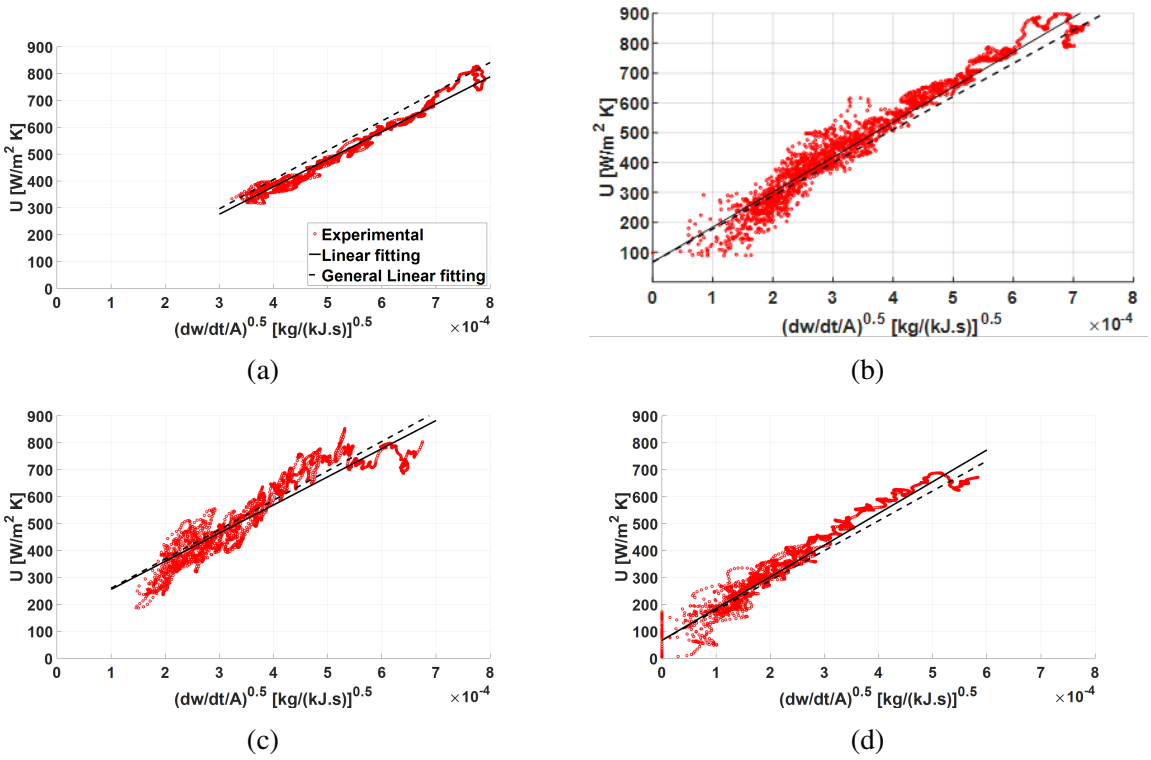

Fig. 8.16 Variation of U against the term $\sqrt{\frac{dw/dt}{A}}$ for all applied sets of operating conditions. (a) 15/30/90°C, (b) 15/35/90°C, (c) 10/30/90°C and (d) 10/35/90°C. Red scattered points represent experimental data, solid and dashed black lines represent the linear fittings

Figure 8.16 presents the experimentally measures U values (scattered red circles) as a function of the term $\sqrt{\frac{dw/dt}{A}}$ at the four applied sets of operating conditions. The solid black lines represent the linear fitting with the given slopes in Table 8.4. The dashed black lines represent the linear fitting with the average slope of 1.089E+06. It can be concluded that, a linear relationship does exist between U and $\sqrt{\frac{dw/dt}{A}}$ for the introduced test unit in Figure 8.1 under each set of the investigated operating conditions.

In order, however, to check, whether the linear relationship between U and $\sqrt{\frac{dw/dt}{A}}$ is valid without limitations or may have an upper limit, both temporal values are presented in Figure 8.17. As can be seen in Figure 8.17a, the term variation of $\sqrt{\frac{dw/dt}{A}}$ attains its maximum value at the operating condition 15/30/90°C followed by the two operating conditions 15/35/90°C and 10/30/90°C. The least values of the term variation of $\sqrt{\frac{dw/dt}{A}}$ are obtained at the operating condition 10/35/90°C. Unless at the first operating condition (15/30/90°C) the temporal U values, depicted in Figure 8.17b do follow the same trend with time as the U values do. Indeed, the maximum obtained evaporator power takes place at

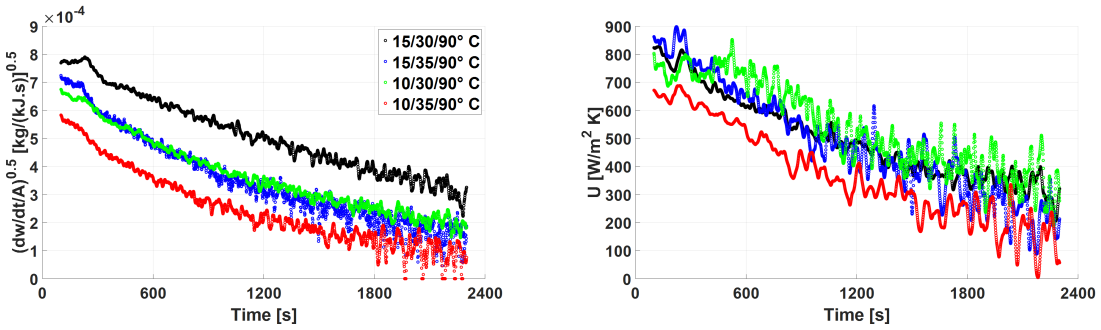

(a) (b)

Fig. 8.17 Temporal variation of the term $\sqrt{\frac{dw/dt}{A}}$ and U at all applied sets of operating conditions, (a) variation of $\sqrt{\frac{dw/dt}{A}}$, (b) variation of U

the operating condition (15/30/90°C), as depicted in Figure 8.10, which is associated with the highest $\sqrt{\frac{dw/dt}{A}}$ values (cf. Figure 8.17a). Both results do not, necessarily, mean that the evaporator's overall heat transfer coefficient $\sqrt{\frac{dw/dt}{A}}$ shall attain its maximum value as depicted in Figure 8.17b. Indeed, the high adsorption rate $\sqrt{\frac{dw/dt}{A}}$ results in a severe reduction in the vapour pressure, and consequently, in the refrigerant (water) temperature (T_{ref}) leading to an increase in the $LMTD$. Based on Equation 8.2, the higher $LMTD$ is responsible for the lower U-values despite the measured higher evaporator power. It can, therefore, be concluded that a linear relationship does exist between $\sqrt{\frac{dw/dt}{A}}$ and the evaporator's overall heat transfer coefficient U until a certain threshold for the $\sqrt{\frac{dw/dt}{A}}$ values, which is defined by the green curve in Figure 8.17a representing the operating condition of 10/30/90°C. Beyond that threshold, the U values tend to decrease again because the $LMTD$ increases due to the induced reduction in the vapour pressure inside the evaporator by the excessively high adsorption rate $\sqrt{\frac{dw/dt}{A}}$.

8.4 Conclusion

This chapter presents the first experimental study on the application of an asymmetric plate heat exchanger, with a closed structure and a horizontal orientation, to act as a stagnant water evaporator heat exchanger under typical operating conditions of an adsorption chiller. The main outcomes of this chapter can be summarized as follows:

- Partially covered (discontinuous) thin film evaporation mechanism was identified by the inserted endoscopes.

- The thermal resistance related to the evaporation heat transfer coefficient (h_f) dominates the total heat transfer resistance and, consequently, the evaporator's overall heat transfer coefficient (U) of the investigated evaporator.
- The film evaporation heat transfer coefficient (h_f) of the investigated evaporator varies from 1330±260 $W.m^{-2}.K^{-1}$ at the beginning of the adsorption-evaporation processes to a minimum of 160±32 $W.m^{-2}.K^{-1}$ upon reaching the end of each process.
- During the evaporation in the investigated plate heat exchanger two scenarios of the following three different scenarios took place, namely Scenario 2 and 3,
  - **Scenario 1**: δ decreases, while A_{wet}=A_{total} and remains invariant
  - **Scenario 2**: δ equals critical value ($\delta = \delta_c$) and remains invariant, while A_{wet}<A_{total} and decreases continuously.
  - **Scenario 3**: both δ and A_{wet}/A_{total} vary with time.
- The values of δ and A_{wet}/A_{total} that best fit the experimental data are in the range of 0.34 to 0.78 *mm* and 0.16 to 0.78, respectively.
- The overall heat transfer coefficient of the evaporator U is linearly proportional to the adsorption rate defined as $\sqrt{\frac{dw/dt}{A}}$, however until a certain threshold, beyond which U decreases because of the excessive pressure reduction and, consequently the increase in the logarithmic mean temperature difference.

The results obtained in this chapter imply the appropriateness of application, which could bring several advantages in terms of the system compactness and, accordingly, the specific power density of the system. Besides, the construction cost of the adsorption appliance may be considerably reduced if the closed-structure PHEs are adopted for use, as there is no need to place the evaporator/condenser inside a vacuum tight chamber, which is quite bulky and costly. The extremely durable operation because of the no corrosion potential is a special added advantage of the introduced technology (Nickel brazing of Stainless-Steel sheets). More investigations are needed, however, to define and optimize the design rules of such special plate heat exchangers for the application in adsorption heat transformation appliances.

Chapter 9

Conclusion and future work

This thesis addresses the application of brazed stainless steel plate heat exchangers in the adsorption appliances as adsorber/desorber (Chapters 3-7) and as evaporator (Chapter 8).

As adsorber/desorber: Commercially available PHEs have been adapted to act as adsorber/desorber and investigated experimentally in the lab. Small-scale adsorbent samples have been prepared in the way that makes them representative to the adsorbent domain inside the investigated APHEs. A Volumetric-Large-Temperature-Jump (V-LTJ) kinetic setup has been used for investigating the adsorption and desoprtion kinetics of the small-scale adsorbent samples under the same applied operating conditions of the APHEs. The small-scale adsorbent samples succeeded to predict the performance of the investigated APHEs. The results of the small-scale adsorbent samples have been utilized in estimating the effective diffusion coefficient of applied adsorbent-adsorbate working pair. The obtained effective diffusion coefficient values have been fed into a newly developed 3D simulation model, which has been validated against the obtained experimental data of the investigated APHEs. The concept of predicting the performance of real APHE using small-scale adsorbent sample and 3D simulation model has been applied on an open structured APHE developed in 2018 by the research team of the Laboratory of Sorption Processes (LSP) at OTH-Regensburg. For better understanding the effect of the heat and mass transfer characteristic lengths (HTCL & MTCL) of the adsorbent domain inside an APHE, adsorbent samples of different HTCL and MTCL have been prepared and investigated using V-LTJ kinetic setup. Finally, the knowledge acquired about the nature of the heat and mass transfer encountered in an APHE have been utilized in developing a large-scale closed structured APHE.

As evaporator: Experimental and analytical investigation on a commercially available closed structured asymmetric PHE oriented horizontally to act as a stagnant water evaporator against a closed structured APHE filled with Siogel. The evaporation mechanism inside

the evaporator has been investigated visually using endoscopes under different operating conditions of an adsorption chiller.

Below, the results and the findings of this thesis are summarized (Section 9.1). Moreover, suggested possible future research are discussed in Section 9.2.

9.1 Summary and conclusion

1- Matching between full-scale and small-scale measurements

The adsorption and desorption kinetics of the two commercial, one of open (GLX30) and one of closed structure (GL50), asymmetric plate heat exchangers adapted to act as adsorbers/desorbers and experimentally investigated in the lab have been compared to the kinetic results of small-scale adsorbent samples dedicatedly prepared to be representative for the adsorbent domains inside the investigated adsorber/desorber plate heat exchangers (APHEs). In addition, the kinetic data of the small-scale adsorbent sample representative to the GLX30 APHE, have been utilized for estimating the expected instantaneous and moving average powers of the evaporator/condenser heat exchanger, against which the GLX30 APHE has been tested. The main outcomes of the study are summarized below:

- A very good matching between the small-scale and full-scale adsorption kinetic measurements has been obtained, with average relative deviation (*RD*) in the characteristic time constant of the exponential form (τ) by 12.3% for the GLX30 and 1.22% for the GL50.

- The APHEs demonstrated faster desorption kinetics than its adsorption kinetics by an average factor of 2.85 for the GLX30 and 3.73 for the GL50. This is in phase with previous measurements and puts in evidence that the duration of the adsorption phase dominates the cycle time of the related adsorption appliance.

- The instantaneous and moving average specific evaporator power estimated from the adsorption kinetics data of the small-scale adsorbent sample representative to the GLX30 APHE matched very well with the ones obtained directly from the evaporator/condenser unit, against which the GLX30 APHE has been tested, with an average relative deviation (*ARD*) between 5.4 and 15.1% for the moving average power.

- The obtained results in this part of the thesis put in evidence the strength of the introduced methodology to mimic the heat and mass transfer characteristics of the adsorbent domain of a plate-type adsorber heat exchanger by dedicatedly design a test

frame for a small-scale adsorbent sample, to be investigated with e.g. the V-LTJ kinetic setup to precisely predict the performance of the real adsorber heat exchangers before building it.

2- Building a 3D simulation model

A heat and mass transfer (HMT) mathematical model was developed to simulate the adsorption and desorption kinetics of an APHE. For estimating the effective diffusion coefficient (D_{eff}) of the water vapour adsorption into the applied adsorbent material (granular Siogel, 0.71-1.0 mm), the model was applied to a 2D geometry representative to a granular Siogel adsorbent sample with negligible interparticle mass transfer resistance, previously investigated using our V-LTJ kinetic setup. The obtained D_{eff} values were fed into the implementation of the mathematical model on the 3D geometries representative of the experimentally investigated APHEs. The main outcomes are summarized below:

- Excellent agreement has been obtained between the numerical results and the experimental data of the two investigated APHEs.
- The distributions of temperature, vapour pressure, and water uptake on the adsorbent domains of the two investigated APHEs were utilized for understanding the effects of the HTCL and MTCL on the APHEs' performance
- The simulation model was used to investigate the effect of the MTCL on the adsorption kinetics of an open-structured APHE. It was found that a MTCL of 28.5 mm or less results in adsorption kinetics very close to the adsorption kinetics obtained in case of negligible interparticle mass transfer resistance (MTCL $\approx$ zero) in the adsorbent domain of an open structured APHE. Strictly speaking, it was found a relative deviation between the time constant (τ) values of the exponential fittings of the adsorption kinetic results obtained at MTCL=28.5 mm and MTCL $\approx$ zero amounts to less than 13.6%.

3- Performance prediction of OTH open-structured APHE

The concept of constructing a test frame to realize a small-scale adsorbent sample representative of a real APHE is applied to predict the performance of a new APHE [82] recently developed by the team of LSP for application in the adsorption appliances. The previously developed transient 2-D and 3-D mathematical models were used to simulate the combined heat and mass transfer in the adsorbent sample under study. The main outcomes of the study are summarized below:

- A micropore diffusion coefficient at infinite temperature (D_∞) of $2 \times 10^{-4}\ m^2 s^{-1}$ and an activation energy of 42.1 $kJ.mol^{-1}$ for the applied AQSOA-Z02-water pair were estimated.

- The obtained results showed the superiority of the introduced APHE over an extruded aluminum heat exchanger coated with a 500 mm thick layer of the same adsorbent. Comparing the obtained results with the literature values for the extruded aluminum heat exchanger, the differential water uptake (8.2 g/100 g) obtained after 300 s of adsorption represents a sound improvement of 310%.

4- Experimental investigation in the HTCL and MTCL effects on the performance of different APHEs

Three adsorbent samples of Siogel grains (0.71-1.0 mm) representative to different APHEs, i.e having different heat and mass transfer characteristic lengths (HTCL and MTCL) were prepared. Sensitivity analysis of the water uptake to the temperature and vapour pressure in the adsorbent domain is applied to interpret the experimental kinetic results. In addition, a new methodology has been introduced to assess the obtained kinetic data in terms of the obtainable *SCP* and the *COP* at different durations for the adsorption-evaporation and desorption-condensation phases in a real intermittent adsorption machine applying the investigated APHEs. Finally, the performance of the investigated APHEs have been compared with an optimized extruded aluminum finned tube adsorber heat exchanger. The main outcomes of the study are summarized below:

- Doubling the HTCL from 1.5 to 3 mm at a MTCL of 58.5 mm resulted in a slight increase in the characteristic time (τ) of the adsorption (less than 19%). This small effect implies that such a MTCL is quite high, so that the mass transfer resistance becomes more dominant than the heat transfer resistance.

- In contrast, doubling the HTCL from 1.5 to 3 mm at a MTCL of 58.5 mm resulted in a significant increase in the characteristic time (τ) of the desorption, up to 52% at the tested boundary conditions.

- At the same HTCL of 1.5 mm (means the same S/m ratio), increasing the MTCL from 27 mm to 58.5 mm results in much slower adsorption kinetics and a slight influence on the desorption kinetics. The characteristic time τ of adsorption increases by 78% and 128% at the operating conditions 5/35/90 and 15/30/90 °C, respectively, while the characteristic time τ of the desorption increases by less than 20%. These results

contradict the known results so far; namely to expect the same adsorption dynamics for samples having the same S/m ratio.

- The obtained results put in evidence the importance of considering the MTCL beside the HTCL upon designing the adsorber plate heat exchangers.
- One of the prepared adsorbent sample is representative to the APHE developed recently by the team of the LSP at OTH Regensburg. The results demonstrated that this APHE offers up to 2.0 times higher *SCP* if compared with the GLX30, which is available in the market as a unique crossflow, gas-liquid plate heat exchanger.
- The optimal *SCP* of the OTH APHE ranges between 157.6 $W.kg^{-1}$, obtained at 5/35/90°C, t_{ads}=140 s and t_{des}=90 s, to 453.6 $W.kg^{-1}$ obtained at 15/30/90 °C and t_{ads} and t_{des} of 190 and 90 s, respectively.
- The OTH APHE performs quite comparably to an optimized extruded aluminium finned-tube heat exchanger [26]. However, the OTH APHE has the advantage of highest resistivity against corrosion, which takes place if aluminium is applied as a construction material with all known refrigerants for TDAd systems.

5- Dedicatedly designed closed structured APHE

The major achievement of this thesis is a novel stainless steel closed asymmetric plate heat exchanger (APHE) designed for application as an adsorber/desorber in adsorption systems. It is the first ever specially designed closed APHE. In addition to the corrosion-free advantage of a stainless steel APHE, the most attractive advantage of using a closed-structured APHE is that it does not need to be housed in a vacuum chamber. Using the previously developed 3D simulation model, a design optimization was performed. The main results are summarized below:

- A quite uniform temperature distribution over the active surface of the plate pairs of the APHE is achieved within two minutes (Figure 7.13b) after the start of the sudden temperature change of the HTF inlet temperature, which corresponds to the operating conditions of 10/30/90 °C of a Siogel-water adsorption chiller. The applied flow rate of the HTF is 1 LPM/plate pair.
- The obtained total pressure drop of the HTF due to hydraulic resistance within a plate pair at 1 LPM/plate pair amounts 0.8 kPa.

- Increasing the flow rate to 2 LPM/plate-pair does not result in a noticeable improvement in the temporal variation of the plate average surface temperature . However, it does result in a noticeable increase in the pressure drop of the HTF, from 1.85 kPa at 1.8 LPM/plate pair to 2.16 kPa at 2 LPM/plate pair.
- The optimal MTCL for the new closed structured APHE is defined as 30 mm.
- At a target *COP* of 0.5, the new closed structured APHE with HTCL=1.5 m demonstrated a *SCP* that is 18.2% higher than the open structured OTH APHE at 10/30/90°C.
- At the 10/35/90°C operating conditions, the new closed-structured APHE provides 158.6 $W.kg^{-1}$ at the target *COP*, while the open structured OTH APHE introduced in Chapter 5 could not achieve a *COP* higher than 0.458.

6- Investigation of a closed structured plate heat exchanger as an evaporator

Experimental study on the application of an asymmetric plate heat exchanger, with a closed structure and a horizontal orientation, to act as a stagnant water evaporator heat exchanger under typical operating conditions of an adsorption heat transformation appliance was performed. The main outcomes can be summarized as follows:

- Partially covered (discontinuous) thin film evaporation mechanism was identified by the applied endoscopes.
- The thermal resistance related to the film evaporation heat transfer coefficient (h_f) dominates the total heat transfer resistance and, consequently, the evaporator's overall heat transfer coefficient (U) of the investigated evaporator.
- The film evaporation heat transfer coefficient (h_f) of the investigated evaporator varies from 1330$\pm$260 $W.m^{-2}.K^{-1}$ at the beginning of the adsorption-evaporation processes to a minimum of 160$\pm$32 $W.m^{-2}.K^{-1}$ upon reaching the end of each process.
- During the evaporation in the investigated plate heat exchanger two scenarios of the following three different scenarios took place, namely Scenario 2 and 3,
  - **Scenario 1**: δ decreases, while A_{wet}=A_{total} and remains invariant
  - **Scenario 2**: δ equals critical value ($\delta = \delta_c$) and remains invariant, while A_{wet}<A_{total} and decreases continuously.

- **Scenario 3**: both δ and A_{wet}/A_{total} vary with time.

- The values of δ and A_{wet}/A_{total} that best fit the experimental data are in the range of 0.34 to 0.78 *mm* and 0.16 to 0.78, respectively.

- The overall heat transfer coefficient of the evaporator U is linearly proportional to the adsorption rate defined as $\sqrt{\frac{dw/dt}{A}}$, however until a certain threshold, beyond which U decreases because of the excessive pressure reduction and, consequently the increase in the logarithmic mean temperature difference.

9.2 Future work

1- Fabrication of the closed structured APHE

The design of the closed structured APHE presented in this thesis should be reconsidered for different adsorbent-adsorbate working pairs. The mechanical stresses associated to the plate forming process should be numerically simulated using COMSOL Multiphysics software. Subsequently, the designs should be discussed with a manufacturer. The design associated to the working pair that gives the best performance should be fabricated and investigated in the laboratory under the relevant operating conditions. If necessary, a design review should be performed.

2- Closed structured evaporator/condenser plate heat exchanger

The evaporation and condensation of water in closed structured asymmetric plate heat exchangers under the relevant boundary conditions of the adsorption appliances has not been fully investigated. To best of our knowledge, only this thesis and the master's thesis of Sebastian Nowak [172] (carried out at the LSP of the OTH Regensburg) have dealt with the appropriateness of the application of such heat exchangers in adsorption appliances.

It is suggested to perform experimental visualisation with higher precision endoscopes and numerical investigations on the evaporation and condensation of different refrigerants (water, methanol and ethanol) in closed-structured asymmetric PHEs to cover the following aspects:

- Better fundamental understanding of the effects of the different design parameters on the evaporation and condensation processes. such as

  (1) Different plate topologies

(2) Different sizes, i.e. different adsorber/desorber to evaporator/condenser ratios

(3) Different brazing materials, mainly nickel and copper, as the brazing material of the PHE has significant effect on the liquid film stability inside the evaporation and the droplets attaching and detaching during the condensation.

- Developing useful correlations for the performance prediction of such special PHEs when employed as evaporators and condensers
- Optimizing the design of such PHEs for application as evaporators and condensers in different adsorption system configurations.
- Develop a comprehensive computational fluid dynamics (CFD) model that is calibrated based on the outcomes of the experimental works.
- Conduct parametric studies based on the developed CFD model.

3- Development of compact vacuum valves

The development of closed-structured plate heat exchangers for use in adsorption systems should result in compact systems. However, the size of the vacuum valves integrated into the adsorption system strongly influences the overall compactness of the adsorption system. The research team of the LSP at OTH Regensburg has recently developed low-cost, vacuum valves for application in the adsorption systems. However, further downsizing of the valves is necessary to realize more compact adsorption systems.

4- 2-bed adsorption chiller prototype integrating the fabricated APHEs

A prototype of a 2-bed adsorption chiller is to be built, utilizing the fabricated APHEs. The prototype is to be investigated in the laboratory under relevant operating conditions. Optimization for the operating cycle time and the control strategy, concerning the time allocation between the adsorption and desorption phases, deems quite necessary. Investigation of the application of heat and mass recovery techniques is also suggested as a future work.

References

[1] IEA, : Iea (2022), heating, https://www.iea.org/reports/heating (2022).
URL https://www.iea.org/reports/heating

[2] A. Martin, Air conditioning biggest factor in growing electricity demand (2020).
URL https://www.statista.com/chart/14401/growing-demand-for-air-conditioning-and-energy/

[3] L. Wang, R. Wang, J. Wu, Y. Xu, S. Wang, Design, simulation and performance of a waste heat driven adsorption ice maker for fishing boat, 03605442 31 (2-3) (2006) 244–259. doi:10.1016/j.energy.2005.03.006.

[4] T. Miyazaki, A. Akisawa, The influence of heat exchanger parameters on the optimum cycle time of adsorption chillers, 13594311 29 (13) (2009) 2708–2717. doi:10.1016/j.applthermaleng.2009.01.005.

[5] F. Meunier, Adsorptive cooling: a clean technology, Clean Products and Processes 3 (1) (2001) 0008–0020. doi:10.1007/s100980000096.

[6] X. H. Li, X. H. Hou, X. Zhang, Z. X. Yuan, A review on development of adsorption cooling—novel beds and advanced cycles, Energy Conversion and Management 94 (2015) 221–232. doi:10.1016/j.enconman.2015.01.076.

[7] R. Best, W. Rivera, A review of thermal cooling systems, 13594311 75 (2015) 1162–1175. doi:10.1016/j.applthermaleng.2014.08.018.

[8] D. Aydin, S. P. Casey, S. Riffat, The latest advancements on thermochemical heat storage systems, Renewable and Sustainable Energy Reviews 41 (2015) 356–367. doi:10.1016/j.rser.2014.08.054.

[9] N. Yu, R. Z. Wang, L. W. Wang, Sorption thermal storage for solar energy, Progress in Energy and Combustion Science 39 (5) (2013) 489–514. doi:10.1016/j.pecs.2013.05.004.

[10] G. An, L. Wang, Z. Wang, J. Gao, Study on working pairs of sorption type air conditioner for electric vehicles under different temperature zones, Journal of Thermal Science 28 (5) (2019) 1004–1014. doi:10.1007/s11630-019-1132-6.

[11] L. Jiang, R. Z. Wang, J. B. Li, L. W. Wang, A. P. Roskilly, Performance analysis on a novel sorption air conditioner for electric vehicles, Energy Conversion and Management 156 (2018) 515–524. doi:10.1016/j.enconman.2017.11.077.

[12] D. Yang, Y. Huo, Q. Zhang, J. Xie, Z. Yang, Recent advances on air heating system of cabin for pure electric vehicles: A review, Heliyon 8 (10) (2022) e11032. doi:10.1016/j.heliyon.2022.e11032.

[13] H. Demir, M. Mobedi, S. Ülkü, A review on adsorption heat pump: Problems and solutions, Renewable and Sustainable Energy Reviews 12 (9) (2008) 2381–2403. doi:10.1016/j.rser.2007.06.005.

[14] F. Meunier, Adsorption heat powered heat pumps, 13594311 61 (2) (2013) 830–836. doi:10.1016/j.applthermaleng.2013.04.050.

[15] U. Močnik, B. Blagojevič, S. Muhič, Numerical analysis with experimental validation of single-phase fluid flow in a dimple pattern heat exchanger channel, Strojniški vestnik – Journal of Mechanical Engineering 66 (9) (2020) 544–553. doi:10.5545/sv-jme.2020.6776.

[16] K. Ng, H. Chua, C. Chung, C. Loke, T. Kashiwagi, A. Akisawa, B. Saha, Experimental investigation of the silica gel–water adsorption isotherm characteristics, Applied Thermal Engineering 21 (16) (2001) 1631–1642. doi:https://doi.org/10.1016/S1359-4311(01)00039-4.

[17] A. Sapienza, A. Velte, I. Girnik, A. Frazzica, G. Füldner, L. Schnabel, Y. Aristov, "water - silica siogel" working pair for adsorption chillers: Adsorption equilibrium and dynamics, 09601481 110 (2017) 40–46. doi:10.1016/j.renene.2016.09.065.

[18] A. Frazzica, A. Freni, Adsorbent working pairs for solar thermal energy storage in buildings, 09601481 110 (2017) 87–94. doi:10.1016/j.renene.2016.09.047.

[19] S. Graf, F. Redder, U. Bau, M. de Lange, F. Kapteijn, A. Bardow, Toward optimal metal–organic frameworks for adsorption chillers: Insights from the scale–up of mil–101(cr) and nh 2 –mil–125, 2194-4288 8 (1) (2020). doi:10.1002/ente.201900617.

[20] A. Freni, L. Bonaccorsi, L. Calabrese, A. Caprì, A. Frazzica, A. Sapienza, Sapo-34 coated adsorbent heat exchanger for adsorption chillers, 13594311 82 (2015) 1–7. doi:10.1016/j.applthermaleng.2015.02.052.

[21] S. Qian, K. Gluesenkamp, Y. Hwang, R. Radermacher, H.-H. Chun, Cyclic steady state performance of adsorption chiller with low regeneration temperature zeolite, Energy 60 (2013) 517–526. doi:https://doi.org/10.1016/j.energy.2013.08.041.

[22] X. Wang, H. T. Chua, K. C. Ng, Experimental investigation of silica gel–water adsorption chillers with and without a passive heat recovery scheme, International Journal of Refrigeration 28 (5) (2005) 756–765. doi:https://doi.org/10.1016/j.ijrefrig.2004.11.011.

[23] K. Alam, M. Khan, A. Uyun, Y. Hamamoto, A. Akisawa, T. Kashiwagi, Experimental study of a low temperature heat driven re-heat two-stage adsorption chiller, Applied Thermal Engineering 27 (10) (2007) 1686–1692, heat transfer and sustainable energy technologies. doi:https://doi.org/10.1016/j.applthermaleng.2006.07.006.

[24] A. Frazzica, G. Füldner, A. Sapienza, A. Freni, L. Schnabel, Experimental and theoretical analysis of the kinetic performance of an adsorbent coating composition for use in adsorption chillers and heat pumps, Applied Thermal Engineering 73 (1) (2014) 1022–1031. doi:https://doi.org/10.1016/j.applthermaleng.2014.09.004.

[25] A. Sapienza, S. Santamaria, A. Frazzica, A. Freni, Influence of the management strategy and operating conditions on the performance of an adsorption chiller, 03605442 36 (9) (2011). doi:10.1016/j.energy.2011.07.020.

[26] F. Lanzerath, U. Bau, J. Seiler, A. Bardow, Optimal design of adsorption chillers based on a validated dynamic object-oriented model, 2374-4731 21 (3) (2015) 248–257. doi:10.1080/10789669.2014.990337.

[27] T. Núñez, W. Mittelbach, H.-M. Henning, Development of an adsorption chiller and heat pump for domestic heating and air-conditioning applications, Applied Thermal Engineering 27 (13) (2007) 2205–2212, heat Powered Cycles – 04. doi:https://doi.org/10.1016/j.applthermaleng.2005.07.024.

[28] Yu I Aristov, M M Tokarev, G Cacciola, G Restuccia, Selective water sorbents for multiple applications, 1. caci2 confined in mesopores of silica gel: sorption properties 59.

[29] Yu.I Aristov, G Restuccia, G Cacciola, V.N Parmon, A family of new working materials for solid sorption air conditioning systems, 13594311 22 (2) (2002). doi:10.1016/S1359-4311(01)00072-2.

[30] A. Pal, K. Uddin, B. B. Saha, K. Thu, H.-S. Kil, S.-H. Yoon, J. Miyawaki, A benchmark for co2 uptake onto newly synthesized biomass-derived activated carbons, Applied Energy 264 (2020) 114720. doi:10.1016/j.apenergy.2020.114720.

[31] A. Pal, K. Thu, S. Mitra, I. I. El-Sharkawy, B. B. Saha, H.-S. Kil, S.-H. Yoon, J. Miyawaki, Study on biomass derived activated carbons for adsorptive heat pump application, International Journal of Heat and Mass Transfer 110 (2017) 7–19. doi:10.1016/j.ijheatmasstransfer.2017.02.081.

[32] F. Jeremias, A. Khutia, S. K. Henninger, C. Janiak, Mil-100(al, fe) as water adsorbents for heat transformation purposes—a promising application, 0959-9428 22 (20) (2012). doi:10.1039/C2JM15615F.

[33] H.-C. Zhou, J. R. Long, O. M. Yaghi, Introduction to metal–organic frameworks, 0009-2665 112 (2) (2012). doi:10.1021/cr300014x.

[34] B. B. Saha, I. I. El-Sharkawy, T. Miyazaki, S. Koyama, S. K. Henninger, A. Herbst, C. Janiak, Ethanol adsorption onto metal organic framework: Theory and experiments, 03605442 79 (2015). doi:10.1016/j.energy.2014.11.022.

[35] M. F. de Lange, B. L. van Velzen, C. P. Ottevanger, K. J. F. M. Verouden, L.-C. Lin, T. J. H. Vlugt, J. Gascon, F. Kapteijn, Metal–organic frameworks in adsorption-driven heat pumps: The potential of alcohols as working fluids, 0743-7463 31 (46) (2015). doi:10.1021/acs.langmuir.5b03272.

[36] K. A. Rocky, A. Pal, T. H. Rupam, M. L. Palash, B. B. Saha, Recent advances of composite adsorbents for heat transformation applications, Thermal Science and Engineering Progress 23 (2021) 100900. doi:10.1016/j.tsep.2021.100900.

[37] Y. I. Aristov, Challenging offers of material science for adsorption heat transformation: A review, 13594311 50 (2) (2013). doi:10.1016/j.applthermaleng.2011.09.003.

[38] L. F. Cabeza, A. Solé, C. Barreneche, Review on sorption materials and technologies for heat pumps and thermal energy storage, 09601481 110 (2017). doi:10.1016/j.renene.2016.09.059.

[39] L.G. Gordeeva, Yu.I. Aristov, Adsorptive heat storage and amplification: New cycles and adsorbents, 03605442 167 (2019). doi:10.1016/j.energy.2018.10.132.

[40] B. B. Saha, K. Uddin, A. Pal, K. Thu, Emerging sorption pairs for heat pump applications: an overview, JMST Advances 1 (1-2) (2019) 161–180. doi:10.1007/s42791-019-0010-4.

[41] S. W. Hong, S. H. Ahn, O. K. Kwon, J. D. Chung, Optimization of a fin-tube type adsorption chiller by design of experiment, 01407007 49 (2015) 49–56. doi:10.1016/j.ijrefrig.2014.09.022.

[42] H. Bahrehmand, M. Bahrami, Optimized sorber bed heat and mass exchangers for sorption cooling systems, 13594311 185 (2021). doi:10.1016/j.applthermaleng.2020.116348.

[43] G. B. Abadi, M. Bahrami, Combined evaporator and condenser for sorption cooling systems: A steady-state performance analysis, 03605442 209 (2020). doi:10.1016/j.energy.2020.118504.

[44] T.X. Li, R.Z. Wang, L.W. Wang, Z.S. Lu, C.J. Chen, Performance study of a high efficient multifunction heat pipe type adsorption ice making system with novel mass and heat recovery processes, 12900729 46 (12) (2007). doi:10.1016/j.ijthermalsci.2006.12.003.

[45] I.S. Girnik, W. Lombardo, A. Sapienza, Yu.I. Aristov, Pressure- and temperature-initiated adsorption of water vapour in a finned flat-tube adsorber, Energy Conversion and Management 258 (2022) 115487. doi:10.1016/j.enconman.2022.115487.

[46] M. G. Gado, S. Ookawara, S. Nada, I. I. El-Sharkawy, Hybrid sorption-vapor compression cooling systems: A comprehensive overview, Renewable and Sustainable Energy Reviews 143 (2021) 110912. doi:10.1016/j.rser.2021.110912.

[47] X. Gai, J. Song, L. Wang, B. He, Numerical analysis of heat pipe-assisted finned adsorber with fam-z02/water pair for vehicle air conditioning, Applied Thermal Engineering 213 (2022) 118715. doi:10.1016/j.applthermaleng.2022.118715.

[48] H. Furukawa, F. Gándara, Y. B. Zhang, J. Jiang, W. L. Queen, M. R. Hudson, O. M. Yaghi, Water adsorption in porous metal-organic frameworks and related materials, 15205126 136 (11) (2014) 4369–4381. doi:10.1021/ja500330a.

[49] A. Sapienza, A. Frazzica, A. Freni, Y. Aristov, Dramatic effect of residual gas on dynamics of isobaric adsorption stage of an adsorptive chiller, 13594311 96 (2016) 385–390. doi:10.1016/j.applthermaleng.2015.09.031.

[50] L. Bonaccorsi, L. Calabrese, A. Freni, E. Proverbio, G. Restuccia, Zeolites direct synthesis on heat exchangers for adsorption heat pumps, Vol. 50, 2013, pp. 1590–1595. doi:10.1016/j.applthermaleng.2011.10.028.

[51] L. Bonaccorsi, E. Proverbio, Synthesis of thick zeolite 4a coatings on stainless steel, 13871811 74 (1-3) (2004) 221–229. doi:10.1016/j.micromeso.2004.06.024.

[52] M. Tatlier, A. e Erdem-S enatalar, The effects of thermal and mass diffusivities on the performance of adsorption heat pumps employing zeolite synthesized on metal supports, 13871811 28 (1999).

[53] A. Freni, B. Dawoud, L. Bonaccorsi, S. Chmielewski, A. Frazzica, L. Calabrese, G. Restuccia, Springer briefs in applied sciences and technology characterization of zeolite-based coatings for adsorption heat pumps (2015).
URL http://www.springer.com/series/8884

[54] A. Freni, F. Russo, S. Vasta, M. Tokarev, Yu I. Aristov, G. Restuccia, An advanced solid sorption chiller using sws-1l, 13594311 27 (13) (2007) 2200–2204. doi:10.1016/j.applthermaleng.2005.07.023.

[55] L. X. Gong, R. Z. Wang, Z. Z. Xia, C. J. Chen, Design and performance prediction of a new generation adsorption chiller using composite adsorbent, Energy Conversion and Management 52 (6) (2011) 2345–2350. doi:10.1016/j.enconman.2010.12.036.

[56] S. Santamaria, A. Sapienza, A. Frazzica, A. Freni, I. S. Girnik, Y. I. Aristov, Water adsorption dynamics on representative pieces of real adsorbers for adsorptive chillers, Applied Energy 134 (2014) 11–19. doi:10.1016/j.apenergy.2014.07.053.

[57] V. Palomba, B. Dawoud, A. Sapienza, S. Vasta, A. Frazzica, On the impact of different management strategies on the performance of a two-bed activated carbon/ethanol refrigerator: An experimental study, Energy Conversion and Management 142 (2017) 322–333. doi:10.1016/j.enconman.2017.03.055.

[58] L. Caprì, A. Frazzica, L. Calabrese, Recent developments in coating technologies for adsorption heat pumps: A review 10 (9) (2020).

[59] L. Calabrese, L. Bonaccorsi, E. Proverbio, Corrosion protection of aluminum 6061 in nacl solution by silane-zeolite composite coatings, 15470091 9 (5) (2012) 597–607. doi:10.1007/s11998-011-9391-5.

[60] A. Sharafian, M. Bahrami, Assessment of adsorber bed designs in waste-heat driven adsorption cooling systems for vehicle air conditioning and refrigeration, Renewable and Sustainable Energy Reviews 30 (2014). doi:10.1016/j.rser.2013.10.031.

[61] Z. Rogala, Adsorption chiller using flat-tube adsorbers – performance assessment and optimization, 13594311 121 (2017). doi:10.1016/j.applthermaleng.2017.04.059.

[62] S. D. Waszkiewicz, M. J. Tierney, H. Saidani Scott, Development of coated, annular fins for adsorption chillers, 13594311 29 (11-12) (2009) 2222–2227. doi:10.1016/j.applthermaleng.2008.11.004.

[63] B. Dawoud, Entwicklung eines innovativen gasbetriebenen Zeolith-Kompaktgerätes; Ein Beitrag zur Steigerung der Energieumwandlungseffizienz und Emmisionsminderung (Phase II), VDI Publishing Ltd, 2013.

[64] E. Proverbio, L. Calabrese, A. Caprì, L. Bonaccorsi, B. Dawoud, A. Frazzica, Susceptibility to corrosion of aluminium alloy components in ethanol adsorption chiller, 09601481 110 (2017) 174–179. doi:10.1016/j.renene.2016.08.042.

[65] A. Sharafian, S. M. N. Mehr, P. C. Thimmaiah, W. Huttema, M. Bahrami, Effects of adsorbent mass and number of adsorber beds on the performance of a waste heat-driven adsorption cooling system for vehicle air conditioning applications, 03605442 112 (2016). doi:10.1016/j.energy.2016.06.099.

[66] J. Canivet, A. Fateeva, Y. Guo, B. Coasne, D. Farrusseng, Water adsorption in mofs: Fundamentals and applications (2014). doi:10.1039/c4cs00078a.

[67] B. Mette, H. Kerskes, H. Drück, H. Müller-Steinhagen, Experimental and numerical investigations on the water vapor adsorption isotherms and kinetics of binderless zeolite 13x, 00179310 71 (2014) 555–561. doi:10.1016/j.ijheatmasstransfer.2013.12.061.

[68] S. Kayal, S. Baichuan, B. B. Saha, Adsorption characteristics of aqsoa zeolites and water for adsorption chillers, 00179310 92 (2016) 1120–1127. doi:10.1016/j.ijheatmasstransfer.2015.09.060.

[69] Y. Aristov, Concept of adsorbent optimal for adsorptive cooling/heating, 13594311 72 (2) (2014) 166–175. doi:10.1016/j.applthermaleng.2014.04.077.

[70] U. Bau, From dynamic simulation to optimal design and control of adsorption energy systems, Phd, Aachen, Germany (2018).

[71] A. Çağlar, The effect of fin design parameters on the heat transfer enhancement in the adsorbent bed of a thermal wave cycle, 13594311 104 (2016) 386–393. doi:10.1016/j.applthermaleng.2016.05.092.

[72] J. Li, M. Kubota, F. Watanabe, N. Kobayashi, M. Hasatani, Optimal design of a fin-type silica gel tube module in the silica gel/water adsorption heat pump, 0021-9592 37 (4) (2004). doi:10.1252/jcej.37.551.

[73] H. Niazmand, I. Dabzadeh, Numerical simulation of heat and mass transfer in adsorbent beds with annular fins, 01407007 35 (3) (2012) 581–593. doi:10.1016/j.ijrefrig.2011.05.013.

[74] M. Kubota, T. Ueda, R. Fujisawa, J. Kobayashi, F. Watanabe, N. Kobayashi, M. Hasatani.

[75] R. Fujisawa, K. Tauchi, F. Watanabe, N. Kobayashi, M. Hasatani, Operating properties of an adsorption heat pump driven by a fuel cell, 0386-216X 28 (3) (2002). doi:10.1252/kakoronbunshu.28.247.

[76] M. M. Abd-Elhady, A. M. Hamed, Effect of fin design parameters on the performance of a two-bed adsorption chiller, 01407007 113 (2020). doi:10.1016/j.ijrefrig.2020.01.006.

[77] B. Golparvar, H. Niazmand, A. Sharafian, A. A. Hosseini, Optimum fin spacing of finned tube adsorber bed heat exchangers in an exhaust gas-driven adsorption cooling system, Applied Energy 232 (2018) 504–516. doi:10.1016/j.apenergy.2018.10.002.

[78] L. Gordeeva, A. Frazzica, A. Sapienza, Y. Aristov, A. Freni, Adsorption cooling utilizing the "libr/silica - ethanol" working pair: Dynamic optimization of the adsorber/heat exchanger unit, 03605442 75 (2014) 390–399. doi:10.1016/j.energy.2014.07.088.

[79] A. Hajji, S. Khalloufi, Improving the performance of adsorption heat exchangers using a finned structure, 00179310 39 (8) (1996) 1677–1686. doi:10.1016/0017-9310(95)00254-5.

[80] M. Darvish, H. Bahrehmand, M. Bahrami, An analytical design tool for pin fin sorber bed heat/mass exchanger, 01407007 131 (2021) 381–393. doi:10.1016/j.ijrefrig.2021.07.027.

[81] S.W. Hong, O.K. Kwon, J.D. Chung, Application of an embossed plate heat exchanger to adsorption chiller, 01407007 65 (2016). doi:10.1016/j.ijrefrig.2016.02.012.

[82] B. Dawoud, European patent application, ep 3 382 313 a1, 03.10 (2018).

[83] U. Bau, P. Hoseinpoori, S. Graf, H. Schreiber, F. Lanzerath, C. Kirches, A. Bardow, Dynamic optimisation of adsorber-bed designs ensuring optimal control, 13594311 125 (2017) 1565–1576. doi:10.1016/j.applthermaleng.2017.07.073.

[84] Y. I. Aristov, Dynamics of adsorptive heat conversion systems: Review of basics and recent advances, 03605442 205 (2020). doi:10.1016/j.energy.2020.117998.

[85] S. Bahrehmand, Development of novel sorber bed heat and mass exchangers for sorption cooling systems, Phd, Surrey, BC, Canada (2020).

[86] R. Wang, L. Wang, J. Wu, Adsorption Refrigeration Technology, Wiley, 2014. doi:10.1002/9781118197448.

[87] A. Sapienza, A. Frazzica, A. Freni, Y. Aristov, Dynamics of Adsorptive Systems for Heat Transformation, Springer International Publishing, Cham, 2018. doi:10.1007/978-3-319-51287-7.

[88] Y. I. Aristov, Adsorptive transformation of ambient heat: A new cycle, 13594311 124 (2017) 521–524. doi:10.1016/j.applthermaleng.2017.06.051.

[89] M. Tokarev, A double-bed adsorptive heat transformer for upgrading ambient heat: Design and first tests, 1996-1073 12 (21) (2019) 4037. doi:10.3390/en12214037.

[90] V. Palomba, A. Sapienza, Y. Aristov, Dynamics and useful heat of the discharge stage of adsorptive cycles for long term thermal storage, Applied Energy 248 (2019) 299–309. doi:10.1016/j.apenergy.2019.04.134.

[91] M.M. Tokarev, Yu.I. Aristov, A new version of the large temperature jump method: The thermal response (t–ltj), 03605442 140 (2017). doi:10.1016/j.energy.2017.08.093.

[92] B. Dawoud, Y. Aristov, Experimental study on the kinetics of water vapor sorption on selective water sorbents, silica gel and alumina under typical operating conditions of sorption heat pumps, 00179310 46 (2) (2003) 273–281. doi:10.1016/S0017-9310(02)00288-0.

[93] Yu I. Aristov, B. Dawoud, I. S. Glaznev, A. Elyas, A new methodology of studying the dynamics of water sorption/desorption under real operating conditions of adsorption heat pumps: Experiment, 00179310 51 (19-20) (2008) 4966–4972. doi:10.1016/j.ijheatmasstransfer.2007.10.042.

[94] B. Dawoud, U. Vedder, E.-H. Amer, S. Dunne, Non-isothermal adsorption kinetics of water vapour into a consolidated zeolite layer, 00179310 50 (11-12) (2007) 2190–2199. doi:10.1016/j.ijheatmasstransfer.2006.10.052.

[95] B. Dawoud, Water vapor adsorption kinetics on small and full scale zeolite coated adsorbers; a comparison, Vol. 50, 2013, pp. 1645–1651. doi:10.1016/j.applthermaleng.2011.07.013.

[96] A. Sapienza, S. Santamaria, A. Frazzica, A. Freni, Y. I. Aristov, Dynamic study of adsorbers by a new gravimetric version of the large temperature jump method, Applied Energy 113 (2014). doi:10.1016/j.apenergy.2013.09.005.

[97] M. Tierney, L. Ketteringham, R. Selwyn, H. Saidani, Calorimetric measurements of the dynamics of a finned adsorbent: early assessment of the activated carbon cloth–ethanol pair with prismatic aluminium fins, 13594311 93 (2016) 1264–1272. doi:10.1016/j.applthermaleng.2015.10.009.

[98] A. Chakraborty, B. B. Saha, Y. I. Aristov, Dynamic behaviors of adsorption chiller: Effects of the silica gel grain size and layers, 03605442 78 (2014) 304–312. doi:10.1016/j.energy.2014.10.015.

[99] I. S. Girnik, Y. I. Aristov, Dynamic optimization of adsorptive chillers: The "aqsoa™-fam-z02 – water" working pair, 03605442 106 (2016). doi:10.1016/j.energy.2016.03.036.

[100] Y. I. Aristov, I. S. Glaznev, I. S. Girnik, Optimization of adsorption dynamics in adsorptive chillers: Loose grains configuration, 03605442 46 (1) (2012). doi:10.1016/j.energy.2012.08.001.

[101] S. Mitra, M. Muttakin, K. Thu, B. B. Saha, Study on the influence of adsorbent particle size and heat exchanger aspect ratio on dynamic adsorption characteristics, 13594311 133 (2018) 764–773. doi:10.1016/j.applthermaleng.2018.01.015.

[102] S. Zhang, X. Niu, Y. Li, G. Chen, X. Xu, Numerical simulation and experimental research on heat transfer and flow resistance characteristics of asymmetric plate heat exchangers, 2095-1701 14 (2) (2020) 267–282. doi:10.1007/s11708-020-0662-7.

[103] R. Eldeeb, V. Aute, R. Radermacher, A survey of correlations for heat transfer and pressure drop for evaporation and condensation in plate heat exchangers, 01407007 65 (2016) 12–26. doi:10.1016/j.ijrefrig.2015.11.013.

[104] Z. H. Ayub, T. S. Khan, S. Salam, K. Nawaz, A. H. Ayub, M. Khan, Literature survey and a universal evaporation correlation for plate type heat exchangers, 01407007 99 (2019) 408–418. doi:10.1016/j.ijrefrig.2018.09.008.

[105] M. Imran, M. Usman, Y. Yang, B.-S. Park, Flow boiling of r245fa in the brazed plate heat exchanger: Thermal and hydraulic performance assessment, 00179310 110 (2017) 657–670. doi:10.1016/j.ijheatmasstransfer.2017.03.070.

[106] J.R. García-Cascales, F. Vera-García, J.M. Corberán-Salvador, J. Gonzálvez-Maciá, Assessment of boiling and condensation heat transfer correlations in the modelling of plate heat exchangers, 01407007 30 (6) (2007) 1029–1041. doi:10.1016/j.ijrefrig.2007.01.004.

[107] A. Jokar, M. H. Hosni, S. J. Eckels, Dimensional analysis on the evaporation and condensation of refrigerant r-134a in minichannel plate heat exchangers, 13594311 26 (17-18) (2006) 2287–2300. doi:10.1016/j.applthermaleng.2006.03.015.

[108] G. A. Longo, G. Righetti, C. Zilio, A new computational procedure for refrigerant condensation inside herringbone-type brazed plate heat exchangers, 00179310 82 (2015) 530–536. doi:10.1016/j.ijheatmasstransfer.2014.11.032.

[109] B. H. Shon, S. W. Jeon, Y. Kim, Y. T. Kang, Review: Condensation and evaporation characteristics of low gwp refrigerants in plate heat exchangers, International Journal of Air-Conditioning and Refrigeration 24 (02) (2016) 1630004. doi:10.1142/S2010132516300044.

[110] A.I. Leontiev, N.A. Kiselev, Yu.A. Vinogradov, M.M. Strongin, A.G. Zditovets, S.A. Burtsev, Experimental investigation of heat transfer and drag on surfaces coated with dimples of different shape, 12900729 118 (2017) 152–167. doi:10.1016/j.ijthermalsci.2017.04.027.

[111] N. K. Burgess, P. M. Ligrani, Effects of dimple depth on channel nusselt numbers and friction factors, 0022-1481 127 (8) (2005) 839–847. doi:10.1115/1.1994880.

[112] J. Turnow, N. Kornev, V. Zhdanov, E. Hassel, Flow structures and heat transfer on dimples in a staggered arrangement, 0142727X 35 (2012) 168–175. doi:10.1016/j.ijheatfluidflow.2012.01.002.

[113] X. Li, J. Sun, C. Xu, Y. Li, R. Zhang, L. Qian, Y. Chen, Visualization of bubble flow in the channel of a dimple-type embossing plate heat exchanger under different fluid inlet/outlet ports, 00179310 145 (2019) 118750. doi:10.1016/j.ijheatmasstransfer.2019.118750.

[114] Y. Rao, B. Li, Y. Feng, Heat transfer of turbulent flow over surfaces with spherical dimples and teardrop dimples, 08941777 61 (2015) 201–209. doi:10.1016/j.expthermflusci.2014.10.030.

[115] D. Lee, D. Kim, S. Yun, Y. Kim, Two-phase flow patterns and pressure drop of a low gwp refrigerant r-1234ze(e) in a plate heat exchanger under adiabatic conditions, 00179310 145 (2019) 118816. doi:10.1016/j.ijheatmasstransfer.2019.118816.

[116] E. Lee, H. Kang, Y. Kim, Flow boiling heat transfer and pressure drop of water in a plate heat exchanger with corrugated channels at low mass flux conditions, 00179310 77 (2014) 37–45. doi:10.1016/j.ijheatmasstransfer.2014.05.019.

[117] V. Palomba, A. Frazzica, Experimental study of a fin-and-tube heat exchanger working as evaporator in subatmospheric conditions, 13594311 175 (2020) 115336. doi:10.1016/j.applthermaleng.2020.115336.

[118] P. C. Thimmaiah, A. Sharafian, M. Rouhani, W. Huttema, M. Bahrami, Evaluation of low-pressure flooded evaporator performance for adsorption chillers, 03605442 122 (2017) 144–158. doi:10.1016/j.energy.2017.01.085.

[119] F. Lanzerath, J. Seiler, M. Erdogan, H. Schreiber, M. Steinhilber, A. Bardow, The impact of filling level resolved: Capillary-assisted evaporation of water for adsorption heat pumps, 13594311 102 (2016) 513–519. doi:10.1016/j.applthermaleng.2016.03.052.

[120] J. Seiler, F. Lanzerath, C. Jansen, A. Bardow, Only a wet tube is a good tube: understanding capillary-assisted thin-film evaporation of water for adsorption chillers, 13594311 147 (2019) 571–578. doi:10.1016/j.applthermaleng.2018.08.024.

[121] F. Giraud, C. Toublanc, R. Rullière, J. Bonjour, M. Clausse, Experimental study of water vaporization occurring inside a channel of a smooth plate-type heat exchanger at subatmospheric pressure, 13594311 106 (2016) 180–191. doi:10.1016/j.applthermaleng.2016.05.151.

[122] J. Y. Song, J. W. Lee, Y. T. Kang, Comparisons of nu correlations for h2o/libr solution in plate heat exchanger for triple effect absorption chiller application, 03605442 172 (2019) 852–860. doi:10.1016/j.energy.2019.02.013.

[123] F. Giraud, P. Vallon, B. Tremeac, Experimental study of water vaporization occurring inside the channel of a smooth-plate type heat exchanger connected to an adsorber and comparison with trends observed in absorption configuration, 01407007 77 (2017) 60–74. doi:10.1016/j.ijrefrig.2017.02.021.

[124] R. Volmer, J. Eckert, G. Füldner, L. Schnabel, Evaporator development for adsorption heat transformation devices – influencing factors on non-stationary evaporation with tube-fin heat exchangers at sub-atmospheric pressure, 09601481 110 (2017) 141–153. doi:10.1016/j.renene.2016.08.030.

[125] B. Dawoud, On the effect of grain size on the kinetics of water vapor adsorption and desorption into/from loose pellets of fam-z02 under a typical operating condition of adsorption heat pumps, 0021-9592 40 (13) (2007) 1298–1306. doi:10.1252/jcej.07WE163.

[126] W. Wagner, H. J. Kretzschmar, International steam tables; properties of water and steam based on the industrial formulation "iapws-if97", 2nd edition, springer verlag berlin heidelberg (2008). doi:10.1007/978-3-540-74234-0.

[127] K. Sztekler, Optimisation of operation of adsorption chiller with desalination function, 1996-1073 14 (9) (2021) 2668. doi:10.3390/en14092668.

[128] M. Rouhani, W. Huttema, M. Bahrami, Thermal conductivity of aqsoa fam-z02 packed bed adsorbers in open and closed adsorption thermal energy storage systems, 01407007 105 (2019) 158–168. doi:10.1016/j.ijrefrig.2018.05.012.

[129] K. Uddin, M. Amirul Islam, S. Mitra, J.-b. Lee, K. Thu, B. B. Saha, S. Koyama, Specific heat capacities of carbon-based adsorbents for adsorption heat pump application, 13594311 129 (2018) 117–126. doi:10.1016/j.applthermaleng.2017.09.057.

[130] A. Pesaran, H. Lee, Y. Hwang, R. Radermacher, H.-H. Chun, Review article: Numerical simulation of adsorption heat pumps, 03605442 100 (2016) 310–320. doi:10.1016/j.energy.2016.01.103.

[131] B. B. Saha, E. C. Boelman, T. Kashiwagi, Computational analysis of an advanced adsorption-refrigeration cycle, 03605442 20 (10) (1995) 983–994. doi:10.1016/0360-5442(95)00047-K.

[132] L. Z. Zhang, L. Wang, Effects of coupled heat and mass transfers in adsorbent on the performance of a waste heat adsorption cooling unit, 13594311 19 (2) (1999) 195–215. doi:10.1016/S1359-4311(98)00023-4.

[133] A. Sakoda, M. Suzuki, Fundamental study on solar powered adsorption cooling system, 0021-9592 17 (1) (1984) 52–57. doi:10.1252/jcej.17.52.

[134] H. T. Chua, K. C. Ng, W. Wang, C. Yap, X. L. Wang, Transient modeling of a two-bed silica gel–water adsorption chiller, 00179310 47 (4) (2004) 659–669. doi:10.1016/j.ijheatmasstransfer.2003.08.010.

[135] M. S. Ray, Diffusion in zeolites and other microporous solids, by j. karger and d. m. ruthven, john wiley, new york, usa (1992). 605 pages. isbn 0-47 1-50907-8, Developments in Chemical Engineering and Mineral Processing 4 (3-4) (1996) 254. doi:10.1002/apj.5500040311.

[136] M. W. Ellis, An evaluation of the effect of adsorbent properties on the performance of a solid sorption heat pump, Phd thesis, Georgia Institute of Technology.

[137] M. Peric, A finite volume method for the prediction of three-dimensional fluid flow in complex ducts, Phd thesis, University of London, London, England (1985).

[138] A. I. Radu, T. Defraeye, P. Ruch, J. Carmeliet, D. Derome, Insights from modeling dynamics of water sorption in spherical particles for adsorption heat pumps, 00179310 105 (2017) 326–337. doi:10.1016/j.ijheatmasstransfer.2016.09.079.

[139] S. Graf, A design approach for adsorption energy systems integrating dynamic modeling with small-scale experiments, (doctoral dissertation), Ph.D. thesis, RWTH Aachen University.
URL http://publications.rwth-aachen.de/record/752022

[140] Y. I. Aristov, M. M. Tokarev, A. Freni, I. S. Glaznev, G. Restuccia, Kinetics of water adsorption on silica fuji davison rd, Microporous and Mesoporous Materials 96 (1) (2006) 65–71. doi:10.1016/j.micromeso.2006.06.008.

[141] B. Dawoud, On the development of an innovative gas-fired heating appliance based on a zeolite-water adsorption heat pump; system description and seasonal gas utilization efficiency, Applied Thermal Engineering 72 (2) (2014) 323–330. doi:https://doi.org/10.1016/j.applthermaleng.2014.09.008.

[142] S. M. Ali, A. Chakraborty, Thermodynamic modelling and performance study of an engine waste heat driven adsorption cooling for automotive air-conditioning, Applied Thermal Engineering 90 (2015) 54–63. doi:10.1016/j.applthermaleng.2015.06.078.

[143] S. Sridhar, A commentary on "diffusion, mobility and their interrelation through free energy in binary metallic systems," l.s. darken: Trans. aime, 1948, vol. 175, p. 184ff, Metallurgical and Materials Transactions A 41 (3) (2010) 543–562. doi:10.1007/s11661-010-0177-7.

[144] C. Charalambous, G. Santori, E. Vilarrasa-Garcia, M. Bastos-Neto, C. L. Cavalcante, S. Brandani, Pure and binary adsorption of carbon dioxide and nitrogen on aqsoa fam z02, Journal of Chemical & Engineering Data 63 (3) (2018) 661–670. doi:10.1021/acs.jced.7b00864.

[145] M. Intini, M. Goldsworthy, S. White, C. M. Joppolo, Experimental analysis and numerical modelling of an aqsoa zeolite desiccant wheel, Applied Thermal Engineering 80 (2015) 20–30. doi:10.1016/j.applthermaleng.2015.01.036.

[146] T. Yamamoto, Y. H. Kim, B. C. Kim, A. Endo, N. Thongprachan, T. Ohmori, Adsorption characteristics of zeolites for dehydration of ethanol: Evaluation of diffusivity of water in porous structure, Chemical Engineering Journal 181-182 (2012) 443–448. doi:10.1016/j.cej.2011.11.110.

[147] P. G. Youssef, S. M. Mahmoud, R. K. AL-Dadah, Performance analysis of four bed adsorption water desalination/refrigeration system, comparison of aqsoa-z02 to silica-gel, Desalination 375 (2015) 100–107. doi:10.1016/j.desal.2015.08.002.

[148] H. W. B. Teo, A. Chakraborty, W. Fan, Improved adsorption characteristics data for aqsoa types zeolites and water systems under static and dynamic conditions, Microporous and Mesoporous Materials 242 (2017) 109–117.

[149] K. Chihara, M. Suzuki, Air drying by pressure swing adsorption, Journal of Chemical Engineering of Japan 16 (4) (1983) 293–299. doi:10.1252/jcej.16.293.

[150] D. B. Riffel, U. Wittstadt, F. P. Schmidt, T. Núñez, F. A. Belo, A. P. Leite, F. Ziegler, Transient modeling of an adsorber using finned-tube heat exchanger, International Journal of Heat and Mass Transfer 53 (7) (2010) 1473–1482. doi:10.1016/j.ijheatmasstransfer.2009.12.001.

[151] AlfaLaval, Alfalaval, glx30.
URL https://www.alfalaval.com/globalassets/documents/products/heat-transfer/plate-heat-exchangers/gas-to-liquid-plate-heat-exchangers/glx/glx30_product-leaflet_en.pdf

[152] J. Monteith, M. Unsworth, Principles of Environmental Physics, 3rd Edition, Academic Press, 2007.

[153] S. Graf, F. Lanzerath, A. Sapienza, A. Frazzica, A. Freni, A. Bardow, Prediction of scp and cop for adsorption heat pumps and chillers by combining the large-temperature-jump method and dynamic modeling, 13594311 98 (2016) 900–909. doi:10.1016/j.applthermaleng.2015.12.002.

[154] S. Graf, S. Eibel, F. Lanzerath, A. Bardow, Validated performance prediction of adsorption chillers: Bridging the gap from gram–scale experiments to full–scale chillers, 2194-4288 8 (5) (2020) 1901130. doi:10.1002/ente.201901130.

[155] V. Gnielinski, G4 heat transfer in flow past a plane wall, VDI Heat Atlas (2010). doi:10.1007/978-3-540-77877-6{\textunderscore}37.

[156] R Lang, Leistungsfähige adsorptionsmodule für eine zeolith-wasser-adsorptionswärmepumpe, Ph.D. thesis, RWTH-Aachen University, Shaker Verlag GmbH, Aachen, Germany.

[157] T Westterfeld, Numerische untersuchung einer periodisch arbeitenden adsorption-swärmepumpe, Ph.D. thesis, RWTH-Aachen University, Shaker Verlag GmbH, Aachen, Germany.

[158] Y. Sato, B. Niceno, Pool boiling simulation using an interface tracking method: From nucleate boiling to film boiling regime through critical heat flux, 00179310 125 (2018) 876–890. doi:10.1016/j.ijheatmasstransfer.2018.04.131.

[159] M. Ishii, T. Hibiki, Thermo-Fluid Dynamics of Two-Phase Flow, Springer New York, 2011. doi:10.1007/978-1-4419-7985-8.

[160] V. K. Dhir, Nucleate pool boiling, Handbook of Thermal Science and Engineering (2017). doi:10.1007/978-3-319-32003-8{\textunderscore}41-1.

[161] K. L. Wolf, Physik und Chemie der Grenzflächen, Springer Berlin Heidelberg, 1957. doi:10.1007/978-3-642-49700-1.

[162] A. Horsthemke, Die benetzung metallischer oberflächen durch wasser, Ph.D. thesis, Technical University of Hannover.

[163] W. A. Zisman, Influence of constitution on adhesion, 0019-7866 55 (10) (1963) 18–38. doi:10.1021/ie50646a003.

[164] Z. I Harmati, Vergleichende untersuchungen über die benetzung metallischer werkstoffe gegenüber wässrigen elektrolytlösungen unter besonderer berücksichtigung des korrosionsverhaltens, Ph.D. thesis, ETH Zürich, switzerland.

[165] A.W. Adamson, A.P. Gast, Physical Chemistry of Surfaces, Interscience, 1967.

[166] J.J Bikerman, Physical surfaces, Academic Press, 1970.

[167] T. Hobler, J. Czajka, Minimum wetting rate of a flat surface 2B (1968) 169–186.

[168] M.M. Dubinin, Progress in surface and membrane science, Academic Press, 1975.

[169] M. Masgrau, Plate for a heat exchanger and a heat exchanger (2015).

[170] P. C. Thimmaiah, A. Sharafian, W. Huttema, C. McCague, M. Bahrami, Effects of capillary-assisted tubes with different fin geometries on the performance of a low-operating pressure evaporator for adsorption cooling system applications, Applied Energy 171 (2016) 256–265. doi:10.1016/j.apenergy.2016.03.070.

[171] K. Montazeri, H. Lee, Y. Won, Microscopic analysis of thin-film evaporation on spherical pore surfaces, 00179310 122 (2018) 59–68. doi:10.1016/j.ijheatmasstransfer.2018.01.002.

[172] S. Nowak, Analytical and experimental investigation of applying an asymmetricplate heat exchanger as an evaporator/condenser in a small-scalethermally driven adsorption chiller, M.sc., Regensburg ,Germany (2021).

Appendix A

Uncertainty analysis

The uncertainty of the full scale and the small scale measurements are presented here. The content of this appendix has been attached as a supplementary material to our article published in Frontiers in Energy research journal, which included most of the results presented in Chapter 3

A.1 Full-scale measurements

The uncertainty in the instantaneous evaporator/condenser power ($\dot{Q}$) is calculated by Eq. (A.1)

$$\sigma_{\dot{Q}} = \left[\left(\frac{\partial \dot{Q}}{\partial \dot{V}_1} \times \sigma_{\dot{V}_1}\right)^2 + \left(\frac{\partial \dot{Q}}{\partial \rho} \times \sigma_{\rho}\right)^2 + \left(\frac{\partial \dot{Q}}{\partial c_p} \times \sigma_{c_p}\right)^2 + \left(\frac{\partial \dot{Q}}{\partial \delta T} \times \sigma_{\Delta T}\right)^2\right]^{0.5} \quad \text{(A.1)}$$

$$= [(\rho C_p \Delta T \times \sigma_{\dot{V}_1})^2 + (\dot{V}_1 C_p \Delta T \times \sigma_{\rho})^2 + (\dot{V}_1 \rho \Delta T \times \sigma_{c_p})^2 + (\dot{V}_1 \rho C_p \times \sigma_{\Delta T})^2]^{0.5}$$

Where, $\sigma_{\dot{Q}}$ is the absolute uncertainty of $\dot{Q}$. The c_p and ρ are the specific heat and density of the evaporator/condenser HTF, respectively. ΔT is the temperature difference between the HTF's inlet and outlet of the evaporator/condenser ($T_{1,in} - T_{1,out}$). As water is used as the HTF, the c_p and ρ amount to 4.2±0.02 kJ.kg^{-1}·K^{-1} and 1000±0.25 kg·m^{-3} (Sur & Das, 2017), respectively. The uncertainty in the instantaneous specific evaporator/condenser power ($\dot{q}$) of the evaporator/condenser unit is calculated as depicted in Eq. (A.2)

$$\sigma_{\dot{q}} = \left[\left(\frac{1}{m_{ads}} \times \sigma_{\dot{Q}}\right)^2 + \left(\dot{Q} \times \sigma_{m_{ads}}\right)^2\right]^{0.5} \quad \text{(A.2)}$$

Where, $\sigma_{m_{ads}}$ is the absolute uncertainty of the dry mass of the adsorbent (m_{ads}).

The uncertainty of the evaporation/condensation energy (q) is given by Eq. (A.3)

$$\sigma_q = \left[(\sigma_{\Delta t} \sum_{i=0}^{N} \dot{q}_i)^2 + (\Delta t \sum_{i=0}^{N} \sigma_{\dot{q}_i})^2 \right]^{0.5} \tag{A.3}$$

The accuracy of measuring the Δt is very high, as its error is negligible. The specific moving average evaporator/condenser power obtained in an adsorption/desorption process ($\bar{\dot{q}}$) is calculated as,

$$\bar{\dot{q}} = \frac{1}{t} . q(t) \tag{A.4}$$

Its uncertainty is obtained from Eq. (A.5),

$$\sigma_{\bar{\dot{q}}} = \left[(\frac{1}{t} \times \sigma_q)^2 + (-\frac{q}{t^2} \times \sigma_t)^2 \right]^{0.5} \tag{A.5}$$

Where, σ_t is the uncertainty of time, which can be neglected.

The water uptake obtained in an adsorption process (w_{ads}) is calculated according to Eq. (A.6) and in a desorption process (w_{des}) to Eq. (A.7).

$$w_{ads}(t) = w_o + \frac{q(t)}{h_{fg}(T_{ev})} \tag{A.6}$$

$$w_{des}(t) = w_o + \frac{q(t)}{m_{ads}.(h_{fg}(T_{cond}) + c_{p,v}(T_v - T_{cond})} \tag{A.7}$$

The term $c_{p,v}(T_v - T_{cond})$ in Eq. (A.7) is very small (less than 3.5% of the latent heat term), $h_{fg}(T_{cond})$, and, therefore, its uncertainty can be neglected. The uncertainty in the measured water uptake can be evaluated for both the adsorption and desorption process by Eq. (A.8).

$$\begin{aligned} \sigma_w &= \left[\left(\frac{\partial w}{\partial w_o} \times \sigma_{w_o} \right)^2 + \left(\frac{\partial w}{\partial q} \times \sigma_q \right)^2 + \left(\frac{\partial w}{\partial h_{fg}} \times \sigma_{h_{fg}} \right)^2 \right]^{0.5} \\ &= \left[(\sigma_{w_o})^2 + \left(\frac{1}{h_{fg}} \times \sigma_q \right)^2 + \left(\frac{-q}{{h_{fg}}^2} \times \sigma_{h_{fg}} \right)^2 \right]^{0.5} \end{aligned} \tag{A.8}$$

σ_{w_o} is the uncertainty of w_o (Frazzica & Freni, 2017) and $\sigma_{h_{fg}}$ is the uncertainty of h_{fg} which amounts to ± 0.02% (Hans-Joachim Kretzschmar & Wolfgang Wagner, 2008).

Table A.1. illustrates the accuracy of the applied individual sensors of the full-scale setup. The results of the accumulated absolute accuracies of measured $\dot{q}$, $\bar{\dot{q}}$ and w of the full-scale setup are listed in Table A.2.

Table A.1. Sensors applied in the full-scale setup and their accuracies.

Sensor	Accuracy	Measured quantity
Balance KERN type EMB 6000-1	±0.1g	Dry weight of adsorbent filled in the adsorber/desorber
Pressure transducers PFEIFFER VACUUM type CMR 362	±0.2% of reading	Vapour pressure inside the adsorber/desorber and evaporator/condenser
RTD temperature sensors TMH type Pt100	1/10 DIN class B $\pm 0.1 \times (0.3 + 0.005T(°C))$	HTF's temperatures at the inlet and outlet of both the adsorber/desorber and evaporator/condenser
Flow meters SIEMENS type Sitrans F M MAG 100	±0.2% of reading	HTF's flow rate at the inlet of both the adsorber/desorber and evaporator/condenser

Table A.2: Absolute uncertainties upon Estimating $\dot{q}$, $\bar{\dot{q}}$ and w of the full-scale setup (**Chapter 3**)

Operating Conditions $T_{ev}/T_{cond}/T_h$[°C]	**Process**	$\sigma_{\dot{q}}$[W/kg]	$\sigma_{\bar{\dot{q}}}$ [W/kg]	σ_w[g/100g]
15/30/90	Ads.	±26.4	±26.4	±0.64
	Des.	±31.7	±31.8	±0.64
15/35/90	Ads.	±26.4	±26.4	±0.41
	Des.	±33.5	±33.5	±0.43
10/30/90	Ads.	±24.7	±24.6	±0.45
	Des.	±31.7	±31.7	±0.44
10/35/90	Ads.	±24.6	±24.6	±0.28
	Des.	±33.5	±33.4	±0.29

A.2 Small-scale sample measurements

The differential water uptake obtained upon conducting LTJ adsorption and desorption processes on the small-scale adsorbent sample has been measured implicitly as explained in (Aristov et al., 2008; Dawoud, 2007, 2013). Strictly speaking, the total pressure drop/increase of the vapour filling the setup's volume has been utilized in evaluating the differential water uptake of the tested sample. The pressure (P) and temperature (T) of the water vapour filling the vapour vessel (V_{VV} =46±0.06 litre) and the measuring cell (V_{MC} =4.5± 0.066 litre) of the setup have been measured at the initial and final states of all conducted adsorption and desorption processes. The equation of state has been applied to calculate the decrease/increase in the mass of the vapour filling the setup volume (Δm), which refers to the amount of water adsorbed/desorbed by the tested sample. Eq. (A.9) describes the increase/decrease in the mass of water vapour filling the setup.

$$\Delta m = \frac{V_{VV}}{R}\left[\frac{P_i}{T_i} - \frac{P_f}{T_f}\right]_{VV} + \frac{V_{MC}}{R}\left[\frac{P_i}{T_i} - \frac{P_f}{T_f}\right]_{MC} \tag{A.9}$$

$$= \frac{V_{VV}}{R}\left[y_i - y_f\right]_{VV} + \frac{V_{MC}}{R}\left[y_i - y_f\right]_{MC}$$

Where $y = \frac{P}{T}$ and its error is described by

$$\sigma_y = \left[(\frac{1}{T}\sigma_P)^2 + (\frac{P}{T^2}\sigma_T)^2\right]^{0.5} \tag{A.10}$$

Therefore, the error in the calculated Δm can be obtained from the following equation

$$\sigma_{\Delta m} = \left[\left(\frac{1}{R}\left[y_i - y_f\right]\sigma_V\right)^2 + \left(\frac{V}{R}\sigma_{y_i}\right)^2 + \left(\frac{V}{R}\sigma_{y_f}\right)^2\right]_{VV} + \left[\left(\frac{1}{R}\left[y_i - y_f\right]\sigma_V\right)^2 + \left(\frac{V}{R}\sigma_{y_i}\right)^2 + \left(\frac{V}{R}\sigma_{y_f}\right)^2\right]_{MC} \tag{A.11}$$

The water uptake (w) in the sample and its error are described in Eq. (A.12) and (A.13)

$$w = w_o + \frac{\Delta m}{m_{ads}} \tag{A.12}$$

$$\sigma_w = \left[(\sigma_{w_o})^2 + \left(\frac{1}{m_{ads}} \times \sigma_{\Delta m}\right)^2 + \left(\frac{\Delta m}{{m_{ads}}^2} \times \sigma_{m_{ads}}\right)^2\right]^{0.5} \tag{A.13}$$

The expected instantaneous specific evaporator power ($\dot{q}_{ev}$) and condenser power ($\dot{q}_{cond}$) estimated from the measured kinetic data of the small-scale sample are calculated based on Eq. (A.14) and (A.15), respectively.

$$\dot{q}_{ev} = \frac{dw}{dt} \,.\, h_{fg}(T_{ev}) \tag{A.14}$$

$$\dot{q}_{cond} = \frac{dw}{dt} \,.\, (h_{fg}(T_{cond}) + c_{p,v}(T_v - T_{cond})) \tag{A.15}$$

Again, the term $c_{p,v}(T_v - T_{cond})$ is very small compared with $h_{fg}(T_{cond})$, and, therefore, its uncertainty can be neglected. The uncertainty of $\dot{q}_{ev}$ and $\dot{q}_{cond}$ is calculated by Eq. (A.16).

$$\sigma_{\dot{q}} = \left[2 \times (\frac{1}{\Delta t} \times h_{fg} \times \sigma_w)^2 + (\frac{dw}{dt} \times \sigma_{h_{fg}})^2\right]^{0.5} \quad \text{(A.16)}$$

The specific moving average evaporation/condensation power is obtained from,

$$\bar{\dot{q}} = \frac{1}{t} . q(t) \quad \text{(A.17)}$$

and its uncertainty is obtained from,

$$\sigma_{\bar{\dot{q}}} = \left[(\frac{1}{t} \times \sigma_q)^2 + (-\frac{q}{t^2} \times \sigma_t)^2\right]^{0.5} \quad \text{(A.18)}$$

Table A.3 illustrates the accuracy of the applied individual sensors of the small-scale setup. The results of the accumulated absolute accuracies of measured $\dot{q}$, $\bar{\dot{q}}$ and w of the small-scale setup are listed in Table A.3.

Table A.3. Sensors applied in the small-scale setup and their accuracies.

Sensor	Accuracy	Measured quantity
Balance KERN type ALS 250-4 A	±0.0007g	Dry weight of the tested sample
Pressure transducers PFEIFFER VACUUM type CMR 362	±0.2% of reading	Vapour pressure inside the vessel and measuring cell
RTD temperature sensors TMH type Pt100	1/10 DIN class B $\pm 0.1 \times (0.3 + 0.005T(°C))$	Vapour temperature inside the vessel and measuring cell and sample holder surface temperature

Table A.4: Absolute accuracies of measured $\dot{q}$, $\bar{\dot{q}}$ and w of the small-scale setup (**Chapter 3**)

Operating Conditions $T_{ev}/T_{cond}/T_h$**[°C]**	**Process**	$\sigma_{\dot{q}}$**[W/kg]**	$\sigma_{\bar{\dot{q}}}$ **[W/kg]**	σ_w**[g/100g]**
15/30/90	Ads.	±15.93	±26.0	±0.46
	Des.	±43.47	±65.2	±1.26
15/35/90	Ads.	±16.32	±26.1	±0.47
	Des.	±55.86	±99.1	±1.63
10/30/90	Ads.	±11.56	±18.8	±0.33
	Des.	±42.68	±75.4	±1.24
10/35/90	Ads.	±11.86	±19.0	±0.34
	Des.	±55.47	±98.8	±1.62

References

Aristov, Y. I., Dawoud, B., Glaznev, I. S., & Elyas, A. (2008). A new methodology of studying the dynamics of water sorption/desorption under real operating conditions of adsorption heat pumps: Experiment. *International Journal of Heat and Mass Transfer*, *51*(19–20), 4966–4972. https://doi.org/10.1016/j.ijheatmasstransfer.2007.10.042

Dawoud, B. (2007). On the Effect of Grain Size on the Kinetics of Water Vapor Adsorption and Desorption into/from Loose Pellets of FAM-Z02 under a Typical Operating Condition of Adsorption Heat Pumps. *JOURNAL OF CHEMICAL ENGINEERING OF JAPAN*, *40*(13), 1298–1306. https://doi.org/10.1252/jcej.07WE163

Dawoud, B. (2013). Water vapor adsorption kinetics on small and full scale zeolite coated adsorbers; A comparison. *Applied Thermal Engineering*, *50*(2), 1645–1651. https://doi.org/10.1016/j.applthermaleng.2011.07.013

Frazzica, A., & Freni, A. (2017). Adsorbent working pairs for solar thermal energy storage in buildings. *Renewable Energy*, *110*, 87–94. https://doi.org/10.1016/j.renene.2016.09.047

Hans-Joachim Kretzschmar, & Wolfgang Wagner. (2008). *International Steam Tables; Properties of Water and Steam based on the Industrial Formulation IAPWS-IF97, 2nd edition, Springer Verlag Berlin Heidelberg*. doi: 10.1007/978-3-540-74234-0

Sur, A., & Das, R. K. (2017). Experimental investigation on waste heat driven activated carbon-methanol adsorption cooling system. *Journal of the Brazilian Society of Mechanical Sciences and Engineering*, *39*(7), 2735–2746. https://doi.org/10.1007/s40430-017-0792-y

Appendix B

Experimental work for estimating the effective coeffcient of water vapour diffusion in Siogel grains

A frame has been made of Polyether Ether Ketone (PEEK) for its low thermal conductivity (k = 0.25 $W.m^{-1}.K^{-1}$) and negligible outgassing characteristics. The frame has a design for placing a granular adsorbent sample having a cuboidal shape. The frame enables the refrigerant vapour (water vapour) to enter/leave the adsorbent sample placed inside from the top surface of the adsorbent sample. Figure B.1 shows the construction of the open test frame.

For preventing the heat transfer through the PEEK frame sides, the thickness of the frame's walls is determined to 5 mm. At the downside of the frame, a stainless-steel substrate of 0.3 mm thickness is mounted to allow the heat transfer between the sample and the surface of the sample holder inside the measuring cell of the kinetic setup. The PEEK frame and the stainless steel substrate is sealed together by a special double-sided adhesive film of 0.5 mm thickness.

For testing the adsorbent sample in the described test frame under the desired operating conditions, the sealed frame is fixed on the sample holder of the measuring cell using silicon-free thermal paste and the planned adsorption and desorption processes are performed.

The adsorption and desorption kinetic tests on the adsorbent sample inside the test frame have been carried out under the operating conditions of evaporator temperatures 5, 10 and 15°C, adsorber-end and condenser temperatures of 30 and 35°C, and a desorption-end temperature of 90 °C. The adsorption and desorption start temperatures, $T_{ads-start}$ and $T_{des-start}$, associated to the planned operating conditions are determined using the water-Siogel equilibrium model introduced in (Sapienza et al., 2017). The thermostats feeding

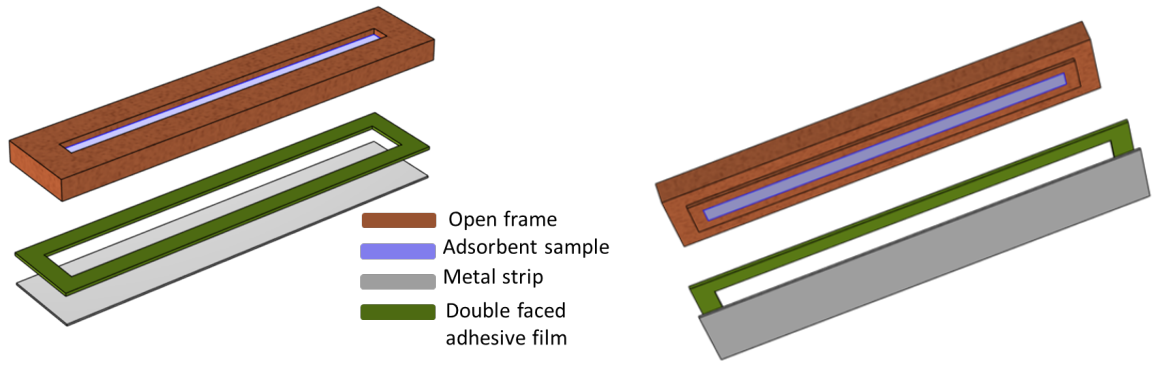

(a) (b)

Fig. B.1 Construction of the open test frame used for estimating D_{eff} of the Siogel-water working pair, (a) top view, (b) down view

the oil circuit of the sample holder of the V-LTJ kinetic setup allow adjusting the sample holder temperature to the start temperature ($T_{ads-start}$ or $T_{des-start}$) and performing sudden temperature change to the sample holder surface until realizing the desired end temperature ($T_{ads-end}$ or $T_{des-end}$). The temporal change of sample holder temperature reaches 95 % of the final value in less than 2 min from the start of the cooling/heating process. The uncertainty analysis of the measured water uptake can be read in Appendix A. The boundary conditions of the conducted adsorption and desorption processes as well as the uncertainty of the measured final differential water uptakes $\sigma_{\Delta w_f}$ are depicted in Table B.1.

The 2-D mathematical model developed in COMSOL Multiphysics environment and presented in Chapter 4 (Section 4.1) for simulating the heat and mass transfer in a cuboidal adsorbent sample is applied. As illustrated in Chapter 4, the optimization module integrated in COMSOL has been applied to obtain the effective diffusion coefficient of water vapour in the Siogel grains (D_{eff}) at all applied operating conditions. Figures B.2 and B.3 show the best fit of the numerically obtained adsorption and desorption kinetics results, respectively, to the corresponding experimental data of the adsorbent sample tested in the above described test frame. The corresponding D_{eff} values are reported and discussed in Chapter 4.

Table B.1 Adsorption and desorption start temperature ($T_{des-start}$, $T_{ads-start}$), initial water uptake (w_o), final differential water uptake (Δw_f), measurement uncertainty of Δw_f ($\sigma_{\Delta w_f}$), time constant of the exponential fitting (τ) and its (R^2), ratios of τ (r_{2-1},r_{3-2} and r_{3-1}) at each operating condition for the top-open tested frame

Operating Condition $T_{ev}/T_{cond}/T_{des}$[°C]	**Adsorption**				**Desorption**			
	$T_{ads-start}$ °C	w_o g/100g	Δw_f g/100g	$\sigma_{\Delta w_f}$ g/100g	$T_{des-start}$ °C	w_o g/100g	Δw_f g/100g	$\sigma_{\Delta w_f}$ g/100g
15/30/90	70.5	3.6	16.9	±0.45	44.5	22.7	-17.9	±1.27
15/35/90	62.4	4.9	11.0	±0.46	55.1	16.9	-10.5	±1.63
10/30/90	66.1	3.6	11.4	±0.33	50.5	16.1	-11.4	±1.24
10/35/90	58.7	4.9	7.5	±0.34	58.8	14.0	-7.6	±1.62
5/30/90	58.5	3.6	7.2	±0.23	57.1	13.5	-7.4	±1.23
5/35/90	53.2	4.9	4.4	±0.24	68.4	10.7	-4.0	±1.61

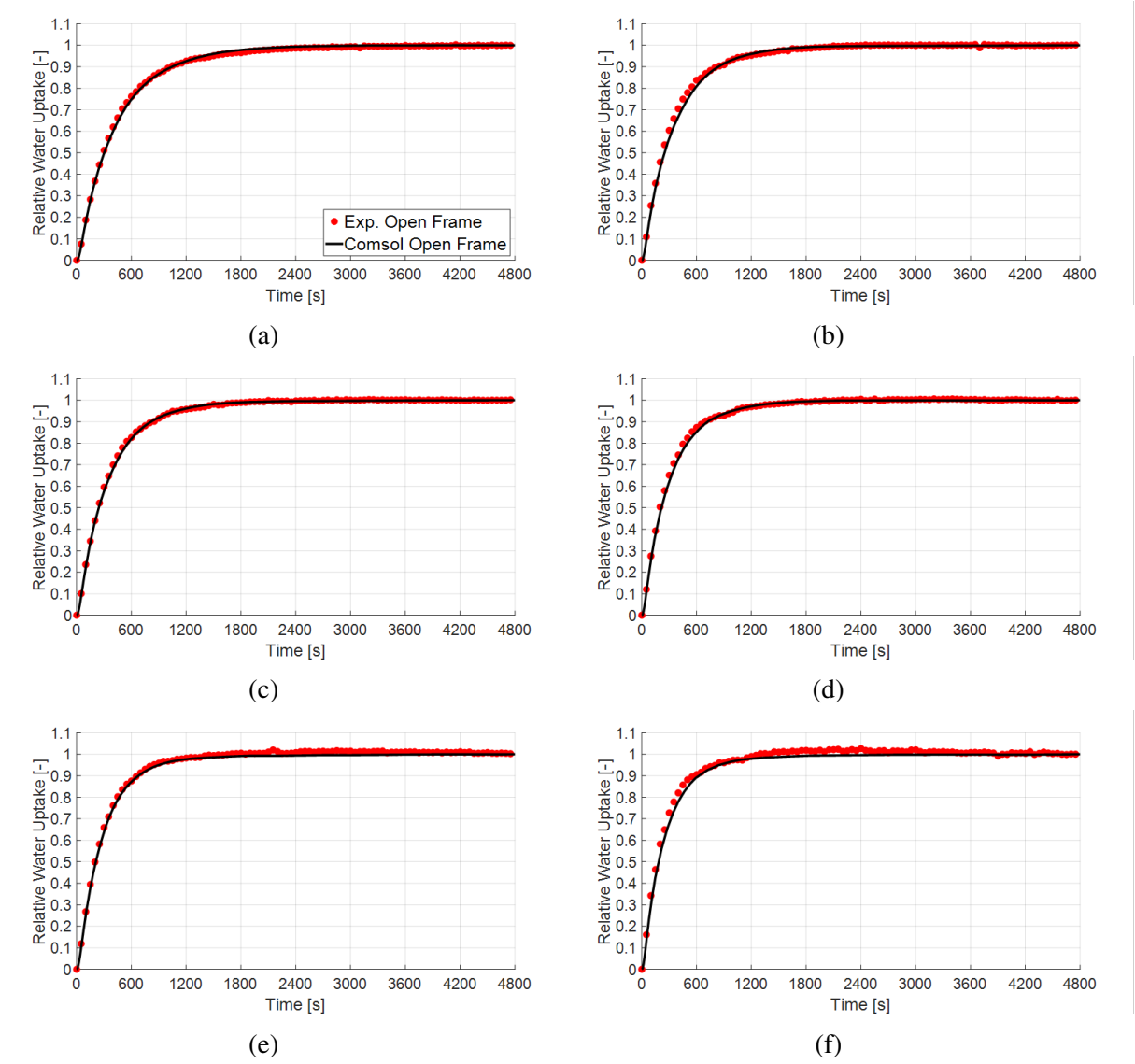

Fig. B.2 Best fitting of the numerical simulation results to the experimental data of the adsorbent sample tested in the open test frame of the GLX30 APHE, **adsorption** processes; a) 15/30/90 °C , b) 15/35/90°C, c) 10/30/90°C, d)10/35/90°C, e) 5/30/90°C and f) 5/35/90°C.

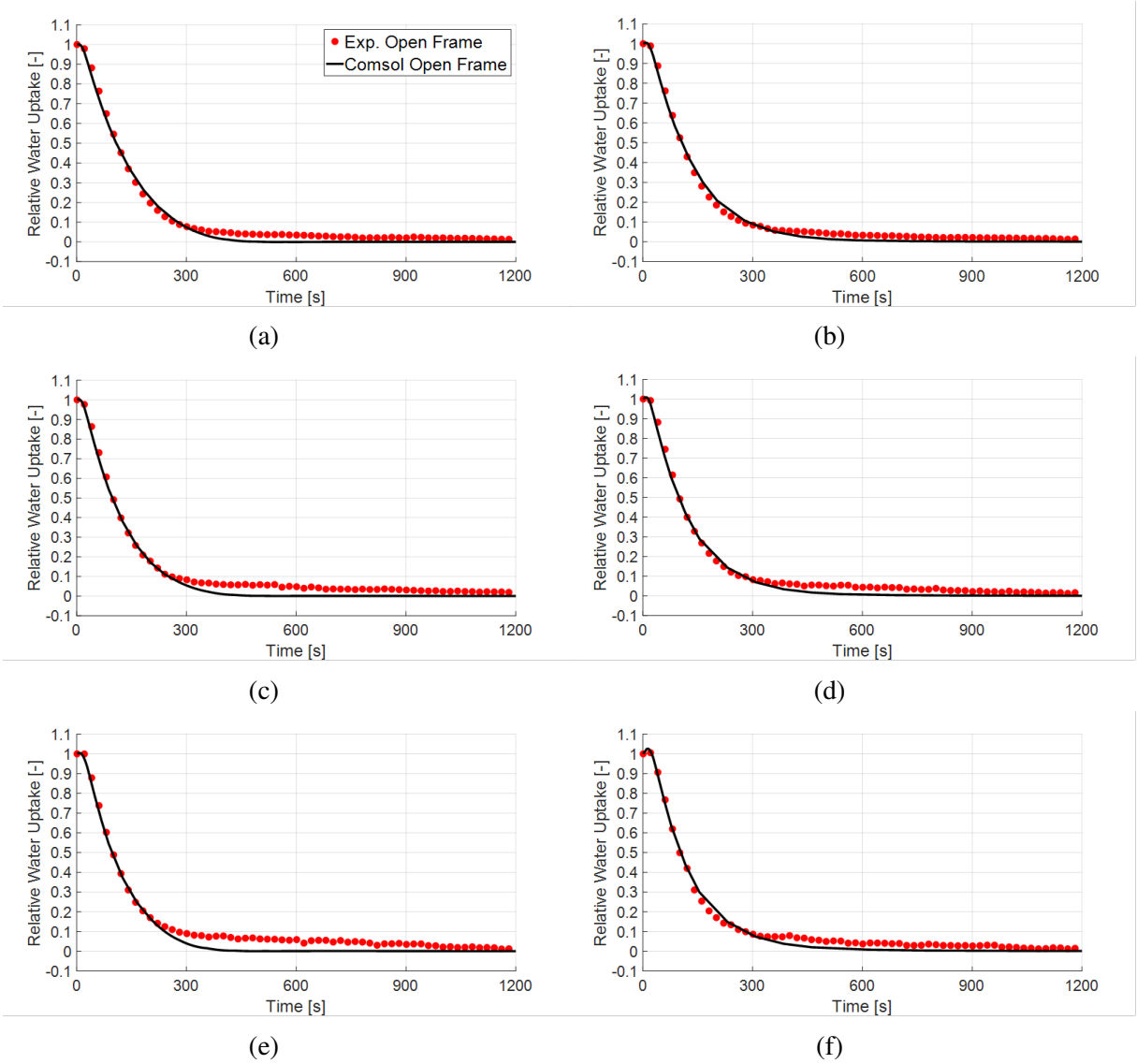

Fig. B.3 Best fitting of the numerical simulation results to the experimental data of the adsorbent sample tested in the open test frame of the GLX30 APHE, **desorption** processes; a) 15/30/90 °C , b) 15/35/90°C, c) 10/30/90°C, d)10/35/90°C, e) 5/30/90°C and f) 5/35/90°C.

References

Sapienza, A., Velte, A., Girnik, I., Frazzica, A., Füldner, G., Schnabel, L.& Aristov Y. (2017). Water - silica siogel working pair for adsorption chillers: Adsorption equilibrium and dynamics, *Renewable Energy*, *110*, 40–46. http://doi.org/10.1016/j.applthermaleng.2011.07.013

Appendix C

Publications and student theses

List of publications

Journal contributions

- M. Mikhaeil, M. Gaderer and B. Dawoud, " On the development of an innovative adsorber plate heat exchanger for adsorption heat transformation processes; an experimental and numerical study". *Energy* 207 (2020). https://doi.org/10.1016/j.energy.2020.118272.

- M. Mikhaeil, M. Gaderer and B. Dawoud, " Experimental investigation of the adsorption and desorption kinetics on an open-structured asymmetric plate heat exchanger, matching between small-scale and full-scale results". *Frontiers in Energy Research* 10 (2022). https://doi.org/10.3389/fenrg.2022.818486.

- M. Mikhaeil, M. Gaderer and B. Dawoud, "On the application of adsorber plate heat exchangers in thermally driven chillers; An experimental and analytical study". *Applied Thermal Engineering* 220 (2023). https://doi.org/10.1016/j.applthermaleng.2022.119713.

- M. Mikhaeil, S. Nowak, V. Palomba, A. Frazzica, M. Gaderer and B. Dawoud, "Experimental and analytical Investigation of applying an asymmetric plate heat exchanger as an evaporator in a thermally driven adsorption appliance". *Applied Thermal Engineering* 228 (2023). https://doi.org/10.1016/j.applthermaleng.2023.120525.

Conference contributions

- M. Mikhaeil, M. Gaderer and B. Dawoud, "Investigation of an innovative adsorber plate heat exchanger for adsorption heat transformation processes", 5^{th} *International Symposium on Innovative Materials for Processes in Energy Systems (IMPRES2019)*. Kanazawa, Japan, October 2019.

- D. Malzkorn, M. Mikhaeil and B. Dawoud, "Assembly and Investigation of a Compact Adsorption Heat Storage Module", *Regensburger Applied Research Conference (RARC2020)*, Regensburg, July 2020

- M. Mikhaeil, M. Gaderer and B. Dawoud, "An experimental study on the effect of the heat and mass transfer characteristic lengths on the adsorption dynamics inside two different open structured plate heat exchangers". 9^{th} *Heat Powered Cycles conference (HPC2021)*. Bilbao, Spain, April 2022.

- A. Crespo, V. Palomba, M. Mikhaeil, B. Dawoud, A. D. Gracia Cuest and L. F. Cabeza, "Experimental study of a LiCl/Silica gel sorption thermal energy storage prototype", *XII National and III International Conference on Engineering Thermodynamics*. Madrid, Spain, June 2022

- M. Mikhaeil, M. Gaderer and B. Dawoud, "A comparative experimental study on the dynamic performance of two different adsorber plate heat exchangers for adsorption energy", 6^{th} *International Symposium on Innovative Materials for Processes in Energy Systems (IMPRES2022)*. Barcelona, Spain, October 2022.

- M. Mikhaeil, A. Frazzica, V. Brancato, M. Gaderer and B. Dawoud, "Experimental investigation of an adsorbent mixture for a closed-structured adsorber plate heat exchanger", 6^{th} *International Symposium on Innovative Materials for Processes in Energy Systems (IMPRES2022)*. Barcelona, Spain, October 2022.

- M. Mikhaeil, W. Lombardo, A. Sapienza, M. Gaderer and B. Dawoud, "Performance prediction of an adsorber plate heat exchanger utilizing two different adsorbents for application in an adsorption chiller", 6^{th} *International Symposium on Innovative Materials for Processes in Energy Systems (IMPRES2022)*. Barcelona, Spain, October 2022.

- V. Brancato, L. Gordeeva, A. Capri, D. Rosa, B. Dawoud, M. Mikhaeil, Y. Aristov, Boreskov and A. Frazzica, "Experimental characterization of thermal energy storage density of composite sorbents under variable operating conditions", 6^{th} *International*

Symposium on Innovative Materials for Processes in Energy Systems (IMPRES2022). Barcelona, Spain, October 2022.

Student theses supervised during this work

- M. Yousfi, "Experimentelle Untersuchung verschiedener Einflussfaktoren auf die Adsorptionskinetik von Wasserdampf in Siogel und SWS zur Optimierung der gekoppelten Wärme- und Stoffübertragung", written in German, Bachelor's thesis, OTH Regensburg (2020).
- D. Malzkorn, "Development and optimization of a vacuum valve and its implementation in a demonstration prototype of a multi-modular seasonal adsorption thermal energy storage", Master's thesis, OTH Regensburg (2021).
- S. Nowak, "Analytical and experimental investigation of applying an asymmetric plate heat exchanger as an evaporator/condenser in a small-scale thermally driven adsorption chiller", Master's thesis, OTH Regensburg (2021).
- M. Khalifa, "Aufbau und Inbetriebnahme einer Latentwärmespeichereinheit zur Validierung eines thermodynamischen Berechnungsmodells", written in German, Bachelor's thesis, OTH Regensburg (2022).